Technical Report

TR-03-07

The Buffer and Backfill Handbook

Part 3: Models for calculation of processes and behaviour

Roland Pusch
Geodevelopment AB

January 2003

Svensk Kärnbränslehantering AB
Swedish Nuclear Fuel
and Waste Management Co
Box 5864
SE-102 40 Stockholm Sweden
Tel 08-459 84 00
+46 8 459 84 00
Fax 08-661 57 19
+46 8 661 57 19

The Buffer and Backfill Handbook

Part 3: Models for calculation of processes and behaviour

Roland Pusch
Geodevelopment AB

January 2003

Contents

1 Symbols and definitions[1]

a_c	=	activity
a_z	=	swelling index
A	=	cross section, creep parameter, weight percentage
A_s	=	contact area
b	=	soil structure coefficient, load factor
B	=	creep parameter
B_s	=	solid phase modulus
B_w	=	bulk modulus
c, c'	=	cohesion
C	=	heat capacity, concentration
C_c	=	compression index, gradation coefficient
C_u	=	uniformity coefficient
d	=	diameter, distance, sample thickness
d_{10}, d_{60}	=	grain diameters
D_a	=	apparent diff. coefficient
D_e	=	effective diff. coefficient
D_p	=	pore diffusivity
D_s	=	surface diffusion coefficient
e	=	void ratio
E	=	modulus of elasticity
F	=	force
g	=	gravity
g_o	=	organic content
g_1, g_c	=	ignition loss
G	=	shear modulus
h	=	settling distance
i	=	hydraulic gradient, activity
I_P	=	plasticity index
I_C	=	consistency index
I_L	=	liquidity index
k	=	(hydraulic) permeability, colorimeter reading
K	=	hydraulic conductivity, compression modulus
K_d	=	sorption factor
l	=	sample length (height)
l_c	=	content of particles with an equivalent stoke diameter smaller than 2 μm
L_S	=	linear shrinkage
m	=	mass, modulus number
m_j	=	modulus number (ref.)
m_s	=	mass of solid matter
m_w	=	mass of water
M	=	oedometer modulus
M^I ,M^{II},M^{III}	=	metal cations
n	=	porosity
p	=	normal stress
p_S	=	swelling pressure
P	=	vapor pressure
q	=	deviator stress
R	=	molar gas constant, roundness
R_S	=	shrinkage ratio
s	=	salt content of pore fluid, scale factor
S	=	expansion ("rebounce"), sphericity
S_r	=	degree of water saturation, vol %
S_t	=	sensitivity
t	=	time
T	=	temperature
u	=	porewater press.
ν	=	Poisson's ratio
V	=	bulk volume
V_d	=	volume of dry soil sample
V_p	=	pore volume
V_s	=	volume of solid matter
V_S	=	volumetric shrinkage
V_w	=	volume of water
V_g	=	volume of gas
w	=	water content (ratio)
w_L	=	liquid limit
w_P	=	plastic limit
w_S	=	shrinkage limit
x	=	variable
y	=	variable

[1] Only major ones are listed

α	=	heat expansion coefficient	ρ_w	=	density of water
α_s	=	swelling index	σ	=	pressure
β	=	stress exponent	σ^1	=	effective press.
ε	=	strain	σ_c^1	=	preconsolidation pressure
γ	=	shear strain	σ_j	=	reference stress
ξ	=	constitutional parameter	τ	=	shear stress
η	=	viscosity	τ_{fu}	=	undrained shear strength
λ	=	heat conductivity	τ_r	=	remoulded shear strength
ν	=	Poisson's ratio	ϕ	=	electrical potential
ρ	=	bulk density	ϕ, ϕ'	=	friction angle
ρ_d	=	dry density	Δl	=	shortening of sample with length (height) l
ρ_s	=	density of solid particles			
ρ_{sat}	=	density of fluid-saturated soil			

Note 1 on "Grain size"
In literature the grain size distribution is expressed as "Percentage finer than", "percent finer by weight", "weight percent passing" etc. They appear in various diagrams quoted from literature sources.

Note 2 on "Symbols"
Some additional symbols that appear in the Handbook are not included here as they are self-explanatory or defined in the text.

2 Introduction

2.1 General

Comprehensive work has been made in the last decades in Sweden and other countries for finding suitable components of the multibarrier system that will make up repositories for radioactive waste. A large number of scientific papers and technical reports have been published on them, e.g. the clay barriers, on which the present document is focused. Much of the work that has been performed since systematic work started some twenty-five years ago has concerned the physical properties of certain reference clays and the chemical stability of smectites under the hydrothermal conditions that prevail in deeply located repositories with highly radioactive waste /1/. It was early recognized that the various laboratory methods and preparation techniques need to be standardized for making results from different laboratories and test sites comparable and this led to the decision to prepare a handbook with Part 1 of a trilogy forming a laboratory manual, Part 2 comprising a material database including preparation and field testing methods, and Part 3 forming a collection of physical and mathematical models and examples of how they can and should be applied.

The present document, which has been prepared by Geodevelopment AB, Lund, Sweden, in cooperation with TVO, Finland, makes up Part 3. The content emanates from an earlier version prepared together with Clay Technology AB and refers to various studies performed in SKB's and TVO's R&D work on the performance of buffers and backfills, as well as to a number of other activities in the fields of soil mechanics and soil physico/chemistry. The intention is to collect conceptual and mathematical models that have been proposed for describing the performance of buffers and backfills and processes in them that are related to their function under repository conditions.

As in the preceding parts the following types of sealing components are defined:

1. Buffers – canister-embedding materials with smectites as most important isolating component. They are prepared in the form of precompacted blocks or by on-site compaction of clay granules.
2. Backfills – mixtures of smectitic clay and ballast of rock-forming minerals with the ballast as most important component.
3. Plugs – smectite clay in the form of precompacted blocks for sealing openings like recesses, boreholes and tunnels and shafts.
4. Grouts – very smectite-rich gels prepared for injection in rock fractures.

The most important function of buffer and backfill in a repository is to provide isolation to the canisters with their radioactive content. By definition, the buffer shall be so composed that radionuclide transport in the clay-based barriers takes place by diffusion and not by water flow, which makes it important to predict the extent and rate of diffusive transport of such elements through the buffer. It depends strongly on the density and homogeneity of the buffer, which in turn depend on the maturation rate and the ultimate degree of homogeneity of the buffer. They are influenced by the temperature and temperature gradient that exist in the initial phase of water saturation, in which the hydraulic interaction with the nearfield rock is also important.

In this context the backfill plays two roles, firstly, to limit the upward movement of the strongly expansive buffer in the deposition holes by having a low compressibility and, secondly, to provide support to the roof and walls of the deposition tunnels by exerting an effective pressure on them.

2.2 Scope

Design of suitable buffer and backfills hence requires that their performance can be quantified, which requires that the various processes can be modeled conceptually and expressed in mathematical form. Based on the present knowledge this can only be made for some of the involved mechanisms and for coupled processes there is still a very limited number of mathematically expressed computational codes.

The design work must also take chemically induced changes of the buffer and backfill porewater and minerals into consideration, which presents additional difficulties since many of the involved processes are not well known. Thermodynamics is commonly applied for this purpose and it will be referred to in the present document. However, since the issue of chemical processes in buffers and backfills is a scientific field per se only models describing the most practically important functions will be described.

The models referred to here are conceptual in the first place, defining the respective processes and material property parameters. The quick development of computational tools, numerical as well as analytical, makes it irrelevant to give detailed descriptions of them, while the various assumptions on which they are based – especially the conceptual models – have been considered in some detail. The models of practical use are only described in general terms and examples at the end of the respective chapter illustrate how they can be utilized.

A very important fact is that transport and rheological processes in a repository are hardly ever of simple nature. They are coupled to other processes and affected by various restrictions such as limited access to water and transient interaction with dissolved species. This makes the issue of coupled models very important but almost all the models and codes that are being used in predicting the behaviour of buffers and backfills in a repository are simplified and incomplete with respect to the hydrothermal processes. This is because of the lack of understanding of the involved physico-chemical mechanisms, for which consideration of the behaviour of the clay on the microstructural level is required. Several workshops dealing with these matters have been held in the last 7 years and some of the findings appear in this part of the Handbook.

There is some deliberate overlap of the contents of the three parts of the Handbook since it should be possible to read and digest the parts individually.

2.3 Major contents of Chapters 3–11

Chapter 3 deals with microstructural issues focusing on particle interaction and void distribution in buffers and backfills with special respect to swelling pressure and permeation of fluids and gas. The chapter makes up a considerable fraction of this part of the Handbook since it is basic to the understanding of all important physical properties of

soils and forms a basis of many of the models describing the various bulk physical properties of buffers and backfills.

Chapter 4 deals with heat transport in fully and partly water saturated buffer clays. It includes mathematical formulation of empirically deduced material models of heat conductivity and gives examples of how this quantity can be evaluated from laboratory experiments.

The accuracy of heat conductivity data is important for predicting the temperature conditions in the buffer and hence for assessing conversion of smectite to non-expanding minerals and for estimating precipitation and cementation effects.

Chapter 5 deals with flow of water in liquid and vapour form in fully and partly water saturated buffers and backfills. The presented material models are intended for practical use and imply that potential theory in the form of Navier/Stoke's laws for analytical solution or numerical methods are valid. These detailed ways of calculation are not described here but merely the features and use of the basic material models.

Chapter 6 gives the basis of currently used material models for anion and cation diffusion through smectitic soil. Complexation may cause considerable deviation from theoretically derived migration rates and only diffusive transport of species that do not undergo chemical reactions is treated here. Focus is on outlining the formulation of theoretical models for evaluation of diffusion coefficients from controlled experiments. The importance of the porewater chemistry in terms of pH, eH and content of dissolved minerals is treated in Chapter 9.

As for water transport, the solution of practical 2 and 3D problems is made by use of potential theory, applying analytical or numerical techniques, which are not treated here.

Chapter 7 deals with gas movement through buffers and backfills. Physically, this process is not totally understood and only simple material models have been proposed in the literature. However, they all imply, although on different premises, that a certain threshold pressure must be overcome for the gas to move in gaseous form and a generalized model based on this criterion is described here.

Solution of gas-related problems represented by large-scale 2D and 3D cases makes it necessary to accurately define the boundary conditions, like the gas production rate and – for gas flow over large distances in the vertical direction – the solubility of gas. This is not included in this section, which is intended to describe the principle of gas transport through clay elements using a simple material model.

Chapter 8 deals with modeling stress/strain/time behavior of buffers and backfills. Focus is on the definition of a general rheological model and its implementation in the ABAQUS code by use of which the strain and stress conditions in fully water saturated buffer can be calculated as a function of time after imposing deformation. The interaction of buffer, rock and canister in deposition hole exposed to tectonically induced shearing is taken as an example of how rheological modeling can be made.

Chapter 9 deals with interacting processes in buffer clay. The issue is very complex and many problems dealing with physical and chemical changes that are in fact coupled are commonly dealt with by considering the respective phase separately without considering transients. The difficulty is that the mutual dependence of the involved mechanisms is commonly not well known. Only few models have been clinically tested to an extent that make them recommendable.

In this chapter we will confine ourselves to describe and exemplify two models, one for the mechanical behavior of unsaturated buffer with respect to heat and moisture flow, and the other dealing with geochemical transients during and after saturation of the buffer in canister deposition holes. The firstmentioned makes use of the ABAQUS code and the second employs the ARASE code. A code for determining the evolution of the chemistry of bentonite porewater (PHREEQE) is referred to as well.

Chapter 10 deals with the longevity of buffers and backfills. It is based on the Arrhenius-type model proposed to SKB as a working hypothesis for smectite-to-illite conversion, taking the temperature and access to dissolved potassium, as well as the activation energy, as controlling parameters. Examples of prediction of the conversion rate are given, using the numerical code FLAC.

Chapter 11, finally, gives rather complete descriptions of two numerical codes for predicting the hydration rate of smectitic buffer clay and the internal strain that takes place in the evolution of the maturing clay mass, considering the interaction with the surrounding rock. It also gives examples of application of the codes referring to the Prototype Repository Project at Äspö.

3 Microstructure of buffers and backfills

This chapter deals with the spacial organization of the solid constituents of buffers and backfills, focusing on particle interaction and void distribution with special respect to swelling pressure and permeation of fluids and gas. The chapter makes up a considerable fraction of this part of the Handbook since it is basic to the understanding of all important physical properties of soils and forms a basis of many of the models describing these properties.

A number of recent results that help to understand the processes that take place in clay-based engineered barriers are integrated in the text.

3.1 General

The performance of buffers with respect to all important functions is strongly dependent on the microstructure. We will confine ourselves here to deal with smectitic clay with montmorillonite as major clay mineral species.

By drying and grinding material from natural bentonite clay beds like those in Wyoming, Greece and Spain, one can obtain air-dry montmorillonite-rich powder that is suitable for preparing dense blocks by applying high pressure, or for mixing it with ballast for preparing backfills. Natural clay with relatively low smectite content can be used for backfilling.

We will consider here a basic case of compressed smectite-rich clay powder with a grain size ranging between 10 μm and 2 mm, representing an element of buffer clay, For such material microstructural models have been developed with the purpose of explaining the dependence of porewater composition on the hydraulic conductivity, gas conductivity and swelling pressure as well as rheological behavior. The first attempt to model the microstructure of matured clay formed by water saturation of highly compacted MX-80 powder, i.e. the GMM model, was proposed in 1990 /2/.

Additional attempts have been made later, yielding the ABAQUS model, the MMM model and the 3Dchan model. Table 3-1 presents the basic features of the three approaches. A tentative conclusion from ongoing testing is that the basic idea of the three models is valid, i.e. that most of the fluid percolation takes place through a very limited number of channels in soft parts of the clay structure, but that the GMM and MMM models can explain a number of bulk properties that the ABAQUS model cannot.

Table 3-1. Features of the four microstructural buffer models.

Approach	Dimensions	Evolution	Capacity to calculate
GMM	3D	Analytically derived final state of microstructure	Hydraulic conductivity and swelling pressure of artificial statistically sized and spaced grain systems (3D)
ABAQUS	2D	Successive evolution of microstructure is modeled	Hydraulic conductivity of simplified grain particle systems (2D)
MMM	3D	Final state of microstructure from digital micrographs	Hydraulic conductivity, swelling pressure, gas conductivity, internal erosion of true clay particle assemblies (3D)
3Dchan	3D	Analytically derived final state of microstructure	Hydraulic conductivity of artificial statistically sized and spaced grain systems (3D)

3.2 Buffer, the GMM model

3.2.1 Conceptual

The model is based on the assumption that the bentonite grains are isotropic and expand to hold 2 or 3 interlamellar hydrates depending on the available space and on the type of adsorbed cation (Na, Ca). Spontaneous exfoliation of stacks of lamellae takes place from parts of the grains that are not compressed and this leads to formation of clay gels in the "external" voids between the expanded grains as shown schematically in Figure 3-1. The density of the gels was taken to depend on the bulk clay density and on the size of the voids according to Table 3-2. For the sake of simplicity and clarity microstructural data refer to three specific clay densities (*A*,*B*,*C*) but extrapolation between them can be made.

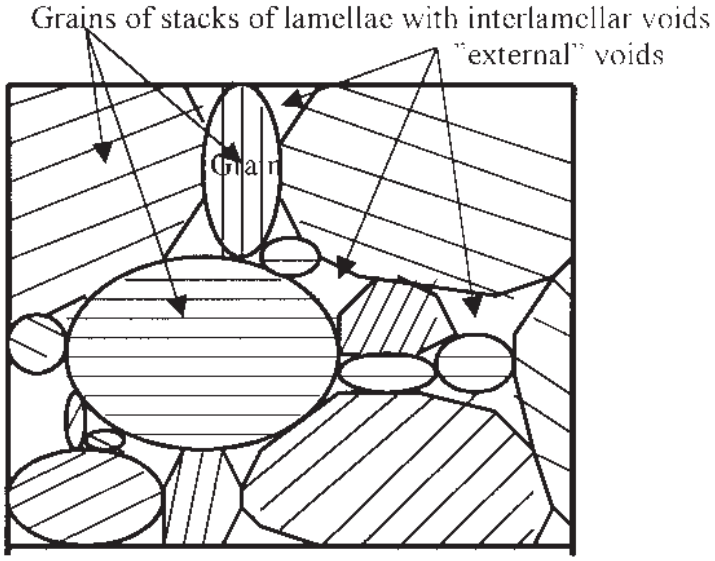

Figure 3-1. *Generalized microstructure of MX-80 clay of compacted powder grains. In conjunction with water uptake from the surroundings the powder grains expand and small aggregates and individual stacks of lamellae exfoliate and form gel fillings with different densities, lowest for the largest voids and highest for the smallest voids.*

Table 3-2. Density and effective porosity (*n*) of air-dry, smectite-rich powder /2/.

Clay type	Bulk density of air-dry powder kg/m^3	Dry density g/cm^3	Density at compl. saturation g/cm^3	*n*
A	2000	1800	2130	0.13
B	1500	1350	1850	0.35
C	1000	900	1570	0.57

Water uptake and expansion of the grains to hold 2 or 3 interlamellar hydrates yields the theoretical effective porosity given in Table 3-3. For the highest initial bulk density (Type *A*) complete uptake to 2 and 3 hydrates is not geometrically possible. A rather arbitrary assumption is that 2/3 of the grains expand to host 2 complete hydrates and that no aggregate takes up 3 hydrates.

3.2.2 Evolution of microstructure – water saturation and homogenization

Size distribution of "external" voids

The external void volume that remains after the expansion of the granules in the wetting process will not contain just pore fluid. Thus, soft clay gels exfoliated from the granules, are formed in the pore space and they largely determine the hydraulic conductivity of the bulk clay (Figure 3-2).

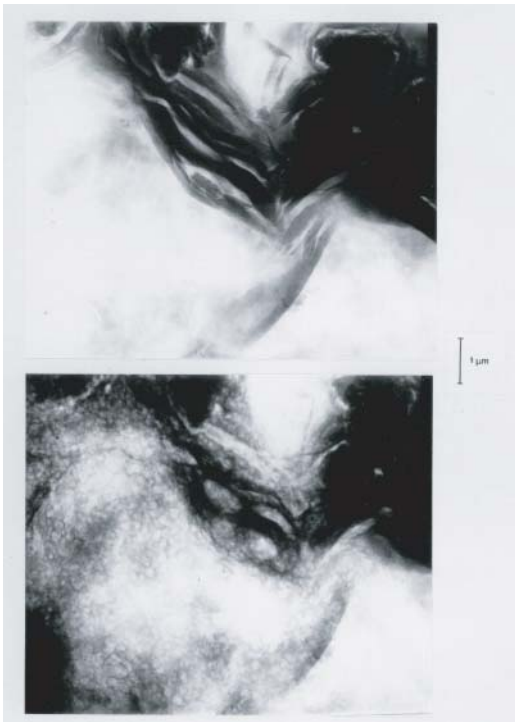

Figure 3-2. *Expansion of vacuum-dried MX-80 clay at hydration in humid cell placed in a 1.5 MV transmisson electron microscope /3/. Upper: Dry state. Lower: Hydrated/expanded state with soft gel adjacent to the aggregate.*

The density of these gels is assumed to depend on the size of the external pores, the size distribution of which is assumed to be log normal. In order to reflect the pore size ranges observed for the three types of clay by light microscopy, means and standard deviations are set to match the following conditions:

1. The minimum pore diameter for the three types of clay is taken as 0.1 μm.
2. For clays *A*, *B* and *C* the maximum pore diameters are 5 μm, 20 μm and 50 μm, respectively.

It is further assumed that 95% of the total pore space falls in the diameter intervals postulated above. The normal distribution will then, by definition, predict a small portion (2.5%) of the total external pore space to consist of pores with diameters larger than the maximum value. These pores are treated as maximum diameter pores when computing the hydraulic conductivity, the distribution functions being adjusted accordingly (Figure 3-3).

Another 2.5% portion will correspondingly fall outside the lower diameter limit, but, having no influence on the conductivity, it does not need to be further considered.

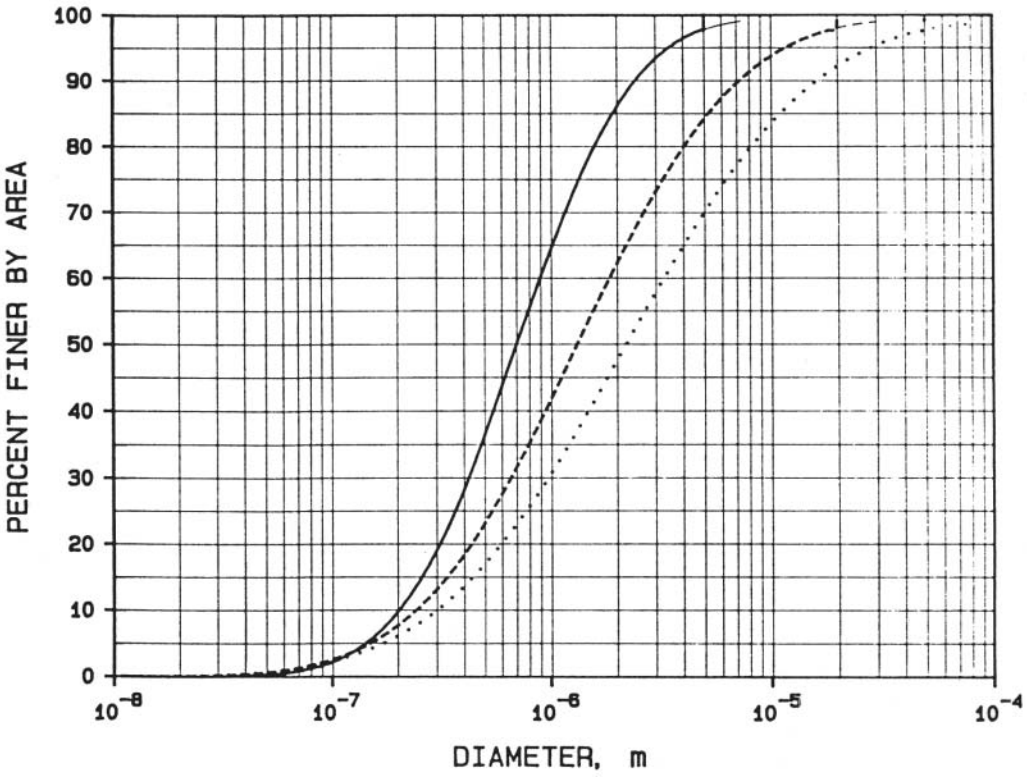

Figure 3-3. *Pore size distributions of clays A, B and C. The fine-pen tails at the upper part of the curves indicate the original log normal distribution functions used for determination of means and standard deviations. Clay A is marked by a full line and B by a broken line. The C-curve is dotted.*

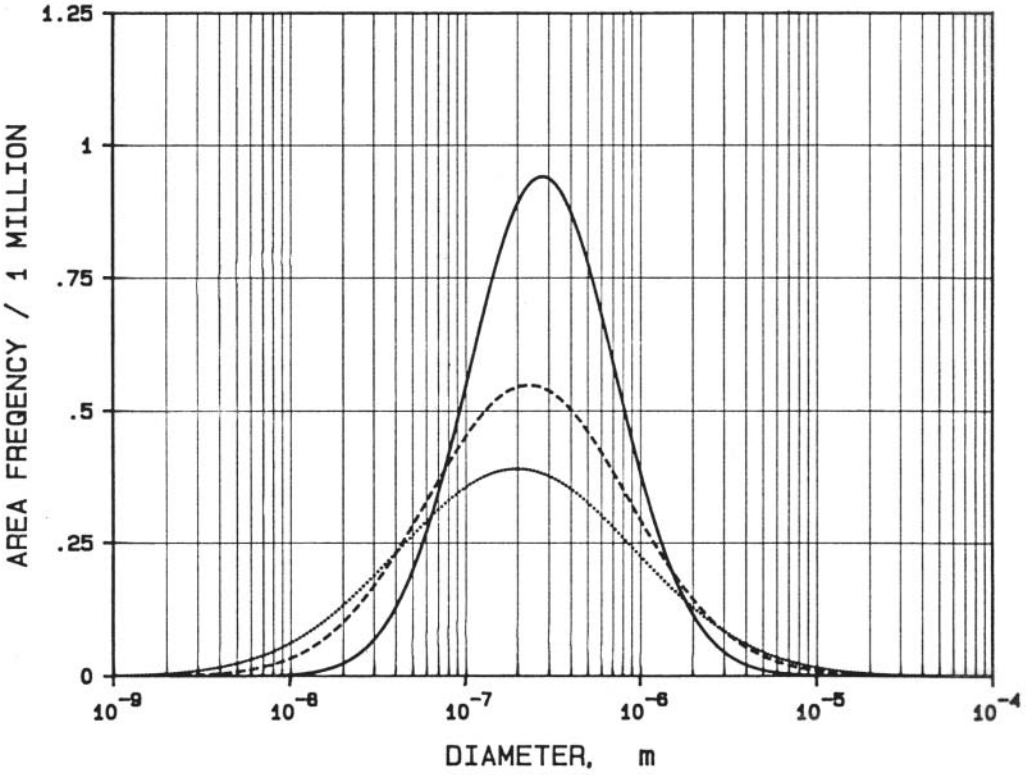

***Figure 3-4**. Distribution of the ratio of the pore cross section area and the total cross section area. Clay A is marked by a full line, B by a broken line and C by a dotted one /2/.*

The fraction of a cross section that is occupied by intersected pores is given by Figure 3-4. From this figure one finds, for example, that for Clay *A* the fraction of intersected pores sized 0.3–1 µm ($3 \cdot 10^{-7}$–10^{-6} m) is approximately 0.45 or 45% (mean value for the interval) x (interval length). The corresponding fraction for Clay *C* is only about 20%.

3.2.3 Density and structure of gel fillings

It is concluded from i.a. high voltage microscopy of hydrated Na montmorillonite gels /2/ that the density of clay gels is related to the bulk density at saturation and that this relation can be roughly generalized as shown in Table 3-3.

Table 3-3. Generalized data of gel density as a function of the bulk density and diameter D_e of external voids (saturated conditions), /2/.

Clay type	Bulk density	Gel density, g/cm³		
	kg/m³	D_e = 1–5 µm	D_e = 5–20 µm	D_e = 20–50 µm
A	2130	1.3	–	–
B	1850	1.3	1.2	–
C	1570	1.3	1.2	1.1

The arrangement of the particles constituting the gel fillings of the external voids can vary depending on how the exfoliation takes place and how released stacks are reoriented and coupled in the gelation phase /2/. For a simple cardhouse-type structure with cubical symmetry one gets the free space (d_1) of a "unit" cell of Na and Ca montmorillonite gels in Table 3-4. Each cell wall is assumed to consist of 1 stack holding 3 flakes in Na montmorillonite and 10 in Ca montmorillonite. Naturally, these assumptions are largely arbitrary and represent weak parts of the model. The smallest d_1 of the gels is hence about 0.03 μm and the largest 1 μm.

In practice, there is of course a stochastic variation in the gel structure, which is expressed by assuming constrictions of the gel void system as generalized in Figure 3-5. The entire arrangement of particles is of course also varying and in calculating flow the model implies that external gel-filled voids are twisted and winded, which is taken into consideration by assuming a crankshaft-type winding that corresponds to an average increase in length of connected external voids by 3 times according to probability analyses /2/. Of course these assumptions are hypothetical and weaken the relevance of this type of model.

Table 3-4. Average free space d_1 in gel fillings /2/.

Gel density	d_1, Å	
kg/m³	Na gel	Ca gel
1300	340	700
1200	570	1100
1100	1230	10000

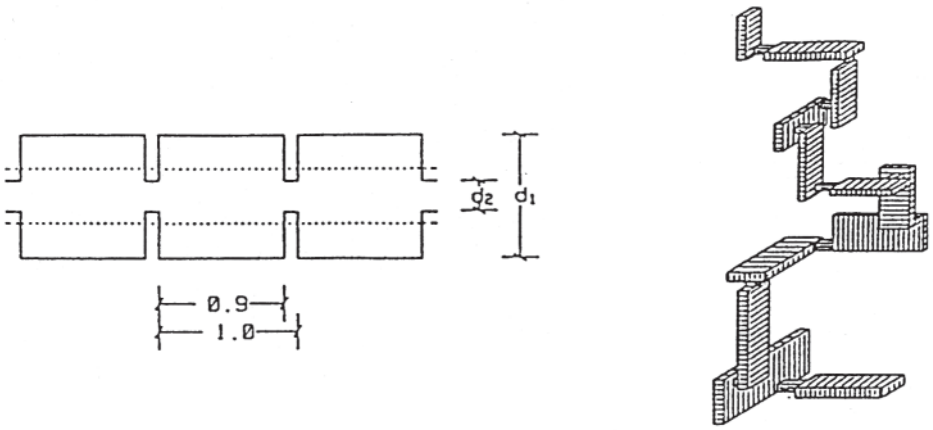

Figure 3-5. *Variations in shape of external voids. Left: Assumed regular constriction of intragel flow paths. For Na clay d_2=0.25 d_1, and n_1=0.9 (fraction length of wide part). Right: Schematic picture of winding external void system.*

3.2.4 Application of the GMM model

Hydraulic conductivity

Using the data in Table 3-4, corrected with respect to constrictions and assuming log normal distribution of the cross section area for each of the assumed clay gel densities 1100, 1200 and 1300 kg/m^3, the hydraulic conductivity of the clay gel network can be obtained by using the Hagen-Poiseuille law:

$$\Delta P = \Sigma \Delta P_i = q \cdot \frac{128\eta}{\pi} \cdot \Sigma \frac{l_i}{{d_i}^4} \tag{3-1}$$

where:

ΔP_i = pressure drop across the tube section with length l_i and diameter = d_i
q = flow through tube
η = dynamic viscosity of fluid

The gross conductivity K of the clay is determined by the conductivity of the clay gels contained in the external voids of the clay. It is defined as in Equation (3-2).

$$K = \frac{p \cdot \pi \cdot g \cdot \rho}{128 \cdot \eta} \int_{x_1}^{x_2} n(x) \cdot x^4 \cdot dx \tag{3-2}$$

where the symbols are the following:

Symbol	Description
x_2	upper diameter limit
x_1	lower diameter limit
n(x)×dx	number of pores per unit pore cross section area in the diameter range (x, x + dx)
p	porosity
g	acceleration of gravity
ρ	density of fluid
η	dynamic viscosity of fluid

n(x) is the log normal distribution of the cross section area of the intragel voids, which, for the three reference clays, is assumed to be as shown in Figure 3-6.

The hydraulic conductivity of the clay gels is evaluated by calculating their porosity from their density and then converting it to represent the aperture of capillary bundles with log normal distribution of the aperture and the same total porosity as of the gels. This gives, for the three specific reference clays in Na form, the data in Tables 3-5 and 3-6.

Table 3-5. Porosity of soft Na clay gels /2/.

Density, kg/m^3	Porosity
1300	0.14
1200	0.17
1100	0.20

Table 3-6. Hydraulic conductivity of soft Na clay gels /2/.

Density, kg/m^3	Hydraulic conductivity, m/s
1300	4E-12
1200	2.1E-11
1100	9.8E-11

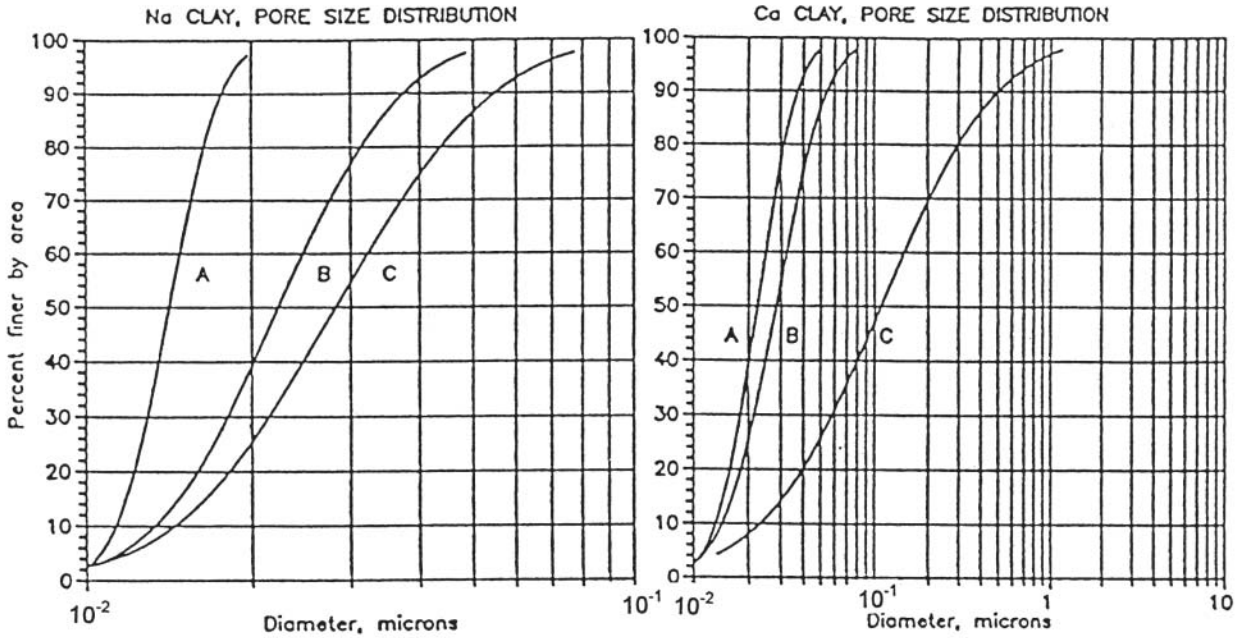

Figure 3-6. Distribution of the cross section area of intragel voids of the three reference clays, considering the representation of the three specific gel densities 1100, 1200 and 1300 kg/m^3 in the respective Na-clay /2/.

While the soft gel fillings are supposed to have a fairly open and regular structure yielding straight flow paths, the tortuous "crankshaft"-shaped branches of the network of continuous external voids implies an increased length of flow that is considered by dividing the derived *K*-value by 3. The evaluated average hydraulic conductivity of the three reference clays is given by Table 3-7 for Na- and Ca-states. Data from laboratory experiments with bentonites in Na and Ca forms agree well with those in the table /2/.

Table 3-7. Average hydraulic conductivity of reference clays *A*, *B*, and *C* /2/.

Clay	Bulk density, kg/m^3	"Effective porosity" (Na-form)	Average hydraulic conductivity, m/s, Na-form	Average hydraulic conductivity, m/s, Ca-form
A	2130	0.015	2.1E-14	7.5E-14
B	1850	0.050	2.6E-13	2.1E-12
C	1570	0.370	4.3E-12	1.1E-9

Gas conductivity

Theoretically, it should be possible to calculate the conductivity of gas by using Equation (3-2) if a relevant viscosity figure is applied, i.e. approximately 1/1000 of that of water. However, propagation of gas under pressure is expected to displace parts of the soft gels in the external voids and change the microstructure /4/. The available space for gas transport will hence be larger than the intra-gel void space in Table 3-4 and it may approach or even exceed that of the external voids, the diameter of which is shown in Table 3-8.

The resistance to gas-induced compression of the clay gels in the external voids is determined by their swelling pressure according to the model. The net diameter of external voids with compressed clay gels coating their walls can be derived by calculating the reduction in free space d_1 in Table 3-4 on consolidation by gas pressure. Thus, an axially oriented gas channel in the center of an external void will grow in diameter on the expense of the volume of the clay gel by which the gel density increases until the swelling pressure equals the gas pressure.

Table 3-9 gives the resulting diameter of the external voids in Na clay. It can probably increase to more than 0.5–1 µm for the most dense clay, which means that the capillary pressure in the widest gel channels (0.02–0.03 µm in Figure 3-6) drops from initially several MPa before gas penetration to around one hundred kilopascals and hence provides very little flow resistance to the gas once it has penetrated the dense clay.

Using the quartz capillary analogy the required gas overpressure ("critical gas pressure") to cause penetration would need to be according to Table 3-9.

The gel channel diameters corresponding to the critical gas pressures in Table 3-9 fit rather well with those in Table 3-4. The pressures appear to be on the same order of magnitude as actually recorded swelling pressures, which is very low for the softest clay *C* and very high for clay *A*. The GMM model hence describes the gas penetration process in a physically feasible fashion independently of whether water is compressed in conjunction with the gel consolidation or expelled from the gel ahead of the propagating gas. Time effects are not included in the model but it is possible to take them into account by modeling the gel consolidation process.

Table 3-8. Mean value and standard deviation of the diameter of gel-filled external voids in Na clay /2/.

Clay	Mean value, µm	Standard deviation, µm
A	0.70	0.42
B	1.32	0.58
C	2.20	0.68

Table 3-9. "Critical gas pressure" p_c of quartz capillaries with diameter *D* /2/.

D, µm	p_c , MPa
200	0.001
20	0.014
2	0.14
1	0.3
0.1	3.0
0.01	30.0

Swelling pressure

No general mathematical expression of the swelling pressure of smectite clay has yet been proposed for the GMM model. However, an attempt has been made to use the model for estimating the bulk swelling pressure by assuming that this pressure is the ratio of the sum of the local repulsive forces acting between aggregates and the total cross section area of a clay element. The gels in the voids between the aggregates were assumed to contribute insignificantly to the bulk pressure. The swelling pressure in bulk p_s was expressed as:

$$p_s = \alpha(\Sigma p_i A_i)/A \qquad (3\text{-}3)$$

where:

p_i = "True" swelling pressure of aggregates (stacks) with only interlamellar water
α = Aggregate orientation factor
A_i = Contact area of interacting particle aggregates
A = Total area of unit cross section

Assuming for isotropically compacted clay that 1/3 of the aggregates are oriented with the crystallographic *c*-axis in the direction of the considered swelling pressure, one gets α=1/3. Applying Yong and Warkentin's theory /5/ and taking the "true" swelling pressure to depend on the number of interlamellar hydrates the data in Table 3-10 are obtained. It is obvious that the fitting is poor except for the B-type. Provided that the model is valid in principle, the misfit for the A clay is believed to be caused by an incorrect orientation factor, while the A/A_i ratio is questionable for the C-type. In fact, the validity of the entire model is debatable on the ground that ordinary colloid-chemical attraction/repulsion theory with both cat- and anions in the interlamellar space may not apply.

Table 3-10. Bulk swelling pressure as predicted on the basis of the GMM model.

Clay type	p_i, MPa	A/A_i	p_s, MPa, Predicted	p_s, MPa, Experimental
A*	12	0.99	3.8	10–15
B	5	0.95	1.6	0.5–1.5
C	5	0.64	1.1	<0.2

* 2/3 of the aggregates host 2 interlamellar hydrates and the rest 1 hydrate layer

Ion diffusion

The GMM model has been used for demonstration that anions are excluded from a large fraction of the clay matrix /4/. Thus, the "effective" porosity n_e, corresponding to the external voids, which is the only space where anions can move according to the Donnan principle, is only 0.015 for the *A*-type clay while it is 0.05 for the *B*-clay and 0.37 for the *C*-clay. Since cations like Li and Na can move through both the interlamellar space and the external voids, the "effective" porosity is higher for them, i.e. 0.34 for the *A*-clay, 0.50 for the *B*-clay and 0.66 for the *C*-clay. This is exemplified by the trend in Figure 3-7, which shows that the effective diffusion coefficient for Cs is about ten times higher than for Cl at a dry density of 800 kg/m^3 (1500 kg/m^3 at complete fluid saturation) while it is about 25 times higher at 2000 kg/ m^3 (2250 kg/m^3 at complete fluid saturation).

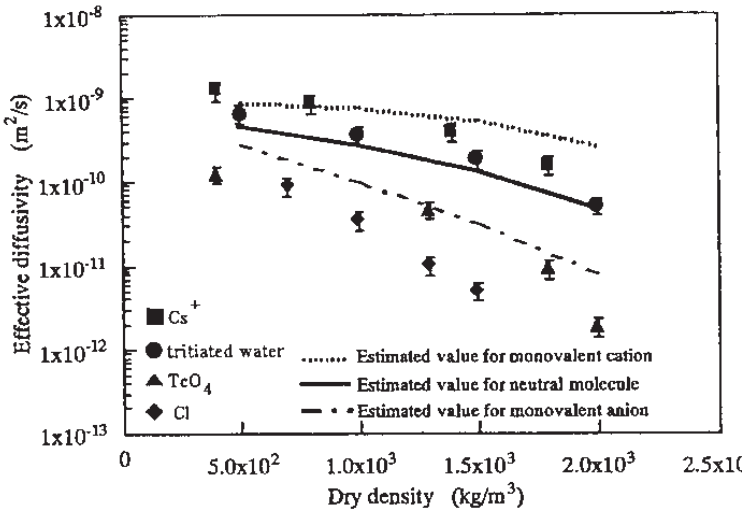

Figure 3-7. *Measured and calculated effective diffusivities for smectie-rich clay /6/.*

3.3 Buffer, the ABAQUS model

3.3.1 General

An attempt was made a number of years ago to investigate how the Hernelind/ Börgesson ABAQUS model, used in THM calculation of the macroscopic behavior of EBS buffers, applies to the microscopic scale and this has given some interesting results, primarily concerning the degree of homogeneity of the clay matrix and the rate of maturation /7/. The calculation procedure and major results are described here.

3.3.2 Calculation of void ratio and pore pressure distribution in maturing MX-80 bentonite using the ABAQUS model

Microstructural model

The bentonite grains, which are assumed to be equally large with a diameter of 1 mm, form an assembly that is shown in Figure 3-8. In 3D it would correspond to the basic case of cubical packing with a porosity of 0.476, or a void ratio of 0.92, while in 2D the void ratio is about 0.40. This corresponds to a dry density of 1950 kg/m^3.

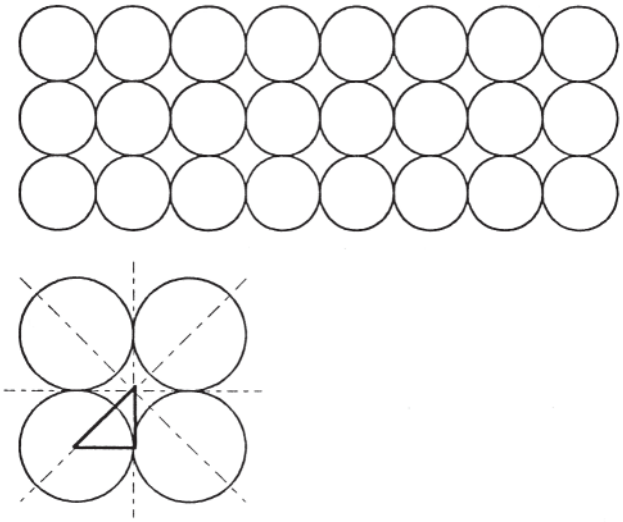

Figure 3-8. *Cubical packing of bentonite grains /7/.*

Material data

Grains

ρ_d = 1980 kg/m^3
ρ_s = 2270 kg/m^3

ρ_s = 2790 kg/m^3
B_s = 2.1·10^8 kPa (bulk modulus of solid particles)

Clay matrix

ρ_d = 1560 kg/m^3
ρ_s = 2000 kg/m^3
e = 0.79

Water

ρ_w = 1000 kg/m^3
B_w = 2.1·10^3 kPa (bulk modulus of the pore water)

The ABAQUS code requires that the hydraulic conductivity is put in and for the present application the bulk conductivity was used. The driving force for hydration of the dense clay grains was taken as the suction, which was assumed to correspond to the swelling pressure with inverted sign.

Hydraulic conductivity

Hydraulic conductivity data are those in Table 3-11.

Table 3-11. Assumed hydraulic conductivity *K* as a function of the void ratio *e*. Distilled water.

Density at saturation, kg/m³	Clay type	*e*	*K*, m/s
2130	A	0.45	E-14
2000		0.70	6E-14
1850	B	1.00	3E-13
1670		1.50	2E-12
1570	C	2.00	7E-12
1430		3.00	4E-11

Pore pressure

$u_0 = -30\ 000$ kPa

where u_o is porewater tension due to the hydration potential. It has the same absolute value as the swelling pressure.

Rheology – Cap plasticity

a = 2.58 (parameter that determines the failure envelop)
c = 2.40 (parameter that determines the critical state line)
b = 0.77 (parameter that determines the curvature of the failure envelope)

$p_f = -25\ 000$ kPa (intersection between the flow surface and the p-axis)
γ = 0.1 (shape of the elliptic cap)
K = 1.0 (relation between the shear strength at triaxial extension to the shear strength at triaxial compression)
$p_b = 30\ 000$ kPa (preconsolidation pressure)

Rheology – Cap hardening parameters (Table 3-12)

Table 3-12. Cap hardening parameters.

p, kPa	$^{e}\log(1+\varepsilon^{v}_{pl})$
100	0
400	0.192
1200	0.299
3500	0.379
8500	0.415
17000	0.444
31000	0.500

p = average stress

ε^{v}_{pl} = plastic volumetric strain

Rheology – Porous elasticity

κ = 0.22
ν = Variable with
ν_0 = 0
ν_{max} = 0.47
η = 0

where:

ν_0 = Basic value of Poisson's ratio
ν_{max} = Maximum value of Poisson's ratio
η = Ratio of q/q_f below which n is constant $(=\nu_0)$

Definition of problem

The problem is to determine the distribution of the void ratio and porewater pressure of a unit volume of clay.

Solution

The clay grains are assumed to be water saturated with a water content of w=14% from start and the voids between them are also assumed to be filled with water from start. The ballast grain are modelled as rigid, fixed bodies.

The finite element net is shown in Figure 3-9. It is in 2D and has three plane, fixed boundaries and consists of 111 plain strain elements with 8 nodes each. The surface of the bentonite grain is curved and free to move as a consequence of the expansion of the grain, which is to be determined.

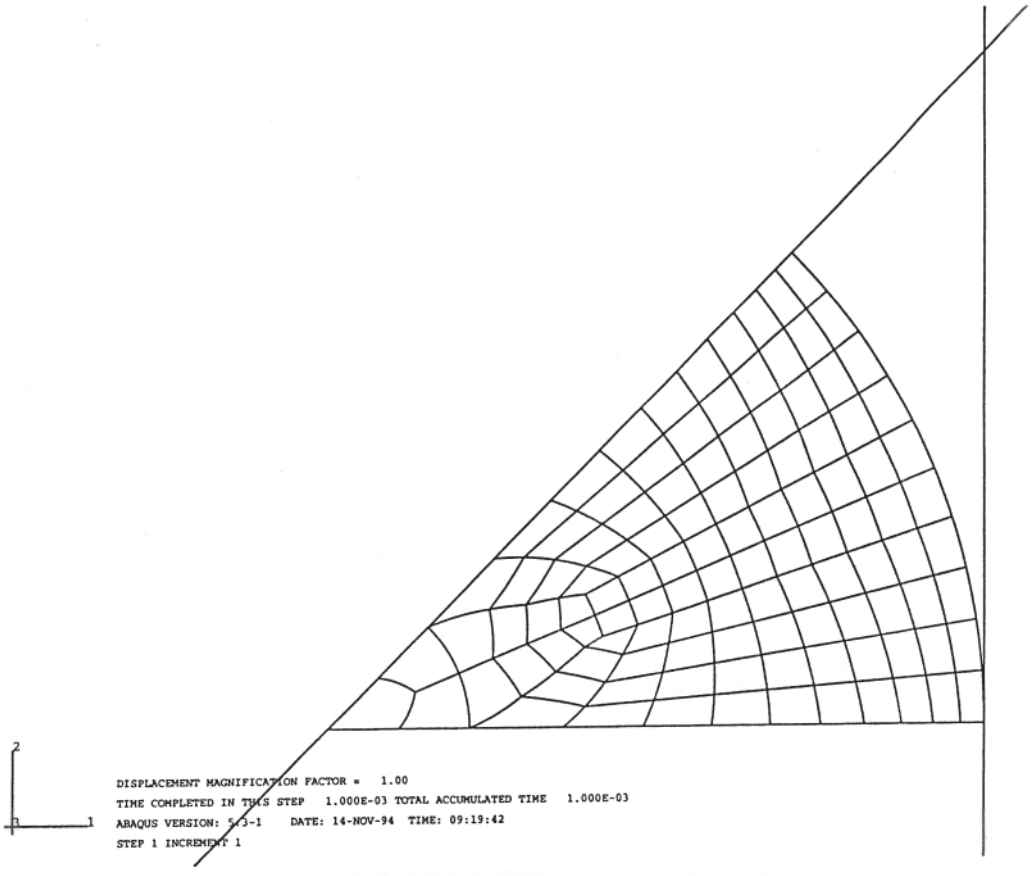

Figure 3-9. *Finite element net /7/.*

Using the ABAQUS code the expansion of the bentonite grain is determined and also the stress conditions and porewater pressure in each element as a function of time. The void ratio and pore pressure are given as contour plots for selected times after onset of the expansion. Figures 3-10 and 3-11 show plots of the void ratio with the deformed element mesh as background.

According to the calculations the initially open void is filled already after about 40 seconds with a clay gel that is very soft with a void ratio of up to e=2.5. However, the pore pressure was far from evened out at that time. Further redistribution of water and solid matter took place at a dropping rate but after some 28 hours the degree of inhomogeneity was still considerable and remained so. The ultimate stage corresponded to a minimum void ratio of about e=0.7 (ρ_d=1630 kg/m^3; ρ_m=2050 kg/m^3) and a maximum void ratio of about e=1.1 (ρ_d=1320 kg/m^3; ρ_m=1850 kg/m^3).

The increase in pore pressure was very strong between 30 and 60 seconds, in which period it changed from –26 MPa to –8 MPa. The dissipation then continued until complete equilibrium was reached.

The ultimate state with water and solids in equilibrium implies that there is an elliptic part (white) with a hydraulic conductivity of more than 5E-13 m/s embedded in the clay matrix, the most parts of which have a conductivity of around 6E-14 m/s. One concludes that this way of modeling gives distributions of the density and conductivity that are similar to those of the GMM. Thus, calculation of the net conductivity with respect to the varying density and assuming flow to take place normal to the edges of the unit element in Figure 3-11 gives K=5E-13 m/s, which is about 5 times higher than experimental data (Table 3-10). It can be assumed that both gas percolation and ion diffusion are similar to what can be derived for Clay *B* using the GMM. Both microstructural models can be used for any type of adsorbed cations.

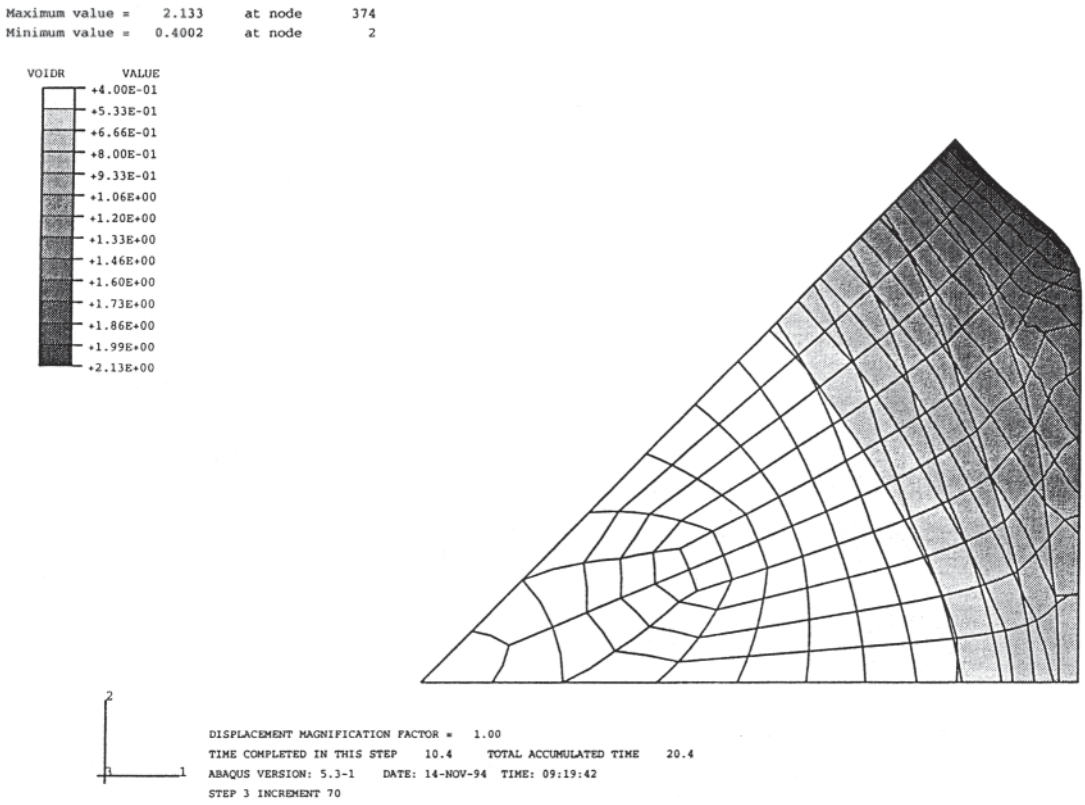

Figure 3-10. *Deformed element mesh and void ratio distribution after 11 seconds. The void is not yet filled at the upper right corner /7/.*

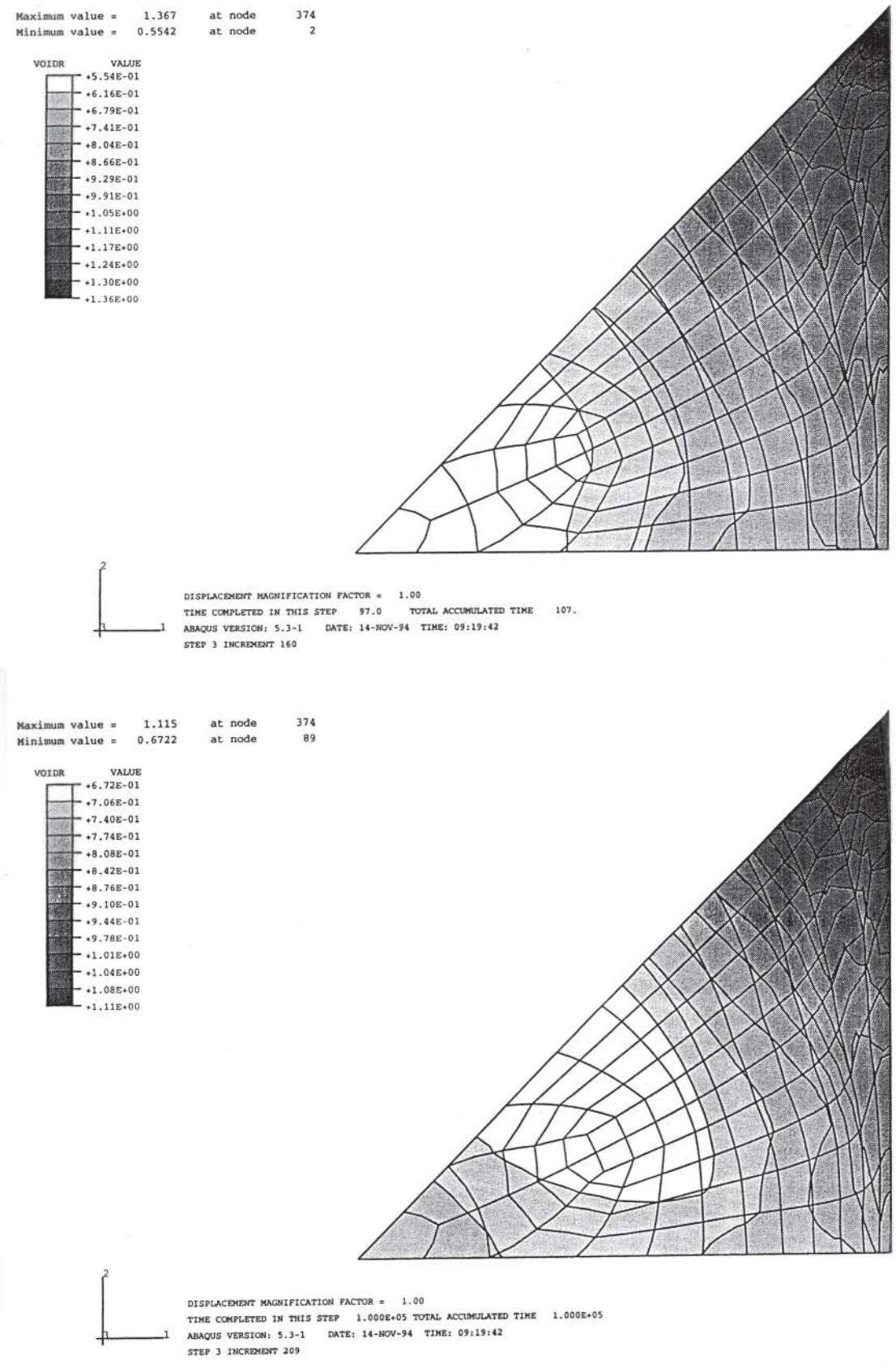

Figure 3-11. *Deformed element mesh and void ratio distribution after 97 s (upper). The lower diagram shows the conditions at equilibrium after 10 000 s /7/.*

While GMM is in principle a 3D model, the ABAQUS model represents 2D conditions in its present form. The major difference between the models is, however, that the last-mentioned allows for unlimited expansion with no reference to the maximum number of interlamellar hydrate layers. The clay is hence considered as a dense colloidal suspension.

3.4 Buffer, the MMM model

3.4.1 Conceptual

This model resulted from an attempt to describe the complete evolution of the microstructure, from the compression of MX-grains via hydration to a final equilibrium state for which the hydraulic conductivity, swelling pressure and ion diffusivity can be evaluated.

3.4.2 Evolution of microstructure

Compaction

The distribution of the grain size of most commercial ground bentonites, like MX-80, is exemplified by Figure 3-12 and it is generalized to consist of only two grain sizes in the MMM model, 0.10 and 0.35 mm. The proportions are taken as 8 small grains per big grain, both types being spherical and forming a system of cubical packing before compaction. Hence, the big grains are separated by small grains at their contacts (6 per big grain) and with small grains (2 per big grain) in the voids. This arrangement gives a density that represents the structure obtained when carefully pouring air-dry MX-80 powder into a cell for compaction, i.e. a dry density of 570 kg/m^3 and a density of 1370 kg/m^3 at water saturation.

At dense layering, representing slight compaction, each big grain is assumed to be surrounded by 8 small ones in cubical arrangement (Figure 3-13). The dry density of the grains, which contain some water-filled isolated very small voids and 1–2 interlamellar hydrates, is defined as 1980 kg/m^3, yielding a dry density of 1210 kg/m^3 (1760 kg/m^3 at water saturation). This state approximately represents Clay *B* of the GMM, while further compression under 50–100 MPa pressure yields microstructural patterns typical of Reference Clay *A* of this model. Reference Clay *C* resembles the softest state described above. It is of little practical importance for modeling purposes.

The grains are assumed to have an initial water content of 10% by weight, which is a commonly found figure for material delivered from clay manufacturers.

Numerical modeling in 3D has been made for determining the microstructural changes induced by compaction of the unit cell in Figure 3-13, which represents. bentonite powder with an initial dry density of 1210 kg/m^3. The calculations were made by use of the BEM code BEASY /8/, assuming the grains to behave elastically.

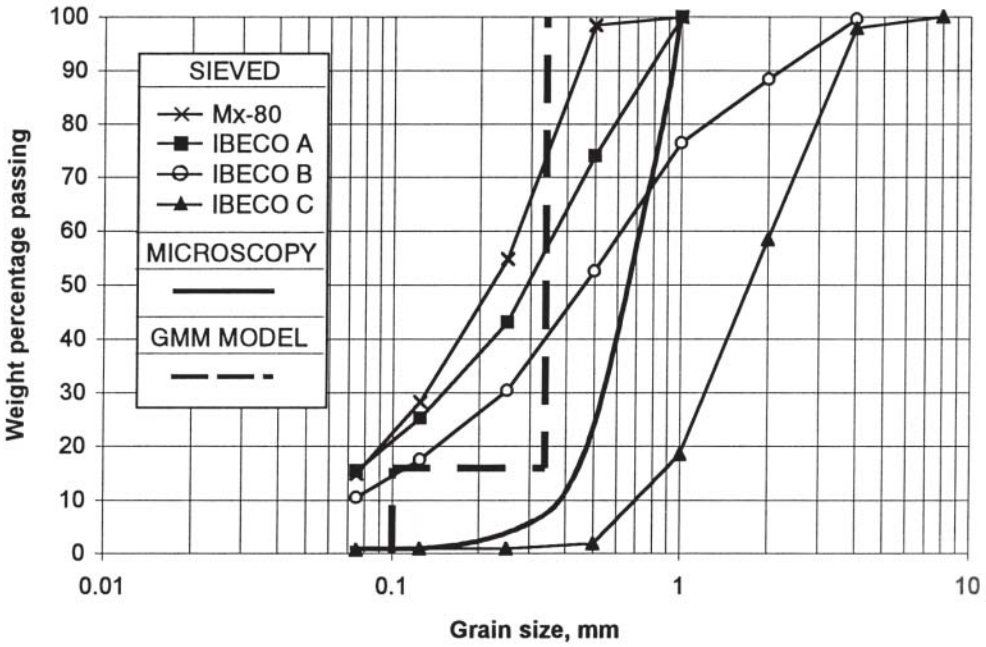

Figure 3-12. *Grain size distribution of commercial bentonite powders determined by sieving and microscopy. The broken curve represents the presently considered material with two grain sizes, which resembles the Greek IBECO A bentonite.*

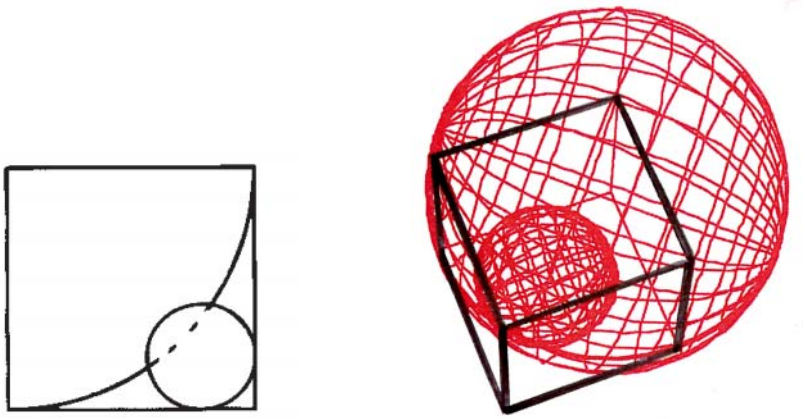

Figure 3-13. *3D arrangement of clay powder grains in dense layering. Each large grain, 0.35 mm in diameter, is surrounded by 8 small ones with 0.10 mm diameter. The cube, which has an edge length of 0.225 to 0.175 mm, represents a unit cell with 1/8 of a large grain and one small grain.*

The following material data were used:

E = 5000 MPa for the powder
ν = 0.3 for the powder
n = 0.45 ("effective porosity of the powder")
ρ_d = 1210 kg/m^3 for the powder

The resulting uniaxial deformation of the system is about 28%, which is on the order of magnitude recorded at practical compression. The reduction in "external" pore volume is 34%, yielding an increase in dry density from 1210 kg/m^3 to 1760 kg/m^3, corresponding to the reference Clay *A*.

Hydration

The stress distribution implies very high normal stresses, up to about 200 MPa, in the central part of the big grain and at the contact between the two grains, meaning that no interlamellar water is left in these regions. Hydration of the deformed cell takes place to an extent that corresponds to the net repulsive pressure between parallel lamellae in the stacks, implying that the highly stressed parts remain unhydrated or nearly so, while the free edges of the grains move out and cause reduction in the size of the voids.

The microstructural changes caused by hydration were calculated by use of BEASY using a thermal analogy and a commonly assumed relation between swelling pressure and number of hydrated lamellae /9/. This leads to the formation of channels with varying width, which is illustrated by Figure 3-14 for the special case of no expansion beyond 3 interlamellar hydrate layers and no exfoliation of stacks of lamellae from the grains.

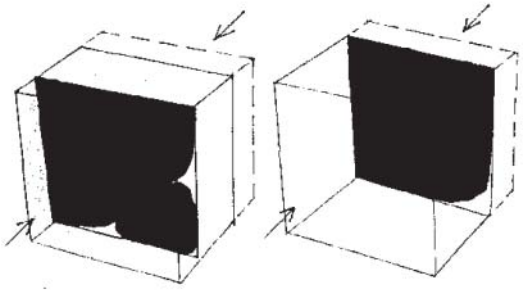

Figure 3-14. *The unit cell of MX-80 powder grain after compaction of initially slightly compacted powder under a uniaxial pressure of 100 MPa, and hydration of the grains. The two pictures represent cross sections through the compressed cell after interlamellar uptake of water to yield stress equilibrium.*

Examination of plotted consecutive sections shows that there are three open channels with 10–80 μm diameter in all sections, which would make the system as permeable as illitic clay. In practice, exfoliation of stacks and aggregates leads to the formation of clay gels in the channels, which significantly changes the void size distribution and density. The hydraulic conductivity is thereby strongly reduced.

The stochastic nature of the distribution of solids and voids of various size in the clay makes it virtually impossible to model the entire evolution on a molecular scale, while the microstructural constitution at equilibrium can be defined although there are problems like paying attention to the presence of other minerals than smectites in the case of MX-80. A very important factor that has to do with this is the scale-dependence. Thus, definition of representative elemental volume – REV – is required.

3.4.3 Conceptual model

Maturation of initially air-dry clay powder undergoing compaction and hydration under confined conditions yields a variation in density that determines the distribution of water flow, swelling pressure, and ion diffusion. Concrete data on the density distribution are required for derivation of expressions for the transport and rheological properties and the MMM model is based on the use of microscopy for this purpose.

Digitalization of transmission electron micrographs of ultrathin sections of suitably prepared, water saturated clay specimens verifies that the microstructure is heterogeneous as illustrated by Figure 3-15. Figure 3-16 shows a typical micrograph of smectitic clay with a density of 1800 kg/m^3 at water saturation.

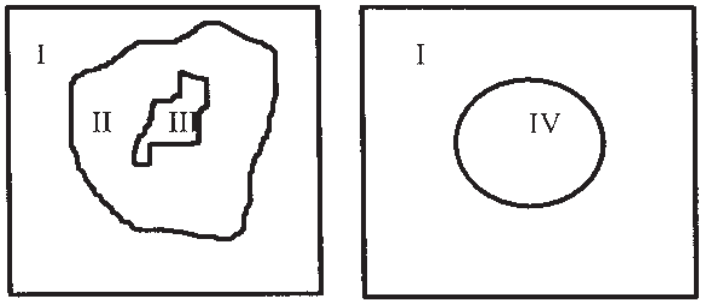

Figure 3-15. *Schematic micrographs. Left: Typical picture of ultrathin section with varying density in soft matrix region (I to III). Right: normalized picture with defined channel cross section and density of the clay gel in the channel (IV) and of the clay matrix (I).*

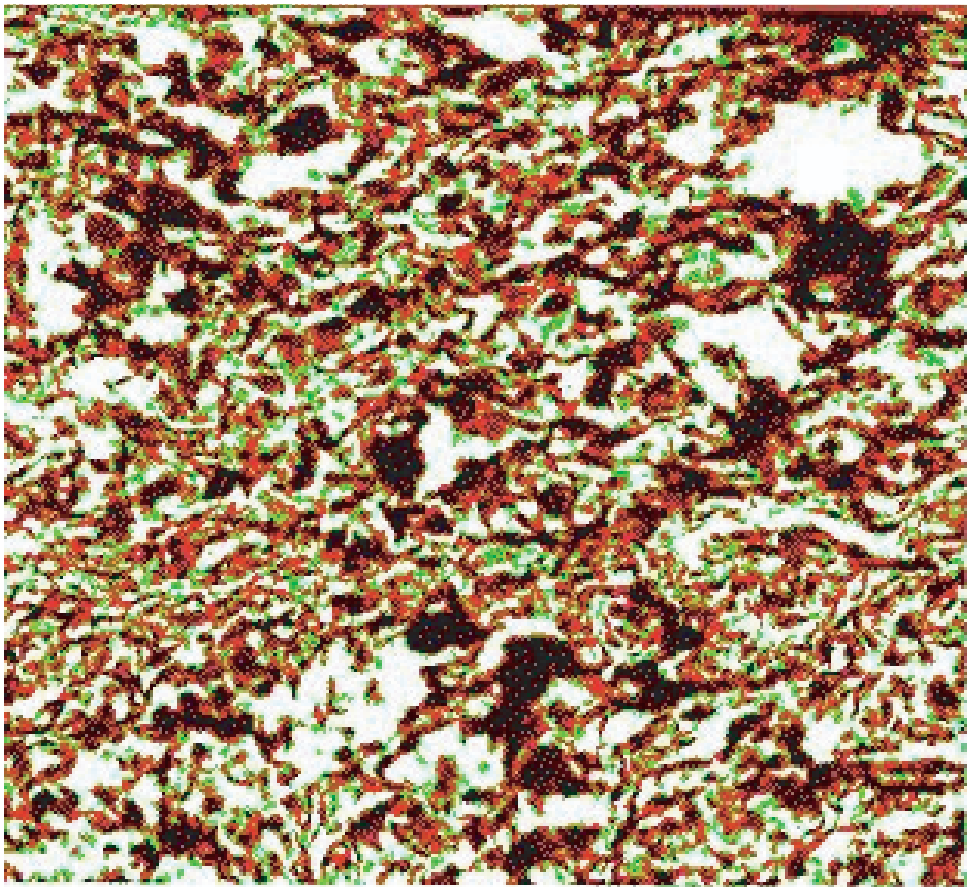

Figure 3-16. *Microstructure of 500 Å ultrathin section of MX-80 clay with a density of 1800 kg/m³ as observed in a transmission electron microscope. The black parts are dense particles of rock-forming minerals, mainly quartz and feldspars, red parts are impermeable dense aggregates of clay minerals, green parts are permeable, softer smectite clay gels, while white parts are open voids or voids filled with soft smectite gels. The edge of the picture is 30 μm.*

3.4.4 Determination of structural parameters for calculation of physical properties in bulk

Parameters

A practical way of quantifying microstructural heterogeneity is defined in Figure 3-17, where *a* represents the clay matrix (I in Figure 3-15), and *b* the soft gel and open space in the channels (IV in Figure 3-15).

The two microstructural components are related through the coefficients F_2 for 2D and F_3 for 3D conditions and their ratio depends on the average and individual bulk densitites.

F_2 and F_3 can be evaluated from digitalized TEM micrographs with different degrees of greyness or colours representing different densities. Depending on the scale, *a* or *b* may dominate. Micrographs with an edge length of at least 30 μm appear to be representative for the larger part of the clay matrix. F_2 and F_3 are related to the average bulk density of saturated MX-80 clay as shown in Table 3-13. They are expressed analytically by Equations (3-4) to (3-7) as functions of the bulk density at saturation ρ_{bs} and the gel density ρ_{gs}.

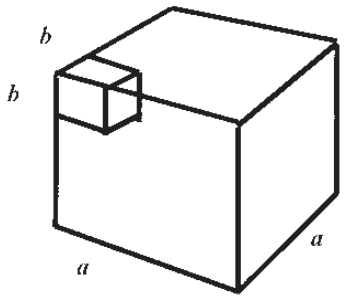

In 2D: $F_2=b^2/a^2$ $b=a(F_2)^{1/2}$

In 3D: $F_3=b^3/a^3$ $F_3=F_2(F_2)^{1/2}=(F_2)^{3/2}$ $\rho_{av}=\rho_b F_3 + \rho_a(1-F_3)$

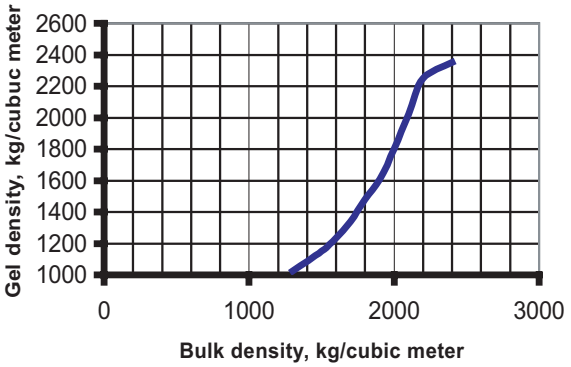

Figure 3-17. *Microstructural parameters is the average bulk density ρ_{av} of the clay and the average density of components a (impermeable clay matrix) i.e. ρ_a, and b (soft gel fillings and open space), i.e. ρ_b. The diagram shows the average gel density versus average bulk density.*

Table 3-13. F-parameters as functions of clay density for MX-80.

Bulk density, kg/m³	Gel density, kg/m³	F_2	F_3
1500	1150	0.85	0.80
1700	1300	0.62	0.50
1800	1500	0.45	0.33
1900	1650	0.32	0.23
2100	2000	0.20	0.10
2200	2200	0.15	0.01

$$F_2 = 10^{(-0.0007875\ \rho_{bs} + 0.745)} \quad (3\text{-}4)$$

$$F_3 = 10^{(-0.00125\ \rho_{bs} + 1.5)} \quad (3\text{-}5)$$

$$F_2 = 10^{(-0.0007142\ \rho_{gs} + 0.7142)} \quad (3\text{-}6)$$

$$F_3 = 10^{(-0.001\ \rho_{gs} + 1)} \quad (3\text{-}7)$$

Relevance and accuracy

The MMM and the ABAQUS models both show that the clay matrix is far from homogeneous at complete equilibrium like in any soil. The latter employs macroscopic physical performance models and data and does therefore not provide proof on the microstructural constitution. The former represents a conceptual model that can be applied directly to MX-80 and other smectitic clays, like the Friedland Ton, and its principal relevance is proven by electron microscopy of undisturbed clay maintained in humic cells /9,10/, and comparison of calculated and actual hydraulic conductivity data. A major question is whether the preparation of ultrathin sections of clay significantly changes the microstructural patterns and this concerns both the distribution of solids by replacing porewater by plastic monomers, and the impact of the thickness of the sections on the evaluation of the variation in density.

Impact of preparation

Specimens are placed in a solution consisting of 50% by weight of ethyl alcohol and 50% distilled water for 30 minutes followed by emplacement in 90/10 ethyl alcohol/ 6water and 99.5% ethyl alcohol for 5 minutes each. It is then transferred to a solution consisting of 85% by weight of butyl methacrylate and 15% methyl methacrylate for 45 minutes, the process being repeated twice. Finally, the specimen is transferred to a solution of 98% monomer and 2% 2.4-dichlorbenzoylperoxide (EMW) catalyst for 90 minutes /11/. Polymerization is obtained by heating to 60°C for 15 hours. The requirement that the impregnation liquid can enter and fill the voids in approximately the same fashion as water, yielding typical swelling pressures, has been validated /10/.

Another important requirement is that the hardened impregnation material must give the clay a strength that permits sectioning without causing mechanical disturbance. Cutting has to be made by use of very sharp glass or diamond knives. Still, where the edge hits quartz, feldspar or heavy minerals theses may not be intersected or truncated but moved by the propagating knife causing much disturbance, like folding and disruption of the clay matrix. This problem is solved by watching the cutting operation for selecting undisturbed specimens.

Evaluation of micrographs for calculation of F-parameters

Digitalized TEM micrographs with different degrees of greyness representing different densities can be converted into different colours for easy interpretation and representation of the variation of density. In the current R&D work this is made by transforming scanned micrographs to digitalized form using the OFOTO 2 code, with subsequent coloring using the GRAPHIC CONVERTER 2.9.1 code on a MacIntosh Power PC6100/66. Using only four colors (cf Figure 3-16), clear distinction can be made of parts representing different densities: black parts, i.e. the most electron-absorbing components being the densest parts of component *a*, and red parts relatively dense parts of the same component. Green are taken as soft, porous parts of component *b* and white representing open parts of this component.

A fundamental law in photography /12/ expresses the ratio of greyness G of the photographic plate, i.e. the micrograph, and the radiation energy amount E, which is the product of the radiation intensity i and time of exposure t:

$$G=A\ E = \log it \qquad (3\text{-}8)$$

where:

G = greyness
A = constant
E = radiation energy
i = radiation intensity
t = time

The greyness G is inversely proportional to the density ρ and thickness d of the film, which, for constant i and t, gives the expression:

$$G=B(\rho d)^{-1} \qquad (3\text{-}9)$$

where:

B = constant
ρ = density
d = film thickness

Disregarding from diffraction and geometry-related optical distortions and from absorption by the void-filling impregnation substance, the greyness of the micrograph intensity on the exit side of an impregnated element is:

$$G=B\ [\Sigma\ (\rho\ d)]^{-1} \qquad (3\text{-}10)$$

Comparing a film with 3 μm thickness with one having 30 μm thickness, the ratio of the G-values is 10. For making direct quantitative comparison of the G-values possible the radiation energy must hence be 10 times higher for the 30 μm film thickness. This may have an impact on the crystal lattice stability, especially the location of alkali ions. Hence, the thickness of ultrathin sections for TEM should not exceed about 1000 μm.

While identification of the most detailed features of clay crystallites requires a resolution power that only films thinner than about 500 Å can provide, certain quantitative microstructural analyses can be made by using significantly thicker films. Thus, if the objective is to interpret different degrees of greyness in terms of density variations it is possible to do so if calibration has been made by analysing ultrathin sections. A 30 μm clay film gives poor information on density variations while films with a thickness of about 5 μm reveals major variations. Micrographs of sections with 1 mm thickness have provided much valuable information although details of the microstructure are obscured.

3.4.5 Application of the MMM model

Hydraulic conductivity

Calculation of the bulk hydraulic conductivity of any soil can be made by applying basic flow theory, taking a permeated clay section to consist of a system of elements with different hydraulic conductivity as derived in Chapter 5, /13/.

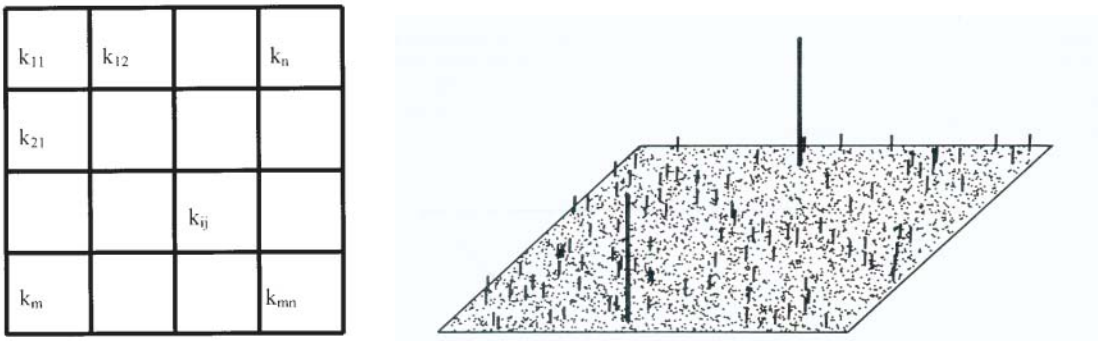

Figure 3-18. *Hydraulically heterogeneous medium Left: System with differently permeable elements. Right: Relative flow rate distribution in clay of type C (1570 kg/m³). Long bars represent 20–50 µm wide channels with soft gels. Medium long bars represent 5–20 µm channels and short bars voids with 1–5 µm width.*

Theoretically, the hydraulic conductivity K of a soil with elements of different conductivity can be expressed in the following way:

$$K=1/m[\Sigma n\ (\Sigma 1/k_{ij})] \qquad (3\text{-}11)$$

where:

K = Average hydraulic conductivity
n = Number of elements normal to flow direction
m = Number of elements in flow direction
k_{ij} = Hydraulic conductivity of respective elements

Plotting of bulk conductivities of MX-80 clay at different degrees of dispersion have given the correlation between bulk density and hydraulic conductivity shown in Figure 3-19, which has been used for representing k_{ij}. These data are much higher than those derived theoretically for the GMM gels (cf Table 3-6), which are not accurate according to the present knowledge.

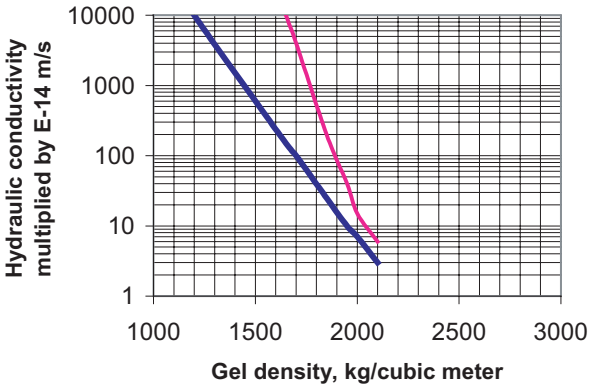

Figure 3-19. *Hydraulic conductivity of clay gels at permeation of distilled water. Right curve represents Ca-form /9/.*

Using Equation (3-11) and relevant *F*-parameter values one gets the theoretical hydraulic conductivity in Tables 3-14 and 3-15 for the three reference MX-80 clay types introduced in the description of the GMM model. The table also gives experimental values that are in excellent agreement except for the softest Ca-clay for which there are two reasons 1) The microstructural network is not stable so flow transports aggregates to clogging positions, 2) The assumption of an average gel density like for Na clay does not apply so the density is higher of aggregates in clogging positions. The agreement supports the relevance of the idea of microstructural heterogeneity of smectite clays in general and of the MMM in particular.

Table 3-14. Microstructural data and conductivities for MX-80 in Na form, percolation with distilled water /9/.

Reference clay	Bulk density, kg/m^3	F_2	Gel density, kg/m^3	Gel conductivity, kg/m^3, Na-form	Theoretical bulk conductivity m/s	Experimental bulk conductivity m/s
A	2130	0.17	2000	7E-14	E-14	2E-14
B	1850	0.24	1650	2E-12	4E-13	3E-13
C	1570	0.80	1200	2E-10	8E-11	8E-11

Table 3-15. Microstructural data and conductivities for MX-80 in Ca form, percolation with strongly brackish Ca-dominated water /13/.

Reference clay	Bulk density, kg/m^3	F_2	Gel density, kg/m^3	Gel conductivity, kg/m^3, Na-form	Theoretical bulk conductivity m/s	Experimental bulk conductivity m/s
A	2130	0.17	2000	2E-13	3E-14	5E-14
B	1850	0.24	1650	8E-11	2E-12	2E-12
C	1570	0.80	1200*	7E-5	3E-6	2E-9

* Underestimated

Swelling pressure

Using the microstructural parameters, MMM predicts the swelling pressure of REVs and hence the bulk pressure. The isotropic swelling pressure is the product of the component *a* and the volume ratio $(a^3–b^3)/a^3$. This ratio is the same as $(1-F_3)$. The swelling pressure of MX-80 clay calculated by use of the Yong/Warkentin theory /5/ for the various densities of the solid (massive) component a is given in Table 3-16 together with the corresponding bulk density, $(1-F_3)$, and theoretical and experimental swelling pressures.

Table 3-16. Calculated and measured swelling pressures (p_s) of MX-80 clay saturated with distilled water /13/.

Reference clay	Bulk density, kg/m^3	$1-F_3$	Density of massive part, kg/m^3	p_s of massive part (a), MPa	Calculated bulk p_s, MPa	Experimental bulk p_s, MPa
A	2130	0.93	2150	11	10	10–15
B	1850	0.80	1900	1.5	1.2	0.5–1.5
C	1570	0.75	1750	0.3	0.2	<0.2

The calculated and experimental data are in very good agreement and fit much better than the corresponding pressures calculated for GMM (cf Table 3-10). Still, the accuracy of the Yong/Warkentin theory is debatable since it is based on conventional colloid-chemical attraction/repulsion theory with both cat- and anions in the interlamellar space, which may not apply. Particularly the pressures derived for low densities are uncertain, which is obvious when performing the calculations for smectite clay in Ca-form. In principle, however, the MMM provides a possibility of predicting the swelling pressure for any smectitic soil and any electrolyte composition of the porewater.

Gas penetration and conductivity

Modelling of gas conductivity is discussed in Chapter 7. Here we will see how the MMM responds to gas pressure as compared to the GMM.

Gas penetrates smectite clay in a finger-like mode when the gas pressure exceeds the sum of the piezometric head and a critical (treshold) pressure, which has been experimentally validated /13/. The microstructural heterogeneity explains why pressurized gas moves in local pathways, which are interconnected, partly or fully gel-filled channels with lower density than the rest of the clay matrix.

The resistance to gas penetration is provided by water pressure, capillary pressure and pressure required for displacing clay gels and separating dense aggregates. It is logical that the latter pressure component is related to the swelling pressure at higher bulk densities while for low densities it is expected that displacement of soft gels in the voids between denser aggregates controls the critical gas pressure.

Ion diffusion

For the case of uniaxial 2D diffusion the ion transport capacity is different for cations and anions as for the GMM. One expects that this capacity is related to the microstructural parameter F_2, which is close to unity for soft clays and very low for high densities. Thus, for Cl ions, which in principle move only in the soft gels (the *b* component) the effective diffusivity would correspond to F_2=0.85 for 1500 kg/m^3 density at fluid saturation and to F_2=0.10 for 2250 kg/m^3, the ratio implying a drop in diffusivity by 8.5 times, which is somewhat less than implied by experimental data (cf Figure 3-7). For the cation Cs the corresponding drop is logically much smaller. The impact of tortuosity has not been introduced in these calculations; it is expected to bring the calculated change in diffusivity to agree with the experimental recordings.

3.5 Buffer, the 3Dchan model

3.5.1 Numerical modelling in 3D

The conclusion from the comprehensive microstructural study and application of the GMM, ABAQUS and MMM models is that practically all porewater flow takes place within a three-dimensional network of gel-filled channels with stochastic properties (Figure 3-20). The channels, which represent the zone termed IV in Figure 3-15, are characterised by their lengths, widths, apertures and transmissivities. The clay matrix is assumed to be porous but impermeable. The basis of the development of the model is the code 3Dchan /14/.

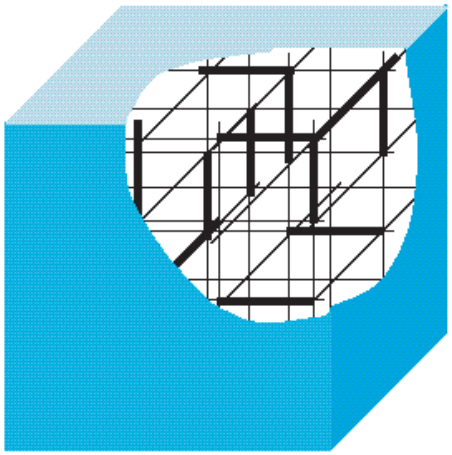

Figure 3-20. *Schematic view of the 3D model concept.*

Calculation of the bulk hydraulic conductivity can be made by assuming that a certain number (commonly 6) of channels intersect at each node of the orthogonal network and that each channel in the network consists of a bundle of N capillaries with circular cross section. Figure 3-21 shows a small part of the channel network with the objective of demonstrating that the channels have different diameters.

The number of channels, which are assumed to have the length L, contain bundles of N capillaries with a diameter (d) that is proportional to the channel width is chosen to match the total porosity of the clay. After complete grain expansion the voids filled with homogeneous clay gels are assumed to have a normal size distribution with the same intervals as in the GMM model, i.e. 1–5 µm for the clay with 2130 kg/m^3 density, 1–20 µm for the clay with 1850 kg/m^3 density, and 1–50 µm for the clay with 1570 kg/m^3 density. The code generates a certain number of channels for a given volume /15/. Using the Hagen-Poiseuille law the flow rate through the channel network is calculated for given boundary conditions assuming a pressure difference on the opposite sides of the cubic grid and no flow across the other four sides. Table 3-17 specifies the density, total porosity n, and resulting bulk hydraulic conductivity of the considered clay types.

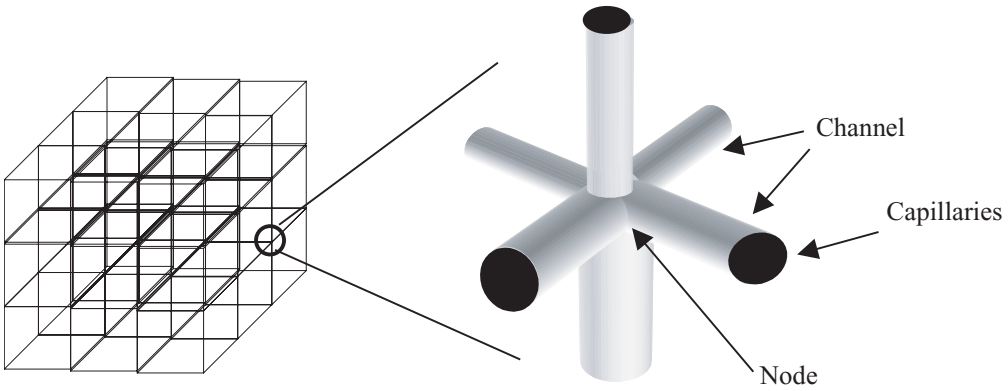

Figure 3-21. *Channel network mapped as a cubic grid with channels intersecting at a node in the grid.*

Table 3-17. Hydraulic conductivity (*K*) of three clay types prepared by compacting MX-80 powder and saturating them with electrolyte-poor water. *n* is the porosity.

Reference clay	Bulk density at fluid saturation, kg/m^3	*n*	Calculated *K*, m/s	Experimental *K*, m/s
A	2130	0.13	3E-12	2E-14
B	1850	0.20	1.3E-11	3E-13
C	1570	0.47	2.4E-10	8E-11

One finds that the calculated bulk conductivity of MX-80 with the density 1570 kg/m^3 at saturation is on the same order of magnitude as typical experimental data, while the model overrates the conductivity of the denser clays. The major reason for the discrepancy is that the model does not account for variations in cross section of the channels and that tortuosity is not included. These features become increasingly important at higher densities.

3.6 Assessment of microstructural models

3.6.1 Applicability

The four microstructural models can all be used in certain contexts but are of limited value in various respects. Thus, the following assessment can be made:

- The GMM is valid in principle but is based on several unsupported assumptions, primarily concerning pore diameters, density, structure and conductivity of clay gels, and makes use of questionable colloid theory for calculating swelling pressures. Anion diffusion is underrated since tortuosity is not included in the model.
- The ABAQUS model is only in 2D but can be extended to 3D. It can be used for calculating hydraulic conductivity and swelling pressure and has the potential for predicting gas penetration and ionic diffusion.
- The MMM gives the best agreement between predicted and recorded hydraulic conductivities and swelling pressures and appears to be useful also for calculating ion diffusion transport and gas penetration. It is also the only model that takes the *actual* stochastic variation in density and void geometry into consideration.
- The 3Dchan model is conceptually valid and can be considered as a fully numerical version of the GMM. It has the potential of being used for prediction of the hydraulic conductivity after bringing in tortuosity and variations in channel geometry.

In conclusion, the microstructural evolution of a mass of compacted MX-80 grains with subsequent hydration yielding a clay matrix that contains interconnected voids filled with clay gels of lower density than the rest of the clay matrix, is described by all the models. It is believed that MMM that makes use of micrograph-derived structural parameter data as a basis for the microstructural build-up is appropriate and particularly suitable for correlation with bulk physical properties.

3.6.2 Extension of the MMM to other conditions

General

MMM in its present form can be used for deriving microstructural parameters for quite different conditions, like shearing, compression, piping (erosion), changes in chemical environment, and mineral alteration. It is required, however, that electron micrographs – or a combination of light and electron microscopy in the case of smectite-poor soils – are taken for evaluation using the described techniques.

A special case is that of backfills with low clay contents and natural smectitic soils with low and moderate contents of smectites. The microstructural constitution of backfill mixtures is strongly dependent on the mixing process and the high degree of heterogeneity requires that the REV size is taken sufficiently large. For smectite-poor natural clays prepared like MX-80 buffer the MMM can be applied without changes. Also in this case, the presence of rock-forming minerals requires selection of sufficiently large REVs.

Water saturation

The role of the microstructure is important in all operative phases of the buffer clay, especially in the water saturation phase for which different boundary conditions are of particular importance. Thus, while the evolution of the microstructure according to the GMM, ABAQUS and 3Dchan models is based on the assumption that water is initially present in the voids between the aggregates, implying that one can calculate their expansion on the expense of the void volume, the real conditions are different. In practice, one can distinguish between three boundary conditions: 1) The clay is contacted with water vapour (RH=100%), 2) The clay is contacted with liquid water that is not pressurized, and 3).The clay is contacted with pressurized water. The different conditions are believed to cause different microstructurally related hydration rates as follows.

Contact with water vapour (Case 1)

Water molecules migrate into the open voids and get sorbed on exposed mineral surfaces interacting with the electrical double layers, which represent the *osmotic potential* and from where they migrate into the interlamellar space that has the highest hydration potential, representing the *matric potential*. Migration takes place along surfaces with differences in water content as driving force, the entire process hence being diffusion-like. The suction potential is lowest for the largest channels and highest for the most dense clay matrix and the former will therefore not be fully saturated until the matrix has reached this state. The saturation process is sufficiently slow to let entrapped air be dissolved and diffuse out from the clay without delaying saturation, which will, however, probably never be complete.

Contact with non-pressurized liquid water (Case 2)

Water is sucked up by capillary forces in the open channels from which water molecules migrate into finer voids and further into the interlamellar space like in Case 1 and the hydration is hence controlled by diffusion. The larger channels may temporarily or permanently contain air bubbles along which film flow takes place in the hydration phase and after since the degree of saturation will probably never be 100%.

One can consider the processes associated with hydration and water uptake of unpressurized liquid water by microstructural units to be significant contributors not only to the development of the wetting front (in the macropores) but particularly to water uptake behind the wetting front (Figures 3-22 and 3-23).

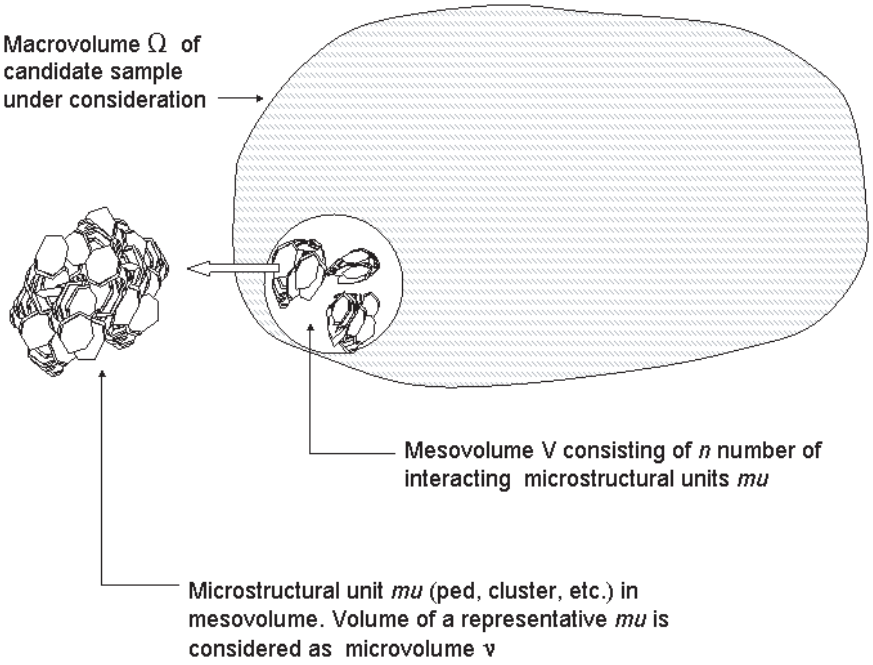

Figure 3-22. *Schematic picture of microstructural units in larger soil element /16/.*

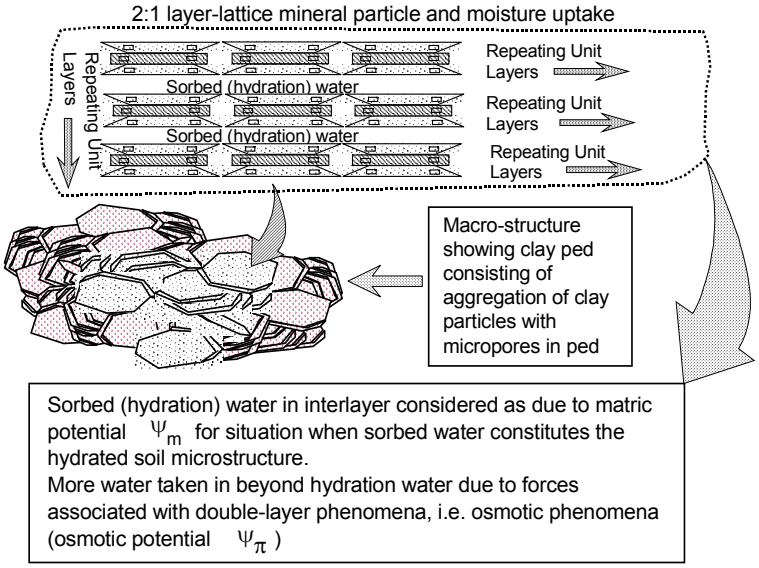

Figure 3-23. *Matric and osmotic sorption potentials related to different microstructural units /16/.*

Interlamellar and interparticle hydration forces reside in the inner Helmholtz plane and can be calculated using the Coulomb relationship: $E_c = z_i e^2/\varepsilon R$. E_c represents the hydration energy, z_i is the valence of the charged species in this plane, ε is the dielectric constant, e refers to the electronic charge, and R is the distance between the centre of the ion i and the negative charge site of the particle /16/.

Using superscripts l and p to indicate interlamellar and interparticle conditions, respectively, the components of the soil-water potential responsible for water uptake into the microstructural units and resultant swelling include: $\Psi_m^p, \Psi_\pi^p, \Psi_m^l$, and Ψ_π^l. Since it is not

possible to separate or measure the contribution to water uptake and swelling from any one of the components of the soil-water potential, a combination of the interlamellar and interparticle potentials into the microstructural unit Ψ_m^{mu} and Ψ_π^{mu} can be used, the superscript *mu* referring to "microstructural unit".

Uptake of water in the microstructural units by hydration processes is a relatively rapid phenomenon when compared to uptake of water by the double-layer mechanisms. Accordingly, the modelling of movement of water into the macroscopic volume will be controlled by the Ψ_π^{mu} values of the various microstructural units that make up the macroscopic volume material. Because of the spatial variability and irregularity of the microstructural units, and therefore the spatial variability and irregularity of Ψ_π^{mu}, stochastic heterogeneity is believed to exist, i.e. they are essentially random. To handle the inherent stochastic nature of Ψ_π^{mu} in the prediction or evaluation of water uptake into the macroscopic soil structure, a scaling technique can be used which allows one to compute the probability of a specific volumetric water content θ at a specific location r. A simple relationship that can be specified is that in Equation (3-12) /17/.

$$\frac{\partial \omega}{\partial \chi} = \frac{\partial}{\partial \zeta}\left[D^* \frac{\partial \omega}{\partial \zeta} \right] - \frac{\partial K^*}{\partial \zeta} \qquad (3\text{-}12)$$

where:

$\omega = \theta/\theta_s$, θ = volumetric water content, θ_s = saturated volumetric water content
$\chi = \alpha_r^3/\theta_s$, α_r = scaling parameter with reference to location r of mesovolume
$\zeta = \alpha_r x$, x = spatial variable
$D^* = K^*(?\Psi/?\omega)$ = scaled soil-water diffusivity
$K^* = K_r \alpha_r^{-2}$ = scaled hydraulic conductivity
Ψ = total soil-water potential = $\Psi_r \alpha_r$

Equation (3-12) implies that hydration takes place as a series of diffusion processes and that the local hydraulic conductivity plays a role for the transport of water through the saturated part of the clay to the "wetting" front. The equation is compatible with the conceptual idea of a finger-like movement of water in any dry clay material undergoing wetting from a boundary providing water. It is hence in agreement with all the microstructural models including the MMM.

Contact with pressurized water (Case 3)

Water is pressed into the largest open channels and moves quickly and deeply into the clay matrix, particularly when the pressure and electrolyte contents are high. The penetrating water displaces air and compresses the unsaturated matrix. Since a considerable fraction of the voids become water-filled quickly, the average degree of saturation is expected to be raised very early and the dominating process hence being redistribution of water from the larger channels into the clay matrix, associated with displacement, reorientation and break-down of particle aggregates. This has been found in experiments with MX-80 clay with a dry density of 1800 kg/m^3 and 50% degree of water saturation to a water pressure of 600 kPa for a few minutes. Before pressurizing the clay, 1 to 2 hydrate layers made up the interlamellar water and the large majority of the void channels were air-filled. Determination of the water content soon after showed that the uptake of water extended to 2–3 cm distance from the pressurized surface and that it corresponded to the volume of the major channels according to all the microstructural models including the MMM. The ultimate degree of saturation will be 100%.

Piping and erosion

Ca smectite does not form stable clay gels at lower bulk densities than about 1600 kg/m^3 as verified by the fact that it does not exert any swelling pressure for this and lower densities. This means that larger voids in the dense matrix do not contain coherent clay gels. High flow rates can hence cause erosion critical rates being E-3 m/s for tearing off 0.5 µm particles, E-4 m/s for 1 µm particles, E-5 m/s for 10 µm particle aggregates, and E-7 for aggregates larger than 50 µm, as evaluated from physical models and experiments /18/. The flow pattern in a water saturated element of smectite clay with the density 1600 kg/m^3 and containing voids representative of this density is illustrated by the FEM calculation in Figure 3-24. The vector flow pattern was calculated for the gradient 1 (m per m) and one concludes that the flow rate in the large central void is on the order of 2E-6 m/s for a gradient of 100, which is a common value in steady-state laboratory percolation experiments. This gradient is in fact much higher in the hydration process and will cause fine-particle transport in the direction of the gradient. Hence, disruption of soft clay gels and migration of small particle aggregates may well take place and this is verified by Figure 3-25, which shows the change in conductivity at reversed percolation of MX-80 clay with 3.5% $CaCl_2$ solution /19/. Transport of eroded particle aggregates caused accumulation of particles at channel constrictions resulting first in an increase and then in a significant decrease in hydraulic conductivity.

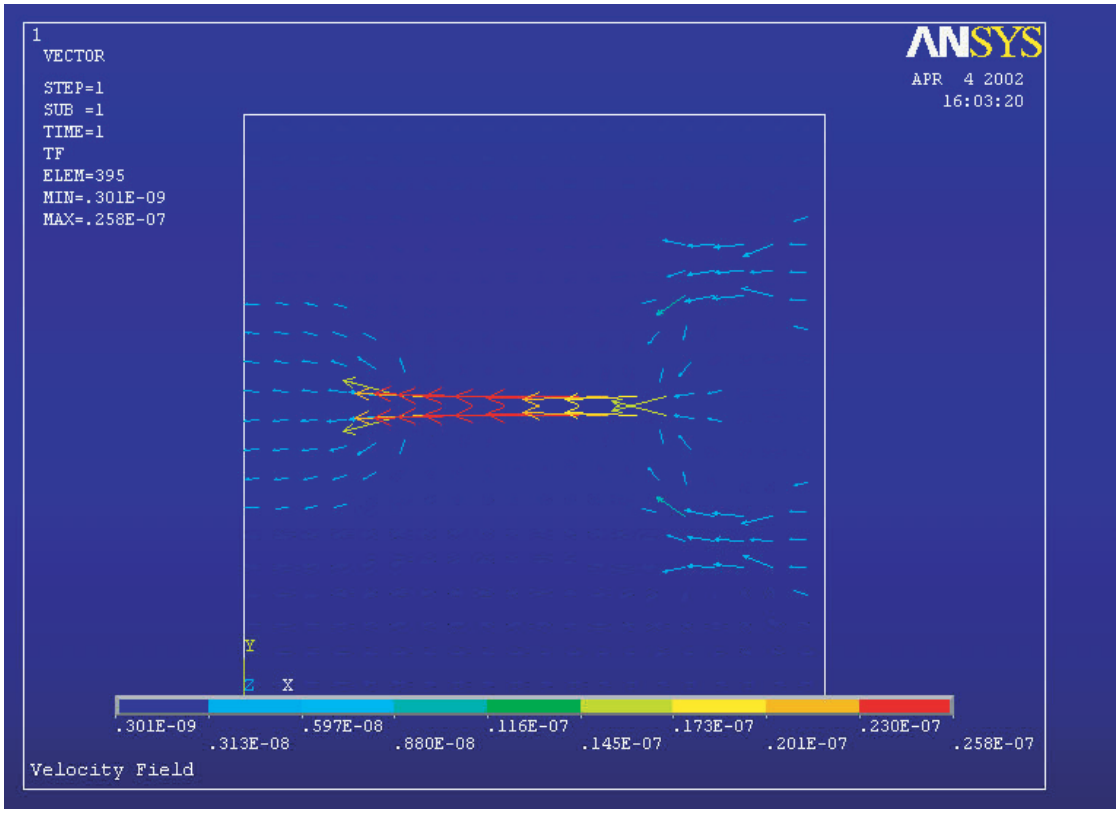

Figure 3-24. *FEM calculation in 2D of flow through 30x30 µm^2 clay element of smectitic clay with 1600 kg/m^3 density. For a hydraulic gradient of 100 the max flow rate is 2E-6 m/s. The flow zones are wide in the matrix where the rate of percolation is low while this rate is high where the water is forced through the narrow voids.*

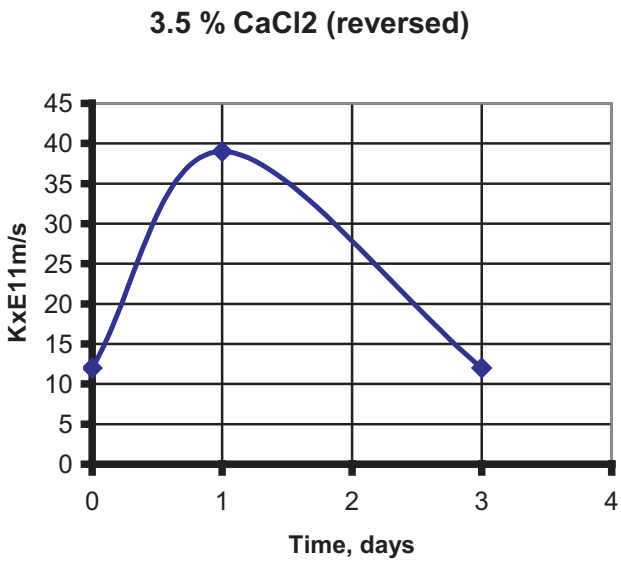

Figure 3-25. *Change in hydraulic conductivity after reversing the flow direction at percolation with 3.5% $CaCl_2$ solution of smectitic clay with a density of 1800 kg/m^3 under a hydraulic gradient of 30. It is believed that the conductivity initially increased in conjunction with disruption of soft clay gels while it then dropped because of accumulation of released particles at channel constrictions /19/.*

Gas penetrability

Gas penetrates clay where it can displace porewater most easily, which is where it hits voids containing soft clay gels. It passes through them and proceeds through the dense matrix like in Figure 3-26 to the next gel-filled void. The pressure required to make the gas penetrate the dense matrix should be on the same order of magnitude as the swelling pressure but the rate of gas penetration may increase this critical pressure since clay gels may be compressed and densified by slowly advancing gas, thereby causing an increased resistance to further gas movement.

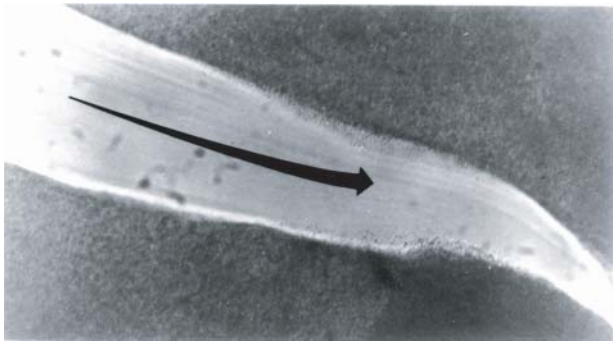

Figure 3-26. *Piping in the form of a hydraulic wedge penetrating into soft clay matrix. 20–50 μm smectite aggregates are moved by the flow (E-4 m/s).*

3.7 Backfills

3.7.1 General

Backfills have two important functions: they need to have a sufficiently low compressibility to make the upward expansion of the buffer in the deposition holes small and they should provide support to the roof and walls of the deposition tunnels. The latter requires that the backfill has some content of smectite, which is offered by a number of natural smectitic soils. They can be used for all sorts of backfilling where tightness is required and both natural soils, of which Friedland Ton described in Part 2 is an example, and mixtures of smectite-rich material like MX-80 and sand/gravel or crushed rock have been used on a full scale. For mixtures one can define the backfill as a mixture of two components, one – the ballast – consisting of coarse-grained particles, and the other of grains of smectite-rich clay. The models described here deal with maturation of such systems.

The density of the clay component of the backfill determines its hydraulic and gas conductivities as well as its expandability, while the interaction between the ballast grains determines the compressibility. For ordinary backfills with sufficient expandability to maintain their volume under a variety of groundwater electrolyte conditions a smectite content of about 15% is believed to be at minimum.

A 2D microstructural model based on the ABAQUS code and that is akin to that for pure MX-80 bentonite has been worked out for bentonite/ballast mixtures and will be described here. It describes the expansion of the bentonite component as a function of the transient change of its hydraulic conductivity and a restraint caused by internal friction. It employs the same material model as specified for the clay component but considers the ballast grains to be incompressible and representing rigid bodies. The arrangement of the grains (rods) is assumed to be such that the clay grains are contained in the voids between equally large and regularly layered ballast grains, which are taken to be infinitely long and column-shaped in this version of the model.

The variables and parameters are as defined for the ABAQUS model for pure clay in Section 3.3. The use of the model is exemplified in Section 3.8.

3.8 Examples

3.8.1 General

This section includes applications of the GMM model, which is particularly suitable for quantifying void sizes and densities in predicting the hydraulic conductivity of smectite clays saturated and percolated by water solutions with different contents of salt or of organic liquids. Also, an example is given of the use of the ABAQUS code for illustrating the difference in microstructural homogeneity that is caused by mixing a rather small amount of smectite clay to ballast material.

3.8.2 Calculation of hydraulic conductivity using the GMM model

Problem: Calculate the average hydraulic conductivity of the three reference clays *A*, *B* and *C*, as specified in Section 3.2.

Basic

Section 3.2.4 gave the basis of the procedure in solving the problem. Hence, one assumes that the laminar flow Q through an individual tube of circular cross section is given by the Hagen-Poiseuille law:

$$Q = \frac{\pi \cdot g \cdot \rho \cdot i}{128 \cdot \eta} \cdot x^4 \qquad (3\text{-}13)$$

where:

g = acceleration of gravity
ρ = density of fluid
η = dynamic viscosity of fluid
x = tube diameter
i = hydraulic gradient along tube

For a medium containing a system of parallel tubes of different diameters the conductivity K is given by:

$$K = \frac{p \cdot \pi \cdot g \cdot \rho}{128 \cdot \eta} \int_{x_1}^{x_2} n(x) \cdot x^4 \, dx \qquad (3\text{-}14)$$

where:

p = porosity associated with the volume taken up by the tubes
x_1 = lower diameter limit
x_2 = upper diameter limit
$n(x)\cdot dx$ = number of pores per unit pore cross section area in diameter range [x , $x+dx$]

For tubes of circular cross section, the fraction of the pore cross section area, a(x)·dx, taken up by pores in the diameter interval [x , $x+dx$] is given by:

$$a(x) = n(x)\cdot\pi\cdot(x/2)^2 \qquad (3\text{-}15)$$

and Equation (3-14) can hence be written as:

$$K = \frac{p \cdot g \cdot \rho}{32 \cdot \eta} \int_{x_1}^{x_2} a(x) \cdot x^2 \, dx \qquad (3\text{-}16)$$

Distribution functions for Clays A through C are given in Figures 3-6 and the porosity of Clays A through C in Table 3-18 /2/.

The porosity represented by internal voids (microporosity) is obtained as the porosity of external voids (macroporosity) times the porosity of the gel material within the latter

Table 3-18. Reference clay porosities /2/.

Clay	Porosity, external voids	Porosity, internal voids
A	0.015	0.0021
B	0.050	0.0085
C	0.370	0.0740

voids. An additional porosity correction is applied to account for conversion to constant aperture tubes and also applied to Equation (3-16) to account for non-circular shape (correction 0.5) and for lengthening of flow paths due to random 3D orientation of tube segments (correction 0.33), /2/. As discussed earlier these rather arbitrary corrections admittedly make the model uncertain but it is still useful in comparing the impact of a significantly changed electrolyte content.

Results

Applying the distribution functions referred to, the conductivities of the three reference clays will be those shown in Table 3-19.

Table 3-19. Conductivity of reference clays in sodium form /2/.

Clay	Macropore conductivity (m/s)	Micropore conductivity (m/s)
A	1.3E-09	2.1E-14
B	4.4E-08	2.6E-13
C	1.6E-06	4.3E-12

Checking of the relevance of the initial microstructural model has been made by saturating and percolating a sample of MX-80 grain powder with carbon tetrachloride, which is a non-polar liquid and hence unable to form clay gels in the "external" voids between the powder grains. The dry density of the clay was about 1200 kg/m^3, corresponding to 1760 kg/m^3 if the clay had been saturated with water, and the calculated conductivity of the system, using the Hagen-Poiseuille law for lyophobic fluids, about 4E-8 m/s represented by the "macropore conductivity" in Table 3-18. The actual recorded conductivity was about E-7 m/s, i.e. in acceptable agreement with the theoretical figure.

3.8.3 Calculation of the void ratio and porewater pressure in bentonite/ballast mixture under water saturation; use of the ABAQUS model

Basic

The calculation refers to a 2D case where the clay grains, which are assumed to be equally large with a diameter of 1 mm, are located in the voids between ballast grains with 2.4 mm diameter. The latter are in cubical packing with the bentonite grains in the center of the voids as shown in Figure 3-27.

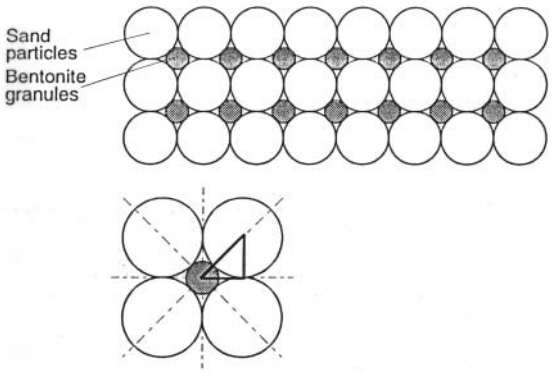

Figure 3-27. *Cubical packing of bentonite grains and ballast grains /7/.*

Material data

Clay grains

ρ_d = 1980 kg/m^3
ρ_s = 2270 kg/m^3

Clay material

ρ_d = 1560 kg/m^3
ρ_s = 2000 kg/m^3
e = 0.79

Friction between clay and ballast particles

The clay matrix in the grain comes in contact with the ballast particle when it swells by which frictional resistance characterized by the friction angle ϕ=10° is mobilized.

Hydraulic conductivity

The model implies that the wetting process is driven by suction of the not yet saturated clay and that this process is retarded by flow resistance for which the hydraulic conductivity must be known. Here, the data in Table 3-10 are applied.

Solution

Three parameters describing the initial conditions in the clay component are needed: 1) Initial void ratio e_0, 2) Initial average effective stress p_0 (corresponding to the swelling pressure) and 3) Initial pore water pressure u_0. The following data are used:

e_0 = 0.40
p_0 = 30 000 kPa
u_0 = –30 000 kPa

The grains are assumed to be partly water saturated to a water content of w=14% from start.

Finite element net

The finite element net is shown in Figure 3-28. It is in 2D and has three plane, fixed boundaries and consists of 111 plain strain elements with 8 nodes each. The surface of the bentonite grain is curved and free to move as a consequence of the expansion of the grain, which is to be determined.

Using the ABAQUS code the expansion of the clay grains is obtained and also the stress conditions including the porewater pressure in each element as a function of time. The void ratio and pore pressure are given as contour plottings for selected times after onset of the expansion. The results can easily be transformed into density plottings from which one calculate the average hydraulic conductivity as the geometrical mean of the conductivity of the respective zones as shown in Section 3.4.5. Flow perpendicularly to the FEM section of course greatly exaggerates the conductivity, while flow parallel to it gives reasonable results.

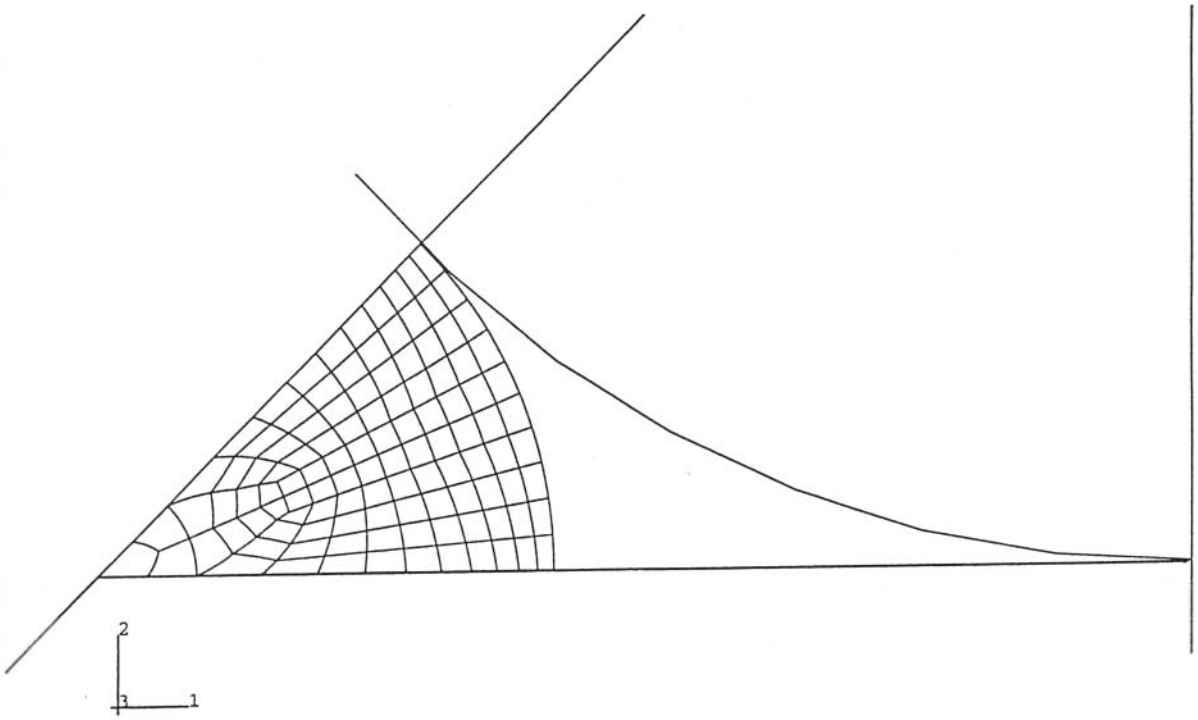

Figure 3-28. *Element mesh for calculation of the homogenisation of bentonite/ballast mixture for backfill /7/.*

Results

Figures 3-29 and 3-30 show plottings of the void ratio superimposed on the deformed element mesh.

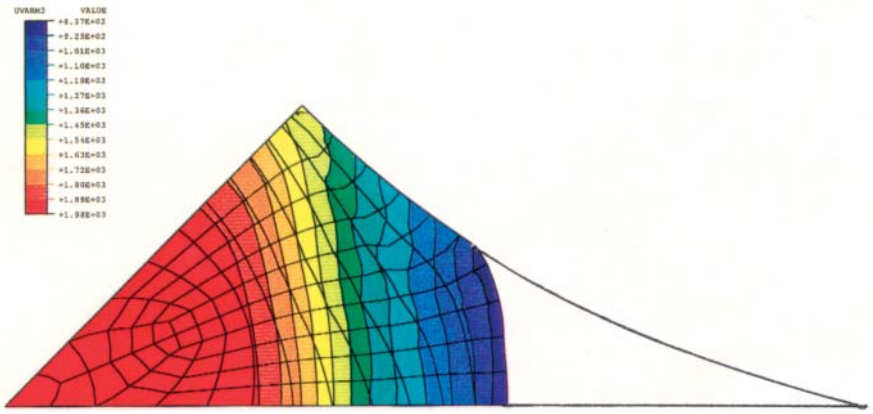

Figure 3-29. *Deformed element mesh and void ratio distribution after 18 seconds. The central red part of the clay grain has a void ratio of 0.4, while this ratio is 2.3 for the softest blue front /7/.*

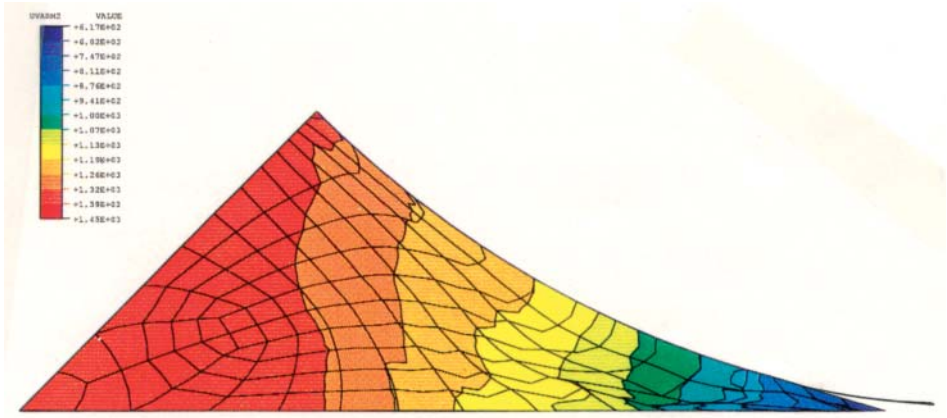

Figure 3-30. *Deformed element mesh and void ratio distribution after E5 seconds, i.e. about 27 hours. The central red part of the clay grain has a void ratio of 0.9, while this ratio is 3.5 for the softest blue front /7/.*

The graphs illustrate the rate of maturation of the mixture. Thus, the diameter of the clay grains expanded by about 20% already after 18 seconds but their central parts were then still unaffected. The initially open void became largely filled with a heterogeneous clay gel after 90 seconds, and even after about a day there was still a very soft gel near the point of contact of adjacent ballast grains. Beyond this period of time very little further homogenization will take place according to the model, which means that the surroundings of ballast contacts are very permeable and easily subjected to erosion.

The density distribution of the clay occupying the voids between the ballast grains is such that about 40% has a density of 1900 kg/m^3, corresponding to a hydraulic conductivity K of about 2E-13 m/s, 45% has a density of 1800 kg/m^3 corresponding to K=E-12 m/s, and 10% a density of 1400 kg/m^3 with a conductivity of 5E-11 m/s. 5% of the cross section is open and this is the part that entirely controls the flow perpendicularly to the cross section of the 2D model. The bulk hydraulic conductivity will be on the order of E-7 m/s, while flow parallel to the section is determined by the clay fraction with 1800 kg/m^3 density, which will give the mixture an approximate hydraulic conductivity of E-13 to E-12 m/s. A perfectly symmetric 3D arrangement (Figure 3-28) with spherical ballast grains is estimated to yield an average isotropic conductivity of the mixture of E-10 to E-9 m/s, which is in line with experimental data.

Figure 3-31. *The timber pile structure of the 2D case and the ball case in 3D naturally give quite different void geometries.*

The successive change in porewater pressure in the course of saturation – not shown here – is very obvious. At the surface of the expanding bentonite grain the suction is high (about 20 000 kPa) in the first 6 seconds, i.e. until the front begins to expand substantially, after which it drops to almost zero after around 10 seconds. In the inner part of the grains the suction is almost constant in the first 60 seconds and then drops to almost zero after about 300 seconds when the grains have been largely water saturated. The evolution of the porewater pressure mirrors the complex interaction of suction, expansion and consolidation.

3.9 References

/1/ **Pusch R, 1994.** Waste Disposal in Rock, Developments in Geotechnical Engineering, 76. Elsevier Publ. Co, ISBN;0-444-89449-7.

/2/ **Pusch R, Karnland O and Hökmark H, 1990.** GMM – A general microstructural model for qualitative and quantitative studies of smectite clay. SKB Technical Report 90-43. Svensk Kärnbränslehantering AB.

/3/ **Pusch, R, 1987.** Identification of Na-smectite hydration by use of "humid cell" High Voltage Microscopy. Applied Clay Science, Vol 2 (pp 343–352).

/4/ **Pusch R, 1994**. Gas transport through smectitic clay and crystalline rock. SKB AR 94-61. Svensk Kärnbränslehantering AB.

/5/ **Yong R N, Warkentin B P, 1975.** Soil properties and behaviour. Elsevier Publ. Co.

/6/ **Kato H, Muroi M, Yamada N, Ishida H, Sato H, 1995.** Estimation of effective diffusivity in compacted bentonite. In: Murakami T, Ewing R C (Ed). Scientific Basis for Nuclear Waste Management XVIII. Mat. Res. Soc. Symp. Proc., Vol 353, MRS Pittsburgh (pp 277–284).

/7/ **Börgesson L, 1995**. Swelling and homogenisation of bentonite granules in buffer and backfill. SKB AR 95-22. Svensk Kärnbränslehantering AB.

/8/ **BEASY User Guide, 2002.** Computational Mechanics BEASY Ltd, Southampoton, UK.

/9/ **Pusch R, Muurinen A, Lehikoinen J, Bors J, Eriksen T, 1999.** Microstructural and chemical parameters of bentonite as determinants of waste isolation efficiency. European Commission, Contract No F14W-CT95-0012, Directorate-General Science, Research and Development.

/10/ **Pusch R, 1999.** Experience from preparation and investigation of clay microstructure. Eng. Geology, Vol 54 (pp 187–194).

/11/ **Pusch R, 1967.** A technique for investigation of clay microstructure. J. Microscopie, Vol 6 (pp 963–986).

/12/ **Windisch O, 1937.** Die neue Fotoschule. Heering-Verlag, Harzburg (p 123).

/13/ **Horseman S T, Harrington J F, Sellin P, 1999.** Gas migration in clay barriers. Eng. Geol. Vol 54 (pp 139–149).

/14/ **Neretnieks I, Moreno L, 1993.** Fluid flow and solute transport in a network of channels, Journal of Contaminant Hydrology, 14, (pp 163–192).

/15/ **Pusch R, 2001a.** Microstructural modelling of transport in smectitic clay buffer. Proc. Int. Symp. on Suction, Swelling, Permeability and Structure of Clays, Eds K Adachi, M Fukue, Shizuoka 11–13 Jan. 2001. Balkema, Rotterdam/Brookfield.

/16/ **Yong R N, 2002.** Modelling approaches used for the engineered barrier system (EBS) and their application in performance assessment, Proc. 2nd. CLUSTER URL's Seminar, Belgium, EUR 19954 (pp 9–10).

/17/ **Warrick A W, Amoozegar-Fard A, 1979.** Infiltration and drainage calculations using spatially scaled hydraulic properties, Water Resources Research, Vol 15 (pp 1116–1120).

/18/ **Pusch R, 1983.** Stability of bentonite gels in crystalline rock – Physical aspects. SKB (SKBF/KBS) Technical Report 83-04. Svensk Kärnbränslehantering AB.

/19/ **Pusch R, 2001.** Experimental study of the effect of high porewater salinity on the physical properties of a natural smectitic clay. SKB TR-01-07. Svensk Kärnbränslehantering AB.

4 Heat transport

This chapter deals with heat transport in fully and partly water saturated buffer clays. It includes mathematical formulation of empirically deduced material models of heat conductivity and gives examples of how thermal parameters can be evaluated from laboratory experiments.

From the point of performance assessment the thermal parameters heat conductivity and capacity should be accurate within +/– 10%, which means that they must be evaluated from careful tests. Underestimation of the buffer temperature by 10–20°C through inadequately performed experiments can have a significant influence on chemical processes like mineral stability .

4.1 Processes

Heat transport in soil takes place in several ways:

1. By conduction through interconnected minerals.
2. By conduction through water in continuous voids.
3. By convection in flowing porewater.
4. By vapor transport in unsaturated soil under the influence of a thermal gradient.

The efficiency of heat conduction through interconnected minerals depends on the kind of minerals and how effectively they are contacted /1/. For smectite-rich bentonite the interconnectivity of the stacks of lamellae is not very good since they are separated by thin water films. The heat conductivity of water saturated bentonite is hence relatively low, i.e. 1.2–1.5 W/m,K.

Knowledge of how heat transport takes place is required for a number of purposes:

1. Prediction of the temperature evolution in buffer as a function of the degree of water saturation and mineral composition.
2. Planning and performance of experiments for determining and evaluating thermal parameters.
3. Prediction of heat transport from a hot canister through the bentonite buffer and into the surrounding rock in the course of water saturation.

4.2 Heat conductivity of bentonite

4.2.1 Kahr and Müller-von Moos /2/

The investigators defined an expression of the heat conductivity of bentonite, Equation (4-1), which empirically describes the relation between the heat conductivity, the bulk density ρ and the water content w with an accuracy of about +/– 0.1 W/m,K:

$$\lambda = 0.56 + 0.60\ \rho + 0.4\ \rho^3\ w/(w + 1) \qquad (4\text{-}1)$$

where:

ρ = bulk density with actual water conten
w = water content

The influence of the temperature was determined on completely dry samples and was found to increase with temperature T(°C) according to Equation (4-2):

$$\Delta\lambda = 0.01 \cdot (\Delta T)^{0.5} \qquad (4\text{-}2)$$

For bentonite close to water saturation, it means that λ will be 0.08 W/m,K higher at the maximum temperature in a repository than at room temperature in the laboratory.

4.2.2 Beziat et al /3/

These investigators derived an expression for a smectitic soil with rather much kaolinite (the French reference clay for buffer material Fo-Ca7), applying the geometric mean model for porous media /4/). Equation (4-3) gives the expression of the heat conductivity:

$$\lambda = \lambda_s^{1-n} \cdot \lambda_w^{n \cdot S_r} \cdot \lambda_a^{n \cdot (1-S_r)} \qquad (4\text{-}3)$$

where:

λ_s = heat conductivity of solids = 2.6 W/m,K
λ_w = heat conductivity of water = 0.6 W/m,K
λ_a = heat conductivity of air = 0.024 W/m,K
n = porosity (pore volume divided to total volume)
n = $e/(1+e)$
S_r = degree of saturation %

The value of λ_s = 2.6 W/m,K was found to give the best agreement with the measured values and it coincides well with what is considered to be an average of soil minerals containing insignificant amounts of quartz. Good agreement between the calculated and measured values were obtained for clay with a void ratio e varying between 0.45 and 1.5 at the water contents 5% and 11%, corresponding to $10\% < S_r < 65\%$, and the measured heat conductivities varied from 0.2 W/m,K to 1.1 W/m,K. The accuracy in this investigations was about +/– 0.2 W/m,K.

4.2.3 Knutsson /5/

Knutsson worked out a hypothesis according to which the heat conductivity λ can be calculated by using Equations (4-4) to (4-8):

$$\lambda = \lambda_0 + K_e (\lambda_1 - \lambda_0) \quad (4\text{-}4)$$

where:

$$\lambda_0 = 0.034 \cdot n^{-2.1} \quad (4\text{-}5)$$

$$\lambda_1 = 0.56^n \cdot 2^{(1-n)} \quad (4\text{-}6)$$

$$K_e = 1 + \log S_r \quad (4\text{-}7)$$

where:

λ_0 = heat conductivity at $S_r = 0$
λ_1 = heat conductivity at $S_r = 100\%$
K_e = coefficient of influence of the degree of saturation S_r
n = porosity

Equation (4-4) was found to be valid with the accuracy +/– 20%.

The influence of temperature and pressure can be modeled by use of Equation (4-8) according to Knutsson:

$$\lambda_2/\lambda_1 = 1 + \beta \cdot \Delta T/100 \quad (4\text{-}8)$$

where:

λ_2 = thermal conductivity at the higher temperature
λ_1 = thermal conductivity at the lower temperature
ΔT = temperature difference
β = parameter ranging from 0.09–0.17

Equation (4-8) yields the same increase in the heat conductivity (0.08 W/m,K) at the maximum temperature in a KBS-3 repository as Equation (4-4).

According to Knutsson's model the combined effect of temperature and pressure will increase the heat conductivity by 0.1–0.15 W/m,K in canister-surrounded buffer.

4.2.4 Comparison of models

The three models for calculating the heat conductivity of bentonite-based buffer materials have yielded good agreement with experimental data. Comparison is made in Figure 4-1, which shows the thermal conductivity λ as a function of the void ratio e at three different degrees of saturation S_r. The diagram shows that the scatter is 0.1–0.3 W/m,K except for S_r=1.0 at low void ratios, for which it is 0.5 W/m,K. Only a few tests were made on completely saturated materials by Knutsson.

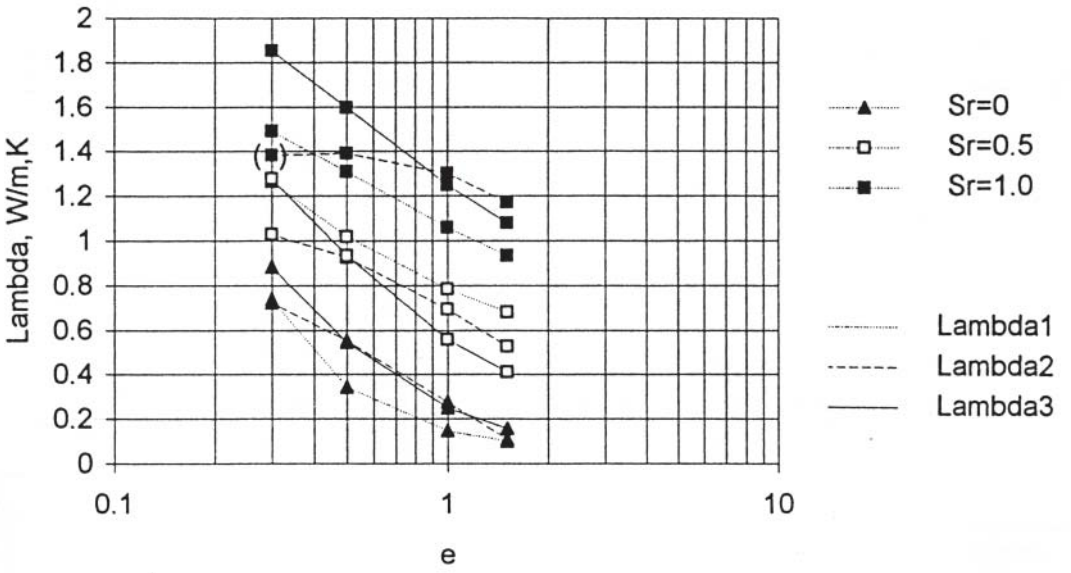

Figure 4-1. *Influence of the degree of saturation and the void ratio on the heat conductivity calculated by three different methods.*
λ_1 – Knutsson
λ_2 – Kahr et al
λ_3 – Beziat et al

Figure 4-2 shows the average values for the respective tests and the scattering. The three methods yield bands within which the heat conductivity values of full-sized bentonite blocks evaluated from field tests are located.

The influence of the degree of saturation on the heat conductivity calculated according to these three methods is illustrated in Figure 4-3. The data do not vary by more than 0.2 W/m,K while the curve shapes are quite different. Thus, the slope (the increase in λ with increasing S_r) increases with increasing S_r for λ_1 according to Knutsson's model while it is almost constant for λ_2 according to the model by Kahr. It decreases with increasing S_r for λ_3 according to Beziat's model.

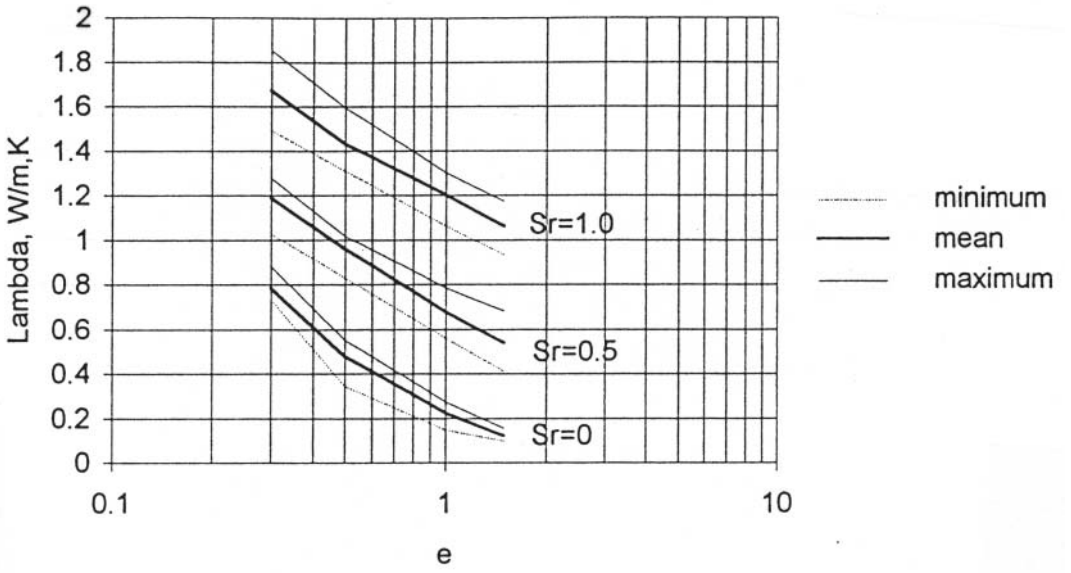

Figure 4-2. *The average theoretical heat conductivities calculated from Figure 4-1.*

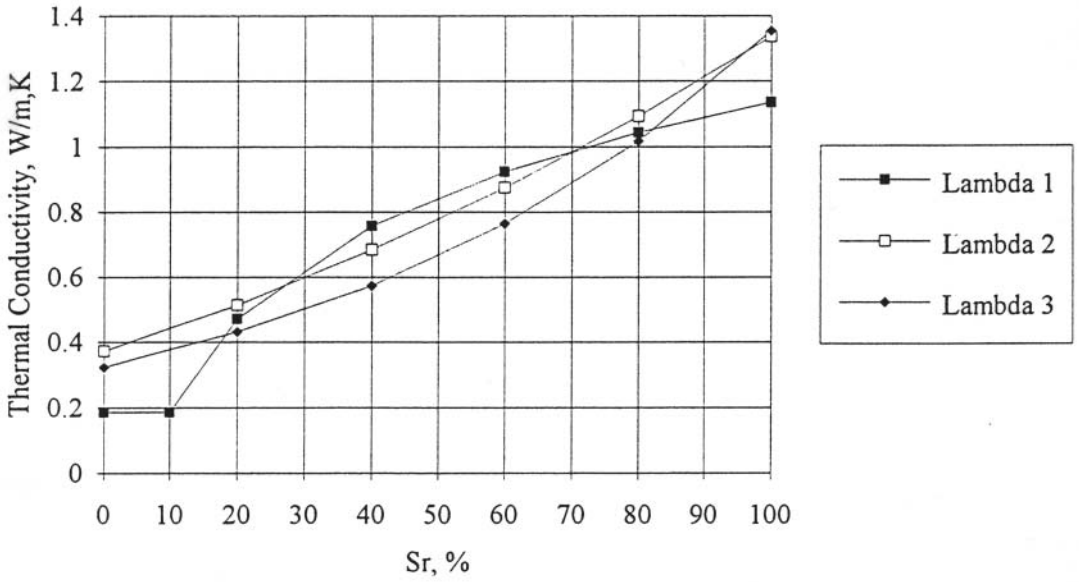

Figure 4-3. *Influence of the degree of saturation on the heat conductivity at the constant void ratio e = 0.8 according to the three different methods.*
λ_1 – Knutsson
λ_2 – Kahr et al
λ_3 – Beziat et al

4.3 Heat conductivity of mixtures of bentonite

Minerals added to bentonite will form a continuous network if they make up a certain minimum fraction of the mixture. Random mixing means that the net heat conductivity of the mixture can be taken as the geometric mean of the respective conductivities /3/. This gives Equation (4-9):

$$\lambda=\lambda_B^{1-q} \; x \; \lambda_q^{\,q} \qquad (4\text{-}9)$$

where:

λ_B^{1-q} = heat conductivity of the bentonite
$\lambda_q^{\,q}$ = heat conductivity of the additive

Taking the example of a mixture with a density at saturation of 2000 kg/m^3 of bentonite and quartz in weight proportions 3:1 and 2:1, with λq as 3.0 W/m,K and λ_B as 0.5, one finds that lambda for the mixtures is about 1.9 and 2.0 W/m,K, respectively. This shows that the quartz content has to be at least 50% to have a strong significant impact on the bulk heat conductivity.

4.4 Examples

4.4.1 Evaluation of the heat conductivity from laboratory experiments

Problem: Determine the heat conductivity from a "probe" experiment with compacted bentonite.

Basic

The most commonly used technique for determining the heat conductivity of soil materials is to apply a stationary heat flow through the sample. This technique is very accurate but difficult in the sense that it requires a constant thermal gradient in the sample. This is a problem in partially water saturated materials since the heat gradient will cause moisture redistribution in the sample. For this reason, a method that is adaptated to transient heat flow conditions and that requires very short measuring time should be used although it is less accurate /6/.

Solution

The probe method can be used for this purpose and it is based on the use of a pin with a length that is much larger than the diameter and that is inserted in the center of the sample and heated with constant power. The temperature is measured in the center of the probe and recorded as a function of time as illustrated by Figure 4-4. If the length/diameter ratio is large enough, the axial heat conduction can be neglected and the central section modelled as a one-dimensional axial symmetric system. The temperature increase in the probe can be calculated according to Equation (4-10) if the probe is considered to be a line source /1/:

$$T = \frac{-q}{4\pi\lambda} \cdot E_i\left(-\frac{r^2}{4\kappa t}\right) \qquad (4\text{-}10)$$

where:

$$E_i(-x) = \int_x^\infty \frac{1}{z} e^{-z} dz \qquad (4\text{-}11)$$

and:

T = temperature increase
q = heat flow per meter length
λ = heat conductivity
r = radius
κ = heat diffusivity
t = time from start heating

The heat diffusivity κ is defined according to Equation (4-12):

$$\kappa = \frac{\lambda}{\rho C_p} \qquad (4\text{-}12)$$

where:

ρ = bulk density
C_p = heat capacity

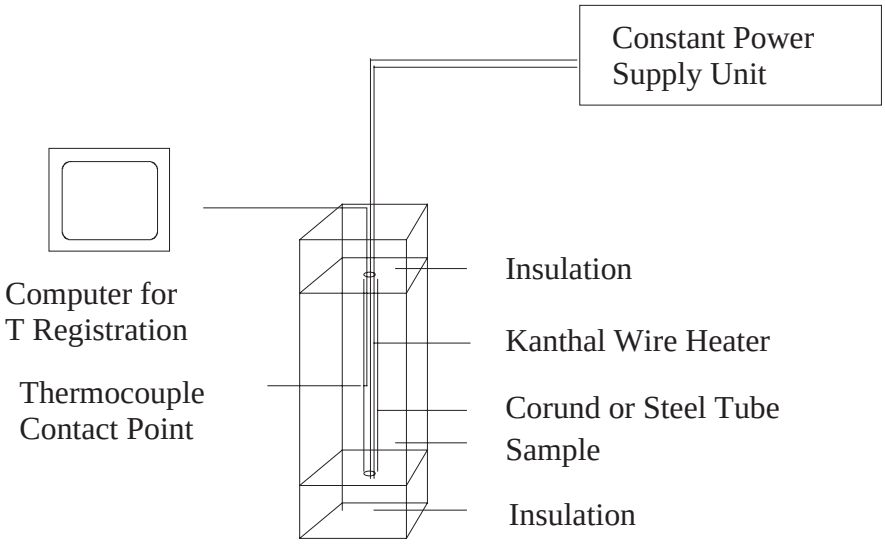

Figure 4-4. *Measurement system for determination of heat conductivity.*

Equation (4-10) can be approximated to the form of Equation (4-13) for long time test conditions and a small probe radius:

$$T_{t2} - T_{t1} = \frac{q}{4\pi\lambda} \ln \frac{t_2}{t_1} \qquad (4\text{-}13)$$

where:

T_{t1} and T_{t2} are the temperature values at times t_1 to t_2, respectively.

Results

The heat conductivity λ can be evaluated by use of Equation (4-14), which is a transformation of Equation (4-13):

$$\lambda = \frac{q}{4\pi\Delta T} \ln \frac{t_2}{t_1} \qquad (4\text{-}14)$$

where:

ΔT = temperature increase of the probe in the time interval t_1 to t_2

The proper time interval for evaluation can be determined if the temperature is plotted as a function of time in a semi-logarithmic diagram. According to Equation (4-13), this relation should be a straight line, deviations from this shape being caused by boundary effects or changes in properties. Figure 4-5 shows an example of a test plotted in this way. The thermal conductivity is graphically evaluated as λ = 1.08 W/m,K.

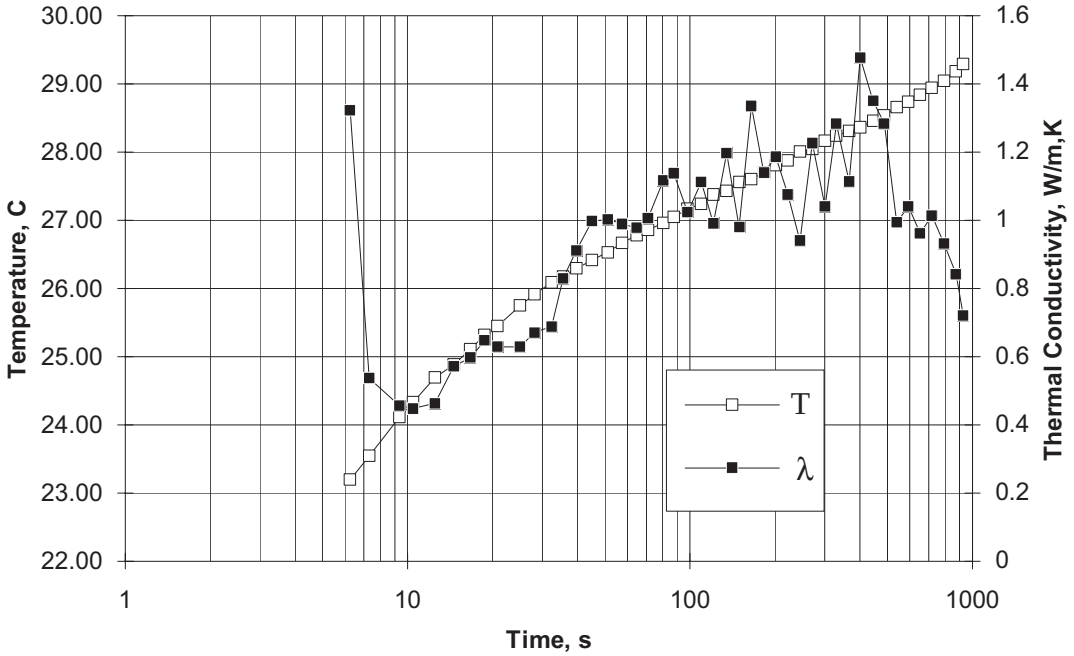

Figure 4-5. *Measured temperature T and evaluated thermal conductivity λ for short time intervals.*

4.4.2 Prediction of the heat evolution in field test simulating a KBS-3 type repository

Problem: Calculate the transient temperature increase due to the heat production of a heater simulating a HLW canister embedded by compacted bentonite and located in a hole with 0.8 m diameter and 4 m depth in granite (half-scale KBS-3). The power of the heater is maintained at 600 W for 3.5 years.

Method

Solution of the problem requires the use of numerical calculation techniques like the finite element mehtod. The heater, bentonite clay and surrounding rock, to which relevant thermal properties have to be ascribed, are divided into elements for which the initial thermal conditions are defined. The heat flow is assumed to take place through diffusion similar to the process in "probe" tests.

Solution

An element mesh with rotational symmetry around the central axis of the heater is used. It consists of 17x32 elements with a distance of 25 m to the radial boundary and 15 m to the boundaries in axial directions (Figure 4-6). The thermal properties of all materials are compiled in Table 4-1.

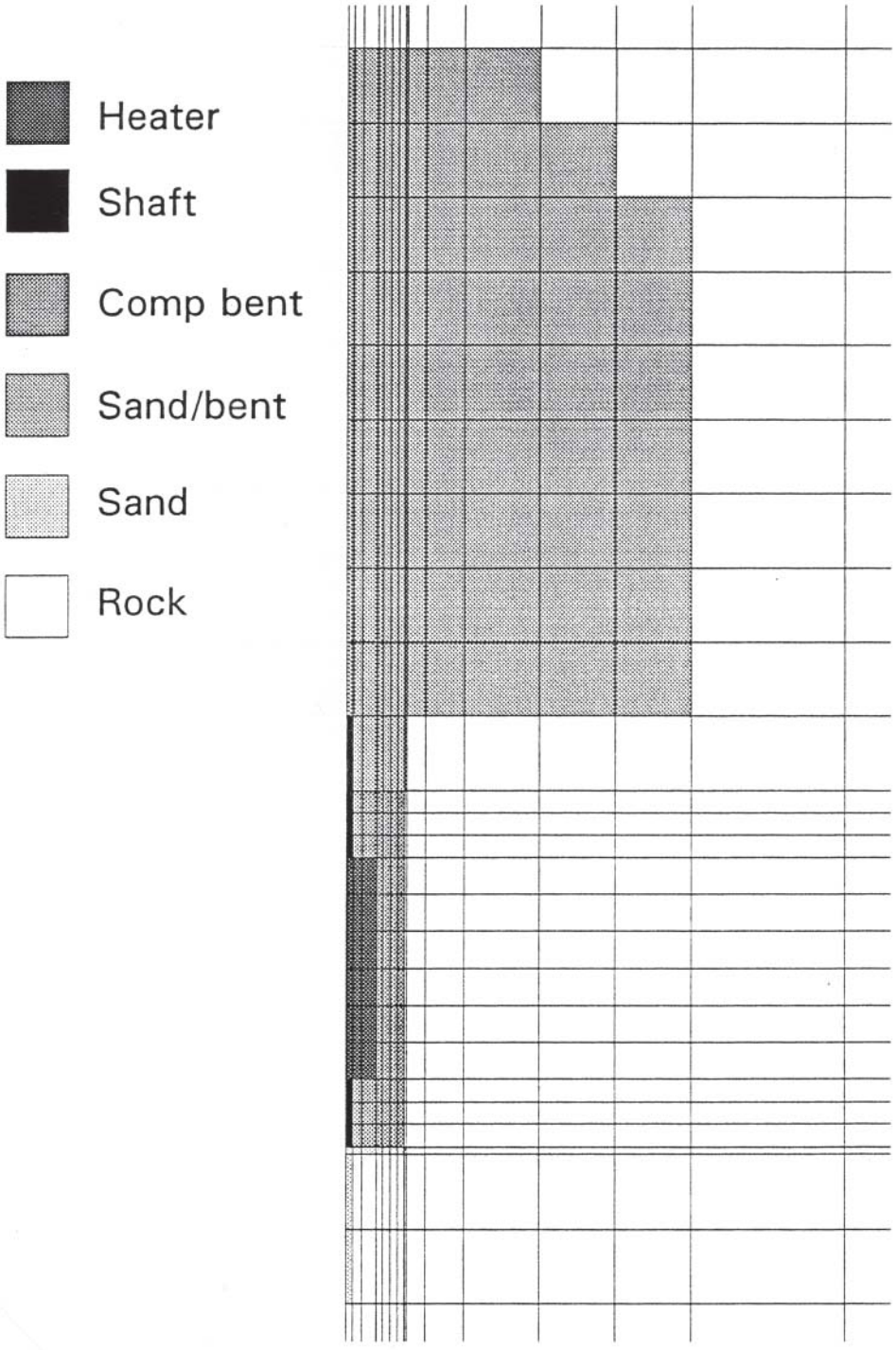

Figure 4-6. *Element mesh and materials with different thermal properties used in the example /6/.*

Table 4-1. Thermal indata for the calculation /6/.

Material	λ W/m,K	C_p Ws/kg,K	ρ kg/m^3
Heater	59	460	7800
Heater shaft	14.75	460	7800
Buffer	1.0–1.45	1100	2170
Backfill	2.2	1400	2150
Sand	2.1	1600	2100
Rock	3.6	800	2700
Slot	0.5	4200	1000

Results

Results from the following three calculations will be given:

BMT7: Calculation simulating the conditions in the beginning of the test with a slot with λ=0.5 W/m,K and bentonite blocks with λ=1.0 W/m,K.

BMT8: Calculation simulating the condition at the end of the test with a water saturated homogeneous buffer with λ=1.35 W/m,K.

BMT9: Do. with λ=1.45 W/m,K.

The calculated temperature distributions at mid-height heater at different times after powering are shown in Figure 4-7. One finds that temperature equilibrium is reached after about 3 years in all the cases. Further, it is demonstrated that if the buffer can be prepared with a water content that yields a heat conductivity of 1.35 W/m,K the maximum buffer temperature can be about 10°C lower than if the heat conductivity is 1.0 W/m,K. Buffer with W=0,75 W/m,K, which corresponds to dense MX-80 with 10% water content, would give a maximum temperature of more than 80°C.

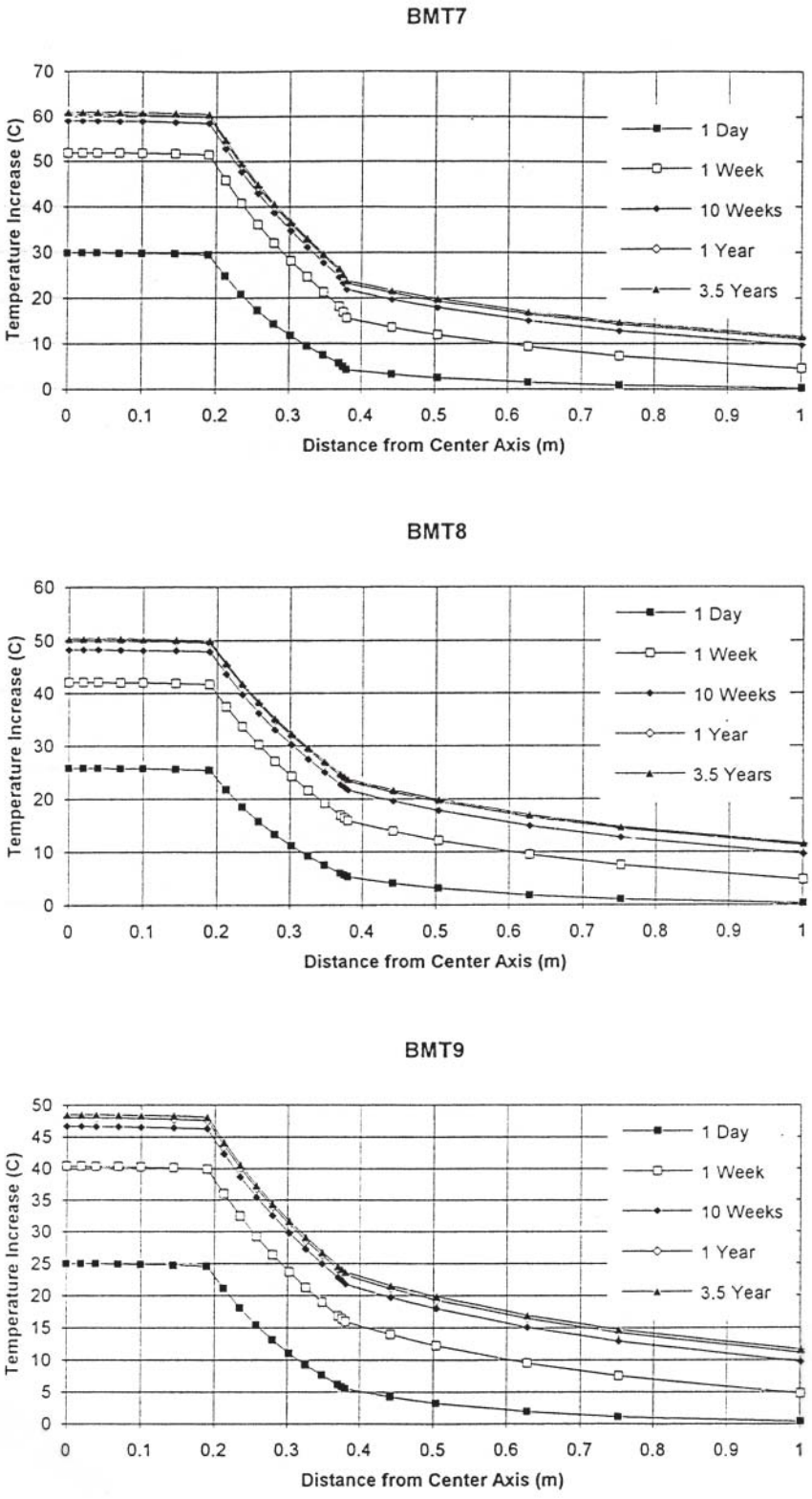

Figure 4-7. *Calculated temperature distribution in the central section of the canister.*
BMT7: Unsaturated blocks with λ=1.0 W/m,K and a slot at the rock.
BMT8: Saturated buffer with λ=1.35 W/m,K.
BMT9: Saturated buffer with λ=1.45 W/m,K.

4.5 References

/1/ **Farouki O T, 1986.** Thermal Properties of Soils. Trans Tech Publications.

/2/ **Kahr G, Müller-vonMoos M, 1982.** Wärmeleitfähigkeit von Bentonit MX-80 und von Montigel nach der Heizdrahtmethode. NAGRA Technischer Bericht 82-06.

/3/ **Beziat A, Dardaine M, Gabis V, 1988.** Effect of compaction pressure and water content on the thermal conductivity of some natural clays. Clays & Clay Minerals Vol 36, No 5.

/4/ **Woodside W, Messmer J M, 1961.** Thermal conductivity of porous media. Journal of Applied Physics, vol 32, No 9.

/5/ **Knutsson S, 1983.** On the thermal conductivity and thermal diffusivity of highly compacted bentonite. SKB TR 83-72. Svensk Kärnbränslehantering AB.

/6/ **Börgesson L, Fredrikson A, Johannesson, 1994.** Heat conductivity of buffer materials. SKB TR 94-29. Svensk Kärnbränslehantering AB.

5 Water transport

This chapter deals with flow of water in liquid and vapor form in fully and partly water saturated buffers and backfills. The presented material models are intended for practical use and imply that potential theory in the form of Navier/Stoke's laws for analytical solution or application of numerical methods are applied. These modes of calculation are not described here but merely the features and use of the basic material models.

5.1 Processes

Water flow through buffers and backfills are controlled by the degree of water saturation and of the pore size distribution and interconnectivity of voids of "external" and "internal" (interlamellar) type. The mechanisms and fundamental processes involved in water flow through buffers and backfills are described in Section 3.1. In the present chapter, practical ways of calculating bulk flow through buffers and backfills is described.

5.2 Fluid flow

Potential theory in the form of Darcy's law forms the basis of calculation of flow through buffers and backfills. The general expression for the flow rate at uniaxial percolation of a porous sample is given by Equation (5-1):

$$v=k\rho gi/\eta \qquad (5\text{-}1)$$

where:

v = velocity
k = permeability
ρ = density
η = viscosity
g = gravity constant
i = hydraulic gradient (dh/dl), h=pressure head, l=flow path length

This expression, which can be used for calculating the influence of heat by inserting relevant viscosity data for any desired temperature, does not contain porosity or void ratio or the content of immobile water but simply gives an average measure of the permeability of a soil element. In practice, i.e. where the density and temperature dependence of water fluidity is of minor importance, the flow is expressed as the average velocity over a cross section of soil without referring to what part of a cross section that is really permeable. The so defined flow rate is expressed in terms of the (average) hydraulic conductivity K in Equation (5-2):

$$v=Ki \qquad (5\text{-}2)$$

where v and K are expressed in m/s and i is dimensionless (m/m).

Hence, knowing the hydraulic gradient, which is determined by applying potential theory using analytical or numerical solutions or graphical flow nets, the flow rate can be calculated for saturated soils and also the flux q using Equation (5-3):

$$q = vA \tag{5-3}$$

where v=average flow rate in m/s and A=total cross section in m^2.

5.3 Deviations from Darcy's law

5.3.1 Influence of microstructural disturbance through erosion and clogging

Water flow through soils in general and in bentonites in particular is very heterogeneous due to the variations in microstructural density /1/. Thus, percolation takes place in a stochastic fashion with most of the flow through a few major channels formed by interconnected zones of lower density than the average. Here, the flow rate may be several times higher than the average rate of percolation by which particles may be teared off and transported, yielding clogging and local reduction in conductivity and thereby alteration of the flow paths. Also, flow initiated by instantaneous application of a pressure gradient may disrupt organized water lattices in the interlamellar space and in very narrow capillaries and they become reorganized with time. These processes may cause successive reduction of the hydraulic conductivity as illustrated by Figure 5-1.

5.3.2 Influence of hydraulic gradients

Microstructural disturbances largely depend on the hydraulic gradient as illustrated by Table 5-1, which is a compilation of data from laboratory investigations of smectitic clays /3/. More recently it has been found that the influence of the hydraulic gradient on the recorded hydraulic conductivity is particularly obvious at percolation of smectite clay with Ca-rich solutions.

Table 5-1. Influence of the hydraulic gradient on the hydraulic conductivity of GEKO/QI bentonite /3/.

Bulk density, kg/m^3	Hydraulic gradient *i*	Hydraulic conductivity *K*,m/s
1800	100	9E-12
1600	100	9E-11
1600	50	6E-11
1300	10	6E-9
1300	5	2E-9
2170 (10/90 bent/sand)	4.2	4E-9
2170 (10/90 bent/sand)	0.42	2E-9
2170 (10/90 bent/sand)	0.08	E-9

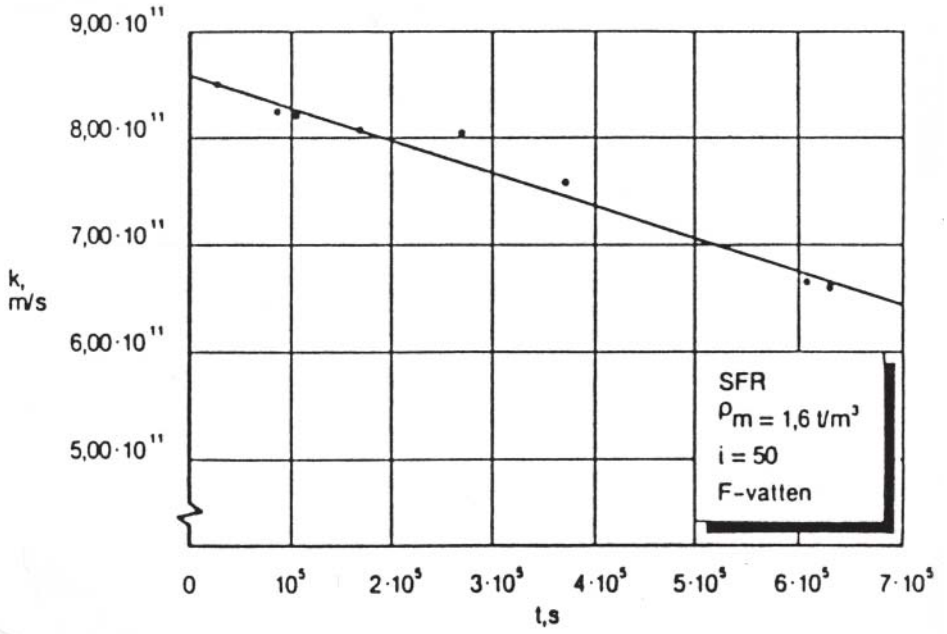

Figure 5-1. *Successive reduction of the evaluated hydraulic conductivity under constant pressure conditions. GEKO/QI bentonite with a dry density of 950 kg/m^3 (1600 kg/m^3 at saturation). Hydraulic gradient=50 /2/.*

These data suggest that the hydraulic conductivity drops roughly in proportion to the drop in gradient for pure bentonite, which is of great importance for bentonite buffers since the hydraulic gradient in a repository will be lower than unity very soon after backfilling the tunnels. The less obvious decrease in conductivity for bentonite-poor mixtures is because a significant part of the flow takes place through clay-free parts of the void system of the ballast (cf Chapter 3).

5.3.3 Influence of temperature

Heating of bentonite under constant effective stress conditions causes the hydraulic conductivity to increase due to the resulting drop in viscosity of the porewater /4/. Hence, k in Equation (5-1) can be calculated for any desired temperature and since v and i are then known, K can be calculated by use of Equation (5-2).

An example of the practical importance of the heat-induced change in hydraulic conductivity of the buffer clay is the impact on porewater chemistry in a KBS-3 repository. Soon after emplacement of the buffer its temperature is at maximum, i.e. about 90°C, while the temperature is back to ambient, i.e. around 10°C, after 3000 years at which time the viscosity is increased by about 3 times and the hydraulic conductivity reduced by the same factor. The larger part of the drop in conductivity takes place in the first few hundred years, which is when the majority of the chemical reactions in the near-field take place.

5.3.4 Influence of porewater chemistry

The composition of the porewater chemistry has the strongest impact on the hydraulic conductivity as outlined in Chapter 3. Any conductivity value to be used in calculating water flow through buffers and backfills must refer to properly conducted laboratory tests or data evaluated from microstructural analyses (cf Chapter 3).

5.4 Hydraulic conductivity of water-saturated system of elements of different conductivity

5.4.1 Soil heterogeneity

Preparation of artificial soils, like buffers and backfills, yields varying density and hydraulic conductivity. This is particularly important in preparing mixtures of different components, i.a. backfills of bentonite, ballast and water since both the mixing operation and on-site compaction will cause variations in the bentonite/ballast ratio and in density. Figure 5-2 shows an example of the evaluated variation in hydraulic conductivity of a mixture of 15% bentonite and 85% sand. For such cases it is of practical importance to be able to calculate the mean hydraulic conductivity, which is described in this section.

The basis of calculations of this sort is shown in Figure 5-3, which indicates that when a system of elements with different hydraulic conductivity is permeated, the flow through the system depends on the direction of flow. For the case with two elements, where $k_2 >> k_1$, one finds that if flow takes place in the y-direction, the low-conductive element will control the entire percolation, while flow in the x-direction will be dominated by the high-conductive element. For the general case in Figure 5-4 the resulting hydraulic conductivity of the system will be as described by Equation (5-4) for the indicated flow direction.

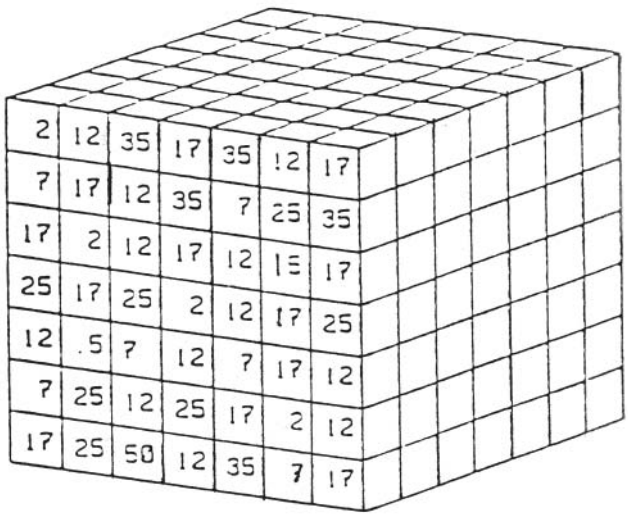

Figure 5-2. *Variation in hydraulic conductivity of bentonite/sand mixture applied on site as evaluated from density determinations /5/. The individual figures for the elements have to be multiplied by 10^{-11} to give the correct hydraulic conductivity.*

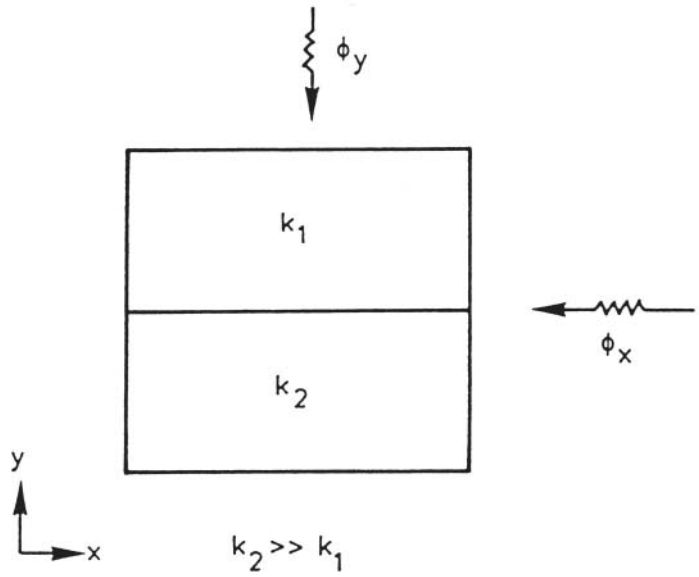

Figure 5-3. *Dependence of the flow direction on the net hydraulic conductivity.*

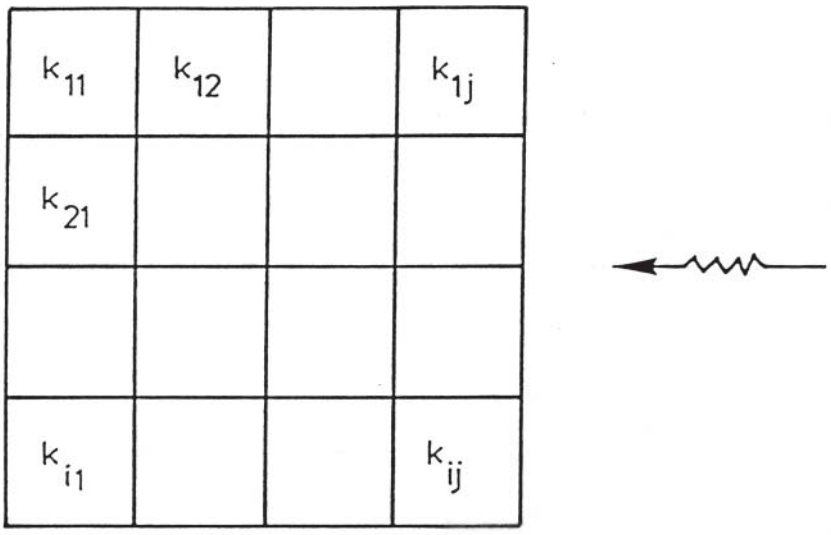

Figure 5-4. *System of elements with different hydraulic conductivity percolated in one direction.*

5.4.2 Mathematical expressions for the hydraulic conductivity of soil with varying permeability

$$K = \frac{1}{m} \cdot \sum_{i=1}^{m} \left[n \cdot \left[\sum_{j=1}^{n} \left[\frac{1}{k_{ij}} \right] \right]^{-1} \right] \qquad (5\text{-}4)$$

If n=1, K is the arithmetic mean, while for $n=m$, K corresponds to the geometric mean.

5.5 Hydraulic conductivity of unsaturated soil

5.5.1 Water flow

Percolation of unsaturated buffers and backfills is very complex because the driving force is both the prevailing hydraulic gradient and the suction power caused by the high affinity for water of smectite clay. Thus, applying a water pressure to one end of an unsaturated buffer element will set up a gradient across the element and a local very high gradient at the wetting front that successively advances into the element. The process is transient and one can therefore not define a hydraulic conductivity of such materials.

One commonly distinguishes between motion of liquid water and water in vapor form. The flux of liquid water is modeled by applying Darcy's law, taking the hydraulic conductivity K_p to be a function of the void ratio, degree of saturation, and temperature. K_p is assumed to be a function of the hydraulic conductivity K of saturated clay as expressed through Equation (5-5):

$$K_p=(S_r)^{\delta}K \qquad (5\text{-}5)$$

where K_p and K are expressed in m/s, and d is an exponent that can vary in the interval 3–7 for soils. It may be taken as 3 as a reasonable average for bentonite.

Equation (5-5) is a simplified version of an expression proposed by Brooks and Corey /6/, adaptated to bentonites /7/.

5.5.2 Vapor flow

Heating of unsaturated buffer produces evaporation of water and an increased vapor pressure that causes diffusion of vapor into regions with lower vapor pressure and lower temperature, where condensation takes place. Hence, water transport takes place from hotter to colder parts of a clay element. The process has been modeled as a diffusion process with the temperature and vapor pressure gradients as driving forces /8,9/. The flow can be expressed as by Equation (5-6):

$$q_v = -D_{Tv} \nabla T - D_{pv} \nabla p_v \qquad (5\text{-}6)$$

where:

q_v = vapor flow
D_{Tv} = thermal vapour flow diffusivity

T = temperature
D_{pv} = isothermal vapor flow diffusivity
p_v = vapor pressure

If the isothermal vapor flow is neglected, Equation (5-6) will simplify to yield:

$$q_v = -D_{Tv}\nabla T \qquad (5\text{-}7)$$

The diffusion coefficient D_{Tv} varies with the degree of saturation since there is a difference in availability of air-filled connections in the buffer as well as a difference in bonding strength between the clay particles and the water at different degrees of saturation.

The water vapor diffusivity D_{tv} can be evaluated from the temperature gradient tests by calibration calculations.The following empirical relations were found to yield fairly accurate results:

$$D_{Tvb}=8.0\text{E-}11 \text{ m}^2/\text{s,K} \qquad 0.3\leq S_r\leq 0.7 \qquad (5\text{-}8)$$

$$D_{Tv} = D_{Tvb=} \cdot cos^6\left(\frac{S_r - 0.7}{0.3}\cdot\frac{\pi}{2}\right) \qquad S_r\geq 0.7 \qquad (5\text{-}9)$$

$$D_{Tv} = D_{Tvb} \cdot sin^6\left(\frac{S_r}{0.3}\cdot\frac{\pi}{2}\right) \qquad S_r\leq 0.3 \qquad (5\text{-}10)$$

The diffusivity is thus constant with a basic value D_{Tvb} between 30% and 70% degree of saturation. It decreases strongly to D_{Tv}=0 at 0% and 100% saturation. Figure 5-5 shows the relation between the diffusion coefficient and the degree of saturation.

The influence of temperature and void ratio on the diffusivity is not known and not considered in the model.

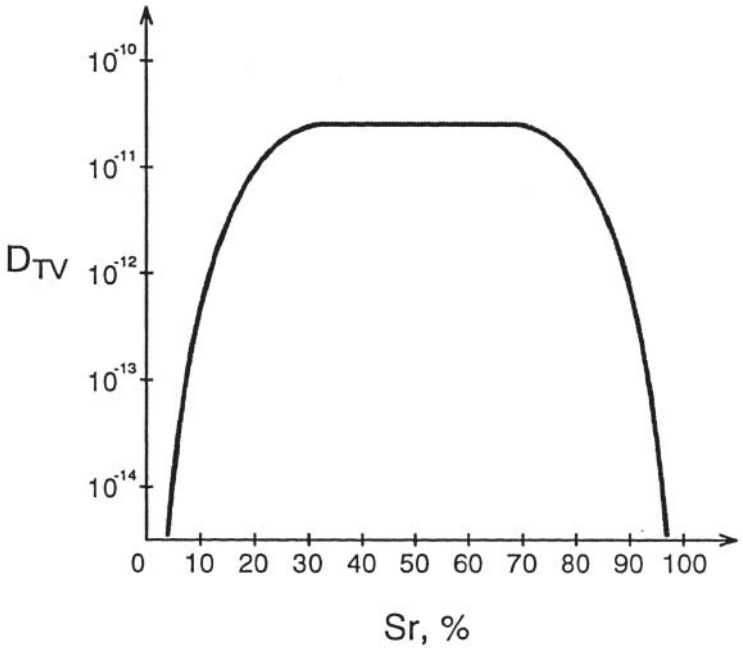

Figure 5-5. *Assumed thermal vapor diffusivity D_{tv} expressed in $m^2/s,K$ as a function of the degree of water saturation S_r for MX-80 clay.*

5.6 Physical aspects

Combination of the Darcy and Kozeny/Carman flow laws yields the expression for the permeability k in Equation (5-11), /10/:

$$k = n^3 / (1-n)^2 b T^2 R^2 \qquad (5\text{-}11)$$

where:

b = pore shape factor (2.5)
T = tortuosity ($\sqrt{2}$)
R = particle surface area per unit volume of solids
n = porosity

Typically, the deviation from theory is as exemplified in Figure 5-6, which can be explained by the impact of the following factors:

1. Electrokinetic coupling for liquid forced through clay causes opposite osmotic flow is neglected.
2. The influence of viscosity is higher than predicted by the Poiseuille law, which is a basis for derivation of Equation (5-11).
3. The pore geometry is more complex than derived from simple patterns of homogeneous pore geometry.
4. The pore size varies in contrast to what is assumed in the derivation of Equation (5-11).
5. The pore size varies with the electrolyte content of the pore liquid due to aggregation or dispersion.

The influence of the factors termed 3, 4, and 5 has been considered in the microstructural models (Chapter 3). The effect of the first factor (1) is obvious by considering the irreversible thermodynamic relationships that apply to the steady state and electrical flows in water-saturated clay /10/. Following Olsen one has, from Onsager's general phenomenological relationships for irreversible phenomena, the following equations:

$$q_w = L_{11}(P/L) + L_{12}(E/L) \qquad (5\text{-}12)$$

$$q_e = L_{21}(P/L) + L_{22}(E/L) \qquad (5\text{-}13)$$

where:

L = element length
q_w = water flow rate
q_e = electrical current flow rate
P/L = hydraulic gradient
E/L = electrical potential gradient
$L_{12} = L_{21}$
L_{11}, L_{12}, L_{21}, L_{22} = phenomenological coefficients

Equation (5-12) implicitely expresses the hydraulic conductivity and it is obvious that if the influence of electrokinetic coupling is negligible or absent, the electrical flow potential term vanishes and the expression gets the form of Darcy's law, i.e. Equation (5-1):

$$q_w = L_{11}(P/L) \qquad (5\text{-}14)$$

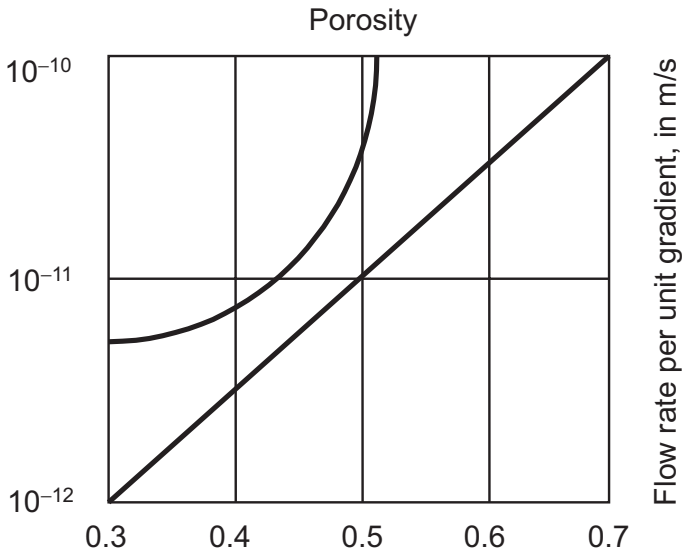

Figure 5-6. *Generalized difference between predicted (straight line) and recorded (curve) relationship of flow rate and porosity for illite percolated by saline Na-dominated water /10/.*

The influence of electrical coupling on hydraulic flow may hence be expressed by the difference between Equations (5-12) and (5-14), which yields Equation (5-15):

$$(q_2 - q)/q = L_{12}/L_{11}(E/P) \qquad (5\text{-}15)$$

where:

q_2 = flow rate aaccording to Equation (5-12)
q = flow rate according to Equation (5-14)

The maximum retardation in flow rate due to electrokinetic coupling occurs when the percolate is electrolyte-free. According to /10/ it is less than 3.3% for dense illite clay in Na form. Assuming that the effect is proportional to the cation exchange capacity one would assume that the corresponding effect on dense smectite clay is less than 10% and hence of little concern.

The influence of factor 2, i.e. the viscosity, is more complex because it involves the fluidity of porewater at different distances from the mineral surfaces, which is a much debated issue. It has been discussed by Olsen in a fashion that is relevant to the micro-structural models described in Chapter 3, i.e. as follows /10/.

Discrepancies between theoretical and experimental conductivity data due to viscosity effects can be defined as q_3/q, where q_3 is the flow rate of water with anomalous viscosity and q the flow rate predicted from Darcy's law and the Kozeny/Carman equation.

Following Olsen the influence of anomalous viscosity can be made obvious by considering a model with capillary tubes with equal radial r, equal length L_e, and internal coatings of immobile liquid having the thickness t adjacent to the tube walls. For the deduction one introduces also the following parameters:

- Total length of permeate=L
- Internal surface area per unit volume=S
- Volume of voids (per unit volume V)=V_v

- Apparent porosity $n_a=(V_v-V_i)/V$ where V_i=volume of immobile liquid films
- Apparent radius $r_a=r-t$

Applying Darcy's law, the discrepancy ratio q_3/q is related to the permeability ratio k_3/k, which yields Equation (5-16):

$$q_3/q=k_3/k \tag{5-16}$$

One has for the flow rate q_3, assuming Z capillary tubes with an immobile water film of thickness t contained in the cross sectional area A, the expression in Equation (5-17):

$$q_3=Z(\pi/8)\rho/\eta i\ r_a^4=k_3\ i\ A \tag{5-17}$$

where:

ρ = density of water
i = hydraulic gradient

Further, one can define an expression for the cross sectional area A by equating the void volume through which flow occurs with the corresponding void volume of the model /10/:

$$n_a\ A\ L=Z\pi\ r_a^2\ L_e \tag{5-18}$$

$$A=Z\pi\ (r_a^2/n_a)L_e/L \tag{5-19}$$

Substituting Equation (5-19) into Equation (5-17), and solving for k_3, one gets:

$$k_3=\ (\pi/8)\rho/\eta(L/L_e)^2\ n_a\ r_a^2 \tag{5-20}$$

One gets the corresponding expression for q, which yields:

$$k_3/k=q_3/q=(n_a/n)(r_a/r)^2 \tag{5-21}$$

Taking S=particle surface area per unit total volume and S_o as the particle surface area per unit solids volume, yielding $S=S_o(1-n)$, one has:

$$S=(Z\ 2\pi\ r\ L_e)/\ (Z\ 2\pi\ r^2\ L_e)=2n/r \tag{5-22}$$

and $r=2n/S$ (5-23)

Further:

$$n_a=n-S\ t \tag{5-24}$$

$$n_a/n=1\ -\ (S\ t)/n \tag{5-25}$$

$$r_a=r-t \tag{5-26}$$

$$r_a/r=1-(t/r)=1-(S\ t)/2n \tag{5-27}$$

Substituting Equations (5-26) and (5-27) into Equation (5-21) one finally gets:

$$q_3/q=1+\beta \tag{5-28}$$

where $\beta\ =3/2(S_o\ t)[(1-n)/n][(S_o\ t)/6\ (1-n)/n\ -1]$ (5-29)

Applying these expressions to kaolinite and illite clays, Olsen arrived at the q_3/q data collected in Table 5-2, from which one finds that the impact on the flow rate is very significant in illite if the immobile layer is 5 Å thick (about 1.5 water molecule layers), while it is negligible in kaolinite except at very low porosities. For smectite clay, which has S_o approaching 1000 m^2/g, the reduction factor gives at least 10 times lower flow rate than in illite. The reason why the real reduction factor is 100 to 1000 is that a major part of the porewater in correspondingly dense smectite clay is immobile.

Table 5-2. Flow reduction factor for illite and kaolinite /11/. n is porosity.

Clay mineral, porosity	*t*, Å		
n	*t*=5 Å	*t*=10 Å	*t*=20 Å
Kaolinite (S_o=11 m^2/g)			
0.2	0.92	0.83	0.67
0.4	0.97	0.94	0.87
0.6	0.99	0.97	0.94
Illite (S_o=100 m^2/g)			
0.2	0.24	0	0
0.4	0.70	0.41	0
0.6	0.86	0.73	0.48

5.7 Examples

5.7.1 Calculation of water flow considering microstructural heterogeneity

Examples of how the hydraulic conductivity can be predicted for clays as based on their microstructural constitution has been given in Section 3.6. In the present section calculation of the distribution of the flow rate over a cross section of Na-bentonite clay will be exemplified. Such analyses are of importance for estimating the risk of erosion and mass transport.

Problem: Calculate the distribution of the flow rate across a section through Reference clays *A*, *B*, and *C* using the "1st" model (GMM), cf Chapter 3. The clays are in Na-form.

Basic

The stochastic character of the microstructural build-up implied by the models described in Chapter 3 means that the distribution of flow is very heterogeneous. The true flow rate can only be calculated by considering the density variation over a cross section.

Solution

The flow variation can be determined by applying the results from the calculations in Chapter 3 with respect to the relative amounts of intersected gel-filled voids. Then, applying an average cross section area of the "capillaries" for the different gel density intervals, the flux distribution is obtained if the hydraulic gradient over the total cross section is taken to be constant.

Results

The content of impermeable or almost impermeable clay matrix and gels of different density determined for the three reference clays *A*, *B* and *C* in Chapter 3 is shown graphically in Figure 5-7. As defined in this section, Clay *A* is only represented by one type of permeable gel-filled voids, namely those with an average density of 1300 kg/m^3, while Clay *B* contains gels with 1300 kg/m^3 and 1200 kg/m^3 and Clay *C* gels with the three densities 1300, 1200 and 1100 kg/m^3 according to the model. The respective fraction of a cross section through the clays is as specified in Table 5-3. Table 5-5 shows the average diameter of the gel-filled intersected voids and the fraction of the total flow through these voids, applying the conductivity data in Table 3-7.

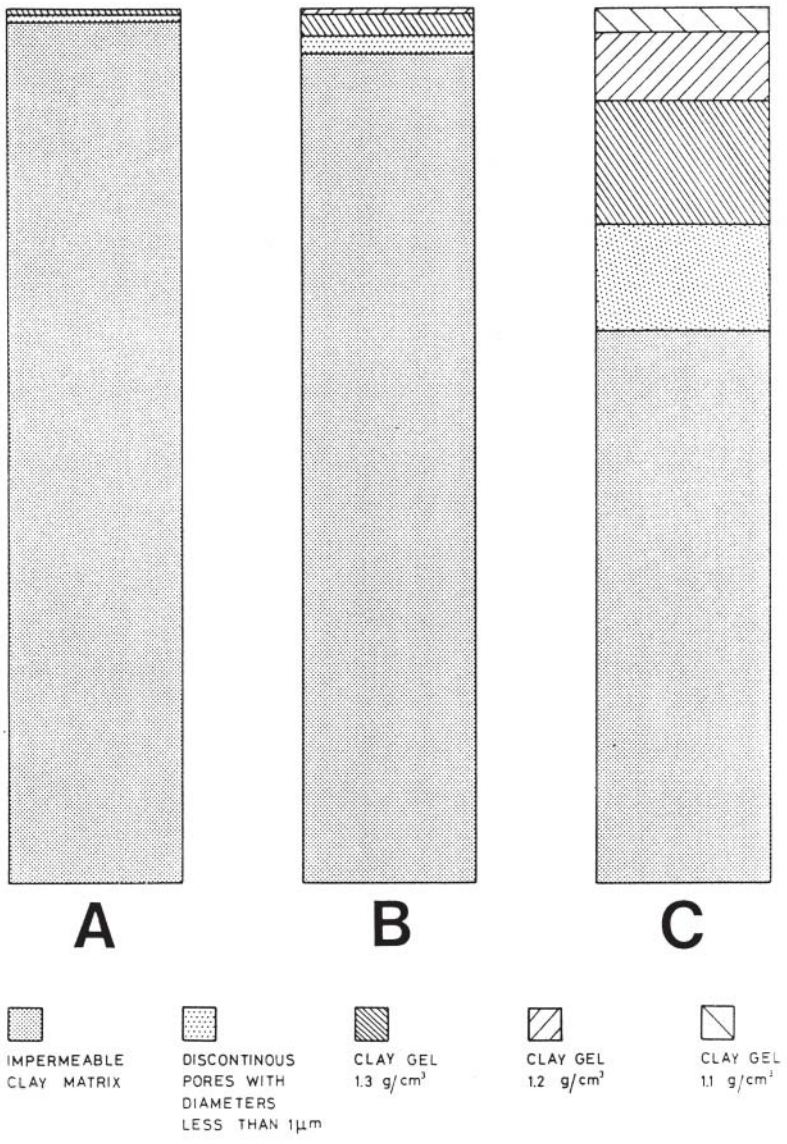

Figure 5-7. *Relative amounts of microstructural units in clays A, B and C.*

Table 5-3. Fractions of a cross section with different gel fillings.

Clay	Density at saturation kg/m^3	Fraction in % of 1300 kg/m^3	Fraction in % of 1200 kg/m^3	Fraction in % of 1100 kg/m^3
A	2130	1.1	–	–
B	1850	4.0	1.1	–
C	1570	23.5	13.0	4.5

Table 5-4. Fraction of flux through voids filled with gels with different densities.

Clay	Density at saturation kg/m^3	Voids with 1300 kg/m^3 gel	Voids with 1200 kg/m^3 gel	Voids with 1100 kg/m^3 gel
A	2130	100%	–	–
B	1850	44%	56%	
C	1570	12%	33%	55%

The distribution of flow is illustrated in Figure 5-8. A practical consequence of the data in Tables 5-4 and 5-5 is that, under the common hydraulic gradient 100 in laboratory experiments, the average flow rate in 4.5% of the percolated cross section of Clay *C*-type samples with 50 mm is about 10^{-5} mm/s, which is not considered to cause significant erosion. If the gradient is increased to 10 000, which corresponds to a water pressure of 1 MPa on a 1 cm thick sample, the flow rate will be 10^{-3} m/s and cause substantial intravoid particle transport /4/.

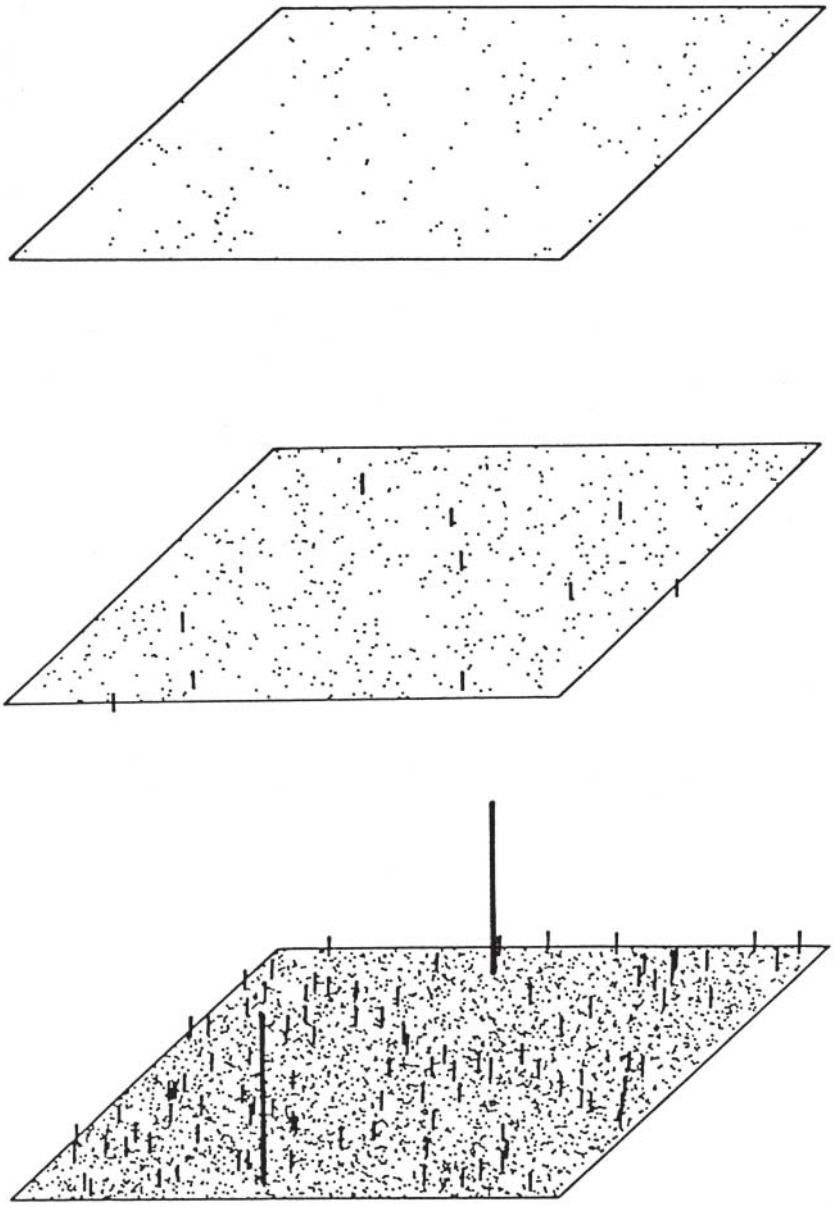

Figure 5-8. *Schematic illustration of the relative flow distribution over a cross section of 250x250 μm² cross section of Na-bentonite with a density at water saturation of 2130 kg/m³ (upper), 1850 kg/m³ (center), and 1570 kg/m³ (lower), /2/. Dots represent 1–5 μm gel-filled voids with 1300 kg/m³ clay gel, short bars 5–20 μm gel-filled voids with 1200 kg/m³ clay gel, and long bars 20–50 μm gel-filled voids with 1100 kg/m³ clay gel.*

5.8 References

/1/ **Hansbo S, 1997.** Aspects of vertical drain design. Geotechnique. (In print.)

/2/ **Pusch R, Hökmark H, Börgesson L, 1987.** Outline of models of water and gas flow through smectite clay buffers. SKB TR 87-10. Svensk Kärnbränslehantering AB.

/3/ **Pusch R, 1985.** Buffertar av bentonitbaserade material i siloförvaret. SKB Arbetsrapport SFR 85-08. Svensk Kärnbränslehantering AB.

/4/ **Pusch R et al, 1995.** The buffer and backfill handbook. Part 1. SKB AR 95-45. Svensk Kärnbränslehantering AB.

/5/ **Pusch R, 1997.** The buffer and backfill handbook. Part 2. SKB Arbetsrapport (in preparation). Svensk Kärnbränslehantering AB.

/6/ **Brooks R H, Corey A T, 1964.** Hydraulic properties of porous media. Colorado State Univ. Hydrol. Paper No 3.

/7/ **Börgesson L, Johannesson L E, 1995**. Thermo-hydro-mechanical modelling of water-unsaturated buffer material. SKB AR 95-32. Svensk Kärnbränslehantering AB.

/8/ **Philip J R, DeVries D A, 1957.** Moisture movement in porous materials under temperature gradients. American Geophysical Union Transactions, Vol 38, No 3, April 1957.

/9/ **Cameron J T, 1986.** A numerical model for coupled heat and moisture flow through porous media. Doctor's thesis, University of California.

/10/ **Olsen H W, 1961.** Hydraulic flow through saturated clays. Dr Thesis, Civ. Eng., MIT.

/11/ **Horseman S T, Harrington J F, 1997.** Study of gas migration in MX-buffer bentonite. Nat. Envir. Research Council, Brit. Geol. Survey, Report WE/97/7.

6 Diffusive transport

This chapter gives the basis of currently used material models for anion and cation diffusion through smectitic soil. Complexation may cause considerable deviation from theoretically derived migration rates and only diffusive transport of species that do not undergo chemical reactions is treated here. Focus is on outlining the formulation of theoretical models for evaluation of diffusion coefficients from controlled experiments. The importance of the porewater chemistry in terms of pH, eH and content of dissolved minerals is treated in Section 9.

As for water transport the solution of practical 2 and 3D problems is made by use of potential theory, applying analytical or numerical techniques, which are not treated here.

6.1 Processes

6.1.1 Impact of microstructure

Diffusive transport of solutes through smectite clays is governed by the microstructure. Thus, the nature and size of the voids, and the tortuosity and constrictivity of interconnected voids, as well as the mineral surface area, determine the rate and capacity of ion transport through diffusion.

A number of detailed investigations have been made for deriving mathematical models for diffusive transport but its complex nature makes this task difficult. Thus, diffusive transport of sorbing cations like Na^+, Cs^+ and Sr^{2+} has repeatedly been reported to be faster than predicted by use of models for diffusion in aqueous phases with immobilization through sorption by minerals. This means that diffusive transport is affected by the conditions in the vicinity of the mineral phase, i.e. in the interlamellar space with cations and water molecules associated to the crystal lattices, and in the electrical double-layers.

The diffusivity of a reactive species undergoing sorption is different from its diffusive migration in free water and a basic expression of diffusive transport of reactive ion species is:

$$D_a = D_w\ (\varepsilon/(\varepsilon + K_d\,\rho_d)\ (\delta_g/\tau^2) \qquad (6\text{-}1)$$

where:

D_a = Apparent diffusivity, m^2/s
D_w = Diffusivity in free water, m^2/s
ε = Porosity (dimensionless)
K_d = Sorption coefficient, m^3/kg
ρ_d = Dry density, kg/m^3
δ_g = Constrictivity (dimensionless)
τ = Tortuosity (dimensionless)

Assuming that the microstructurally related ratio (δ_g/τ^2) stays constant, an increased density yields a reduced porosity, and for constant K_d Equation (6-1) hence implies that the apparent diffusivity D_a drops. This logical trend is validated by experiments but the predicted D_a values are about 5 times lower than experimental data /1/. Attempts have been made to eliminate this discrepancy by enhancing the cation transport capacity of the models through introduction of an electrostatic contribution to the constrictivity, i.e. by increasing the thickness of the electrical double layers. This approach is not theoretically founded but leads to data that fit experimental values relatively well. An alternative, physically attractive theory that also yields good agreement with experimental data is the one worked out by Trygve Eriksen and co-workers /2/. It will be described here after an introductory section on chemical issues.

6.1.2 Impact of chemical processes

Diffusive transport of dissolved elements is often accompanied by chemical reactions, like carbonization and hydroxylation, and loss or uptake of protons making certain species amphoteric. This may cause significant pH-changes and precipitation and fixation of radionuclides yielding strong deviation of the true concentration profile from theoretical ones (Figure 6-1).

The limited understanding of what chemical processes that may take place in conjunction with diffusive ion transport makes it necessary to confine the description of theoretical models to cases with ion transport taking place without reactions of complexation type. Such an example is visualized in Figure 6-2, which shows the concentration of Cu as a function of the distance from the high-concentration end of the diffusion cell. The reasonably good agreement between recorded and calculated profiles suggests that Cu has moved through diffusion at a rate that corresponds to a diffusion coefficient of about 10^{-11} m^2/s.

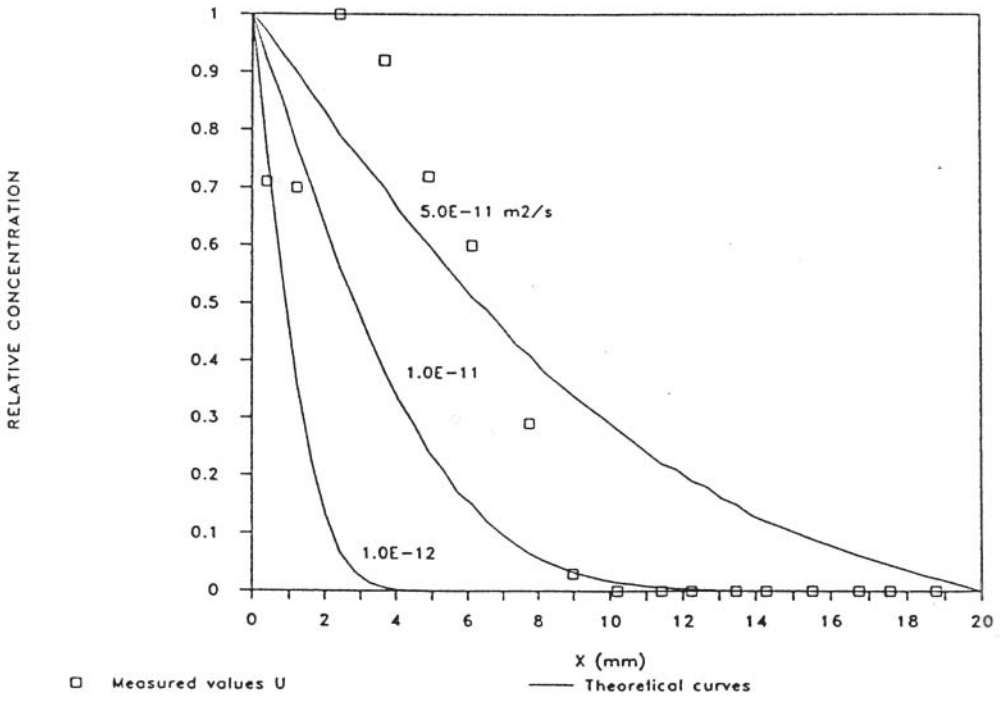

Figure 6-1. *Example of concentration profile that cannot be fitted to a theoretical diffusion profile. Test with uranium chloride (100 ppm U), dry density of the MX-80 clay 800 kg/m³. Three theoretical curves are plotted, representing the diffusion constants D=5·10⁻¹¹, 10⁻¹¹, and 10⁻¹² m²/s /3/.*

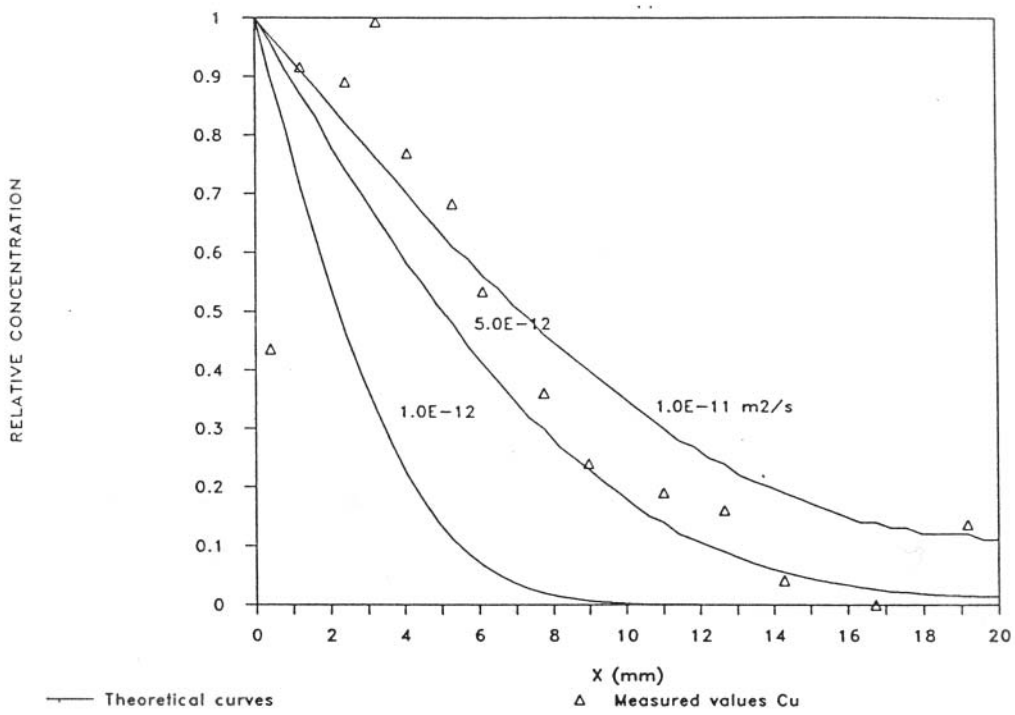

Figure 6-2. *Example of concentration profile that can be fitted to a theoretical diffusion profile. Test with copper chloride (100 ppm Cu), dry density of the MX-80 clay 800 kg/m³ (1504 kg/m³ at saturation), /4/.*

6.2 Diffusion models

6.2.1 General

General expressions for diffusive ion transport are cited in a large number of literature reports. In this chapter the evaluation of diffusion coefficients (cf Part 1) from laboratory tests under well defined conditions is focused on. The tests are assumed to be performed by use of a diffusion cell of the type shown in Figure 6-3.

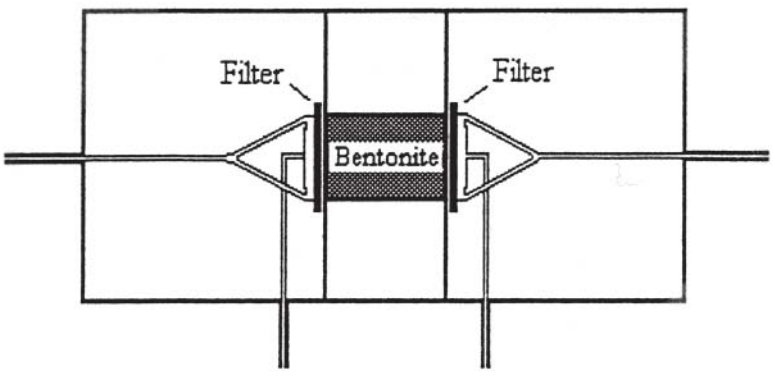

Figure 6-3. *Schematic drawing of diffusion cell. (After Eriksen).*

6.2.2 Required data from test

Evaluation of diffusion coefficients from cell tests requires that the sorption of ions has been determined in preceding tests through batch experiments (cf Part 1) and that the diffusion properties of the sample-confining filter has been determined by weighing the filters saturated with solution and in dry form. The models refer to the use of radionuclides.

6.2.3 Anion diffusion

In practice one can disregard from sorption of anions on smectite and the effective and apparent diffusion constants are hence evaluated using Equations (6-1) and (6-2), respectively /4/:

$$D_e = JL / A\left[C_o - C_t\right] \tag{6-1}$$

$$D_a = L^2 / 6t_e \tag{6-2}$$

where:

D_e = effective diffusion constant
D_a = apparent diffusion constant
J = flux through the diffusion cell (Bq s^{-1})
L = thickness of the bentonite plug
A = surface area perpendicular to the diffusion direction (m^2)
C_o = concentration in the inlet reservoir (const) (Bq m^{-3})
C_t = concentration in the outlet reservoir (Bq m^{-3})
t_e = time lag, the point where the asymptote of the break through curve intercepts the time axis in diagrams

6.2.4 Cation diffusion

For sorbing diffusants like Cs^+ and Sr^{2+} evaluation of the diffusion parameters using Equations (6-1) and (6-2) will be strongly influenced by the presence of filters in short diffusion cells. In evaluating the experimental diffusion data for Cs^+ and Sr^{2+} an analysis of the complete diffusion system, as represented schematically in Figure 6-4, is therefore required.

The diffusive transport through the inlet filter (–F<x<0) is given by Equation (6-3):

$$J = -A\varepsilon_f D_f \left(\partial C_1 / \partial x\right) \tag{6-3}$$

and the boundary conditions

$$C(-F,t) = C_0$$

where:

ε_f = filter porosity
D_f = apparent diffusion constant in filter (m^2/s)
F = filter thickness (m)
C_1 = concentration in filter (Bq/m^3)
C_0 = concentration in inlet solution (Bq/m^3)

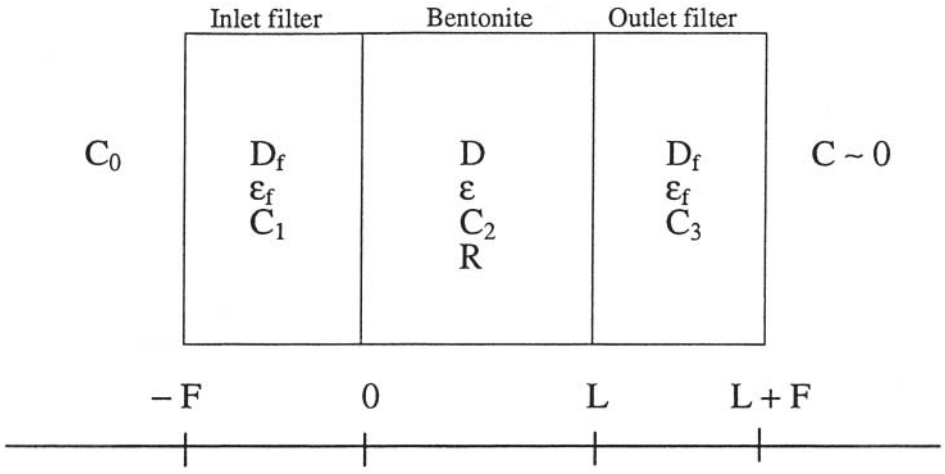

Figure 6-4. *Schematic representation of the barriers in the diffusion cell.*

The diffusive transport through the compacted bentonite (0<x<L) is given by Equation (6-4):

$$J = -A\varepsilon D_a R\left(\partial C_2/\partial x\right) \tag{6-4}$$

where:

R = capacity (retardation) factor defined as the ratio of the overall concentration of diffusant in the compacted bentonite to the concentration in the solution accessible for diffusion ($R = \varepsilon + \rho K_d/\varepsilon$)
C_2 = concentration in pore solution (Bq/m^3)

At the boundary between the inlet filter and the compacted bentonite we have the conditions expressed by Equations (6-5) and (6-6):

$$C_1(0,t) = C_2(0,t) \tag{6-5}$$

$$\varepsilon_f D_f\left(\partial C_1/\partial x\right)_{x=0} = \varepsilon D_a R\left(\partial C_2/\partial t\right)_{x=0} \tag{6-6}$$

The corresponding transport equation and boundary conditions for the discharge filter are given by Equations (6-7) to (6-10):

$$J = -A\varepsilon_f D_f\left(\partial C_3/\partial x\right) \tag{6-7}$$

$$C_2(L,t) = C_3(L,t) \tag{6-8}$$

$$\varepsilon D_a R\left(\partial D_2/\partial x\right)_{x=L} = \varepsilon_f D_f\left(\partial C_3/\partial dx\right)_{x=L} \tag{6-9}$$

$$C_3(L+F,t) = 0 \tag{6-10}$$

The accumulated ion transport through the discharge filter $Q(t)$ is given by the flux through the boundary $x = L+F$ integrated from time zero to t as expressed by Equation (6-11):

$$Q(t) = A\varepsilon_f D_f \int_0^t \left[\left(\partial C_3(x,t)/\partial x \right)_{x=L+F} \right] dt \qquad (6\text{-}11)$$

An analytical solution of Equation (6-11), defining the break through curve, can be obtained by employing Laplace transform methods. Alternatively, one can use finite difference methods for numerical calculations. The code ANADIFF /5/ can be employed for calculating the apparent diffusion coefficient D_a and the sorption coefficient for transport K_d. In the simulations A, ε_f, D_f, C_0, F, L and ρ are kept constant while D_a and K_d are varied.

6.3 Examples

Problem 1: Evaluate the effective diffusion coefficient of iodide, cesium and strontium from experiments with Na bentonite clay with a density at saturation of 2130 kg/m^3 contacted with a source material containing either of the substances.

Basic

Diffusion is assumed to take place without any chemical reaction between the migration ions and the solid substance. Anions are taken to move through the clay without interference by sorption while cations are considered to be retarded by exchange processes.

Solution

Evaluation of the apparent diffusivity is directly made by applying the numerical code ANADIFF. Neglecting possible slight sorption effects, the I^- transport can be assumed to take place by pore water diffusion only. The relation between the apparent and effective diffusion constant is thus given by $D_e = D_a e_p$. Hence, using the effective porosity e_p calculated by use of microstructural models, the effective diffusion coefficient can be calculated for the anion. For the cations one has $D_e = D_a(e_p + \rho K_d)$, where K_d is evaluated from batch tests of bentonite slurry mixed with the respective cationic solution.

Results

Iodide

The apparent diffusion constant (D_a) for I^- is assumed to have been evaluated by curve fitting yielding the data in Table 6-1.

The effective porosity e_p is approximately 0.02 as reported in Chapter 3, which yields the effective diffusion coefficient D_e in Table 6-1.

The evaluated average effective diffusion coefficient for iodide is hence 1.7E-12 m^2/s for this density. It is concluded to provide very effective resistance to diffusion of anions.

Table 6-1. Diffusion constants and porosities for I^- in bentonite with 2130 kg/m^3 at saturation equilibrated with a 0.218 mole/liter saturation.

I^--conc. mole/liter	D_a m^2/s	D_e m^2/s
10^{-2}	8.6E-11	1.72E-12
10^{-4}	8.7E-11	1.74E-12
10^{-6}	8.6E-11	1.72E-12

Cesium and strontium

Batch experiments are assumed to have yielded the K_d-values in Table 6-2, which also gives the evaluated coefficient of apparent diffusivity and the calculated effective diffusion coefficient for cesium and strontium. The diffusion coefficient obviously varies very little with the ion strength for this density.

Table 6-2. Evaluated apparent diffusivity D_a and batch-derived distribution coefficients K_d for Cs^+ and Sr^{2+} in bentonite with 2130 kgm^3 at saturation equilibrated with a 0.218 mole/liter solution.

Ion	Conc. mole/liter	D_a m^2/s	K_d m^3/kg	D_e m^2/s
Sr^{2+}	E-4	1.05E-11	0.011	2.02E-12
	E-6	1.4E-11	0.009	2.20E-12
Cs^+	E-2	5.0E-12	0.041	3.59E-11
	E-4	2.6E-12	0.047	2.13E-11
	E-6	3.2E-12	0.047	2.63E-11
	E-8	2.0E-12	0.080	2.80E-11

Problem 2: Evaluate the apparent diffusion coefficient of cesium and cobalt from experiments with Na bentonite clay with a density at saturation of 2130 kg/m^3 in a field experiments.

Basic

SKB performs a series of field experiments (LOT) at Äspö Hard Rock Laboratory for investigating buffer performance and testing conceptual and theoretical models. Diffusion experiments are included for evaluating the diffusion characteristics of the two cations Cs^+ and Co^{2+} with the tracers ^{134}Cs and ^{57}Co, respectively. Cs^+ was chosen because sorption of this cation is simply by ion exchange while it is surface complexation for Co^{2+}.

The experiments were made by using MX-80 buffer clay contained in 4 meter deep holes with 300 mm diameter (Figure 6-5). The tests referred to here ran for 6 months and samples were than extracted and sliced for measuring the radioactivity. Considering the conditions for the test a major question is whether the clay has been sufficiently hydrated to reach a high degree of water saturation. Theoretically, the clay should have become largely saturated to approximately the distance where the radioactive source was located provided that the rock gave off as much water to the clay that it could absorb in this period of time. This is not known very well but since the initial degree of water saturation was more than 50% one can assume that the diffusion process took place without hindrance.

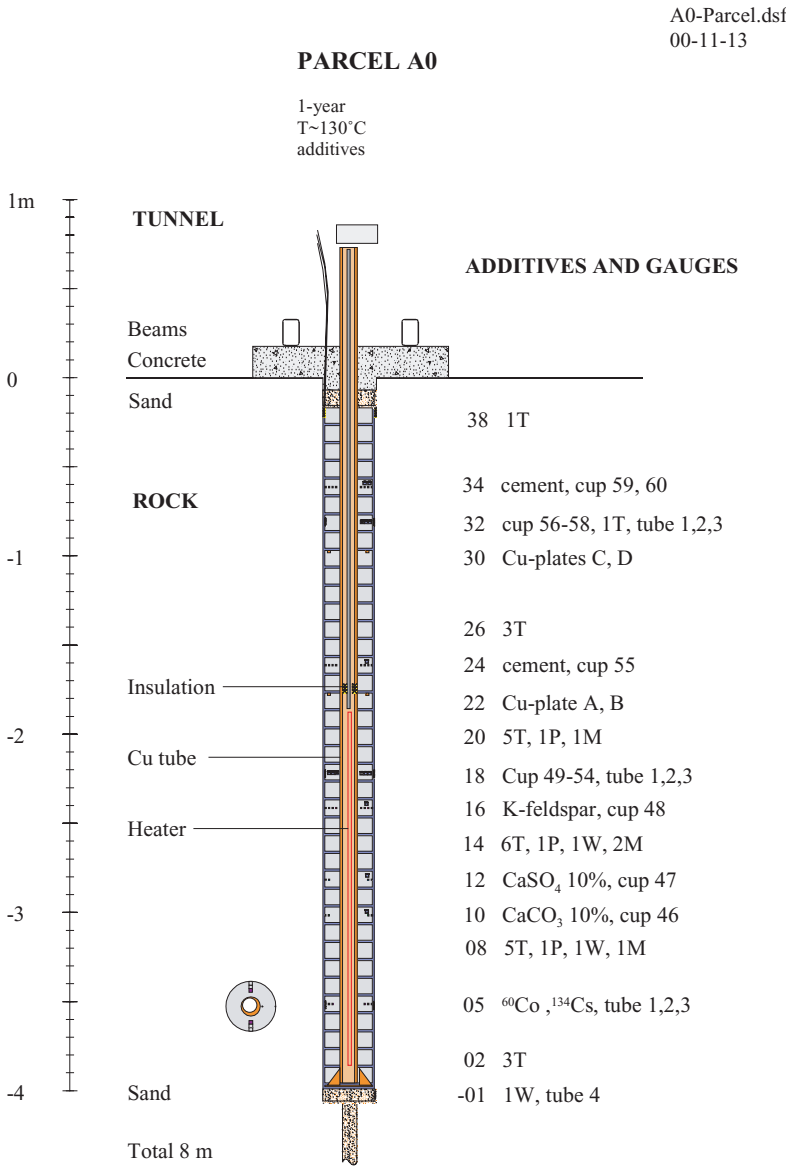

Figure 6-5. *Schematic drawing of test arrangement. The doped clay elements serving as ion sources were placed in block 5.*

Solution

The case is that of a finite source giving off ions into an infinite medium. The initial volume containing the radionuclides was treated as a sphere. The concentration at distance r is obtained using Crank's classical deduction: expression:

$$C(r,t) = \frac{1}{2}C_0\left\{\operatorname{erf}\frac{a+r}{2\sqrt{(Dt)}} + \operatorname{erf}\frac{a-r}{2\sqrt{(Dt)}}\right\} - \frac{C_0}{r}\sqrt{\left(\frac{Dt}{\pi}\right)}\left\{e^{\frac{(a+r)^2}{4Dt}} - e^{\frac{(a-r)^2}{4Dt}}\right\} \qquad (6\text{-}12)$$

where C_0 is the initial concentration, a is the radius of the sphere and D the diffusivity, or as in this case, the apparent diffusivity, D_a.

Results

Cobalt

Figure 6-6 shows the concentration profiles for cobalt, yielding an average apparent diffusion coefficient of about 2.5E-13 m^2/s by use of Equation (6-12). This value is very low and it can be assumed that the insignificant ion movement was caused by ion fixation through complexation. In fact, it could also be at least partly caused by incomplete water saturation.

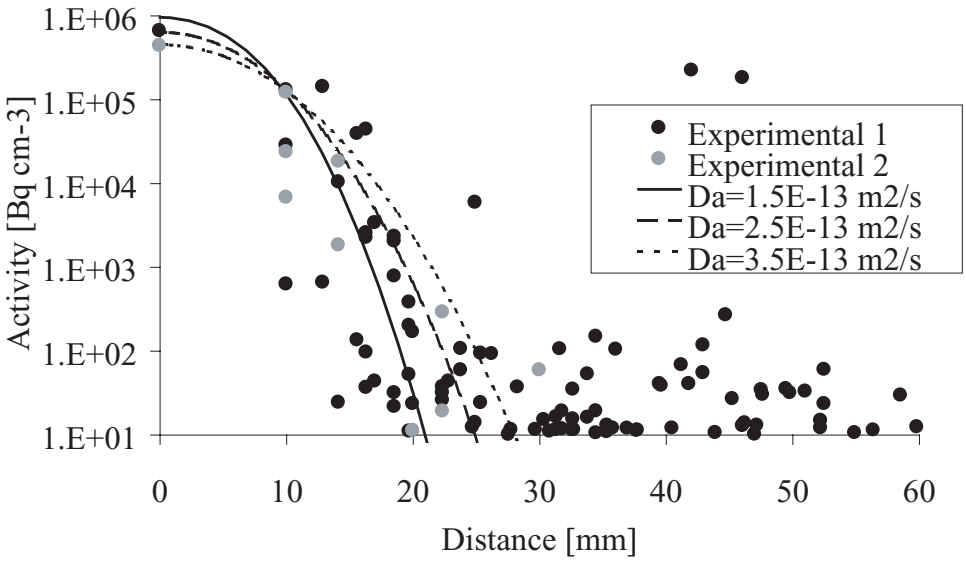

Figure 6-6. *Experimentally determined concentration of cobalt.*

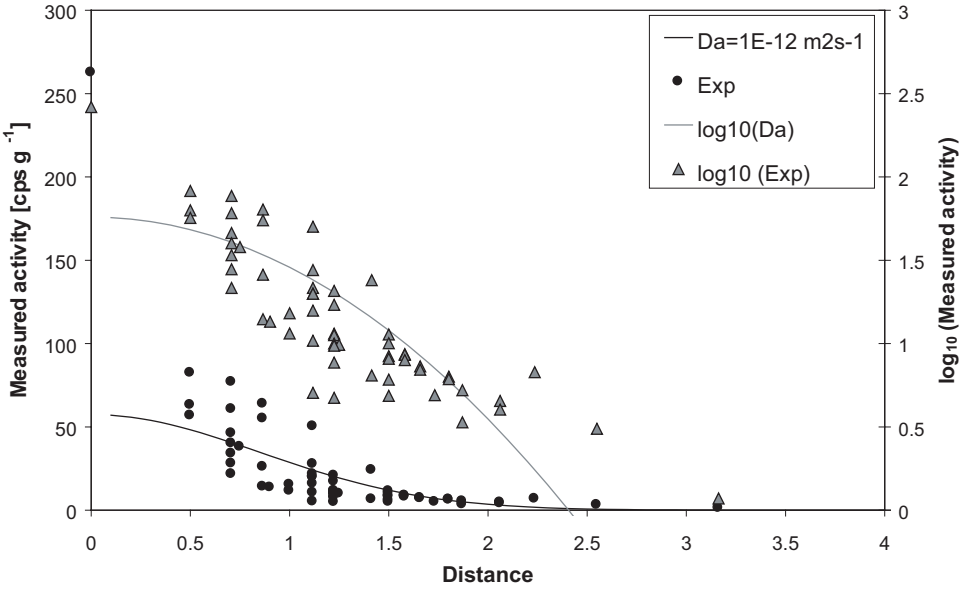

Figure 6-7. *Experimentally determined and example of predicted concentration of cesium assuming D_a=E-12 m^2/s.*

Cecium

Figure 6-7 shows the cesium distribution in the surrounding of the doped specimen. The obtained apparent diffusivity, D_a, is about $2 \cdot 10^{-12}$ m^2 s^{-1}, which is in good agreement with predictions using Eriksen's model and well defined laboratory experiments.

6.4 References

/1/ **Ochs M, Boonekamp M, Wanner H, Sato H.** A quantitative model for ion diffusion in compacted bentonite. Radiochim. Acta (in press).

/2/ **Eriksen T E, Jansson M, 1996.** Diffusion of I^-, Cs^+ and Sr^{2+} in compacted bentonite – Anion exclusion and surface diffusion. SKB TR 96-16. Svensk Kärnbränslehantering AB.

/3/ **Pusch R, Karnland O, Muurinen A, 1989.** Transport and microstructural phenomena in bentonite clay with respect to the behavior and influence of Na, Cu, and U. SKB TR 89-34. Svensk Kärnbränslehantering AB.

/4/ **Eriksen T E, Jacobsson A, 1984.** Diffusion in clay. Experimental techniques and theoretical models. SKB KBS TR 84-05. Svensk Kärnbränslehantering AB.

/5/ **Eriksen T E, 1995.** ANADIFF. Dept. Nuclear Chem. KTH, Stockholm.

7 Gas transport

This chapter deals with gas movement through buffers and backfills. Physically, this process is not entirely understood and only simple material models have been proposed in the literature. However, they all imply, although on different premises, that a certain threshold pressure must be overcome for the gas to move in gaseous form and a generalized model based on this criterion is described here.

Solution of problems represented by large-scale 2D and 3D cases make it necessary to accurately define the boundary conditions, like the gas production rate and – for gas flow over large distances in the vertical direction – the solubility of gas. This is not included in this section, which is intended to describe gas transport through a clay element in the form of a simple material model.

7.1 General

The matter of gas movement through buffers and backfills has been investigated experimentally and different conceptual models have been proposed /1,2/. The microstructural conditions for gas penetration has been discussed earlier in Part 3 in conjunction with the description of the heterogeneity of the microstructure of artificially prepared, compacted clay. A different view taken by Horseman and Harrington /3/ is that water saturated smectite clay is homogeneous and that gas paths are formed when separation of neighboring particles takes place by overcoming the bond strength.

In the present chapter we will describe gas transport by use of a mathematical model that is based on the concept of critical pressure and defer from giving a specific physico/chemical explanation of it. In practice, gas propagation and penetration may be controlled by capillary retention, by the tension strength of the clay matrix and by the swelling pressure.

7.2 Intrinsic permeability

Laboratory data on swelling pressure versus void ratio and hydraulic conductivity versus void ratio can be used to derive an expression of the intrinsic permeability, with the form shown in Equation (7-1), /3/:

$$k_i = 7.0 \cdot 10^{-20} / p_s \qquad (7\text{-}1)$$

where:

k_i = intrinsic permeability in m^2
p_s = swelling pressure in MPa

Equation (7-1) is compatible with the general fact that increasing density reduces the permeability and increases the swelling pressure. The physical meaning is that the permeability is inversely proportional to the swelling pressure, implying that water makes its way through the clay matrix by forcing it aside while producing channels for water percolation. The channels exist in the clay at zero hydraulic gradient as assumed for the microstructural models described in Chapter 3 and they may expand when the hydraulic gradient is increased.

The model works also for gas penetration and percolation but the microstructure undergoes more changes through penetration by gas than by water because gas will pass through fewer channels at much higher flow rates yielding consolidation and erosion. The main difference is that for a stepwise increased gas pressure there is a threshold (critical) pressure that has to be exceeded for initiating and pursuing gas penetration (cf Part 1).

7.3 Flow law

7.3.1 Basic law

Following /3/ laminar flow of gas through the cross-sectional area A_s of a clay specimen is given by Equation (7-2):

$$Q = -\frac{k_{rg} k_i A_s}{\eta_g}\left(\frac{dp_g}{dx}\right) \tag{7-2}$$

where Q ($m^3,\cdot s^{-1}$) is the volumetric flux, k_i (m^2) is the intrinsic permeability, k_{rg} (dimensionless) is the relative permeability to gas, η_g is the gas viscosity (Pas) and dp_g/dx is the pressure gradient ($Pa\cdot m^{-1}$) in the direction of the flow.

The product $k_{rg}k_i$ is the apparent gas permeability of the specimen and is assumed to be constant in the following analysis:

$$k_{rg}k_i = k_g = const. \tag{7-3}$$

Assuming ideal gas behavior, the density ρ_g of the gas is related to its pressure p_g by:

$$\rho_g = \frac{Mp_g}{RT} \tag{7-4}$$

where M is the molar mass of the gas, R is the gas constant and T is the temperature. The mass flux of gas passing through cross sections is $\rho_g Q$ given by:

$$\rho_g Q = \frac{M}{RT} p_g Q = -\frac{Mk_g A_s p_g}{RT\eta_g}\left(\frac{dp_g}{dx}\right) \tag{7-5}$$

Referring to the experimental set-up, the pressure p_g in the gas injection system is equal to the pressure of the gas just inside the specimen at the upstream end. The gas pressure just inside the specimen at the downstream end is p_{po}. Since the product $\rho_g Q$ is constant, Equation (7-5) can be integrated as follows:

$$\rho_g Q \int_0^{L_s} dx = -\frac{M k_g A_s}{RT\eta_g} \int_{p_{gi}}^{p_{go}} p_g dp_g \tag{7-6}$$

where L_s is the length of the specimen, leading to:

$$\rho_g Q = \frac{M k_g A_s}{2RT\eta_g L_s} \left({p_{gi}}^2 - {p_{go}}^2 \right) \tag{7-7}$$

It is convenient to express the flow rate at standard temperature and pressure (STP) conditions. Using (7-4), the density of the gas at STP is given by:

$$\rho_{st} = \frac{M p_{st}}{RT_{st}} \tag{7-8}$$

where T_{st} = 273.15 K and p_{st} = 0.1 MPa (1 bar). The volumetric flux of gas corrected to STP conditions is then given by:

$$Q_{st} = \frac{M k_g A_s}{2RT\rho_{st}\eta_g L_s} \left({p_{gi}}^2 - {p_{go}}^2 \right) \tag{7-9}$$

which an also be written as:

$$Q_{st} = \frac{v_{mst} k_g A_s}{2RT\eta_g L_s} \left({p_{gi}}^2 - {p_{go}}^2 \right) \tag{7-10}$$

where v_{mst} (= 0.0224 m^3) is the molar volume of the gas at STP.

Although gas pressure p_{go} cannot be measured directly in ordinary experiments, it can be related to the backpressure of the water at the downstream end of the sample, p_{wo}, by the relationship:

$$p_{go} = p_{wo} + p_{co} \tag{7-11}$$

where p_{co} is the apparent value of the capillary pressure or more general the threshold pressure for gas penetration. Equation (7-10) can therefore be rewritten as:

$$Q_{st} = \frac{v_{mst} k_g A_s}{2RT\eta_g L_s} \left({p_{gi}}^2 - \left(p_{wo} + p_{co} \right)^2 \right) \tag{7-12}$$

7.3.2 Equivalent capillary bundle interpretation

Based on the concept of "pathway flow", one can image a capillary bundle model that exhibits an equivalent overall response to that of Equation (7-12), /3/. The volumetric flux of gas through a single capillary of uniform, but arbitrary, cross-sectional shape is given by:

$$Q_c = -\frac{R_H{}^2 A_c}{\Gamma \eta_g}\left(\frac{dp_g}{dL}\right) \tag{7-13}$$

where A_c is the cross-sectional area of the capillary, Γ is the shape factor, d_{pg}/dL is the pressure gradient along the path of the capillary and R_H is the hydraulic radius defined by:

$$R_H = \frac{cross-sectional\ area\ of\ capillary}{perimeter\ length\ of\ capillary} \tag{7-14}$$

For a circular capillary, $\Gamma = 2$, $A_c = \pi a^2$ and $R_H = a/2$, where a is the radius of the capillary. For a narrow, slot-like, capillary with a rectangular profile, $\Gamma = 3$ and $R_H = \delta/2$, where δ is the aperture of the slot. The average velocity of the gas within the capillary is:

$$v_c = \frac{Q_c}{A_c} = -\frac{R_H{}^2}{\Gamma \eta_g}\left(\frac{dp_g}{dL}\right) \tag{7-15}$$

The tortuosity, τ, is defined as the average ratio of the microscopic path length, L, to the macroscopic path length, x, in the medium, or

$$\tau = \frac{L}{x} \geq 1 \tag{7-16}$$

so that (7-15) can be expressed in the terms of the macroscopic gas pressure gradient:

$$v_c = -\frac{R_H{}^2}{\Gamma \eta_g}\left(\frac{dp_g}{dx}\right) \tag{7-17}$$

If there are N capillaries per unit area of a plane normal to the flow direction, the actual number of capillaries transmitting gas through the clay specimen is NA_s where A_s is the cross-sectional area of the specimen. The effective gas porosity of the clay is given by:

$$n_g = \frac{NA_s A_c}{A_s} = NA_c \tag{7-18}$$

The relationship between the Darcy velocity, v_d, within the specimen and the average velocity of flow along each capillary, v_c, is given by:

$$v_d = \frac{Q}{A_s} = \frac{n_g v_c}{\tau} = \frac{NA_c v_c}{\tau} \tag{7-19}$$

where Q is the volumetric flux of gas through a clay specimen with a cross-sectional area A_s. Substitution in (7-17) leads to:

$$Q = -\frac{NA_c R_H^2}{\Gamma \tau^2 \eta_g}\left(\frac{dp_g}{dx}\right) \tag{7-20}$$

Equating (7-2) with (7-20), the gas permeability of the clay specimen can be expressed as:

$$k_g = \frac{NA_c R_H^2}{\Gamma \tau^2} \tag{7-21}$$

Substitution of (7-20) into (7-12) leads to the equivalent flow law for the capillary bundle model.

7.4 Examples

7.4.1 Evaluation of gas flow parameters from oedometer-type test of saturated clay

Problem: Consider an oedometer case with A_s=2·10^{-3} m^2, L=10^{-2} m, in which MX-80 clay with a density at saturation of 1600 kg/m^3 is percolated by gas under steady flow conditions with p_{gi}=1 MPa. Calculate the gas permeability k_g and the gas flow through the sample.

Basic

A gas flow experiment of simple type comprises water saturation of the sample in an oedometer and then exposure of the sample to a successively increased gas pressure at one end until breakthrough takes place while maintaining a water pressure at the opposite end. The gas pressure is held constant for recording the gas flow /3/. In practice, a water backpressure is required for maintaining a high degree of water saturation of the clay but this is omitted in the present example. The deduction is made on the conditions that the water pressure at the "downstream" end of the sample (p_{wo}), the apparent capillary pressure (p_{co}), and the gas permeability (k_g) are each taken as constant.

Following /3/, application of the flow law Equation (7-9) one gets the expression for the gas flow through the specimen after breakthrough in the form of Equation (7-22):

$$Q_{st} = \frac{v_{mst} k_g A_s}{2RT\eta_g L_s}\left(p_{gi}^2 - p_{go}^2\right) \tag{7-22}$$

where:

$$P_{go} = p_{wo} + p_{co} \tag{7-23}$$

The water pressure at the downstream end of the sample, p_{wo}, and the apparent capillary pressure, p_{co}, and the gas permeability, k_g, are each taken as constant in the following analysis. If n is the number of moles of gas contained in the upstream gas injection, one can write:

$$v_{mst}\frac{dn}{dt} = \frac{v_{mst}k_g A_s}{2RT\eta_g L_s}\left(p_{go}{}^2 - p_{gi}{}^2\right) \tag{7-24}$$

The ideal gas equation in which the gas volume V appears, can be written as:

$$p_{gi}V_{gi} = nRT \tag{7-25}$$

which leads to:

$$RT\frac{dn}{dt} = V_{gi}\frac{dp_{gi}}{dt} + p_{gi}\frac{dV_{gi}}{dt} \tag{7-26}$$

Substituting (7-28) into (7-30) gives

$$V_{gi}\frac{dp_{gi}}{dt} + p_{gi}\frac{dV_{gi}}{dt} = B\left(p_{go}{}^2 - p_{gi}{}^2\right) \tag{7-27}$$

where:

$$B = \frac{k_g A_s}{2\eta_g L_s} \tag{7-28}$$

Solution

The expression in Equation (7-27) isused for evaluation i.a. the evolution, with time, of the upstream gas pressure from the initial condition $p_{gi} = p_{gi0}$ *at* t = 0 for uniaxial gas percolation tests. With the gas pump running at a constant finite rate one can evaluate the gas permeability k_g from Equations (7-20) and (7-22). It is only valid for the post-breakthrough phase of gas migration.

Hence, given the data from the test arrangement as listed below, one can evaluate the gas permeability and, from this, the gas conductivity for the tested clay, taking it to behave as a capillary bundle. The number of gas flow paths and their geometric dimensions can be derived from the microstructural models as described in Chapter 3.

V_{gi} = Volume of gas in the "upstream system" (inlet end)
p_{gi} = Measured pressure of gas in the "upstream system" (inlet end)

For steady state conditions $dp_{gi}/dt=0$ and $dV_{gi}/dt=0$.

$B=N{\cdot}A_c{\cdot}A_s(R_H)^2/2\Gamma(\tau)^2\eta_g{\cdot}L_s$ where N=number of capillaries per unit penetrated area, A_c and R_H are the cross-sectional area and hydraulic radius of each pathway, A_s and L_s are the cross-sectional area and the length of the specimen, Γ a shape factor (1 for circular and 3 for narrow slot), and τ the tortuosity of each pathway (average ratio of the path length L to the macroscopic length; 3 is arguable).

Results

The expression for the volumetric flow in Equation (7-20) is used. Referring to Chapter 3 one can assume that there are 2 pathways with 50 μm diameter per 250x250 μm^2 cross section through which the large majority of the gas will move.

Taking Γ=1, τ =3, N=10^8 per m^2, A_c=$2 \cdot 10^{-9}$ m^2, and R_H=$3 \cdot 10^{-6}$ m one gets k_g=$4 \cdot 10^{-13}$ m^2. This corresponds to a gas conductivity of about $4 \cdot 10^{-6}$ m/s, which is about 1000 times higher than the hydraulic conductivity.

The gas flow through the sample, expressed in STP-form, is the product of the cross section area A_s=$2 \cdot 10^{-3}$ m^2, the gas conductivity k_g, and the pressure drop 100/0.01, yielding a flow rate of $8 \cdot 10^{-4}$ m^3/s.

7.5 References

/1/ **Pusch R, Karnland O, Hökmark H, 1990.** GMM – A general microstructural model for qualitative and quantitative studies of smectite clays. SKB TR 90-43. Svensk Kärnbränslehantering AB.

/2/ **Pusch R, 1994.** Gas transport through smectitic clay and crystalline rock. SKB AR 94-61. Svensk Kärnbränslehantering AB.

/3/ **Horseman S T, Harrington J F, 1997.** Study of gas migration in MX-80 buffer bentonite. Nat. Envir. Research Council, British Geol. Survey, Report WE/97/7.

8 Rheology

This chapter deals with modeling stress/strain/time behavior of buffers and backfills. Focus is on the definition of a general rheological model and its implementation in the ABAQUS code, by use of which the strain and stress conditions in fully water saturated buffer can be calculated as a function of time after imposing deformation. The interaction of buffer, rock and canister in deposition hole exposed to tectonically induced shearing is taken as an example of how rheological modeling can be made.

8.1 General

Rheological models have been worked out for various purposes using different material models and calculation methods. No standard models or procedures have yet been proposed and much remains to be done before general expressions can be proposed, particularly since the physics involved in most stress/strain/time-related processes is still not well understood.

Modelling of stress and strain with special respect to time is common in soil mechanics, especially for predicting long-term stability of slopes and for estimating the settlement of buildings on clay underground. For the very dense clay buffer in a KBS-3 repository stability will not be a problem and compressive strain will be insignificant while expansion – swelling – is important but foreseeable. In fact, there is normally no need for accurate prediction of buffer strain except for one purpose namely tectonically induced shearing of rock buffer and canisters and this is the reason why rather much space is given to the item rheology.

An attempt to derive a general rheological model has been made by Börgesson /1,2/ and it will be cited here. It is based on a material model that has been defined in Part 1 and that was used for illustrating microstructural evolution ("ABAQUS" model) in Chapter 3. The model has been calibrated against empirical data from laboratory testing of sodium-dominated MX-80 bentonite and calcium-dominated Erbslöh bentonite. It does not include changes in porewater composition or mineral content, nor cementation effects due to chemical processes.

8.2 Basic rheological models of buffer

8.2.1 General

The material models for the bentonite buffer have been developed on the basis of the results from many laboratory tests and verification calculations. For taking plastic behaviour into consideration the Drucker Prager concept was deemed superior to that of Cam Clay. None of them is perfect for describing the behaviour of bentonite but the generalized Drucker Prager model used here is advantageous.

The elastic part of the Drucker Prager model is "Porous Elastic", which implies that the relation between the void ratio and the logarithm of the average stress is linear.

Since water-saturated bentonite is a two-phase material and the pore water plays an important role for the behaviour, the properties of pores and and soil structure are treated and modeled individually. The Effective Stress Theory is the basis for this modeling. The ways of modelling can be summarized as follows:

- Modeling of Drucker-Prager Plasticity.
- Modeling of Porous Elasticity.
- Modeling of Pore and Particle properties.
- Modeling of Thermal and Thermo-mechanical behaviour.
- Initial conditions.

For the Drucker-Prager Plasticity model the influence of the average stress (friction angle $\phi \neq 0$) can be taken into account. Cohesion (c) can also be simulated.

The model is illustrated in Figure 8-1, which shows that the stress dependence is caused by the "friction angle" β in the σ_j–p plane and the parameter d representing the "cohesion". If the plastic flow $d\varepsilon^{pl}$ is included, the angle $\psi=\beta$ and the flow are perpendicular to the yield surface. In order to decrease the resulting dilation it is necessary to assume non-associated flow by taking $\psi<\beta$. When the stress path enters the plastic region ds^{pl}, the yield surface is moved upwards until it reaches the failure surface.

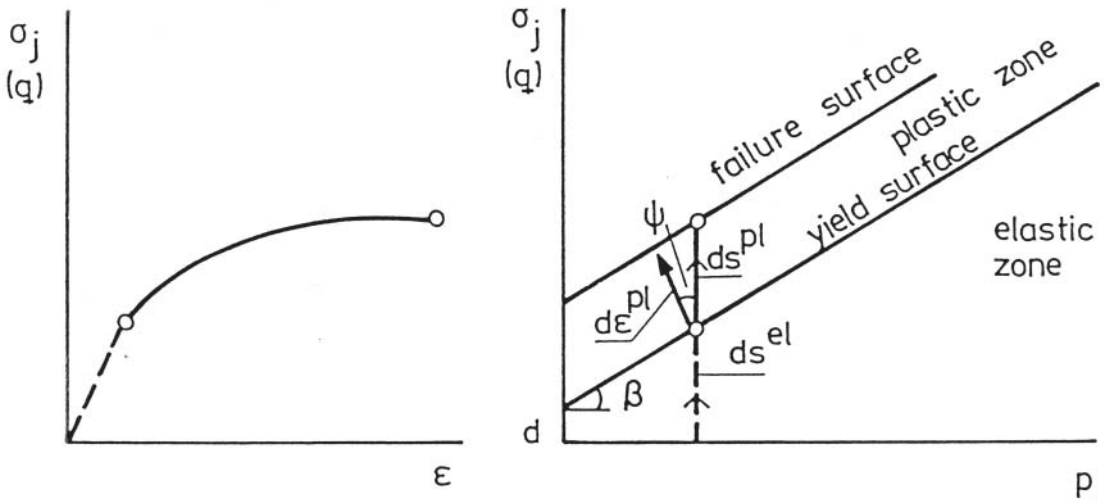

Figure 8-1. *Drucker-Prager Plasticity Model.*

The model also includes a constant K that controls the impact of the yield surface on the intermediate principle stress. The yield surface is defined so that K is the ratio of the yield stress in triaxial tension and the yield stress in triaxial compression. The classical Drucker Prager model is obtained for K=1.0 and ψ=β.

The parameters needed for using the extended Drucker-Prager model are β, d, K, ψ and the yield function f. The basic values of these parameters are taken to be:

β = 20°
d = 100 kPa
ψ = 2°
K = 0.9

Yield function

σ_j (kPa)	ε_y
113	0
138	0.005
163	0.02
188	0.04
213	0.1

σ_j is the Mises stresses and ε_y the plastic strain for a stress path that corresponds to uniaxial compression, i.e. without confining pressure. Linear interpolation is made between the values.

8.2.2 Description of model

The conclusions from the comparison of calculations and tests are that the models are acceptable for making rough calculations and for estimating the relative importance of the various parameters. The following features are essential but not yet fully implemented:

- The failure envelope should be curved so that no cohesion intercept is required. Figure 8-2 shows that the failure envelope may be drawn as a straight line in a log-log diagram over a large range of stresses. A shape of the failure envelope that fits the desired relation between the average effective stress p and the Mises' stress q can be expressed as $q = ap^b$.
- The stress-strain relation at deviatoric stress increase in the elastic part of the stress space is non-linear. This can be achieved either by applying hypo-elasticity or by letting Poisson's ratio ν be a function of the deviatoric stress q.
- A "cap" to limit the elastic part in the p-direction makes the model general and allows calculation of compression of bentonite with initially low density.
- Post-failure reduction in strength (strain-softening) is needed.

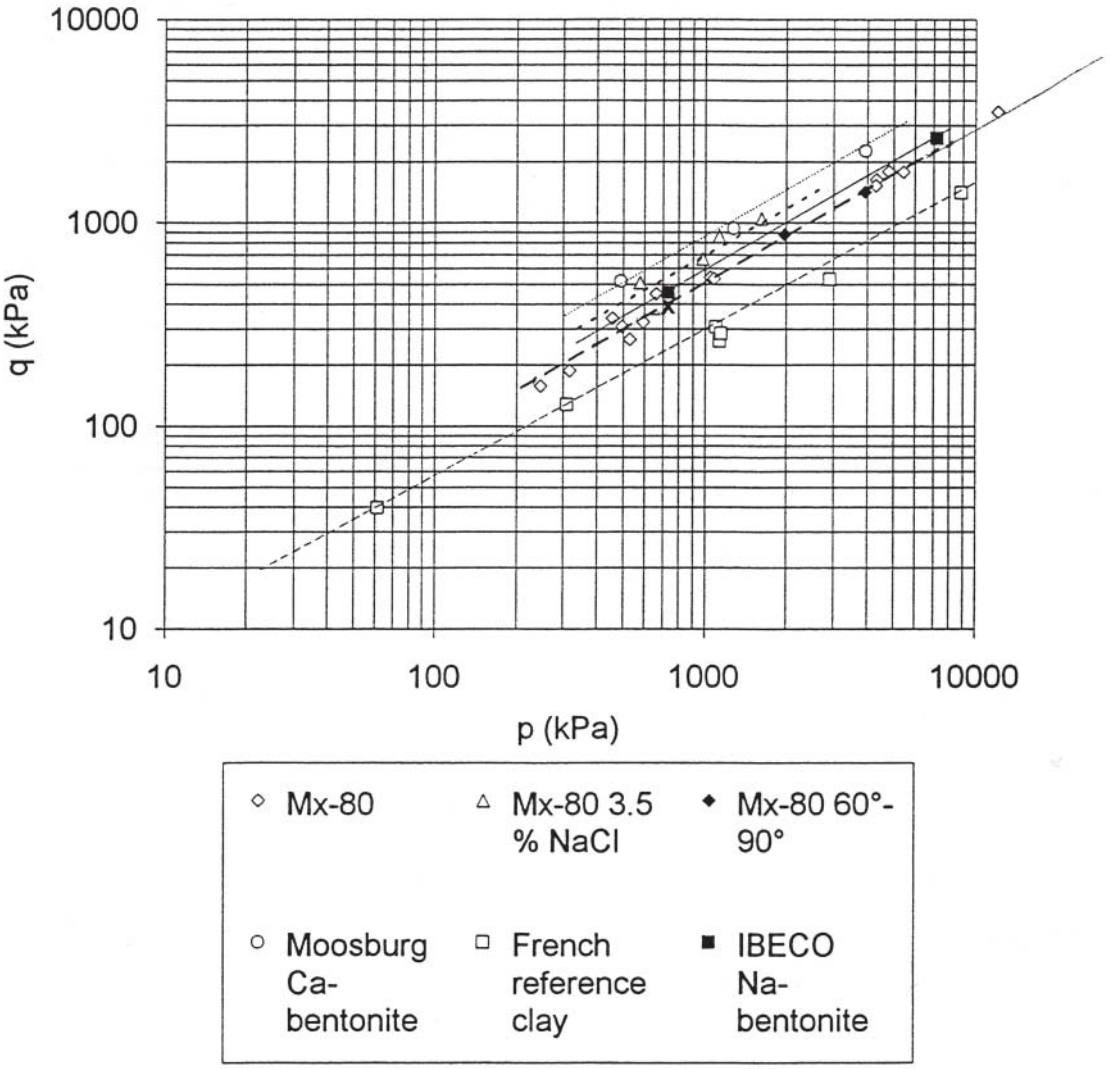

Figure 8-2. *Triaxial test results plotted in a double logarithmic diagram. x represents triaxial extension (MX-80).*

Cap plasticity

A model of the described type is shown in Figures 8-3 and 8-4. Figure 8-3 shows the yield and failure surfaces in the q–p plane as well as the flow surface. The conditions in the q–p plane are controlled by two lines that limit the allowable Mises' stress q:

$$q = ap^b \tag{8-1}$$

$$q = cp^b \tag{8-2}$$

where $a<c$.

The upper curve is a combined yield and failure surface (1) of the over-consolidated state ("dry side") while the lower line is the failure surface (4) on the normally consolidated side ("wet side") corresponding to the critical state line of the Cam Clay model /1/. The lower line is also the top point of the yield surface of all states. The other parts of the yield surface are the elliptic cap (3), which intersects the p-line at p_b and an elliptic transition surface between the other two parts (2). The yield surface is the boundary of the zone with elastic behavior ("porous elasticity").

The plastic behavior at the yield surface is controlled by the flow surface (plastic potential), which is also shown in Figure 8-3. The flow surface consists of two ellipses, one for parts 1 and 2, where the flow is not associated since the tangent of the flow surface does not coincide with the tangent of the yield surface, and one for the cap (3). By letting the ellipses at 1 and 2 be large, the inclination of the flow surface and hence the dilatancy can be made small.

The behavior is illustrated in Figure 8-4, where the stress/strain conditions (q-ε) and the change in location of the yield and failure surfaces are shown for two stress paths. The upper stress path from A to B shows the performance on the wet side. It first leads into the elastic region but when the stress path intersects the cap the material starts to plasticize, decrease in volume, and move the cap upwards with the top following the lower failure line. The stress path from C to D shows the behavior in the over-consolidated dry part. It is located entirely in the elastic domain and remains so until it intersects the combined failure and yield surface, where the material starts to yield and increase its volume. The volume increase makes the cap of the yield surface shrink at constant q until the transition surface has reached the point D. Here, there is a new yield surface, which is illustrated by broken lines in the figure. If the strain is increased further, q will decrease and the cap further reduces until the top part hits point E, where no further change in q or volume will take place.

The following three parameters are required for defining cap plasticity:

p_b = location of the cap
p_f = location of the elliptic non-associated flow surface on the dry side (flow surface 1 and 2)
γ = ratio of the two axis in the elliptic transition surface (yield surface 2)

The location of the cap is defined by the intercept p_b of the cap and the p axis. The location of the flow surface is defined by the intercept p_f between the flow surface and the p axis (usually a high negative value). The shape of the elliptic transition surface needs to be defined and this is achieved by defining the ratio γ of the size of the minor and the major axes of the ellipse.

Yield surface

1 Shear failure surface
$q = ap^b$
2 Transition surface (elliptic)
3 Cap (elliptic)

Failure surface

1 Shear failure surface
$q = ap^b$
2 Transition surface (elliptic)
4 Shear failure surface
(Critical state line)
$q = cp^b$
$a > c$

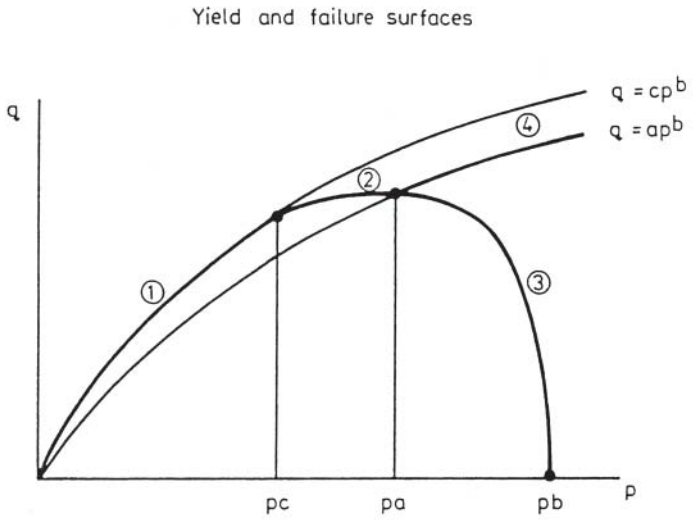

Flow surface

1, 2 elliptic non associated
3 elliptic associated

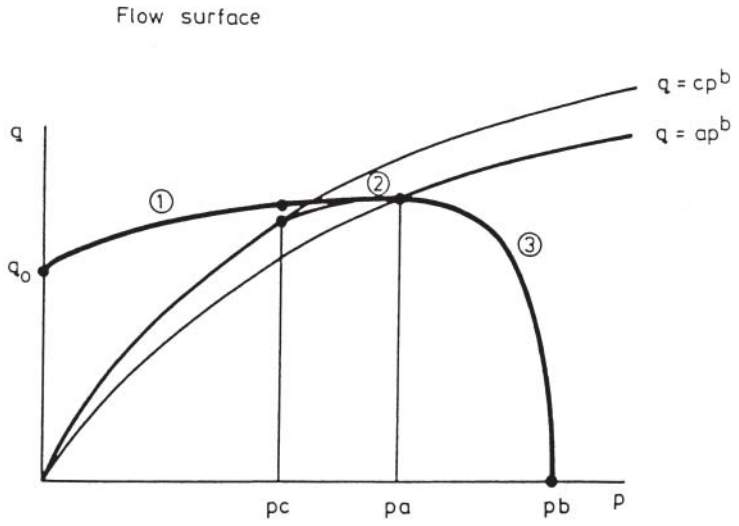

Figure 8-3. *Material model. Yield and failure surfaces (upper) and plastic flow surface (lower).*

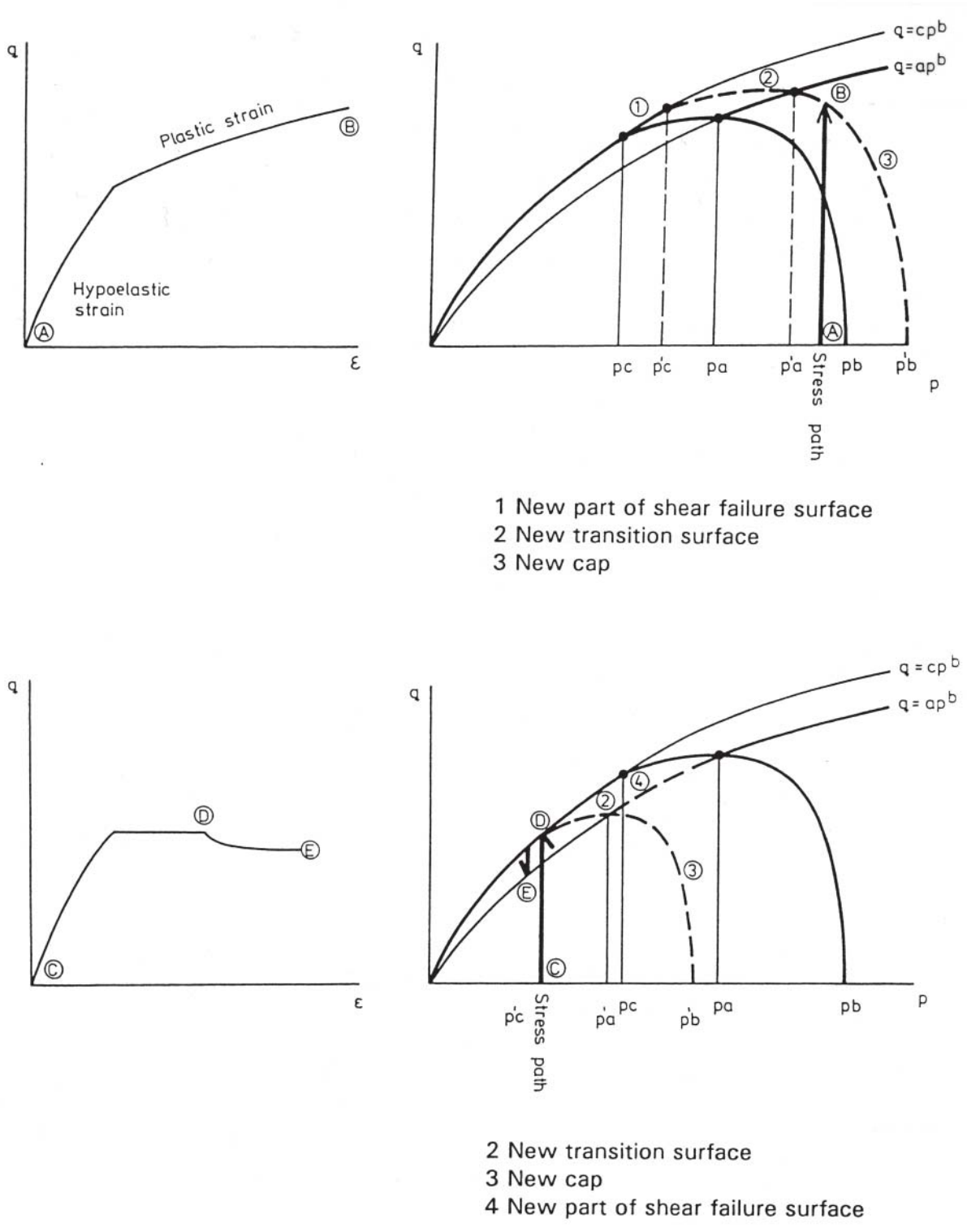

Figure 8-4. *Behavior of the proposed material model for two stress paths.*

Cap hardening

When the average stress p exceeds the "preconsolidation pressure" p_b the result will be a non-recoverable plastic volume decrease and the cap will expand. The total volume decrease is the sum of the elastic and plastic volume decreases. The expansion of the cap is called "cap hardening" and is defined as the relation between the average stress p and the logarithmic plastic volumetric strain ${}^{e}log(1+\varepsilon^{v}_{pl})$ where $\varepsilon^{v}_{pl}=\Delta V_{pl}/V$ is the "engineering strain" /1,2/.

The code ABAQUS, in which the material model has been implemented, uses logarithmic strain, which differs from the engineering strain definition. Thus, the strains are added according to Equation (8-3):

$${}^{e}log(1+\varepsilon^{v}_{tot})={}^{e}log(1+\varepsilon^{v}_{el})+{}^{e}log(1+\varepsilon^{v}_{pl}) \quad (8\text{-}3)$$

where:

ε^{v}_{tot} = total volumetric strain (=ΔV/V)
ε^{v}_{el} = elastic volumetric strain (=$\Delta V_{el}/V$)
ε^{v}_{pl} = plastic volumetric strain (=$\Delta V_{pl}/V$)

The cap hardening implies that the plastic strain increases with increasing average stress as shown in Table 8-1.

Table 8-1. Cap hardening relation used for MX-80 Na-bentonite.

p (kPa)	${}^{e}log(1+\varepsilon^{v}_{pl})$
100	0
200	0.103
400	0.192
750	0.264
1200	0.299
2000	0.323
3500	0.379
5500	0.396
8500	0.415
17000	0.444
30000	0.490

Porous elasticity

The model also includes a non-linear stress-strain relation for deviatoric stress increase in the elastic part. The non-linearity is received by letting Poisson's ratio ν vary with the degree of mobilized friction, which can be expressed by the relation between the applied Mises stress q and the Mises stress at failure $q_f(p)$ for the same average stress p. The relation is suggested to be as specified in Equations (8-4) and (8-5):

$$\nu = \nu_0 \text{ for } q/q_f \leq \eta \quad (8\text{-}4)$$

$$\nu = \nu_0 + \frac{q/q_f - \eta}{1-\eta}\cdot(\nu_{max} - \nu_0) \text{ for } q/q_f > \eta \quad (8\text{-}5)$$

where:

ν_0 = basic value of the Poisson ratio
q = Mises' stress
q_f = Mises' stress at failure at constant average stress
ν_{max} = maximum value of the Poisson ratio
η = ratio of q/q_f below which n is constant ($=\nu_0$)

The Poisson ratio is thus constant at $q/q_f \leq \eta$ and varies between ν_0 and ν_{max} in proportion to the excess degree of mobilized friction at $q/q_f > \eta$. The ultimate case with the conditions:

ν_0 = 0
ν_{max} = 0.5
η = 0

is assumed to be an acceptable approximation of the Poisson ratio at the first increase in Mises stress but not at unloading or reloading. The choice of parameters in Equations (8-4) and (8-5) must thus be made with respect to the loading conditions. ν_{max}=0.5 gives a very smooth transition to plastic behavior at the ultimate Mises stress, but the Poisson ratio close to 0.5 yields numerical problems. Therefore, ν_{max}=0.48 has been used in the calculations, which in combination with ν_0=0 and η=0, yields the following expression for the Poisson ratio:

$$\nu = 0.48\ q/q_f \qquad (8\text{-}6)$$

8.2.3 Mathematical definition of the model, implementation into the ABAQUS code, and code verification

General

The models are described in detail in the ABAQUS Theory Manual and the ABAQUS User's Manual /1,2/ and will not be described in this report. They have the following features:

- Curved failure surface: $q=ap^b$.
- Curved critical state line: $q=cp^b$.
- Elliptic yield transition surface.
- Non-associated elliptic plastic potential function (called flow surface in Figure 8-2).
- Variable Poisson's ratio according to Equations (8-3) and (8-4).

Additional

Subroutines for the mathematical functions of the yield and flow surfaces as well as the differential coefficients are required for the modeling. Code verification calculations have been made for swelling/compression tests.

Additional input parameters required for the model are the following /1,2,3/:

a, b, c parameters for Equations (8-1) and (8-2)
p_f intersection between the elliptic flow surface and the p-axis
γ relation between the two axes of the elliptic yield transition surface

The variable Poisson ratio has been included as a special subroutine in the Porous Elastic Model with the input parameters:

v_0, v_{max}, η as described in Equations (8-4) and (8-5)

For definition of the cap the following input data are required:

p_b = intersection between the cap and the p-axis
p *vs.* $^e\log(1+\varepsilon^v_{pl})$ = cap hardening relation

8.3 Material models for interaction of buffer, canister and rock for the special case of rock shearing

8.3.1 General

Calculation of the integrated behavior of buffer, copper/steel canisters, and rock requires that relevant material models are taken as a basis. The one for the buffer clay has been described in this section and in Part 1 but a more complete version, including also thermo/mechanical properties is given here. The copper and steel parts of the KBS-3 canister are described using traditional elasto/plastic metal models. The rock behaves as a rigid boundary or as a very stiff elastic porous medium.

Porous Elasticity

The stress/void ratio relation is expressed by use of the porous elasticity model with the volumetric behavior defined according to Equation (8-7):

$$\frac{\kappa}{1+e_0} ln\left(p_0/p\right) = J^{el} - 1 \qquad (8\text{-}7)$$

where:

e_0 = initial void ratio
p_0 = initial average stress
κ = the inclination of the e-log$p$ relation
J^{el} = the elastic volume ratio

The key parameters are κ, i.e. the logarithmic bulk modulus, and the Poisson ratio. The basic values of these parameters are:

κ = 0.21
v = 0.4

Pore and particle properties

The density ρ_w and the bulk compression modulus B_w of the pore water, and the bulk modulus of the solid particles B_s are:

ρ_w = 10 000 kg/m^3
B_w = 2.1·10^6 kPa
B_s = 2.1·10^8 kPa

The flow of water through the clay is expressed by Darcy's law with the hydraulic conductivity K being a function of the void ratio e (interpolation between the values). The following basic relation is used:

e	K (m/s)
0.45	$1.0 \cdot 10^{-14}$ m/s
0.70	$6.0 \cdot 10^{-14}$ m/s
1.00	$3.0 \cdot 10^{-13}$ m/s

Thermal and thermo/mechanical behavior

The thermal behavior is expressed through the thermal conductivity λ, the specific heat c and the bulk density ρ. In thermo/mechanical problems the thermal expansion coefficients of water and solids (α_w and α_s) and the bulk moduli (B_w and B_s) control the behavior. Since $\alpha_w >> \alpha_s$ the latter coefficient can be assumed to be 0. The basic values of the parameters are:

λ = 1.4 Wm/K
c = 1600 Ws/kg,K
ρ = 2100 kg/m^3
α_w = $3.0 \cdot 10^{-4}$ l/K
α_s = 0 l/K

Initial conditions

Only four parameters describing the initial situation in the buffer are needed namely: 1) the initial void ratio e_0, 2) the initial average stress p_0 (corresponding to the swelling pressure), 3) the initial pore water pressure u_0 and 4) the initial temperature T. In the rock displacement calculations the following values are generally assumed:

e_0 = 0.65
p_0 = 8000 kPa
u_0 = 5000 kPa
T = 15°C

8.3.2 Canister

Although the geometry and composition of the canisters are different in the various concepts, the material components of the canisters are generally modeled in the same way. The models and parameters used can be grouped as follows:

- Modeling of the mechanical behavior applying Linear Elasticity and Metal Plasticity
- Modeling of the Thermal and Thermomechanical behavior

Three materials have been modeled:

- Copper
- Steel
- The interior (UO_2 and Cu) of HIP canisters

The first two will be described here while the latter will be described in connection with the calculation.

Copper

The elastic parameters are the modulus of elasticity E and Poisson's ratio ν:

$E = 1.14 \cdot 10^8$ kPa
$\nu = 0.35$

The plastic strain is described by the following yield function in the same way as for the Drucker-Prager model:

σ_j (kPa)	ε_y
$50 \cdot 10^3$	0
$80 \cdot 10^3$	0.015
$130 \cdot 10^3$	0.065
$180 \cdot 10^3$	0.154
$210 \cdot 10^3$	0.288

The thermal properties are:

$\lambda = 380$ Wm/K
$c = 390$ Ws/kg,K
$\rho = 8930$ kg/m^3
$\alpha = 1.6 \cdot 10^{-5}$ l/K

Steel

The elastic parameters are:

$E = 2 \cdot 10^8$ kPa
$\nu = 0.30$

The plastic strain is described by the following yield function in the same way as for the Drucker-Prager model:

σ_j (kPa)	ε_y
$300 \cdot 10^3$	0
$412 \cdot 10^3$	0.023
$542 \cdot 10^3$	0.078
$697 \cdot 10^3$	0.147

The thermal properties are:

$\lambda = 59$ Wm/K
$c = 460$ Ws/kg,K
$\rho = 7800$ kg/m^3
$\alpha = 1.2 \cdot 10^{-5}$ l/K

8.3.3 Rock

The rock can be considered as an infinite rigid body in all the rock shear scenarios. In thermo/mechanical calculations the rock is modeled as a linear plastic medium with the following parameter values:

$E = 5 \cdot 10^6$ kPa
$\nu = 0.20$

The thermal properties are:

$\lambda = 3.6$ Wm/K
$c = 800$ Ws/kg,K
$\rho = 2700$ kg/m^3
$\alpha = 8.3 \cdot 10^{-6}$ l/K

8.4 Rheological models of interaction of buffer, canister and rock for the special case of rock shearing

8.4.1 Case definition

General

The case considered is the one shown in Figure 8-5. Tectonically induced shearing is assumed to take place along a slip plane in the rock and this induces stresses in the softer buffer clay, which, in turn, produces stresses in the canister, which undergoes both shearing and compression. The tunnel is assumed to be located at 500 m depth, yielding a piezometric pressure of 5 MPa. The tectonically induced shearing is assumed to take place in the course of 30 days allowing the clay to consolidate and creep for 30 years after the shearing. These conditions are not conservative since much quicker shearing may in fact take place and the assumed consolidation will bring the clay and canister in less critical conditions than during shearing. Hence, less conservative cases should be investigated in future R&D.

The calculations were made by use of the finite element code ABAQUS, which has been developed to include major soil mechanical functions /2/. The detailed performance of the calculations is not given here. The element net used in calculations of the effect of rock shearing is illustrated in Figure 8-6.

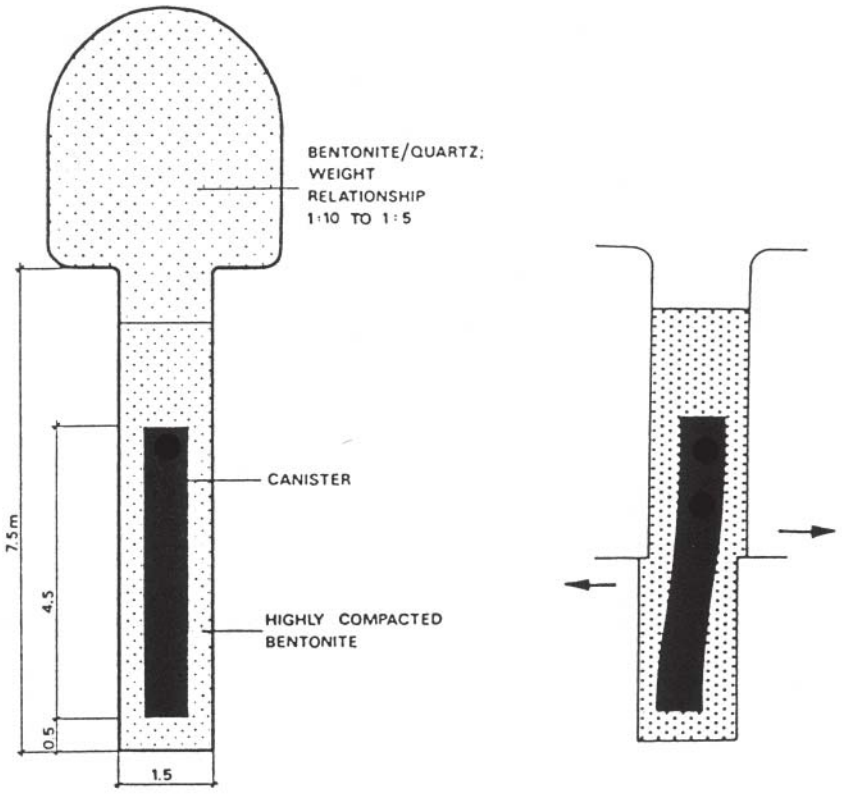

Figure 8-5. *Rock shearing, involving rock, buffer and canister.*

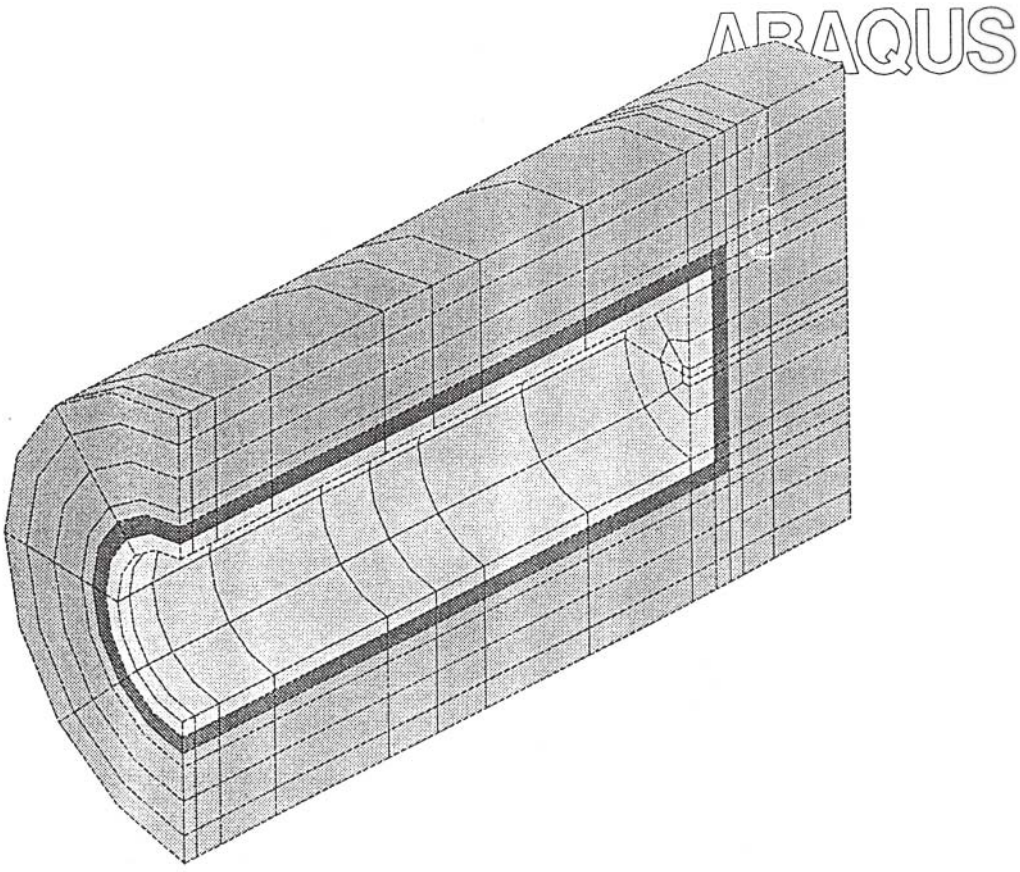

Figure 8-6. *Element mesh for calculation of stresses and deformations of the KBS-3 prototype copper/steel canister /3/. Outer, medium-gray: Buffer. Dark gray: Copper. Light gray: Steel.*

Performance of buffer clay

The shearing event is assumed to take place after complete hydration with the swelling and pore pressures fully developed and in equilibrium with the surroundings. This means that, initially, a uniform swelling pressure is exerted on the canister and on the walls of the deposition hole and shearing is hence superimposed on the initial stress field.

The stresses generated in the clay and canister will relax with time through creep and consolidation or expansion due to pore pressure dissipation.

Performance of the KBS-3 copper/steel canister

The steel/copper canister has an internal slot of 1 mm between the copper and the steel, which means radial compression under sufficiently high stresses will close this gap and make the inner steel container carry the load through its higher modulus of elasticity and strength.

Performance of the rock

Shearing along flatlying long-extending discontinuities in the rock is the most critical case. It is assumed that the shear strain is developed with a constant rate of strain during 30 days and then stops, which is not a very conservative case since shearing can be almost instantaneous. However, by definition deposition holes in a KBS-3 repository should not be intersected by discontinuities of lower order than D4 /4/, along which instantaneous shearing in conjunction with an earthquake is not expected to be more than a few millimeters. Aftershocks and creep along the shear plane in the rock may yield additional strain of the magnitude assumed in the considered case and it may accumulate to larger strain. It should be mentioned that shearing along planes that do not intersect the point of gravity of the canister may represent more critical conditions and they should be investigated as well.

8.5 Examples

8.5.1 General

This section describes calculations that have been performed by use of the ABAQUS code and the rheological models described in the preceding text, taking the detailed design of the KBS-3 canister into consideration. The examples are of general character, the actual complexity making a detailed description out of the scope of this Handbook. They merely indicate what sort of problems that can be treated by use of the described models.

8.5.2 Effect of rock shearing on buffer clay and canister

The case of transversal shearing in Figure 8-5 will be considered, the canister having the dimensions shown in Figure 8-7. There is a gap of 1 mm between the copper and steel cylinder. The openings for fuel rods in the steel were assumed to be empty in the calculations.

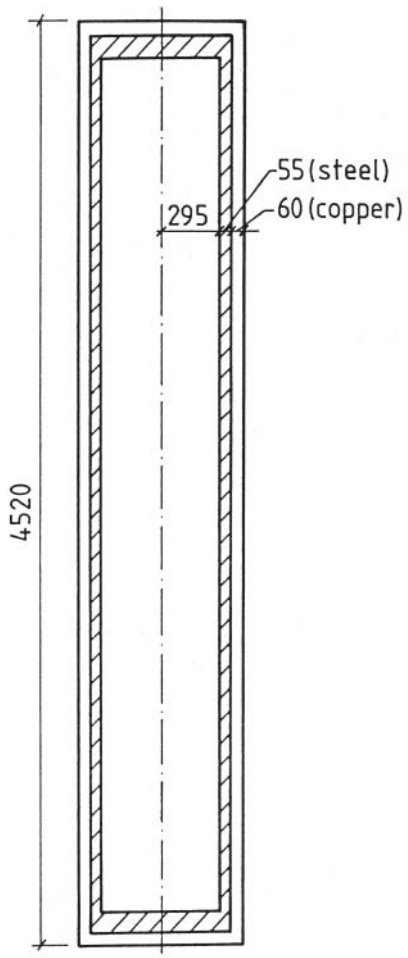

Figure 8-7. *Geometry of the double-walled copper/steel canister (mm). The end plates of copper are welded to the copper cylinder.*

The stresses and strains in the hollow, double wall copper/steel canister have been investigated by making the following calculations:

1. The effect of the swelling pressure from the bentonite and the water pressure from the rock.
2. The effect of rock shear through the center of the canister (symmetry) with 30 days duration.
3. The same as in 2) adding also the effect of 30 years of consolidation and pore pressure dissipation in the bentonite after the rock shear.
4. The same as in 3) adding also the effect of creep in the copper.
5. The effect of asymmetric rock shear.

8.5.3 Effect of the swelling pressure from the bentonite

Assumptions

The rock shear was assumed to take place after complete saturation, swelling and pore pressure equilibration. The rock shear calculation was hence preceded by a calculation of the swelling of the bentonite to establish contact with the rock and canister. The deformed and stressed model was then taken as starting point for the rock shear calculation.

The canister and clay were geometrically modeled in the fashion shown in Figure 8-8, the element mesh with different shadings representing the different materials. The 1 mm gap between the copper and steel canisters was simulated by interface elements.

The axial plane is one of symmetry, while the radial plane with 90° intersection of the hole axis, is an anti-symmetric plane simulating the shear plane. The surrounding rock was mechanically modeled as infinitely stiff. The contacts between the bentonite and the rock and between the bentonite and the canister were modeled as having an infinitely high friction, while there was no friction between the two canister components when the 1 mm gap was closed, bringing the steel in contact with the copper.

Results

The resulting void ratio and average stress in the bentonite after complete swelling and drainage are shown in Figure 8-8. The figure shows that the void ratio has increased a little from 0.650 to 0.653 in the central part of the hole, while the change is less than 0.001 close to the end of the canister. The increase in void ratio results in a reduction in average stress, as shown in the same figure. The reduction is about 1 MPa, i.e. from 8 to 7 MPa.

The effect on the copper component of the canister is shown in Figure 8-9. The picture of the deformed canister (with a high displacement magnification factor) shows that the copper unit does not carry the total pressure from the water and the bentonite and that the copper canister is pressed against the steel canister along the entire periphery and also in the central part of the lid. The lower picture shows that the plastic strain in the copper canister varies between 0.1 and 0.4% with an average of 0.2% along most of the canister. The maximum strain is found to be 0.4% at the connection between the lid and tube of copper.

Conclusions

The main conclusions concerning the effect of the swelling pressure from the bentonite and the water pressure in the rock is:

- the 1 mm gap between the copper and steel will be closed except at the edges of the lid,
- the copper canister will plasticize along a large part of the canister with a plastic strain of about 0.2%.

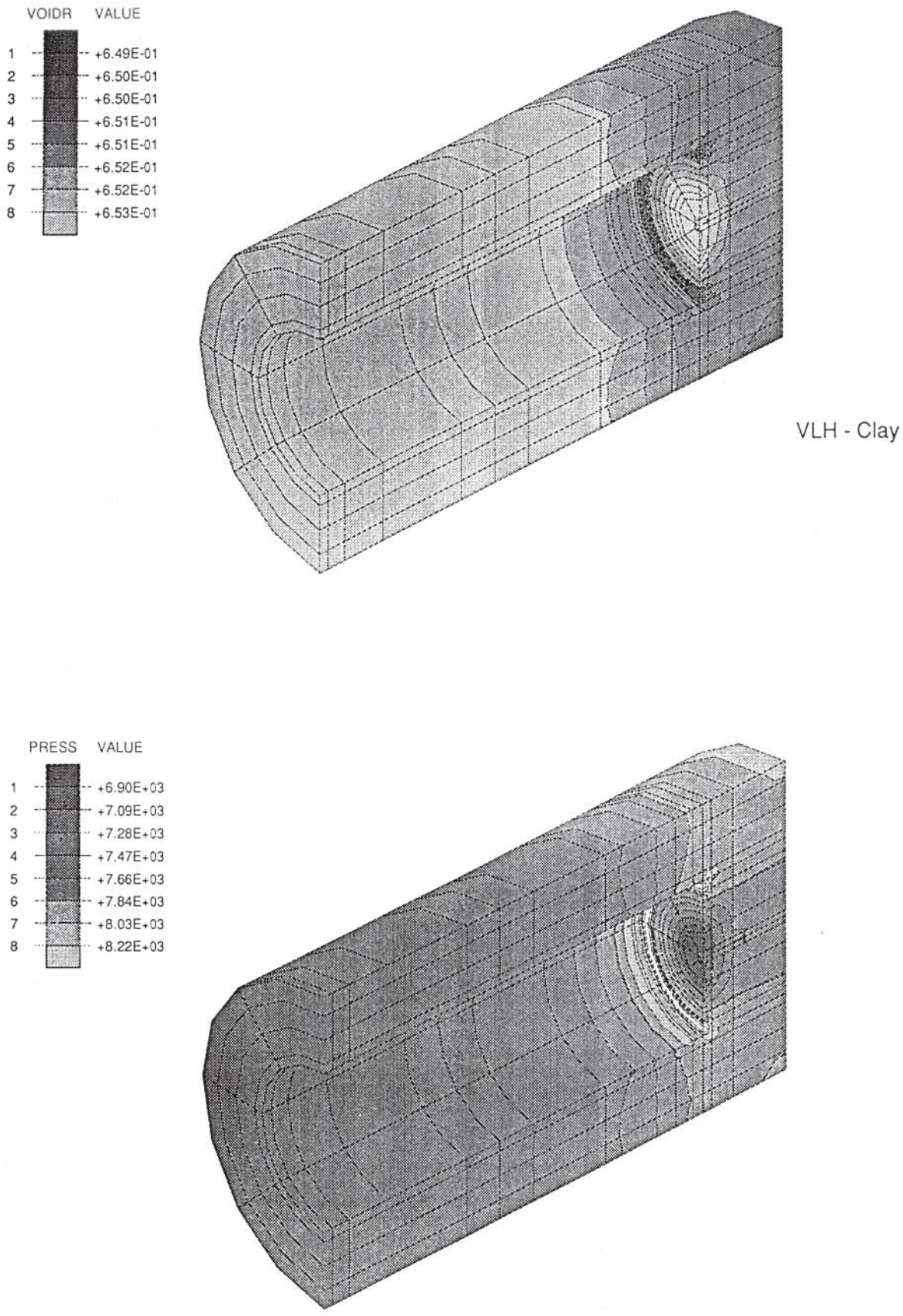

Figure 8-8. *The calculated void ratio (upper) and average stress in kPa (lower) in the bentonite clay after swelling to reach equilibrium.*

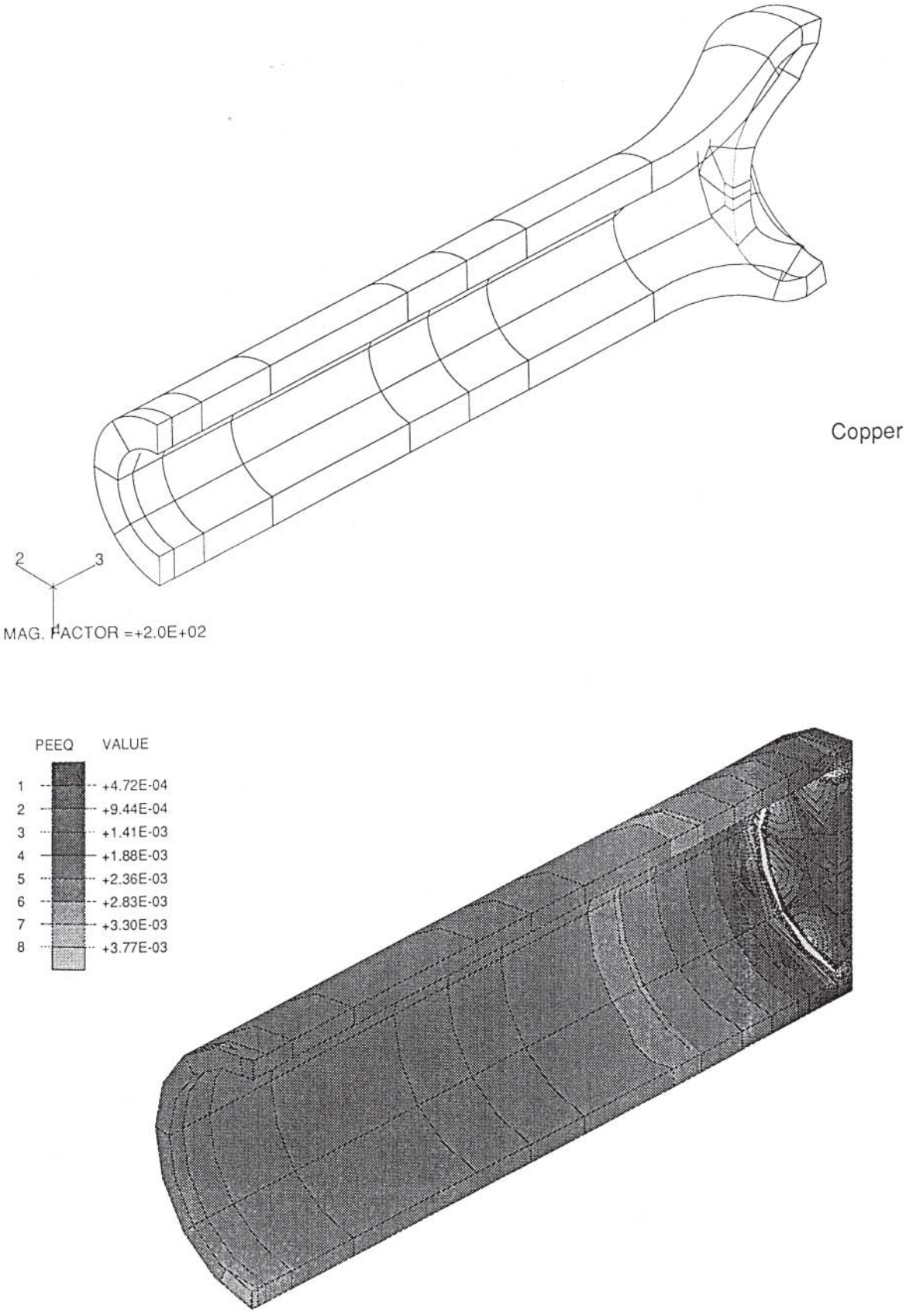

Figure 8-9. *Deformed copper canister (F_m=200) and the plastic strain in the copper at equilibrium after swelling.*

8.5.4 Effect of rock shear through the center of the canister

Assumptions

Shearing after complete water saturation was simulated as a rather slow rock displacement by 10 cm during 30 days with a constant rate of strain. Since the boundary conditions for the pore water pressure were represented by a completely drained rock with a constant pressure of 5 MPa, some drainage of the bentonite was expected to take place.

The shearing was simulated by displacing the entire rock boundary and the top boundary of the bentonite while locking the bottom boundary in the tangential and radial directions, i.e. allowing only axial displacements.

Results

The deformed structure after completed shear is shown in Figure 8-10. The characteristic large axial strain of the clay in contact with the canister close to the shear plane is seen in the figure as well.

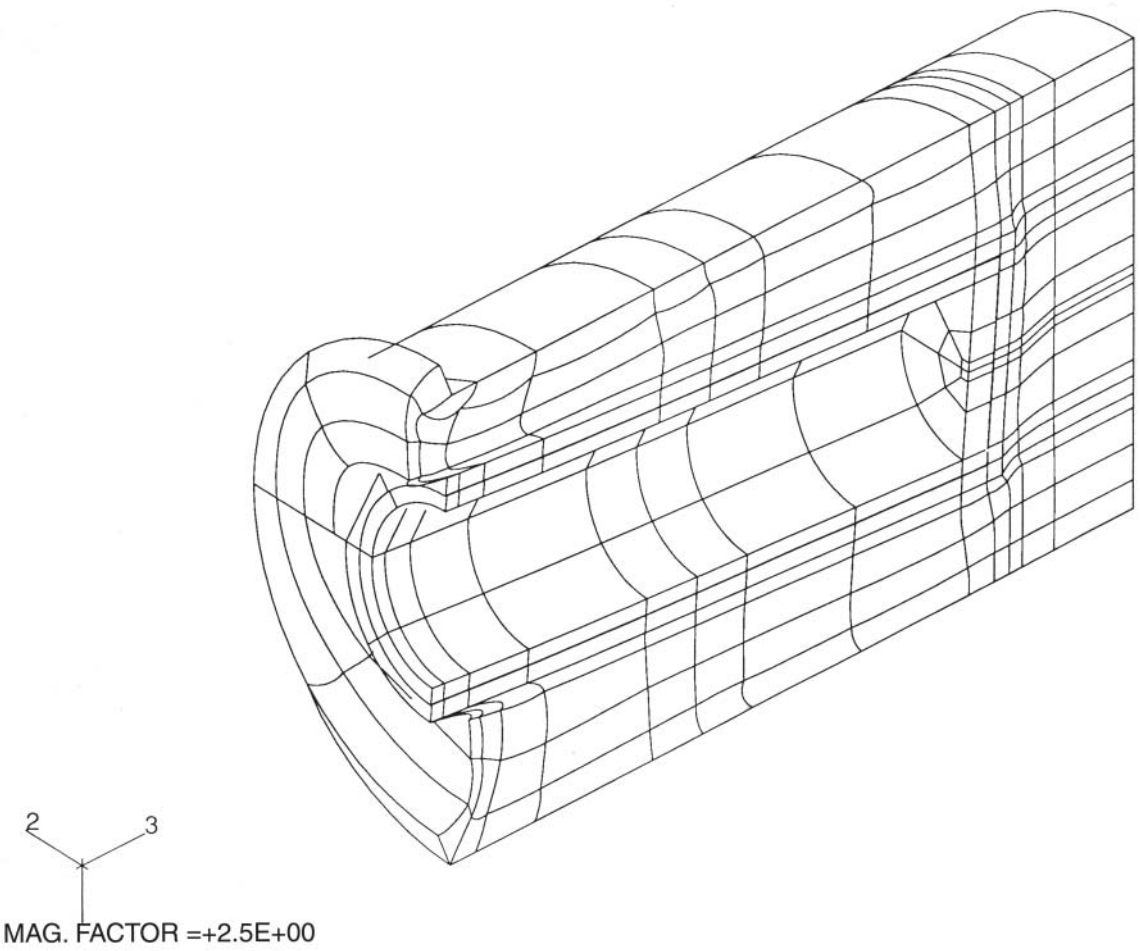

Figure 8-10. *Deformed structure after 10 cm rock shear.*

Bentonite

The pore pressure and the plastic strain in the bentonite after completed shearing are shown in Figure 8-11. The pore pressure distribution shows the following:

- very high values (>17 MPa) on the compressed side of the canisters,
- negative values (<–1.5 MPa) on the opposite side of the canister close to the shear plane.

The entire clay is plasticized except close to the rock at the end of the hole. The plot of the plastic equivalent strain shows that some parts close to the canister are strongly plasticized with plastic strains larger than 160%.

Copper canister

The deformed copper canister and the plastic strain in the copper are shown in Figure 8-12. The picture of the deformed mesh shows that bending of the canister is small. A minor tilting can be seen if the direction is compared to the direction of the canister in the picture below, in which no magnification of the displacements has been introduced.

The plastic strain shown in the lower picture is significant but not very large; it exceeds 1% inside the tube on the compressed side and outside the tube on the opposite side close to the shear plane. In the rest of the canister, the plastic strain is smaller than 0.5% with possible exception of the edges of the lid.

Steel canister

The calculations show that the copper and steel components are in contact along almost the entire interface, with a maximum normal stress of about 30 MPa. However, on the passive side and at the lid there is no contact between the materials, meaning that the copper that was pressed against the steel through the swelling of the bentonite has come off on the passive side in the shear phase.

The steel canister was found to be plasticized close to the shear plane in a similar way as the copper canister. A maximum plastic strain of about 0.4% is concluded to take place inside the canister on the active side and outside the canister on the passive side.

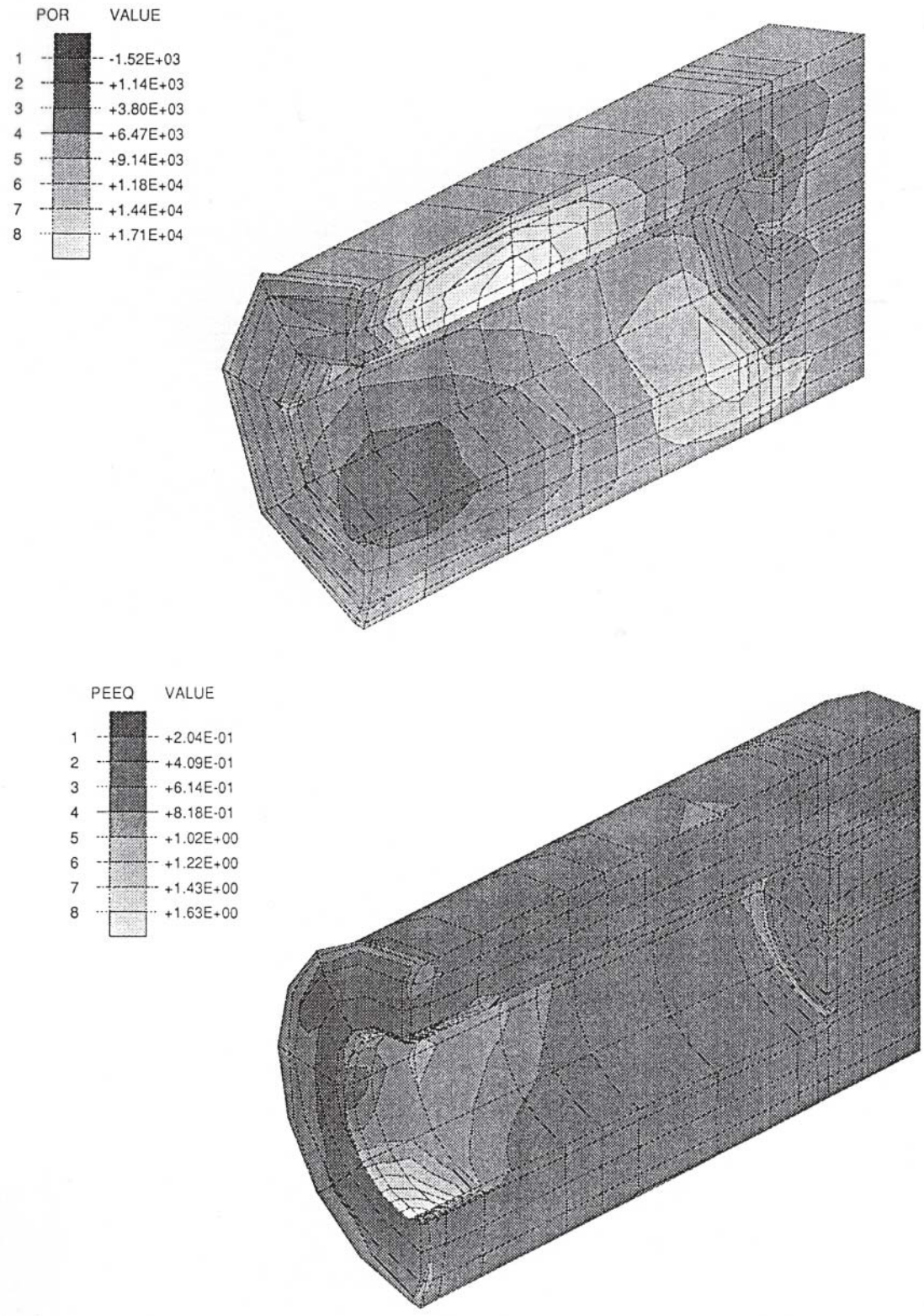

Figure 8-11. *The calculated pore pressure in kPa (upper) and plastic strain in the bentonite clay after rock shear.*

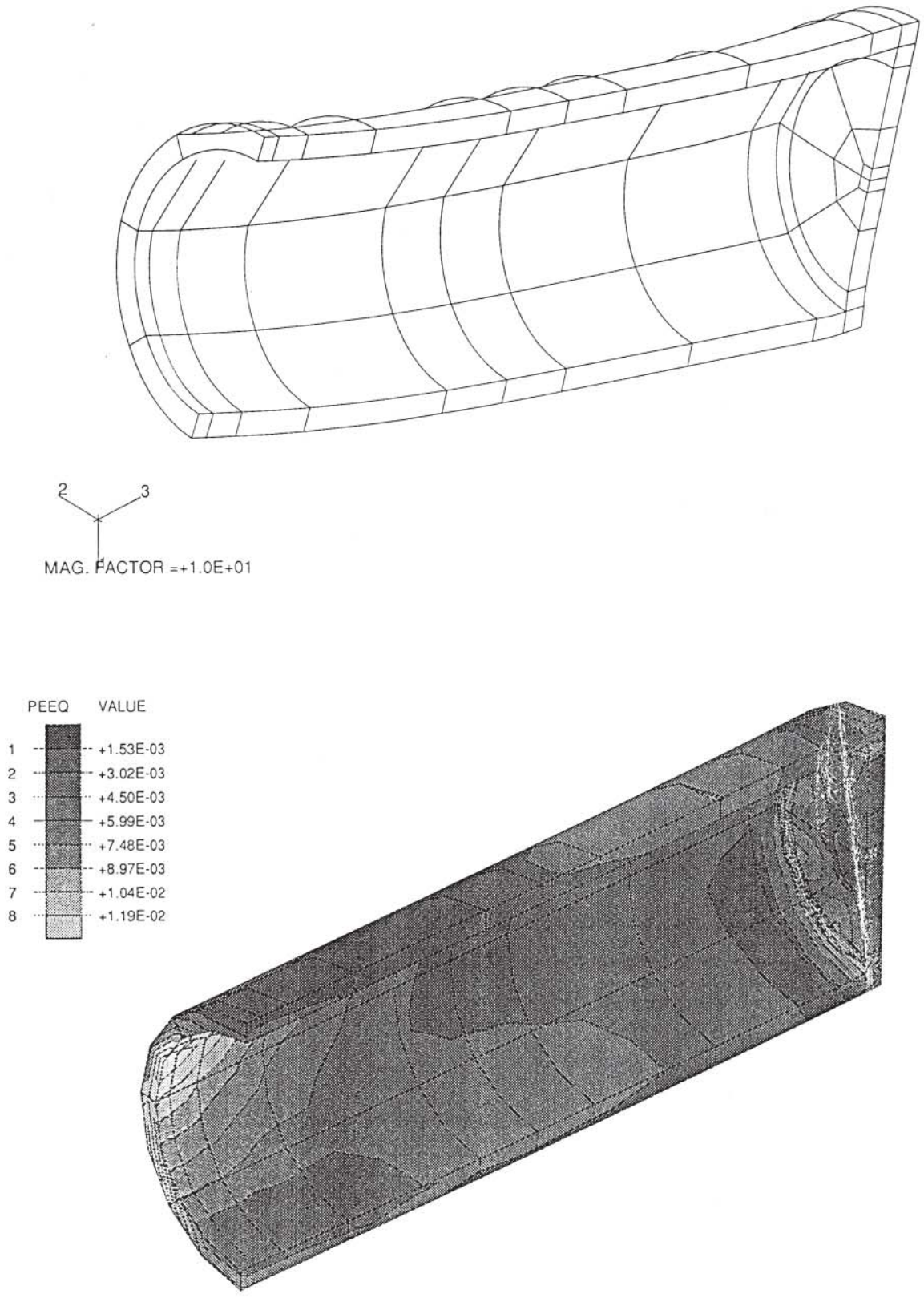

Figure 8-12. *Deformed canister (F_m=10) and plastic strain in the copper after rock shear.*

Conclusions

The major conclusions from the calculations of a 10 cm rock displacement through the center of the composite canister are the following:

- the shearing will generate very high pore pressures in the clay on the compressed side (≈17 MPa),
- low negative pore pressures will be generated on the passive side which probably will result in a temporary slot between the clay and the canister,
- plastic strain in the copper of 1% at maximum,
- plastic strain in the steel of 0.4% at maximum,
- the contact between the two canisters produced by the swelling of the bentonite will be partly lost on the passive side.

8.6 References

/1/ **Börgesson L, 1988.** Modeling of buffer material behavior. Some examples of material models and performance calculations. SKB TR 88-29. Svensk Kärnbränslehantering AB.

/2/ **Börgesson L, 1993.** Modelling of the physical behaviour of water saturated clay barriers. SKB Arbetsrapport 93-49. Svensk Kärnbränslehantering AB.

/3/ **Börgesson L, 1992.** Interaction between rock, bentonite buffer and canister. FEM calculations of some mechanical effects on the canister in different disposal concepts. SKB TR 92-30. Svensk Kärnbränslehantering AB.

/4/ **Pusch R, 2001.** Jämförelser av bergmekaniska funktionssätt hos KBS-3V, KBS-3H och MLH. Projekt JADE. Geovetenskapliga studier. SKB R-01-32. Svensk Kärnbränslehantering AB.

9 Coupled processes

This chapter deals with interacting processes in buffer clay. The issue is very complex and many problems dealing with physical and chemical changes that are in fact coupled are commonly dealt with by considering the respective phase separately without considering transients. The difficulty is that the mutual dependence of the involved mechanisms is commonly not well known. Only few models have been clinically tested to an extent that make them recommendable but it is expected that they will be numerous in the future.

In this section we will confine ourselves to describe and exemplify two models, one dealing with modeling of the mechanical behavior of unsaturated buffer with respect to heat and moisture flow, and the other dealing with geochemical transients during and after saturation of the buffer in canister deposition holes. The firstmentioned makes use of the ABAQUS code and the second the ARASE code. A code for determining the evolution of the chemistry of bentonite porewater (PHREEQE) is mentioned as well.

9.1 General

A number of interacting processes take place in a repository, like reactive chemical transport and water saturation leading to swelling and dehydration associated with microstructural reorganization in buffer clay exposed to thermal gradients. Practically all processes in the buffer are in fact coupled to a variety of chemical and physico-chemical mechanisms but only little has been made

9.2 Physical performance of unsaturated buffer under the influence of a thermal gradient

9.2.1 General

The buffer clay surrounding the canisters may not be water saturated from start and will be exposed to a thermal gradient that causes redistribution of the water content and solids. The involved processes, which depend on each other and are hence coupled, are the following:

1. Rheological changes
2. Heat flow
3. Water liquid flow
4. Water vapor flow
5. Chemical alteration

Analytical expressions for the constitutional equations describing the interacting processes are not available with a few exceptions. One concerns the rheological behavior and the water liquid flow which can be calculated with today's version of ABAQUS that includes a new non-linear relation between the pore pressure and the effective stress in unsaturated clay.

9.2.2 Behavior of unsaturated buffer material without considering water vapor flow

General

For unsaturated material without considering water vapor flow, material models will be described for the processes listed under the heading "Material models" below. Assumptions concerning the impact of suction, hydraulic conductivity, swelling pressure and stress/strain properties are discussed under separate headings.

Material models

- The suction of water in partly water filled pores. This can be described as a negative pore pressure.
- The decrease in hydraulic conductivity that is caused by the unfilled parts of the pores.
- The influence of the suction (negative pore pressure) on the effective stress.
- The influence of the swelling pressure on the effective stress in relation to the suction.

Suction

The suction exerted by water in an unsaturated porous material is caused by capillary forces in silt and sand. In clay and especially swelling smectite-rich clay, suction is more complex but can still be modeled as a negative pore pressure. The magnitude of this negative pressure is a function of the degree of saturation S_r and the void ratio e. It is usually not the same in wetting (absorption) and drying (exsorption), which means that there is a hysteresis in the relation between the suction pressure and the water ratio as shown in Figure 9-1.

It has been shown that the suction pressure s_w in water saturated bentonite is identical to the swelling pressure /1/. It is also known that the suction pressure in unsaturated porous material is primarily a function of the water content irrespective of the void ratio /2/. The suction (negative pressure) of MX-80 can be approximately expressed as in Equation (9-1):

$$s_w = -Ae_{Bw} \qquad (9\text{-}1)$$

where:

s_w = suction (kPa)
w = water content

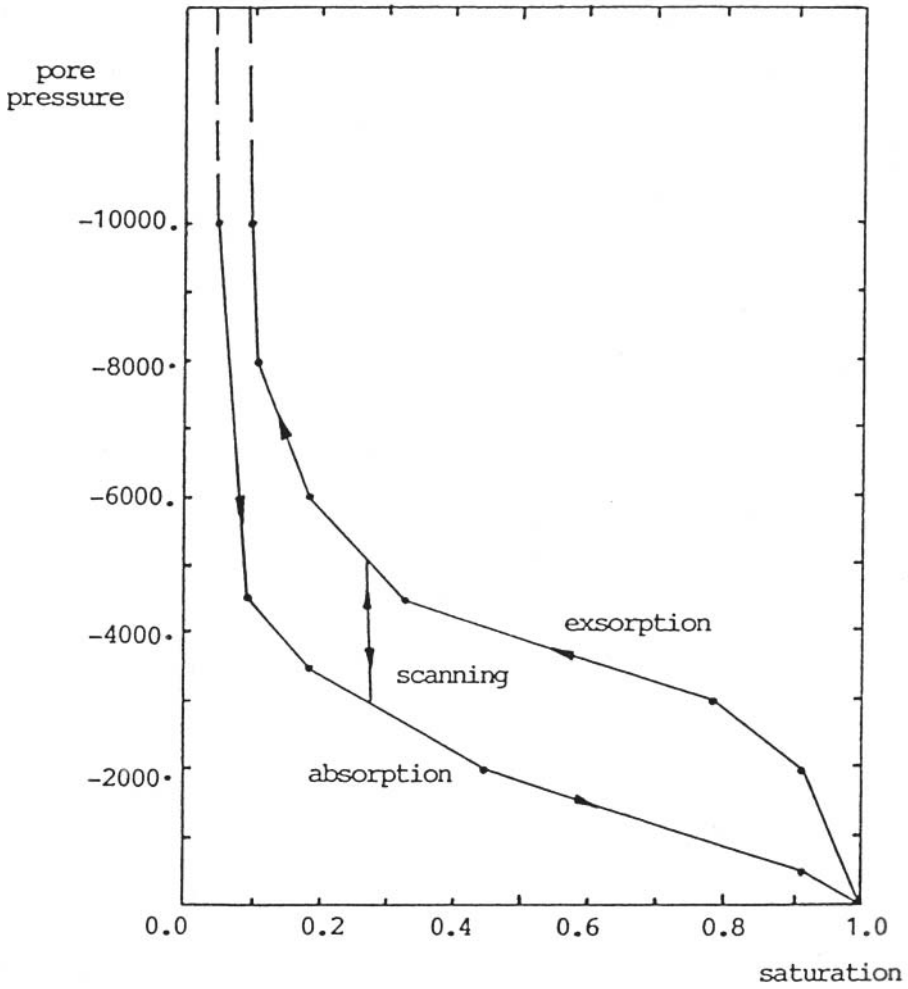

Figure 9-1. *Example of absorption/exsorption curves for porous material. The pore pressure (suction) is plotted as a function of the degree of saturation (1=100%).*

The water content can be written as a function of the degree of saturation and the void ratio according to Equation (9-2):

$$w = eS_r \frac{\rho_w}{\rho_s} \tag{9-2}$$

where:

e = void ratio
S_r = degree of water saturation
ρ_w = density of water
ρ_s = density of solids

Influence on hydraulic conductivity

The suction pressure transports water in the void system according to Darcy's law along the pressure gradient in the water-filled parts. Since only a part of the pore system is water-filled, the hydraulic conductivity will be lower than at complete saturation. The influence of the degree of water saturation (S_r) can be expressed by Equation (9-3):

$$K_p = S_r^{\delta} k \tag{9-3}$$

where:

K_p = hydraulic conductivity of partly saturated soil (m/s)
K = hydraulic conductivity of completely saturated soil (m/s)
δ = parameter that can take values between 3 and 7

Influence of suction on the effective stress

The effective stress theory cannot be applied directly to unsaturated materials since the negative water pressure only affects part of the particle structure. Rewriting according to Equation (9-4) is required /2/:

$$p' = p - \alpha s_w \tag{9-4}$$

p' = effective average stress (kPa)
p = total average stress (kPa)
α = factor that determines what part of the suction in the pore water that is distributed to an average pore pressure $u=\alpha s_w$

α is a function of the degree of saturation and the void ratio. The assumption $\alpha=S_r$ has been used in the test calculations /2/.

Swelling pressure and its influence on the effective stress

The swelling pressure in unsaturated bentonite is related to the porewater phase and is assumed to affect the effective stresses in the same way as the pore pressure. This means that the swelling pressure at the initial void ratio and degree of saturation is equal to the effective stress p' according to Equation (9-5):

$$p' = \beta s_s \tag{9-5}$$

where:

s_s = swelling pressure (kPa)
β = factor that determines what part of the "grain" pressure between the particles that contributes to the bulk effective stress

Furthermore, the swelling pressure can be considered to be a function of the water content analoguous to that of suction:

$$s_s = Ce^{-Dw} \tag{9-6}$$

In a sample of highly compacted bentonite the stresses are in equilibrium, which means that the initial effective stress must be identical to the negative pore pressure but with opposite sign if there is no external pressure on the sample. This can be achieved by letting the original swelling pressure be equal to the pore pressure.

Stress-strain properties of unsaturated buffer material

The rheological properties are expressed by using the same material models as the saturated buffer materials. The compressibility is thus modeled by the Porous Bulk Modulus k according to Equation (9-7):

$$\kappa = \frac{\Delta e}{\Delta \ln p'} \tag{9-7}$$

Since the suction and hence the swelling pressure are high in air-dry bentonite due to the low water content in the unsaturated material the influence of an externally applied pressure is lower and the stiffness of an unsaturated material higher than of a saturated material.

9.3 Reactive chemical transport in buffer

9.3.1 General

The complexibility of many geochemical processes requires development of codes for solving problems that deal with reactive chemical transport and a code of this sort, ARASE, has been worked out by Grindrod and Takase /3/. Its use will be described here in a condensed form, referring to these authors.

9.3.2 Geochemical transients during and after buffer saturation

General

In the course of the wetting of the buffer in the deposition holes there is a source of both oxygen and carbonate species due to dissolution of minerals. At the saturation both aerobic and anaerobic corrosion of the buffer/canister interface is possible, the transport taking place both through advection and diffusion. The ARASE code makes it possible to consider a number of aqueous and mineral species that are relevant to metal corrosion and mineral changes /3/. Also, dissolution/precipitation causing changes in rheological behavior and coupled changes in water and gas transport capacities can be calculated.

Model equation

Processes of primary interest occur in the water saturated part of the buffer, which is taken to be radially symmetric. Aqueous species are assumed to advected by groundwater flow and by diffusion. Following /3/ the model can be described as follows.

The starting point is to specify a system of reaction-diffusion-advection equations for n solute species, with concentrations in mols per unit fluid volume denoted by $u=(u_1, \ldots .u_n)^T$ and m solid species with concentrations $w=(w_1 \ldots .w_n)^T$, where T refers to transport. Both u and w distributions depend on spacial location, denoted x, and time, t. The porosity is termed $\theta=\theta(x,t)$. v will denote the Darcy flow rate (v/θ is the mean fluid velocity).

Distinction is made between fast, instantaneous, and slow reactions, which are treated kinetically. p fast reactions $[F(u)=(F_1 \ldots .F_p)^T]$ and q slow reactions $[S(u,w)=(S_1 \ldots .S_q)^T]$ are assumed to take place. Hence, if the j_{th} fast reaction is of the form in Equation (9-8):

$$\alpha[u_1] + \beta[u_2] \Rightarrow \gamma[u_3] + \delta[u_4] \qquad (9\text{-}8)$$

where α,β,γ and δ are stoichiometric constants, the reaction proceeds to the right or to the left according to whether the term F_j in Equation (9-9) is positive or negative:

$$F_j=-a_1^{\alpha}\, a_2^{\beta}\, K + a_3^{\gamma}\, a_4^{\delta} \qquad (9\text{-}9)$$

Here, $a_j=a_1(u_i)$ is the activity of species i.

The rate of reaction is given by $R_f F_f$ where R_f is a large positive constant. For fast reactions F=0. If the j_{th} slow reaction involves precipitation/dissolution of the form in Equation (9-10) then the corresponding slow kinetic reaction term is that in Equation (9-11):

$$\alpha u_1 + \beta u_2 \Rightarrow \gamma w_q \tag{9-10}$$

$$S_j = -k_{1j} a_1^{\alpha} a_2^{\beta} + k_{2j} A(w_1) \tag{9-11}$$

where the k-factors are the rates of forward and back reactions and A the activity of the mineral species w_1, which depends upon specific area (S_j) among other features.

Mass conservation implies that:

$$(\eta u) = T(u) + \eta B_S S(w,u) + \eta B_F R F(u) \tag{9-12}$$

where $T(u)$ denotes the net rate of increase in mass per unit volume due to transport of solutes (diffusion and advection). η is the porosity of the porous medium, R=diag($R_1 \ldots R_p$) is a (pxp) matrix of fast reaction rates, and B_F and B_S are (nxp) and (nxq) matrices containing the stoichiometric coefficients of the fast and slow reactions, respectively.

For complete reactions with t=∞ the RF terms must be eliminated which yields a new system governing the $n–p$ degrees of freedom. One introduces an nx(n–p) matrix C such that $C^T B_F$=0. This yields, after some rearrangements, the relationship in Equation (9-13):

$$(\eta U)_t = C^T T(u) + \eta C^T B_S S(w,u) \tag{9-13}$$

At any time t>0 one solves Equation (9-13) together with the algebraic system in Equations (9-14) and (9-15):

$$0 = F(u) \tag{9-14}$$

$$U = C^T u \tag{9-15}$$

which yields u in terms of U. In general Equation (9-13) must be coupled with the equations for the mineral species:

$$w_t = B_S(w,u) \quad (w>0) \tag{9-16}$$

where B_s denotes the stoichiometry matrix for the mineral precipitation and dissolution reactions.

The mineralogy distribution may be coupled back to the transport terms $T(u)$ via the volumetric change and the displacement of pore water. One has:

$$\eta = g(w) \tag{9-17}$$

where g is some known function describing porosity in terms of the current mineralogy, and pore water mass conservation implies:

$$\eta_t + \nabla \Delta) \cdot v = 0 \tag{9-18}$$

where v satisfies Darcy's law:

$$v = -k(\eta)\ \Delta \cdot P \tag{9-19}$$

where k is the permeability, which depends on the porosity and may be altered by the chemical processes, and P is the water pressure.

In these terms one can write:

$$T_t = \Delta(h\eta D_t\ \Delta u_j - u_i \quad (9\text{-}20)$$

where D_t is the diffusion-dispersion tensor for the i^{th} species.

The approach is to solve Equations (9-13) to (9-20) simultaneously by employing a non-linear solver with variable time stepping. The result is the change in mineral composition accompanied by precipitation and cementation or increase in porosity and hydraulic conductivity. As to the boundary conditions one must impose conditions on the solute species, i.e. flux or concentration conditions.

9.3.3 Porewater chemistry

General

An important issue is the chemical composition of buffer porewater, for which the geochemical simulation code PHREEQE appears to be useful /4/. This code is founded on the principle that all equilibrium mass action equations are transformed into a set of nonlinear simultaneous expressions. Basic to the model is the chemical composition of the buffer for which the Gibbs free energy for formation has to be calculated., which is made by applying the oxide summation technique /5/. The enthalpi of formation is also required when there is a change in temperature, like in a repository. It may be derived, empirically, from the relationship $\Delta G_f/\Delta H_f = 0.93$.

Influence of pyrite on the porewater chemistry

Dissolution of smectite in controlled laboratory experiments is known to yield an increase in pH and a drop in Eh. Chemical reactions explaining this are the following pyrite-magnetite redox couple reactions:

$$3\ FeS_2 + 28\ H_2O = Fe_3O_4 + 6\ SO_4^{2-} + 44\ e^- + 56\ H^+ \quad (9\text{-}21)$$
Pyrite *Magnetite*

The equilibrium constant K can be written as:

$$K = [SO_4^{2-}]^6\ [e^-]^{44}\ [H^+]^{56}/[H_2O]^{28} \quad (9\text{-}22)$$

$$\log K = 6\log[SO_4^{2-}] - 44(pe + pH) + 12\ pH = -287.69 \quad (9\text{-}23)$$

From this one has the redox Equation (9-24):

$$pe + pH = 6.53 + 0.136\log[SO_4^{2-}] - 0.273pH \quad (9\text{-}24)$$

Pyrite initially present in bentonite like MX-80 is gradually dissolved in the porewater while magnetite is precipitated. Alternative reactions are pyrite-to-hematite (Equation (9-25)) and pyrite-to-goethite (Equation (9-26)), but as demonstrated by Figure 9-2 /6/, laboratory investigations indicate that magnetite is probably the ultimate reaction product after a sufficiently long period of time, and that it is assumed to control the redox equilibrium.

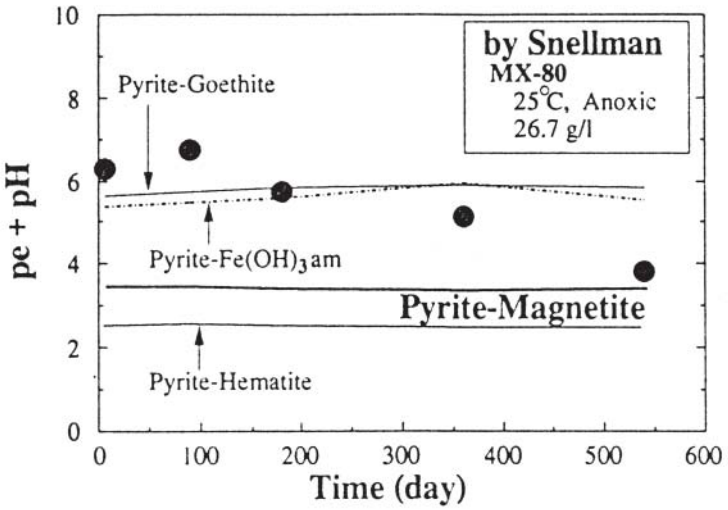

Figure 9-2. *Change in pe + pH as a function of time in experiments at 25° /6/ compared with PHREEQE-calculated values /4/.*

Pyrite-to-hematite

$$pe + pH = 5.39 + 0.133 \log[SO_4^{2-}] - 0.267\ pH \quad (9\text{-}25)$$

Pyrite-to-goethite

$$pe + pH = 6.468 - 0.133 \log[SO_4^{2-}] - 0.133\ pH \quad (9\text{-}26)$$

pH in the porewater as a function of ion exchange processes in the buffer

It is obvious from laboratory experiments that pH in the porewater is controlled by ion exchange reactions /7/ and PHREEQE can be used to model them. Considering Na-bentonite pH is largely controlled by exchange reactions between Na^+ and H^+ in the following way:

$$BENTONITE\text{-}Na + H^+ = BENTONITE\text{-}H + Na^+ \quad (9\text{-}27)$$

PHREEQE can not handle simultaneous ion exchange reactions, like, for instance, exchange reactions between Ca^{2+} and Mg^{2+} in a system of smectite, calcite and dolomite. However, treating ion exchange reactions as fictitious complexations, reactions between the smectite and several cations can be modeled /4/. One can define equilibrium constants for any ion interaction in the following fashion:

$$K_{na} = [BENTONITE\text{-}Na]/[BENTONITE^-]\ [Na^+] \quad (9\text{-}28)$$

$$K_H = [BENTONITE\text{-}H]/[BENTONITE^-][H^+] \quad (9\text{-}29)$$

$$K_K = [BENTONITE\text{-}K]/[BENTONITE^-][K^+] \quad (9\text{-}30)$$

$$K_{ca} = [BENTONITE_2\text{-}Ca]/[BENTONITE^-]^2[Ca^{2+}] \quad (9\text{-}31)$$

$$K_{Mg} = [BENTONITE_2\text{-}Mg]/[BENTONITE^-]^2[Mg^{2+}] \quad (9\text{-}32)$$

Cases with different liquid-to-solid ratios and different concentrations of Na^+ and total carbonate (HCO_3^- and CO_3^{2-}) and pH have been investigated /4/, according to the following procedure:

1. Assume a certain amount *W* of clay be dispersed in 1 kg of pure water.
2. Consider dissolution and precipitation equilibria of the smectite content and the contents of calcite, dolomite, gibbsite, and gypsum.
3. Take the partial pressure of carbon dioxide to be $10^{-3.5}$ bar.
4. Consider simultaneous exchange of Na^+, K^+, Ca^{2+}, Mg^{2+}, and H^+.
5. The hypothetical component $BENTONITE^-$ and the four cations are introduced in the porewater.
6. SO_4^{-2} is added (0.14 mol/g).
7. Eh is fixed at pe=3.47 (experiments in air atmosphere).
8. The amount *W* of clay is changed, repeating procedures 5 and 6.

The results of calculations assuming an amount W of Kunigel bentonite (cf Part 2) equal to $6.2 \cdot 10^{-4} \cdot W$ mol indicate an acceptable fit to experimental data as shown in Figure 9-3.

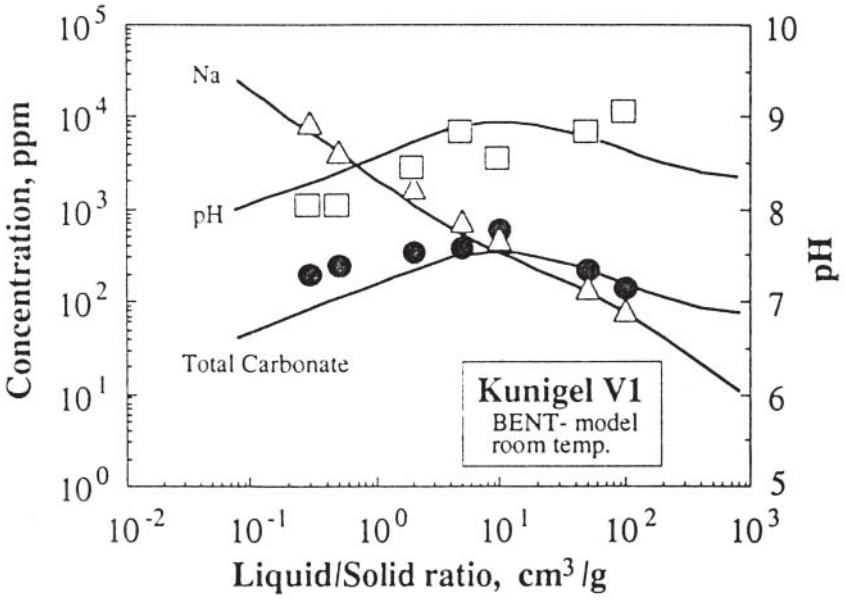

Figure 9-3. *Bentonite/water reactions as a function of the water content expressed as liquid-to-solid ratio /4/. The curves represent data calculated by use of PHREEQE.*

Comments

The PHREEQE code and the BENTONITE model give results that are in reasonable agreement with actually recorded data and they appear to have a great potential in future predictions of pH and eH in smectite buffers. Still, more testing of the models must be made to find out possible limitations.

9.4 Examples

9.4.1 Saturation of clay confined in an oedometer

Problem: Predict the degree of saturation and the void ratio in an MX-80 bentonite sample with 5 cm length and diameter confined in an oedometer. The sample is exposed to water at one end while the other is closed.

Basic

The possibility of calculating the behavior of unsaturated buffer materials with ABAQUS has been examined by several test calculations compared with oedometer test results.

Solution

The model of unsaturated behavior described in Section 8 is applied.

The sample is assumed to be confined in an oedometer with the same geometry as the sample. Water is assumed to be evenly supplied over one end of the sample while the other boundaries are assumed to be completely watertight. The water pressure at the wet end is set at 0 kPa. Since the models are complete with respect to rheology and water transport, the change in void ratio, effective stress, and degree of saturation is calculated during the entire process until complete saturation is achieved. The starting conditions of the sample are the following:

Void ratio $e = 0.78$
Water content $w = 10\%$

which yields:

Degree of saturation $S_r = 36\%$
Density at saturation $\rho_m = 2000$ kg/m^3
Dry density $\rho_d = 1556$ kg/m^3

Results

The initial suction s_w and swelling pressure s_s is 57.6 MPa according to Equations (9-1) and (9-6). The low degree of saturation reduces the effective pressure to 28.8 MPa according to Equation (9-5).

Assuming all nodes in the element mesh to be free and the sample to be free to behave as in a real test, one gets the results in Figures 9-4 and 9-5 for 138 h test interval. The degree of saturation S_r, the void ratio e, the effective average stress p' and the pore pressure u are plotted as a function of x/L where x is the distance in cm from the water inlet and L is the length of the sample (5 cm).

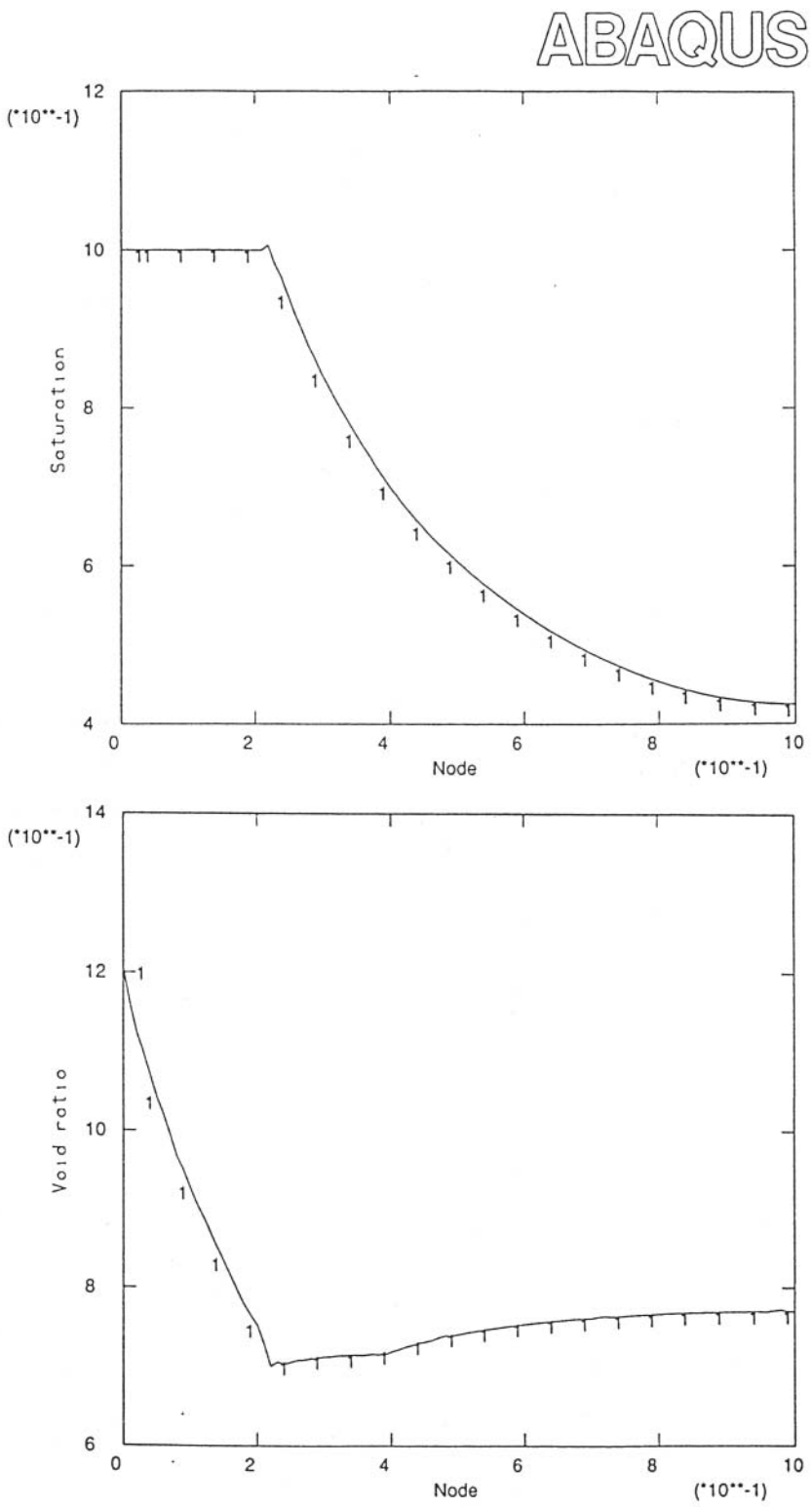

Figure 9-4. *Calculated degree of saturation and void ratio as a function of the relative distance from the water inlet in the 5 cm long sample after 138 hours.*

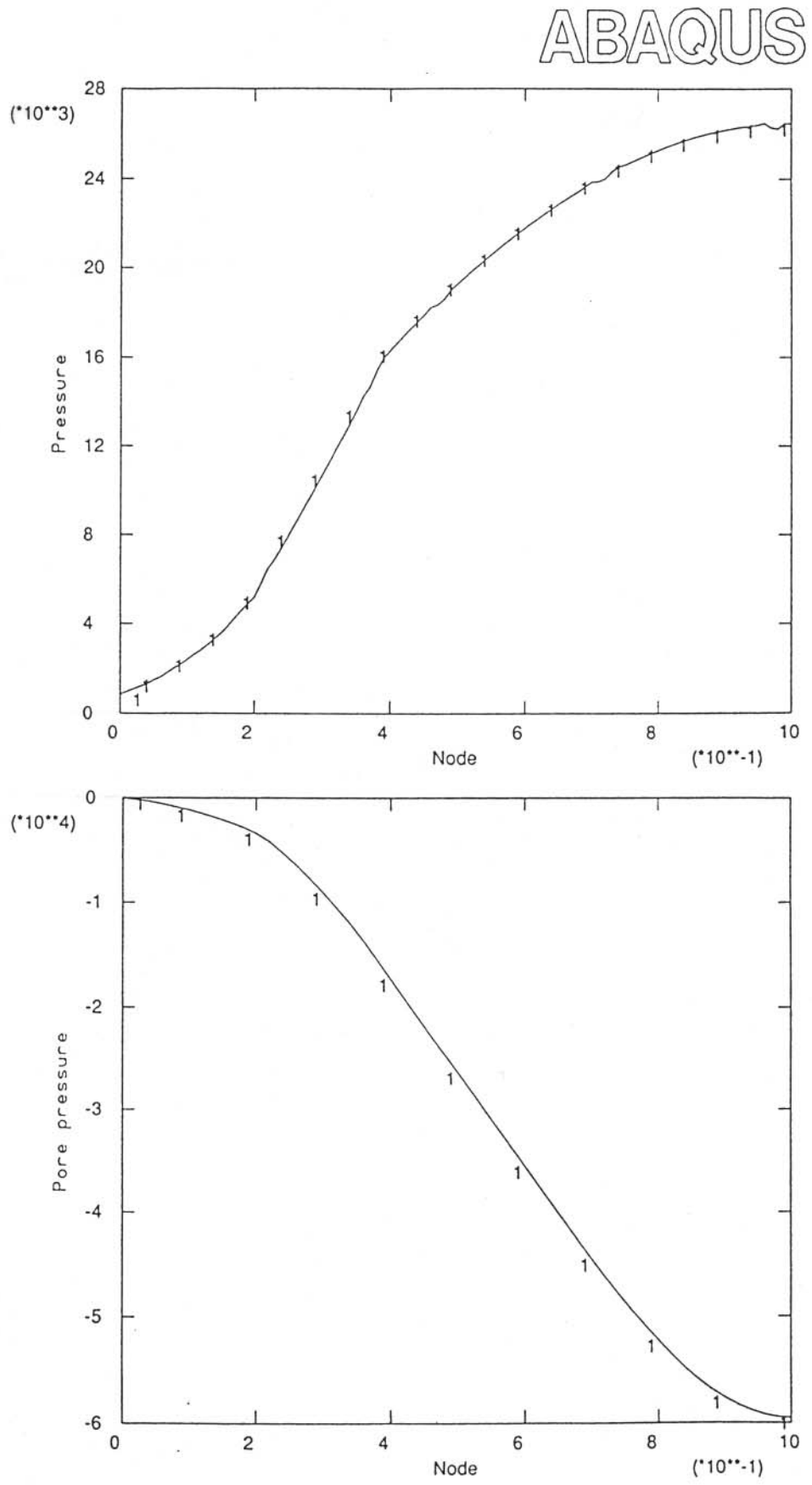

Figure 9-5. *Calculated average effective stress (pressure) and pore pressure as function of the relative distance from the water inlet in the 5 cm long sample after 138 hours.*

The calculations resulted in a degree of saturation of 100% within about 1 cm distance from the wetted end and a decrease to 42% at the closed end of the sample. The saturation yielded swelling within 80% of the saturated part from the void ratio e=0.78 up to e=1.20 at the water inlet. The rest of the sample decreased in volume to the minimum value e=0.70. The effective average stress p' increased from 1 MPa at the water inlet to 26 MPa at the inner end of the sample while the suction pressure s_w decreased from 0 MPa to –60 MPa at the end of the sample. The total pressure p on the boundaries, which can be calculated by use of Equation (9-4) was still only about 1 MPa in the whole sample.

The calculation indicates that full saturation of the sample will be obtained after about 900 hours. The final void ratio distribution after complete equilibrium (1388 hours) is shown in Figure 9-6. The large difference in void ratio that was indicated during the water uptake disappeared and the remaining inhomogeneity corresponds to a difference in water content of about 3%. This is close to what was observed in an experiment where the sample was cut in 0.5 cm thick slices for determination of the water content.

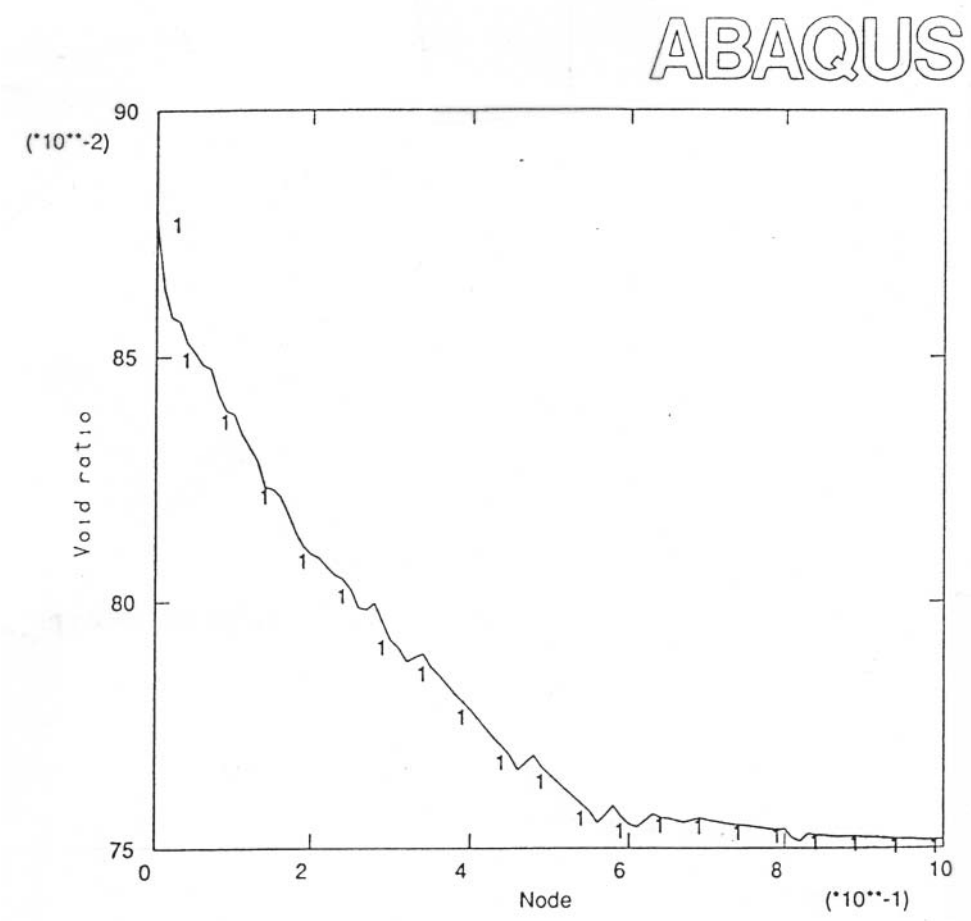

Figure 9-6. *Calculated void ratio after completed saturation (1338 hours) as a function of the relative distance from the water inlet.*

Comments

The models yield logical results. They have not yet been calibratedand only few tests have been performed that can be compared with the calculations. Hence, considerable uncertainties prevail concerning the validity of coupled models.

Two major conclusions can be drawn from application of the model for water saturation:

- The true rate of water uptake is faster than predicted theoretically.
- The change in density with swelling of the saturated part and compression of the unsaturated part is stronger than measured.

9.4.2 Formation of laumontite by quartz reacting with anorthite /2/

Problem: Calculate the extent of precipitation of laumontite and dissolution of anorthite in buffer clay with the smectite left unaffected. Oedometer case with 7 cm sample length.

Basic

The chemical reactions considered are /3/:

$SiO_2 + 2H_2O = H_4SiO_4$

$CaAl_2Si_2O_8 + 8H_2O = Ca^{2+} 2H_4SiO_4 + 2Al(OH)_4^-$

$CaAl_2Si_4O \;\; 2.4\ H_2O \;\; 8H_2O = Ca^{2+} 4H_4SiO_4 \;\; 2\ Al(OH)_4^-$

where the left membrum is anorthite and the right membrum laumontite.

Solution and results

Applying the ARASE code for a one-dimensional case the transformation of laumontite formed and the anorthite lost as a function of the distance from the initial boundary (x=0) is illustrated in Figure 9-7 /3/. The curves represent times 10^6, $2{\cdot}10^6 ... 10^7$ seconds.

One concludes that the mineral conversion starts upp at a high rate but is strongly retarded. Thus, the “front” of the altered mass ratio in the diagrams represent about 2 months, and complete conversion is not expected in less than several years. This is an example of the need of using limited thicknesses in laboratory tests with smectitic clay.

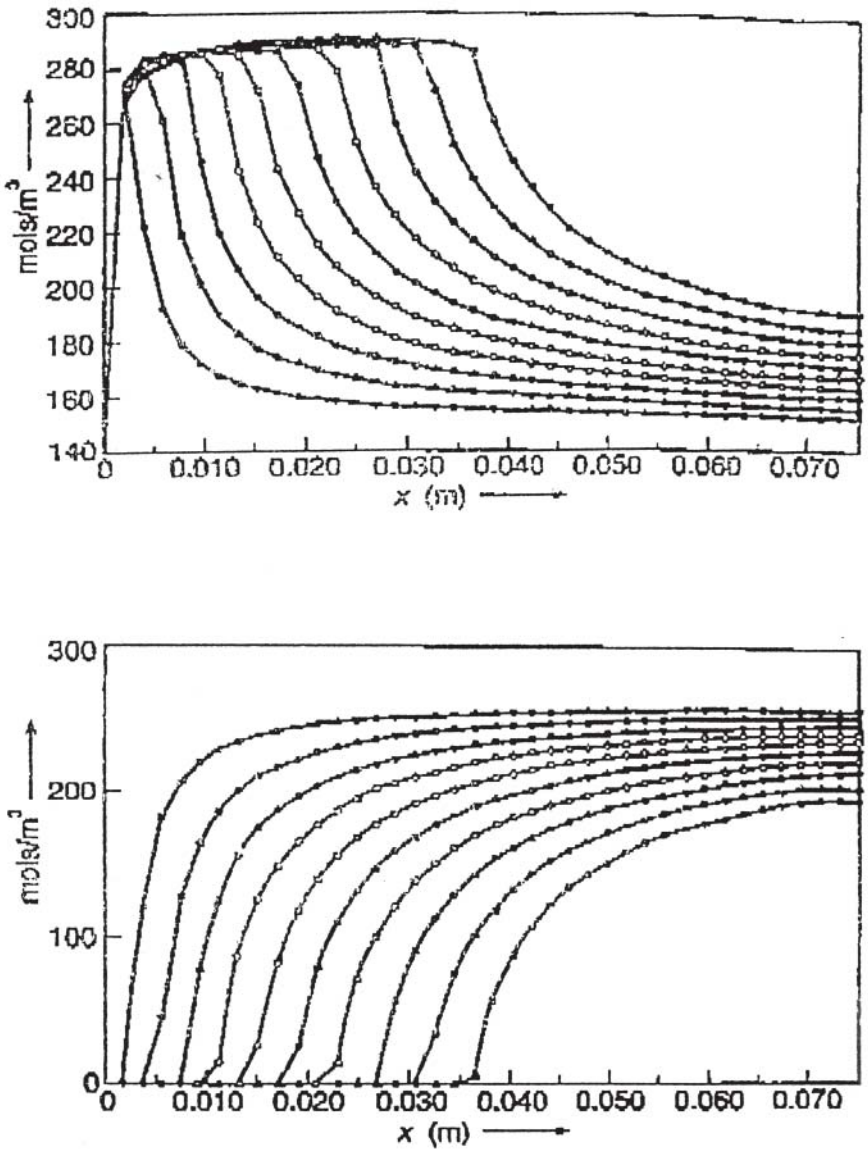

Figure 9-7. *Upper: Concentration of Laumonite, $CaAl_2Si_4O_1$ 2.4 H_2O, at times 1E6, 2E6, 3E6..., 1E7, seconds at positions x along the flow path. Lower: Concentration of Anorthite, $CaAl_2Si_2O_5$, at times 1E6, 2E6, 3E6, ..., 1E7, seconds at positions x along the flow path.*

9.5 References

/1/ **Kahr G, Kraehenbuehl F, Müller-Vonmoos M, Stoeckli HF, 1986.** Wasseraufnahme und Wasserbewegung in hochverdichtetem Bentonit. NAGRA Technischer Berich 86-14.

/2/ **Börgesson L, 1993.** Modelling of the mechanical behaviour of unsaturated bentonite-based buffer materials with heat and moisture flow. SKB AR 93-47. Svensk Kärnbränslehantering AB.

/3/ **Grindrod P, Takase H, 1993.** Reactive chemical transport within engineered barriers. Fourth Int. Conf. on the chemistry and migration behaviour of actinides and fission products in the geosphere, Charleston, SC USA, December 12–17. R Oldenburg Verlag 1994 (pp 773–779)

/4/ **Ohe T, Tsukamoto M, 1997.** Geochemical properties of bentonite pore water in high-level-waste repository condition. Nuclear Technology, Vol 118, April (pp 49–57).

/5/ **Tardy Y, Garrels R M, 1974.** A method of estimating the Gibbs energies of formation of layer silicates. Geochim. Cosmochim. Acta, Vol 38, (p 1101).

/6/ **Snellman N, Uotila H, Rantanen J, 1987.** Laboratory and modeling studies of sodium bentonite/groundwater interaction. Material Research Soc. Symp., Proc. Vol 84, (p 781).

/7/ **Takahashi M, 1986.** Properties of bentonite clay as buffer material in high-level waste geological disposal. Part 1: Chemical species contained in bentonite, Nuclear Technology, Vol 50, (p 187).

10 Long-term performance of buffer and backfill

This chapter deals with the longevity of buffers and backfills. It is based on the Arrhenius-type model proposed to SKB as a working hypothesis for smectite-to-illite conversion, taking temperature and access to dissolved potassium as well as the activation energy for conversion as controlling parameters. Examples of prediction of the conversion rate are given, using the numerical code FLAC.

10.1 Mineral alteration

Alteration of clay minerals in the buffer will affect its long-term performance. Conversion of smectites to non-expandable minerals, for instance, will result in increased hydraulic conductivity of the buffer materials. One such alteration process, discussed in numerous investigations, is conversion of smectite to illite with fixation of potassium ions in cation exchange positions /1,2,3/. In the investigation reported here, a kinetic model for this process, proposed by Huang et al /4/, is used for analyzing the rate of conversion of the highly compacted bentonite buffer in a KBS-3 repository. It depends on the combined effect of S/I conversion and availability to potassium.

The geotechnical finite difference code FLAC /5/ has been applied to a large number of rock mechanical problems, related to high level waste deposition. The versatility of this code makes it, however, applicable also to problems in which no mechanical aspects are included. The basic idea is to use the FLAC system with its model generation routines, screen graphics, plotting facilities and explicit timestepping solution procedure as a platform, while the FLAC built-in programming facilities are used for implementing the reaction mechanism that controls the process under study. Diffusive transport can be simulated using either the thermal logic or the flow logic. In the present study the FLAC thermal logic was employed for simulating diffusion of potassium ions using the FLAC temperature to represent the porewater potassium concentration. The model referred to in this section was worked out by Harald Hökmark, Clay Technology AB, Sweden.

10.1.1 Kinetic Model

Following Huang et al /4/ the rate of smectite/illite conversion can be expressed as:

$$-\frac{dS}{dt} = [K^+]\, k\, S^2 \qquad (10\text{-}1)$$

where:

S = smectite fraction
k = rate constant, (L/mol,s)
$[K^+]$ = porewater potassium concentration, (mol/L)

The rate constant k is given by:

$$k = A \exp\left(\frac{-E_a}{RT}\right) \tag{10-2}$$

where:

A = frequency factor, (L/mol,s)
E_a = activation energy, (cal/mol)
R = gas constant (cal/mol,Kelvin)
T = temperature, (Kelvin)

If the porewater potassium concentration is constant over time and the initial smectite fraction is S_0, Equation (10-1) has the solution:

$$S = \frac{S_0}{1 + S_0 [K^+] k t} \tag{10-3}$$

Equation (10-3) applies if dissolution of potassium in the nearfield and potassium transport, in the nearfield and within the buffer, keep pace with the potassium consumption associated with the mineral conversion. If no potassium is supplied to the buffer, i.e. if a limited quantity, given by the buffer porosity and the initial porewater potassium concentration $[K^+]_0$, is available, Equation (10-1) changes to:

$$-\frac{dS}{dt} = \left([K^+]_0 - \frac{\rho_w p}{w m}(S_0 - S)\right) k S^2 \tag{10-4}$$

where:

ρ_w = density of water, (g/L)
p = mass fraction of potassium in completely converted smectite
w = water content
m = mol mass of potassium, (g/mol)

10.1.2 Potassium availability

The initial K^+ concentration, required for complete conversion, is given by:

$$[K^+]_0 - \frac{\rho_w p}{w m} = 0 \tag{10-5}$$

The mass fraction parameter p should be about 0.05 /3/. For highly compacted and water saturated bentonite w is about 0.26. The initial porewater concentration, required for complete conversion would then be about 5 mol/L, a value that exceeds the concentration in normal rock porewater and in sea water by several orders of magnitude. The quantities of dissolved potassium, contained in the rock porewater that is supplied to the buffer during water saturation, will thus suffice to convert only insignificant fractions of the smectite in highly compacted 100% bentonite. This means that availability to potassium from external sources is necessary if smectite-to-illite conversion should take place on any significant scale in the buffers surrounding KBS-3 HLW canisters. Restrictions in potassium transport capacity, within the buffer as well as between buffer and potassium

source, are consequently important for the conversion time scale. In this study transport is assumed to take place by diffusion only.

For bentonite/ballast mixtures in tunnel backfills, ballast particles containing potassium-bearing minerals may serve as internal sources and promote conversion in the bentonite component. Tunnel backfills without bentonite component, or with completely or partly converted bentonite components, may serve as external potassium sources for canister buffers in the deposition holes. The amounts of potassium that can be supplied from the backfill to the highly compacted bentonite buffer in the deposition holes are determined by chemical weathering rates that depend on a number of factors like the mineral composition and the specific area of the backfill ballast. The possible production of dissolved potassium in the tunnel backfill has been shown to be considerable /3/. In the numerical study referred to here it is assumed that the backfill and the surrounding rock have the potential of supplying the potassium quantities that would be needed for complete conversion of the deposition hole buffers.

10.2 Modelling method[2]

All simulations presented here are performed using version 3.22 of the finite difference code FLAC /5/. FLAC is a recognized tool for analyzing rock mechanical and soil mechanical problems, and contains logic for simulation of fluid flow and heat diffusion.

The problem domain, which can be two-dimensional or axisymmetric, is discretized into a mesh of quadrilateral zones with gridpoints in the zone corners. An explicit timestepping solution procedure is employed that updates all zone variables and all gridpoint variables throughout the model every timestep. The duration of one timestep is automatically set to a value that is small enough to ensure numerical stability, and is determined by zone sizes and by values of parameters that control the velocity at which disturbances are propagated, i.e. elastic moduli (mechanical models), heat diffusivity (thermal models) and conductivity (flow models).

FLAC contains a built-in programming language, FISH, that enhances the power and versatility of FLAC considerably. User-written FISH routines can be called from the FLAC input file, either explicitly at specified instances in the command sequence, or automatically every timestep. FISH routines can be used to define new scalar variables or gridpoint variables and to assign values to them. Also values of predefined standard FLAC gridpoint variables can be tested and modified. In the present study, smectite-to-illite conversion was implemented by use of this programming language. Two FISH functions were defined: one for initializing the problem and one containing an algorithm for managing the kinetic model. Schematic descriptions are given below:

Initialization

1. Define scalar variables for parameters included in Equations (10-2) and (10-4), i.e. for E_a, T, R, w, m, S_0, ρ_w and p.
2. Define new extra gridpoint smectite fraction variable, *S(i,j)*.
3. Assign constant values to the scalar variables and initial values to *S(i,j)*.

[2] This section is based on a procedure suggested by Harald Hökmark, Clay Technology AB

Conversion algorithm

For each gridpoint *i,j*:

1. Test the value of current local K^+ concentration (i.e. FLAC temperature) and the value of the FLAC timestep, and calculate the reduction in smectite fraction ΔS during the timestep by direct use of Equation (10-1).
2. Calculate the reduction of porewater K^+ concentration ΔC, associated with the smectite fraction reduction ΔS, by using the values of p, S_0, ρ_w and m.
3. Update values for gridpoint variables representing porewater K^+ concentration and smectite fraction, i.e. FLAC temperature and *S(i,j)*.

The coupled process of potassium diffusion and simultaneously progressing S/I conversion was simulated by calling the initialization function and then putting the thermal logic in operation, i.e. starting the timestepping solution procedure, with calls to the conversion algorithm function every timestep. Parameter values for the thermal material properties had to be set with regard to the intended effective potassium diffusivity, taking into account the effects of porosity. Since the thermal logic was engaged for simulating potassium diffusion, no heat conduction calculations could be made, meaning that the real temperature of the system had to be represented by an additional, specifically defined variable. In the simulations performed in this study, a global temperature was assumed, but there are no principal difficulties in defining a gridpoint temperature variable and to prescribe any variation in time and space for it.

The default time step, which is automatically determined and set by the FLAC thermal logic, ensures numerical stability and sufficient accuracy in heat conduction calculations. This timestep may, however, be too large for the conversion algorithm to perform properly, and a lower value may have to be prescribed in the FLAC input file.

10.3 Verification of the simulation procedure

10.3.1 General

The curves with discrete plot symbols in Figure 10-1 for a case with the parameters specified below were obtained numerically by applying a Runge-Kutta method to Equation (10-4), while the curves show corresponding FLAC results obtained by using the FISH procedure described above.

The following parameter values represent the case reported in Figure 10-1.

ρ_w = 1000 g/L
w = 0.26
m = 39 g/mol
$[K^+]_0$ = 0.01 mol/L
S_0 = 1
T = 423 K, i.e. 150 degrees centigrade

p, the parameter representing the required potassium mass fraction of the solid material to yield complete conversion of smectite to illite, is varied in Figure 10-1 and two different activation energies (22 and 23 kcal/mole) are used. One finds that the conversion algorithm performs very accurately since the values calculated by use of the Runge-Kutta

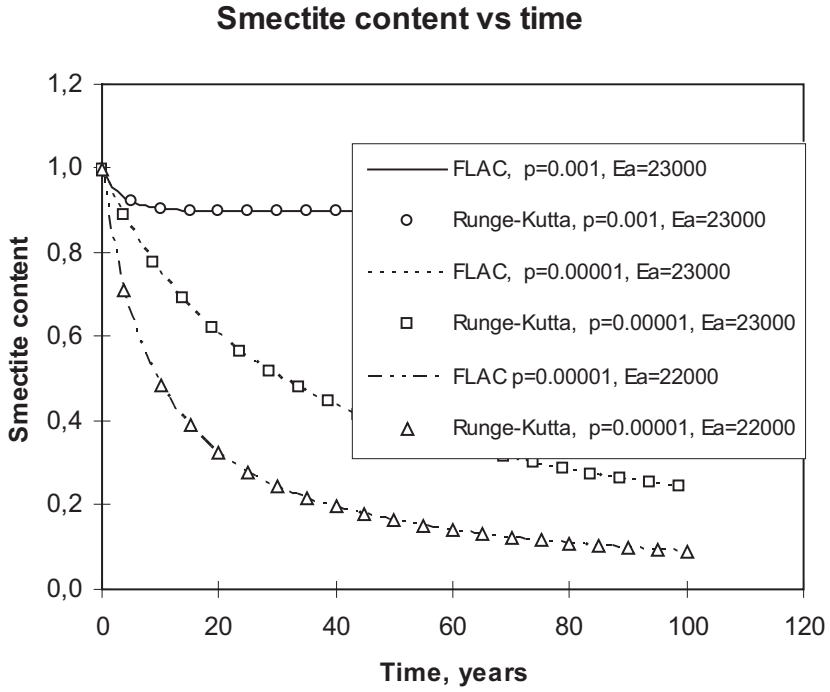

Figure 10-1. *FLAC results compared with solutions of Equation (10-4).*

method and the FLAC results agree within about 0.1%. It should be added that the activation energies used here are considerably lower than those evaluated from natural analogs, which tend to give values between 26 and 28 kcal/mole.

10.4 Moving S/I interfaces

If the potassium diffusion is slow and smectite conversion by potassium fixation is fast, the diffusing ions will be captured almost instantaneously and get irreversibly immobilized as soon as regions of incomplete conversion are encountered. This means that a distinct I/S interface with zero porewater potassium concentration will form, and that diffusion will take place only in the converted region between the outer boundary and that interface. The interface moves from the concentration boundary at the same rate at which conversion takes place in the interface region. If the amount of potassium per unit volume that is required for complete conversion is not too small, a steady state approximation of the concentration distribution can be used to calculate the position of the I/S interface as function of time /6/. Figure 10-2 illustrates schematically diffusion and conversion in systems with moving I/S interfaces that separate regions of converted material (I) from unconverted regions (S). The upper part represents one-dimensional diffusion (linear steady state concentration distribution) and the lower part diffusion in an axisymmetric geometry.

In the axisymmetric system the steady state concentration distribution is given by:

$$C(r) = \frac{C\,ln(r/r(t))}{ln(Ro/r(t))} \qquad (10\text{-}6)$$

where $C(r)$ is the concentration in any position r between the outer boundary at Ro (concentration = C) and the S/I interface at $r(t)$ (concentration = 0). Equations (10-7) and (10-8) below apply for the position of the S/I interface in the one-dimensional and axisymmetric cases, respectively:

$$l(t) = \sqrt{\frac{2\, D_e\ \ m\, C\ \ t}{\rho_d\ \ p}} \tag{10-7}$$

$$r(t)^2\left(\ln\frac{Ro}{r(t)}+\frac{1}{2}\right)-\frac{Ro^2}{2}+\frac{2\,m\,C\ D_e\ t}{p\ \ \rho_d}=0 \tag{10-8}$$

where $l(t)$ is diffusion length, ρ_d the dry density, D_e the effective potassium diffusivity, m the potassium mol mass and p the potassium mass fraction in completely converted material. The other symbols are in accordance with Figure 10-2.

Equation (10-8) gives the $r(t)$ vs t relation in implicit form. A numerical equation solving method, e.g. Newton-Raphson, has to be employed to calculate $r(t)$ for a given time t. Figure 10-3 shows concentration profiles, calculated using Equations (10-6) and (10-8), compared with corresponding FLAC results obtained from axisymmetric model with reaction rate parameters set to give fast conversion (cf Figure 10-2, lower). Figure 10-4 shows corresponding smectite fraction profiles. The vertical lines show interface positions calculated using Equation (10-8). The FLAC run appears to reproduce the propagation of the S/I interface as well as the shape of the concentration profiles very satisfactorily.

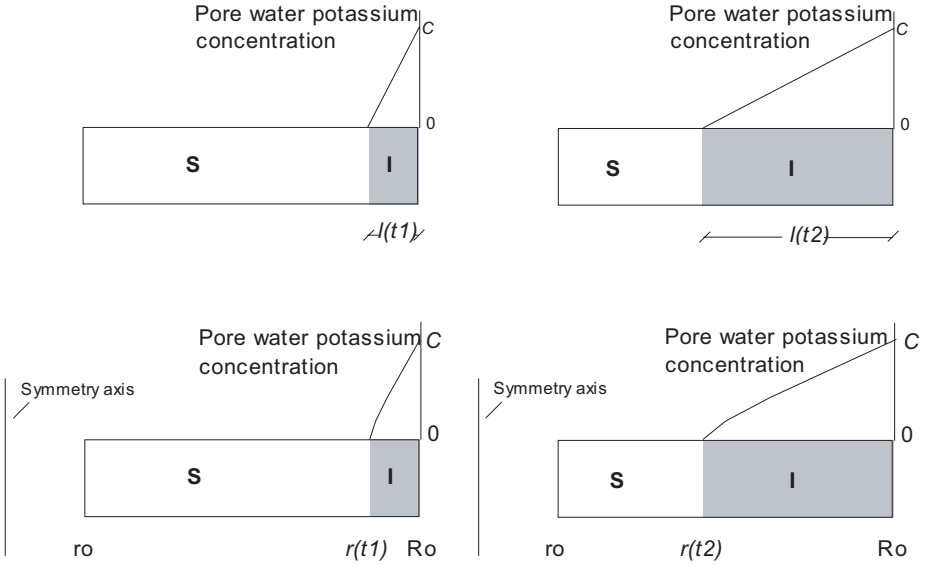

Figure 10-2. *Schematic illustration of one-dimensional system (upper) and axisymmetric system (lower) with quasi steady state diffusion between outer boundary with constant concentration C and moving, zero concentration, I/S interface. The positions of the interface at times t_1 and t_2 are denoted by the diffusion length l(t) and distance to symmetry axis r(t). The potassium concentration between outer boundary and I/S interface is indicated by dashed lines.*

10.5 Examples[3]

10.5.1 General

This section describes an application of the technique developed for modeling such chemical processes in buffer materials that are controlled by reaction rates and by transport of one component essential for the process in question to occur. The application described here is illitization of smectite by fixation of potassium ions in cation exchange positions, and with diffusion of dissolved potassium being the transport process. The technique is verified by comparison with analytical solutions. An overview, based on submodels, is given which outlines under what constellations of assumptions the time scale for conversion of the buffer is controlled by reaction rate parameters and under which conditions transport controls this time scale. Examples are given of calculations performed for deposition holes, with potassium being supplied from the surroundings to the upper parts of the highly compacted bentonite buffer. It is concluded that restrictions in nearfield transport capacity have a very significant effect on the conversion time scale. Towards the end of the assumed period of heating (20 000 years) about 98% of the smectite is found to remain, even for reaction rates and buffer transport conditions that would have left only 10% of the smectite unconverted without nearfield transport restrictions. It is also concluded that the modeling technique can be applied to other, similar, transport/conversion processes.

10.5.2 Calculation of illitization of buffer in deposition hole

Problem: Predict the rate of conversion of MX-80 buffer to illite in KBS-3 deposition hole.

Basic

Figure 10-3 shows a schematic view of a KBS-3 deposition hole and a close-up of a section between waste canister and borehole wall. Two types of models, both axisymmetric, will be analyzed:

- small models (close-up view), and
- full models of 8 m deep deposition hole.

The small models is used for analyzing the fundamental features of the transport/conversion process in the buffer, without regarding restrictions in transport capacity between potassium source and buffer boundary. The full models include assumptions also regarding this capacity.

The following data, which correspond to compacted bentonite with a density of 2000 kg/m^3 at water saturation, were assumed for all models:

Water content, w = 0.26
Porosity, n = 0.41
Dry density, ρ_d = 1590 kg/m^3
Potassium mass fraction of solid, completely converted material, p = 0.05

[3] The examples are provided by Harald Hökmark, Clay Technology AB

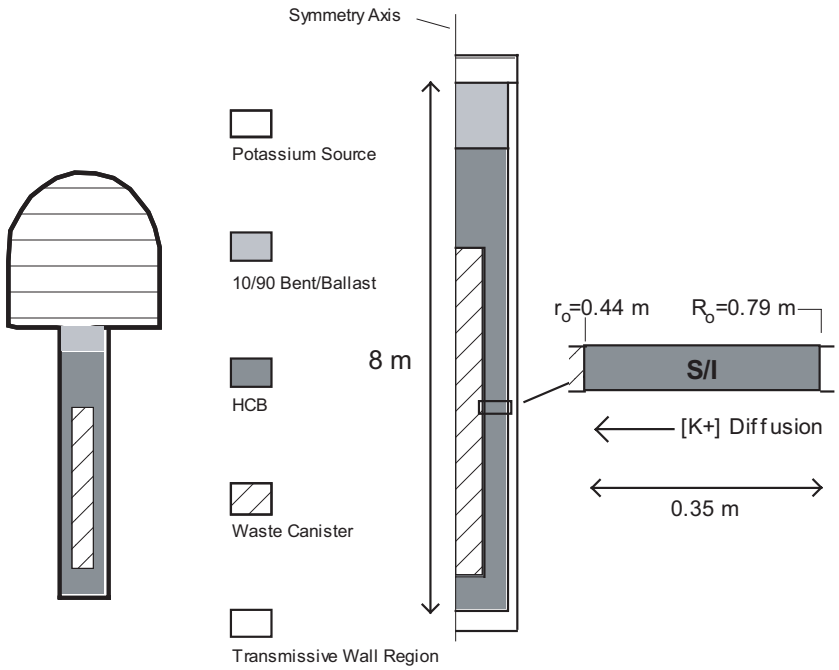

Figure 10-3. *Left: KBS-3 deposition hole in the floor of backfilled deposition tunnel. Right: Conceptual axisymmetric model with close up showing geometry of the small model.*

Conditions regarding diffusivity, potassium concentration and rate constant parameters were varied between the different runs.

Small Models

The following cases will be analyzed:

- **Case 1:** Constant boundary K^+ concentration at the periphery of the deposition hole and constant rate constant, i.e. constant temperature.
- **Case 2:** The K^+ concentration at the cylindrical boundary decreases as potassium is transported into the buffer. The temperature is kept constant.
- **Case 3:** The K^+ concentration at the cylindrical boundary is constant. The conversion rate (i.e. temperature) is reduced with time.

Figure 10-4 shows the results of a large number of runs performed assuming case 1 conditions. The horizontal axis (effective diffusivity times boundary concentration) represents transport, the vertical axis (rate constant times boundary concentration) represents conversion. In the lower left corner both transport and conversion are slow, giving long buffer lifetimes. In the upper right corner both transport and conversion are fast, giving short buffer life times. In the upper left corner conversion is fast, but transport is slow, which means that the buffer life time is controlled mainly by restrictions in transport capacity. In the lower right corner transport is fast, and the buffer life time is controlled by the rate constant, i.e. by temperature, activation energy and frequency factor according to Equation (10-3).

The vertical dotted straight lines in Figure 10-4 represent $[K^+]\cdot D_e$-values that would leave a certain percentage of the 0.35 m buffer unconverted after 5000 years also if conversion would occur instantaneously, i.e. independently of temperature, activation

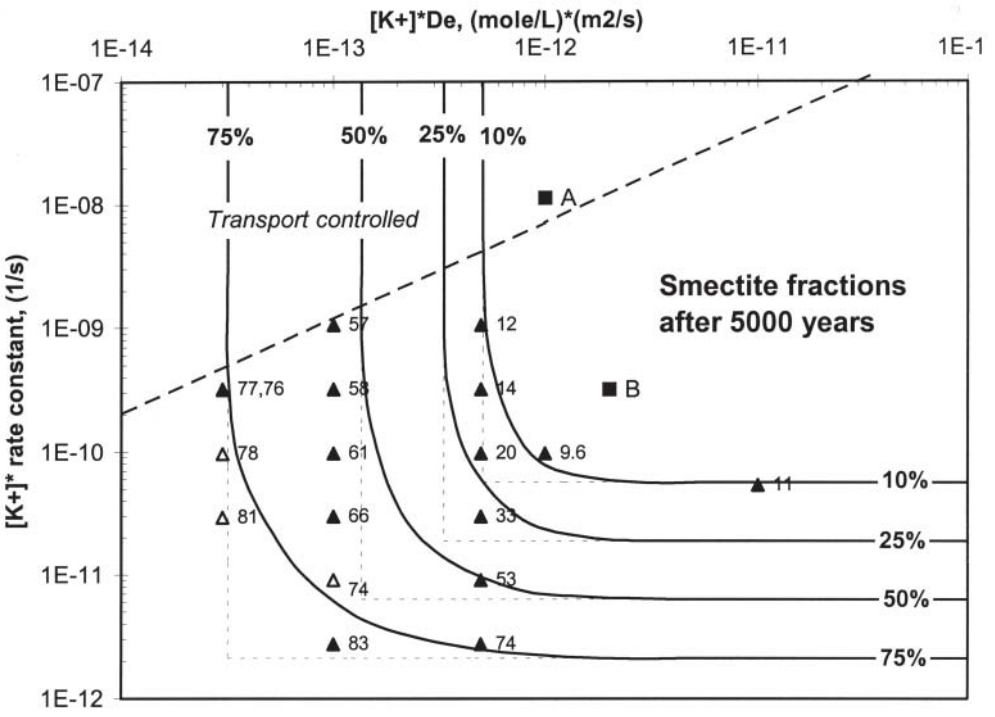

Figure 10-4. *Smectite fractions after 5000 years, assuming boundary concentration and rate constant to be fixed. Filled symbols represent simulations performed with boundary concentration set at 0.01 mole/L. Unfilled symbols represent boundary concentrations ranging between 0.001 and 0.01 mole/L. The region above the dashed line represents constellations of reaction/transport data that would mean a transport-controlled time scale for conversion of the buffer.*

energy and frequency factor. These $[K^+]\cdot D_e$-values are calculated using Equation (10-8). For example: the interface position corresponding to 50% remaining smectite is $r(t)$ = 0.639 m (for the specific radial geometry assumed here). Putting this figure for $r(t)$ and 5000 years (in seconds) for t in Equation (10-8) and then solving for $C\cdot D_e$ gives the value 1.374E-13 (mol/L)*(m^2/s).

The horizontal dotted straight lines in Figure 10-4 represent such values for $[K^+]\cdot k = [K^+]\cdot A\cdot\exp(-E_a/RT)$, that would leave a certain percentage of the buffer unconverted after 5000 years also without transport capacity restrictions. These values are obtained by direct use of Equation (10-3).

The discrete plot symbols in Figure 10-4 represent FLAC results. The labels denote calculated smectite fractions in percent after 5000 years.

The solid curves connecting dotted vertical lines to corresponding horizontal lines are percentage isolines based on the FLAC results, i.e. on the discrete plot symbols.

The filled plot symbols in Figure 10-4 represent runs with boundary porewater potassium concentration = 0.01 mol/L, while unfilled symbols represent concentrations ranging between 0.001 mol/L and 0.01 mol/L. Note that filled and unfilled symbols fit equally well in the isoline system.

Figures 10-5 and 10-6 show smectite fraction profiles obtained for runs performed assuming case 2 conditions, i.e. with decreasing concentration at the buffer boundary. Effects of a well-stirred tank surrounding the buffer is obtained by appending a small

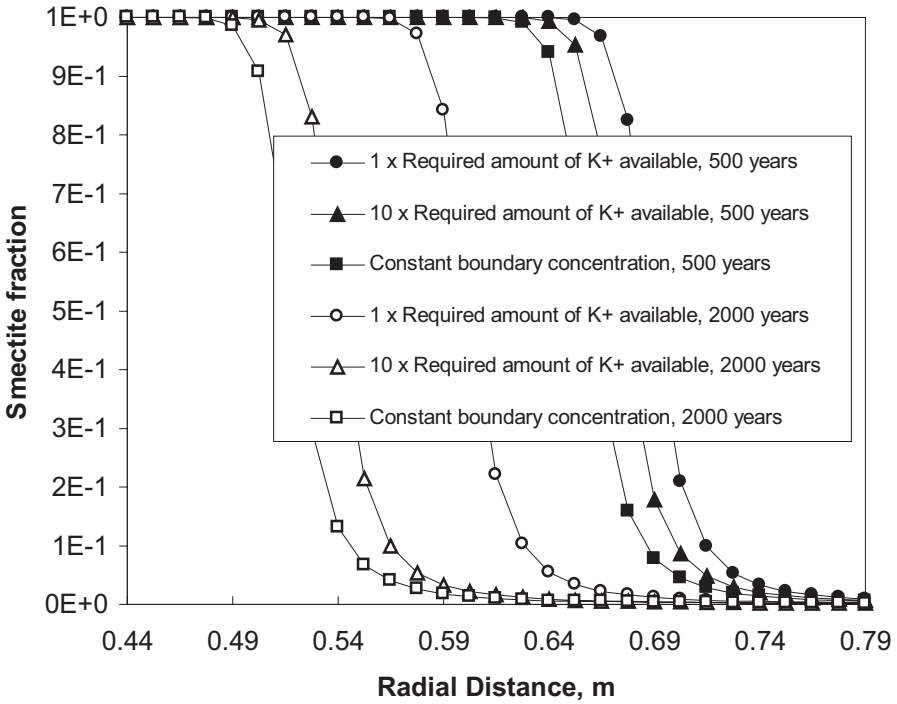

Figure 10-5. *Effects of limitations in potassium availability. Smectite fraction profiles obtained in axisymmetric model with initial conditions corresponding to data point A (Figure 10-4).*

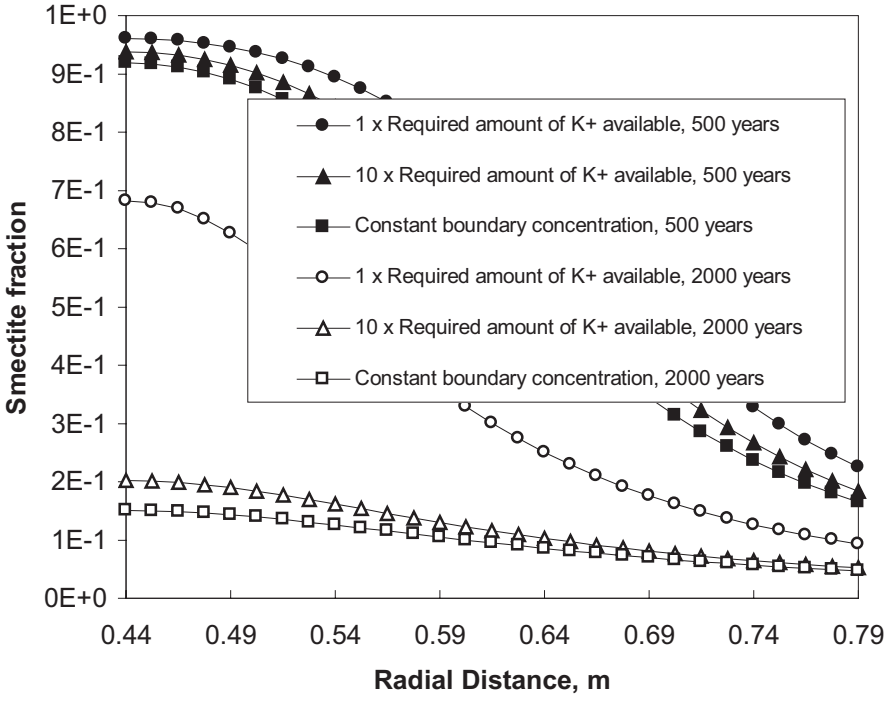

Figure 10-6. *Effects of limitations in potassium availability. Smectite fraction profiles obtained in axisymmetric model, with initial conditions corresponding to data point B (Figure 10-4).*

number of zones outside the buffer boundary, and by assigning FLAC thermal properties representing a specified potassium content and a specified initial potassium concentration to them. Two sets of initial conditions are assumed, represented by the data points labeled A and B in the transport/conversion plot in Figure 10-4. Both sets correspond to fast conversion and fast diffusion, with point A in the transport controlled part. Two assumptions are made regarding the well-stirred tank:

1. It contains exactly the quantity of potassium that is necessary for complete conversion.

2. It contains ten times the necessary quantity.

Corresponding results obtained assuming constant boundary concentration are shown along with the well-stirred tank results.

Figure 10-7 shows smectite fraction profiles obtained assuming case 3 conditions. The initial conditions correspond to data point B in the transport/conversion plot (Figure 10-4). The temperature is assumed to be constant = 423 K during the first 200 years after deposition and then drop linearly to 323 K within the subsequent 1800 years. Corresponding results for the constant temperature system are shown for comparison.

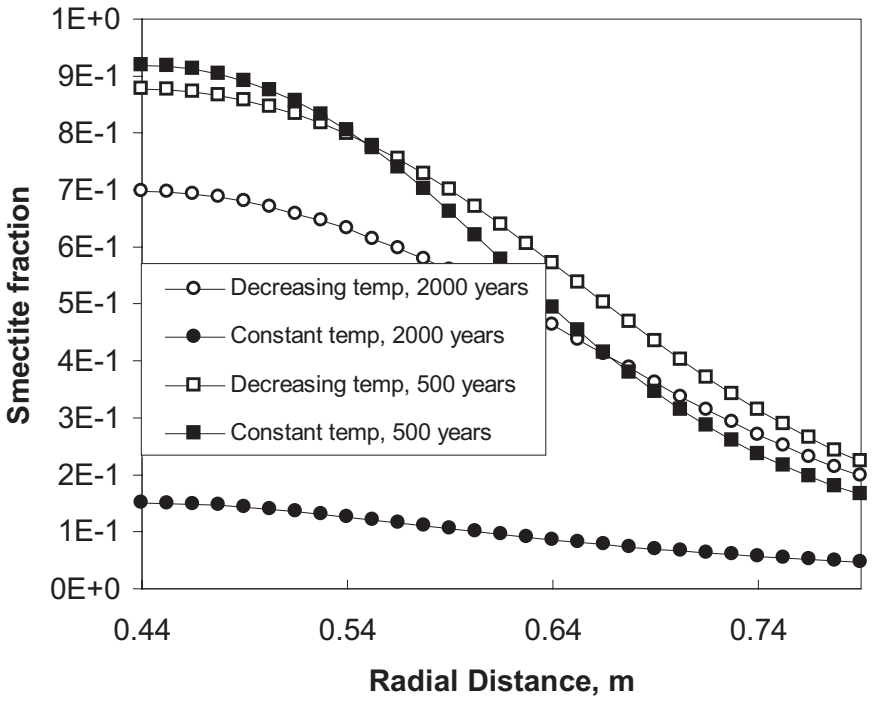

Figure 10-7. *Smectite fraction profiles obtained in axisymmetric model assuming temperature to be constant = 423 K during first 200 years after deposition and then drop to 323 K within the next 1800 years. Filled symbols show corresponding results for constant temperature. The initial conditions correspond to point B in Figure 10-4.*

10.5.3 Full Models

Results from one simulation are presented below. The initial conditions for the buffer and for the boundary concentration correspond to data point B in the transport/ conversion plot (Figure 10-4), i.e.:

A = 80 800 L/(mol,s)
E_a = 24 000 cal/mol
T = 423 K
$[K^+]$ = 0.01 mol/L
D_e = 2E-10 m^2/s
p = 0.05

The temperature is assumed to be constant during the 2000 years that were simulated, i.e. no effects of decreasing conversion rate were accounted for.

Instead of having a constant porewater K^+ concentration at the radial boundary of the buffer volume as for the small models, the concentration boundary is located at the tunnel floor 1 m above the upper part of the buffer. This means that transport of potassium from the tunnel to the buffer is an essential process in these models. The potassium transport is assumed to take place by diffusion through the 1m thick 10/90 bentonite/ballast mixture between HCB buffer and tunnel floor, and through an assumed transmissive, 0.05 m wide, annulus around the borehole periphery. The following additional conditions are assumed:

- Potassium fixation in the 10/90 mixture is not accounted for, i.e. potassium was assumed to diffuse without delay through this 1 m barrier.
- The diffusivity of the 10/90 mixture and the diffusivity of the 0.05 m wide annulus around the borehole periphery are both set to 5E-9 m^2/s.

Figures 10-8 and 10-9 show smectite fraction contours and porewater potassium contours, respectively. It is evident that restrictions in nearfield transport capacity have a very significant effect on the buffer life time. About 98% of the buffer remains after 2000 years despite conservative assumptions, while, for corresponding initial conditions, less than 10% is found to remain in the case of constant concentration on the buffer boundary (Figure 10-4).

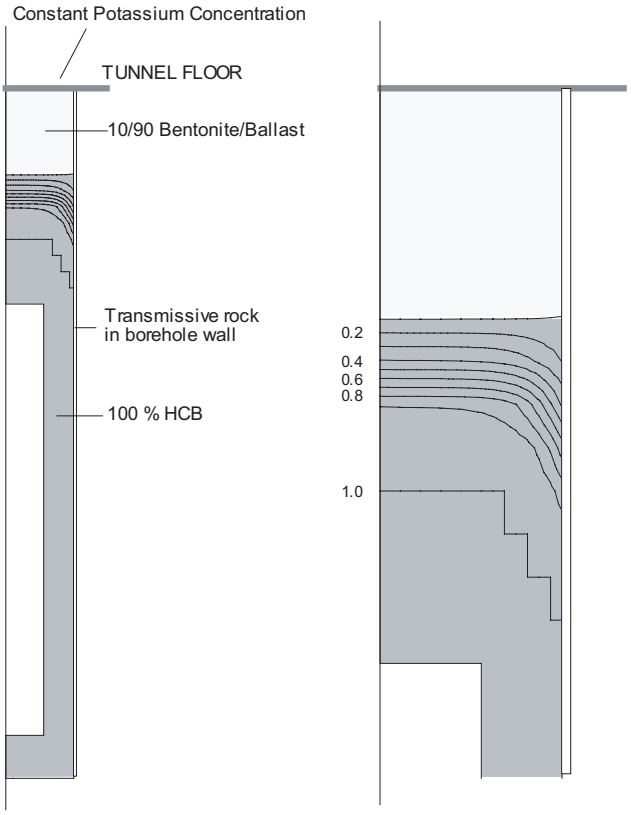

Figure 10-8. *Smectite fraction contours after 2000 years.*

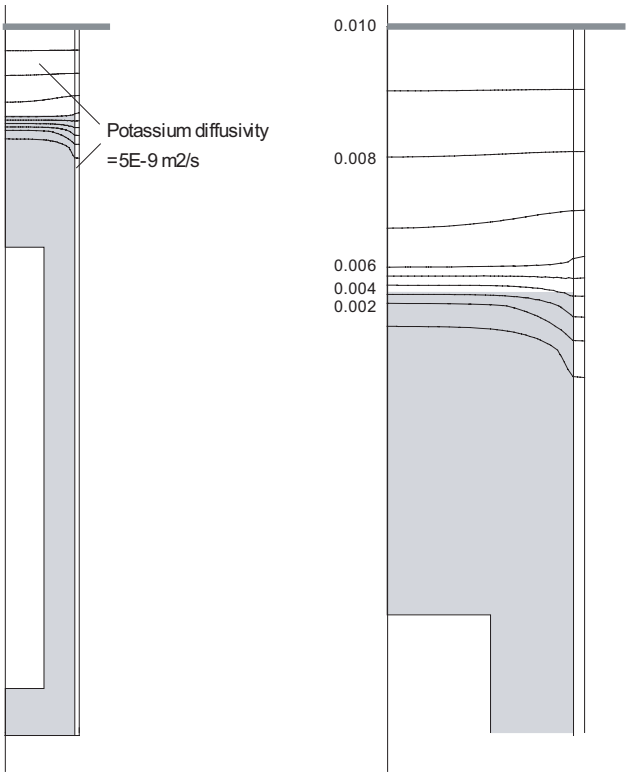

Figure 10-9. *Porewater K^+ concentration contours after 2000 years.*

10.5.4 Comments

It has been demonstrated that the system used in this investigation for simulating the coupled process of potassium transport and illitization gives results that are logical and consistent with the input assumptions. For cases that could be checked with analytical solutions, the results were found to be correct and accurate. Since no really certain data exist regarding conversion rate parameters and potassium concentrations in the tunnel backfill, the calculations have been performed as a series of unprejudiced numerical experiments with parameter values selected only within ranges in which both transport restrictions and reaction rate control the buffer life time. The parameter values proposed by Huang et al, 1993, (E_a=28 000 cal/mol), for instance, would give a system in which reasonable restrictions in transport capacity would have a very small effect on the time scale for conversion of KBS-3 buffers, and have not been included for this purely formal reason. There is, however, no reason to doubt that the simulation system presented here would be capable of describing the conversion process at any level of detail with good accuracy for any set of parameter values.

Predictive and more detailed analyses would require that the change in temperature distribution over time be included, and that an additional gridpoint variable, representing smectite fraction dependent potassium diffusivity, be defined. These modifications could easily be added to the system. In principle it is also possible to simulate the dissolution of potassium in the backfill, provided that the dissolution rate can be approximated with a function of known quantities (e.g. temperature, specific area of ballast, porewater potassium concentration) for which FLAC variables exist or can be defined by use of FISH functions.

10.6 References

/1/ **Pusch R, Karnland O, 1988.** Geological evidence of smectite longevity. The Sardinian and Gotland cases. SKB TR 88-26. Svensk Kärnbränslehantering AB.

/2/ **Pusch R, 1993.** Evolution of models for conversion of smectite to non-expandable minerals. SKB TR 93-33. Svensk Kärnbränslehantering AB.

/3/ **Karnland O, Warfinge P, Pusch R, 1995.** Smectite-to-illite conversion models. Factors of importance for KBS-3 conditions. SKB AR 95-27. Svensk Kärnbränslehantering AB.

/4/ **Huang WL, Otten G A, 1987.** Smectite illitization: effects of smectite composition. In Program and abstracts, 24th Annual Meeting, The Clay Minerals Society, Socorro, New Mexico 75.

/5/ **Itasca, 1993.** Fast Lagrangian Analysis of Continua, Itasca Consulting Group, Internal Report.

/6/ **Crank J, 1975.** The mathematics of diffusion. Oxford University Press.

11 Integrated THMCB modelling

In the design of the engineered barrier system of a repository, modelling of the integrated performance of all the near-field components is required and this is exemplified by the international co-operative work that is performed as part of the EU-supported "Prototype Repository Project" that is a full-scale test of the KBS-3 concept at about 400 m depth in crystalline rock at Äspö, Oscarshamn. The models and some of the major findings are summarized in this chapter.

11.1 Introduction

In this chapter models for predicting the evolution of the buffer and backfill in a KBS-3 repository are summarized and applications exemplified. The models have been worked out by international research groups working for SKB and corresponding organizations in several EU countries and they are presently being used in the international Prototype Repository Project for predicting and evaluating major physical and chemical processes. The behavior of the buffer and backfill is being modelled with respect to temperature (T), water migration (H), stress and strain (M), as well as to chemistry (C) and biology (B). The basis for the development and application of these numerical tools for predicting and evaluating the processes in the engineered barriers is a simplified conceptual model.

11.2 Conceptual buffer performance model

11.2.1 General

Some of the development of THMCB models for current use in repository design is based on the experience from earlier large-scale experiments, primarily the Stripa Buffer Mass Test /1/, which gave rich information with respect to physico/chemical processes that will take place in the buffer at different stages. From these earlier tests it was concluded that the following changes will occur in the system of highly compacted smectitic blocks (MX-80) confined by the overlying backfill and the surrounding rock as indicated in Figure 11-1:

1. Thermally induced redistribution of the initial porewater.
2. Maturation of the 50 mm thick pellet backfill, implying homogenisation and consolidation of this buffer component under the swelling pressure exerted by the hydrating and expanding blocks.
3. Uptake of water from the rock and backfill leading to hydration of the buffer.
4. Expansion of the buffer yielding displacement of the canisters and overlying backfill.
5. Dissolution of buffer minerals and precipitation of chemical compounds in the buffer.

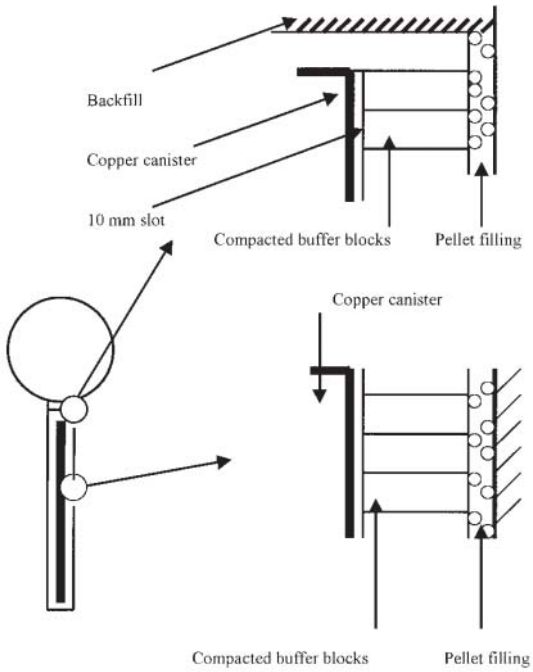

Figure 11-1. *KBS-3 deposition hole with copper-shielded canister embedded in compacted buffer blocks and bentonite pellet filling.*

11.2.2 Redistribution of intially contained porewater in the buffer

Porewater moves in vapour form from the hot part of the buffer towards the cold part where condensation takes place with water moving back by film transport towards the hot part etc. The main consequences of the water redistribution are:

a) The heat conductivity of the inner part of the buffer clay is decreased while the outer part becomes more heat-conductive.

b) The outer, wetted part expands and undergoes some drop in dry density while the inner part shrinks and fractures.

11.2.3 Maturation of the 50 mm gap with pellet backfill

The pellets in the intial 50 mm water-filled gap disintegrate quickly and form a rather soft clay gel from which water is sucked by the very dense clay blocks which thereby expand and consolidate the gel to become as dense as the expanded blocks. The process has a B-effect implying that microbes can enter the pellet filling and survive and multiply until the density of the filling has approached 1600 kg/m^3. The major consequences of the maturation of the pellet filling are:

a) The hydraulic conductivity of the outermost part of the buffer drops and the inflow of water from the rock into the deposition holes decreases.

b) There is competition with respect to water between the densifying pellet filling and the softening buffer blocks.

c) The consolidated clay gel becomes anisotropic because of the induced vertical particle orientation.

11.2.4 Uptake of water from the rock

Uptake of water from the rock and backfill is the THMC process that ultimately yields complete water saturation and the final density distribution. If the rock gives off very little water to the deposition holes the backfill may serve as the major water source. The water transport from the backfill to the buffer is controlled by the water pressure and by the suction of the buffer, as well as by the degree of water saturation of the backfill. The water pressure in the permeable backfill at the contact between buffer and backfill may rise relatively quickly if it is supplied with water from intersected hydraulically active fracture zones but may otherwise be rather low.

The rock around the deposition holes gives off water through discrete hydraulically and mechanically active or activised discontinuities. The hydraulic transport capacity depends on the frequency and conductive properties of the discontinuities, while the distribution over the periphery of the holes is controlled both by the location of the intersecting fractures and by the conductivity of the shallow boring-disturbed zone (EDZ).

The hydration of the buffer and backfill by uptake of water from the rock is associated with expansion of the upper part of the buffer and consolidation of the backfill as well as with axial displacement of the canisters.

The wetting has a C-effect since Ca^{2+}, Mg^{2+}, SO_4^{-2} and Cl^- will be precipitated in the form of minerals with reversed solubility, like sulphates and carbonates, at the wetting front, which moves towards the canister. A rather large part of the buffer may hence contain such precipitates which can interact with the smectite minerals and the canister. The temperature gradient has a C-effect since silicate minerals including the smectite component will dissolve to a larger extent close to the heater than close to the rock by which released silica migrates towards the rock and precipitates in the outer part of the bentonite. The silicification causes cementation and brittleness of the clay. The major consequences of the water uptake are:

a) Water uptake from gives the desired condition of the canisters being completely embedded by a practically impermeable clay medium.

b) The canister may undergo displacement in the course of the wetting of the buffer and afterwards.

c) Expansion of the upper part of the buffer and compression of the contacting backfill changes their hydraulic conductivities. Thermally or tectonically induced compression and shearing of hydraulically active rock discontinuities may have an impact on the ability of the rock to give off water to the buffer in the deposition holes.

d) If the rate of water uptake is slow, salt precipitation in the buffer close to the canisters is enhanced and hence also corrosion of the copper canisters. Also, exposure to vapour given off from the wetting front will affect the clay minerals and cause dissolution and precipitation of silica.

11.3 Numerical codes

11.3.1 General

Several numerical codes are being used in the current modelling of the engineered barriers in the Prototype Repository Project of which two will be described here.

11.3.2 Code "COMPASS", H R Thomas and P J Cleall, Cardiff University, UK /2/

COMPASS (**CO**de for **M**odelling **PA**rtly **S**aturated **S**oil) is based on a mechanistic theoretical formulation, where the various aspects of soil behaviour under consideration, are included in an additive manner. In this way the approach adopted describes heat transfer, moisture migration, solute transport and air transfer in the material, coupled with stress/strain behaviour.

General description of formulation employed

Partly saturated soil is considered as a three-phase porous medium consisting of solid, liquid and gas. The liquid phase is considered to be pore water containing multiple chemical solutes and the gas phase as pore air. A set of coupled governing differential equations can be developed to describe the flow and deformation behaviour of the soil.

The main features of the formulation are described below.

- Moisture flow considers the flow of liquid and vapour. Liquid flow is assumed to be described by a generalised Darcy's Law. Vapour transfer is represented by a modified Philip and de Vries approach.
- Heat transfer includes conduction, convection and latent heat of vaporisation transfer in the vapour phase.
- Flow of dry air due to the bulk flow of air arising from an air pressure gradient and dissolved air in the liquid phase are considered. The bulk flow of air is again represented by the use of a generalised Darcy's Law. Henry's Law is employed to calculate the quantity of dissolved air and its flow is coupled to the flow of pore liquid.
- Deformation effects are included via either a non-linear elastic, state surface approach or an elasto-plastic formulation. In both cases deformation is taken to be dependent on suction, stress and temperature changes.
- Chemical solute transport for multi-chemical species includes diffusion dispersion and accumulation from reactions due to the sorption process.

Heat transfer

Conservation of energy is defined according to the following classical equation:

$$\frac{\partial \Omega_H}{\partial t} = -\nabla.\mathbf{Q} \qquad (11\text{-}1)$$

where Ω_H, the heat content of the partly saturated soil per unit volume is defined as:

$$\Omega_H = H_c(T - T_r) + LnS_a\rho_v$$

T is the temperature, T_r the reference temperature, H_c the heat capacity of the party saturated soil, L is the latent heat of vaporisation, n is the porosity, S_a is the degree of saturation with respect to the air phase and ρ_v is the density of the water vapour.

Following the approach presented by Ewen and Thomas the heat capacity of unsaturated soil H_c at the reference temperature, T_r, can be expressed as:

$$H_c = (1-n)C_{ps}\rho_s + n\left(C_{pl}S_l\rho_l + C_{pv}S_a\rho_v + C_{pda}S_a\rho_{da}\right) \tag{11-2}$$

where C_{ps}, C_{pl}, C_{pv} and C_{pda} are the specific heat capacities of solid particles, liquid, vapour and dry air respectively, ρ_s is the density of the solid particles, ρ_{da} is the density of the dry air, ρ_l is the density of liquid water and S_l the degree of saturation with respect to liquid water.

The heat flux per unit area, **Q**, can be defined as:

$$\mathbf{Q} = -\lambda_T \nabla T + (\mathbf{v_v}\rho_v + \mathbf{v_a}\rho_v)L + \left(C_{pl}\mathbf{v_l}\rho_l + C_{pv}\mathbf{v_v}\rho_l + C_{pv}\mathbf{v_a}\rho_v + C_{pda}\mathbf{v_a}\rho_{da}\right)(T - T_r) \tag{11-3}$$

where λ_T is the coefficient of thermal conductivity of the partly saturated soil and $\mathbf{v_l}$, $\mathbf{v_v}$ and $\mathbf{v_a}$ are the velocities of liquid, vapour and air respectively.

The governing equation for heat transfer can be expressed, in primary variable form as:

$$C_{Tl}\frac{\partial u_l}{\partial t} + C_{TT}\frac{\partial T}{\partial t} + C_{Ta}\frac{\partial u_a}{\partial t} + C_{Tu}\frac{\partial \mathbf{u}}{\partial t} = \nabla.[K_{Tl}\nabla u_l] + \nabla.[K_{TT}\nabla T] + \nabla.[K_{Ta}\nabla u_a] + V_{Tl}\nabla u_l + V_{TT}\nabla T + V_{Ta}\nabla u_a + V_{Tc_s}\nabla c_s + J_T \tag{11-4}$$

where C_{Tj}, V_{Tj}, K_{Tj} and J_T are coefficients of the equation (j = l, T, a, c_s, $\boldsymbol{u}$), and $\boldsymbol{u}$ is a deformation vector.

Moisture transfer

The governing equation for moisture transfer in a partly saturated soil can be expressed as:

$$\frac{\partial(\rho_l n S_l)}{\partial t} + \frac{\partial(\rho_v n(S_l - 1))}{\partial t} = -\rho_l \nabla.\mathbf{v_l} - \rho_l \nabla.\mathbf{v_v} - \nabla.\rho_v \mathbf{v_a} \tag{11-5}$$

where t is the time. The velocities of pore liquid and pore air are calculated using a generalised Darcy's law, as follows:

$$\mathbf{v_l} = -K_l\left(\nabla\left(\frac{u_l}{\gamma_l}\right) + \nabla z\right) + K_l^{c_s}(\nabla c_s) \tag{11-6}$$

$$\mathbf{v_a} = -K_a \nabla u_a \tag{11-7}$$

where K_l is the hydraulic conductivity, $K_l^{c_s}$ is the hydraulic conductivity with respect to chemical solute concentration gradient, K_a is the conductivity of the air phase, γ_l is the specific weight of water, u_l is the pore water pressure, z is the elevation, u_a is the pore air pressure and c_s the chemical solute concentration.

The inclusion of an osmotic flow term in the liquid velocity allows the representation of liquid flow behaviour found in some highly compacted clays. The definition of vapour velocity follows the approach presented by Philip and de Vries. The governing equation for moisture transfer can be expressed, in primary variable form as:

$$C_{ll}\frac{\partial u_l}{\partial t}+C_{lT}\frac{\partial T}{\partial t}+C_{la}\frac{\partial u_a}{\partial t}+C_{lu}\frac{\partial \mathbf{u}}{\partial t}=\nabla.[K_{ll}\nabla u_l]+\nabla.[K_{lT}\nabla T]+\nabla.[K_{la}\nabla u_a]+\nabla.[K_{lc_s}\nabla c_s]+J_l \tag{11-8}$$

where C_{lj}, K_{lj} and J_l are coefficients of the equation (j = l, T, a, c_s, **u**).

Dry air transfer

Air in partly saturated soil is considered to exist in two forms: bulk air and dissolved air. In this approach the proportion of dry air contained in the pore liquid is defined using Henry's law.

$$\frac{\partial[S_a+H_sS_l]n\rho_{da}}{\partial t}=-\nabla.[\rho_{da}(\mathbf{v_a}+H_s\mathbf{v_l})] \tag{11-9}$$

where H_s is the coefficient of solubility of dry air in the pore fluid.

The governing equation for dry air transfer can be expressed, in primary variable form, as:

$$C_{al}\frac{\partial u_l}{\partial t}+C_{aT}\frac{\partial T}{\partial t}+C_{aa}\frac{\partial u_a}{\partial t}+C_{au}\frac{\partial \mathbf{u}}{\partial t}=\nabla.[K_{al}\nabla u_l]+\nabla.[K_{aa}\nabla u_a]+\nabla.[K_{ac_s}\nabla c_s]+J_a \tag{11-10}$$

where C_{aj}, K_{aj} and J_a are coefficients of the equation (j = l, T, a, c_s, **u**).

Chemical solute transfer

Where a chemical solute is considered non-reactive and sorption onto the soil surface is ignored the governing equation for conservation of chemical solute can be defined as:

$$\frac{\partial(nS_lc_s)}{\partial t}=-\nabla.[c_s\mathbf{v_l}]+\nabla.[D_h\nabla(nS_lc_s)] \tag{11-11}$$

where D_h is the hydrodynamic dispersion coefficient defined as:

$$D_h = D + D_d \tag{11-12}$$

D_h includes both molecular diffusion, D_d, and mechanical dispersion, D.

The governing equation for chemical solute transfer can be expressed, in primary variable form, as:

$$C_{c_s l}\frac{\partial u_l}{\partial t}+C_{c_s a}\frac{\partial u_a}{\partial t}+C_{c_s c_s}\frac{\partial c_s}{\partial t}+C_{c_s u}\frac{\partial \mathbf{u}}{\partial t}=\nabla.\left[K_{c_s l}\nabla u_l\right]+\nabla.\left[K_{c_s T}\nabla T\right]+\nabla.\left[K_{c_s a}\nabla u_a\right]+\nabla.\left[K_{c_s c_s}\nabla c_s\right]+J_{c_s} \quad (11\text{-}13)$$

where $C_{c_s j}$, $K_{c_s j}$ and J_{c_s} are coefficients of the equation (j = l, T, a, c_s, **u**).

The approach has been extended to a multi-chemical species form with a sink term introduced to account for mass accumulation from reactions due to the sorption process. This is then coupled to a suitable geochemical model.

Stress-strain relationship

The total strain, ε, is assumed to consist of components due to suction, temperature, chemical and stress changes. This can be given in an incremental form, without loss of generality, as:

$$d\varepsilon = d\varepsilon_\sigma + d\varepsilon_{c_s} + d\varepsilon_s + d\varepsilon_T \quad (11\text{-}14)$$

where the subscripts σ, c_s, T and *s refer* to net stress, chemical, temperature and suction contributions.

A number of constitutive relationships have been implemented to describe the contributions. In particular for the net stress, temperature and suction contributions both elastic and elastoplastic formulations have been employed. To describe the contribution of the chemical solute on the stress-strain behaviour of the soil, as a first approximation, an elastic state surface concept was proposed which described the contribution of the chemical solute via an elastic relationship based on osmotic potentials.

The governing equation for stress-strain behaviour can be expressed, in primary variable form as:

$$C_{ul}du_l + +C_{uT}dT + C_{ua}du_a + C_{uc_s}dc_s + C_{uu}d\mathbf{u} + d\mathbf{b} = 0 \quad (11\text{-}15)$$

where C_{uj} *are* coefficients of the equation (j = l, T, a, c_s, ***u***) and **b** is the vector of body forces.

Numerical solution

A numerical solution of the governing differential equations presented above is achieved by a combination of the finite element method for the spatial discretisation and a finite difference time stepping scheme for temporal discretisation.

The Galerkin weighted residual method is employed to formulate the finite element discretisation. For the flow equations a shape function N_m is used to define an approximation polynomial:

The general flow equation

$$\frac{\partial M}{\partial t} + \nabla . \underline{q} = 0 \tag{11-16}$$

where M refers to mass or enthalpy and $\underline{q}$ refers to the flux term, can be discretised via the Galerkin method as:

$$\int_{\Omega} \left(N_m^t \frac{\partial M}{\partial t} + \nabla N_m^t . \underline{q} \right) d\Omega + \int_{\Gamma_1} N_m^t . \underline{q}^* \, d\Gamma = 0 \tag{11-17}$$

where $\underline{q}^*$ is a flux prescribed at boundary Γ_1.

The same method can be applied to the stress equilibrium equation, which with the use of a shape function N_f, yields:

$$\int_{\Omega} \left(\mathbf{B}^t \mathbf{D} \left(\mathbf{B} du + \mathbf{A_s} du_l - \mathbf{A_s} du_a - \mathbf{A}_{c_s} dc_s - \mathbf{A_s} dT \right) \right) d\Omega - \int_{\Gamma_1} N_f^T \left(\nabla du_a + db_i \right) d\Omega - \int_{\Gamma_1} N_f^T \underline{\tau} d\Gamma = 0 \tag{11-18}$$

where $\mathbf{B}$ is the strain matrix and $\underline{\tau}$ is the surface traction.

Applying this methodology to the governing differential equations, yields, in matrix form:

$$\begin{bmatrix} \mathbf{K_{ll}} & \mathbf{K_{lT}} & \mathbf{K_{la}} & \mathbf{K_{lC_s}} & \mathbf{0} \\ \mathbf{K_{Tl}} & \mathbf{K_{TT}} & \mathbf{K_{Ta}} & \mathbf{K_{TC_s}} & \mathbf{0} \\ \mathbf{K_{al}} & \mathbf{0} & \mathbf{K_{aa}} & \mathbf{K_{aC_s}} & \mathbf{0} \\ \mathbf{K_{C_sl}} & \mathbf{K_{C_sT}} & \mathbf{K_{C_sa}} & \mathbf{K_{C_sC_s}} & \mathbf{0} \\ \mathbf{0} & \mathbf{0} & \mathbf{0} & \mathbf{0} & \mathbf{0} \end{bmatrix} \begin{bmatrix} u_l \\ T \\ u_a \\ c_s \\ \underline{u} \end{bmatrix} + \begin{bmatrix} \mathbf{C_{ll}} & \mathbf{C_{lT}} & \mathbf{C_{la}} & \mathbf{C_{lC_s}} & \mathbf{C_{lu}} \\ \mathbf{C_{Tl}} & \mathbf{C_{TT}} & \mathbf{C_{Ta}} & \mathbf{C_{TC_s}} & \mathbf{C_{Tu}} \\ \mathbf{C_{al}} & \mathbf{C_{aT}} & \mathbf{C_{aa}} & \mathbf{C_{aC_s}} & \mathbf{C_{au}} \\ \mathbf{C_{C_sl}} & \mathbf{C_{C_sT}} & \mathbf{C_{C_sa}} & \mathbf{C_{C_sC_s}} & \mathbf{C_{C_su}} \\ \mathbf{C_{ul}} & \mathbf{C_{uT}} & \mathbf{C_{ua}} & \mathbf{C_{uC_s}} & \mathbf{C_{uu}} \end{bmatrix} \begin{bmatrix} \dot{u}_l \\ \dot{T} \\ \dot{u}_a \\ \dot{c}_s \\ \dot{\underline{u}} \end{bmatrix} + \begin{bmatrix} f_l \\ f_T \\ f_a \\ f_{c_s} \\ f_u \end{bmatrix} = 0 \tag{11-19}$$

where $\mathbf{K_{ij}}$ and $\mathbf{C_{ij}}$ represent the corresponding matrices of the governing equation (i,j=l,T,a,c_s,u).

Equation (11-19) can be rewritten, in a more concise notation, as:

$$\mathbf{A}\phi + \mathbf{B}\frac{\partial \phi}{\partial t} + \mathbf{C} = \{0\} \tag{11-20}$$

where $\boldsymbol{\phi}$ represents the variable vector $\{u_l, T, u_a\ c_s, \boldsymbol{u}\}^t$.

To solve Equation (11-20) a numerical technique is required to achieve temporal discretisation. In this case an implicit mid-interval backward difference algorithm is

implemented since it has been found to provide a stable solution for highly non-linear problems. This can be expressed as:

$$\mathbf{A}^{n+½}\phi^{n+1} + \mathbf{B}^{n+½}\left[\frac{\phi^{n+1} - \phi^{n}}{\Delta t}\right] + \mathbf{C}^{n+½} = \{0\} \tag{11-21}$$

where the superscript represents the time level (the superscript *n* represents the last time interval and *n+1* represents the time level where the solution is being sought). Rearrangement of Equation (11-21) yields:

$$\phi^{n+1} = \left[\mathbf{A}^{n+½} + \frac{\mathbf{B}^{n+½}}{\Delta t}\right]^{-1}\left[\frac{\mathbf{B}^{n+½}\phi^{n}}{\Delta t} - \mathbf{C}^{n+½}\right] \tag{11-22}$$

A solution can be found to Equation (11-22) if **A, B** and **C** can be evaluated. This is achieved via an iterative scheme. For each iteration a revised set of **A, B** and **C** are calculated and the resulting solution checked for convergence against the following criteria:

$$\left|\frac{\phi_i^{n+1} - \phi_{(i-1)}^{n+1}}{\phi_{(i-1)}^{n+1}}\right| \langle \mathbf{TL}_{rel} \tag{11-23}$$

where $\mathbf{TL}_{rel}$ is the relative tolerance and *i* represents the iteration level. Successive iterations are performed until this criteria is satisfied.

With appropriate initial and boundary conditions the set of non-linear coupled governing differential equations can be solved via the numerical solution presented above.

The software package, COMPASS, has been developed to implement the numerical approach detailed above. The package has a modular structure to aid the implementation of suitable code and documentation management systems. It has two main components, namely, a pre and post processor and an analysis 'engine'.

The pre and post processor is a Microsoft Windows graphic user interface (GUI) written in VISUAL BASIC. The GUI allows the definition of problems (including geometry, material parameters, initial conditions and boundary conditions), the generation of finite element meshes and the display of results as contour plots, mesh displacement animations and x–y profiles.

The engine, written in FORTRAN 90, is a modularly structured finite element analysis programme. An extensive library of finite elements is included which allows 1D, 2D plane, 2D axisymmetric and 3D geometry problems to be analysed.

Generic repository

A descriptive example investigated here involves the placement of a full-size heater with a bentonitic buffer material (Figure 11-2). The example has been divided into three distinct phases; the construction of the facility, a 'dwell' period to allow stabilisation of pore water pressures between the buffer, and the rock, and a heating period.

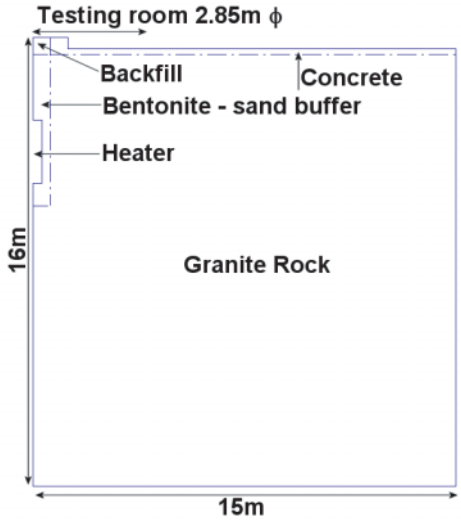

Figure 11-2. *Axisymmetric domain.*

The numerical modelling followed the phases of construction, with the influence from the construction of the underground caverns considered first. Following placement of the buffer a dwell period of 170 days was modelled. Results showed that during the dwell period desaturation occured within the rock for a distance of approximately 1.5 m from the centre of the heater. Finally the heating stage was addressed via a coupled temperature and mass analysis. The results for 210 days of heating are shown in Figure 11-3. The effect of the varying value of thermal conductivity, due both to the different materials and the effect of drying near to the heater, can be clearly seen with distinct changes of gradient in the temperature profile.

Results for the pore water pressures during the heating period are shown in Figure 11-4. It can be seen that in the numerical results the pore water pressure is still increasing after 200 days and the results have not yet peaked.

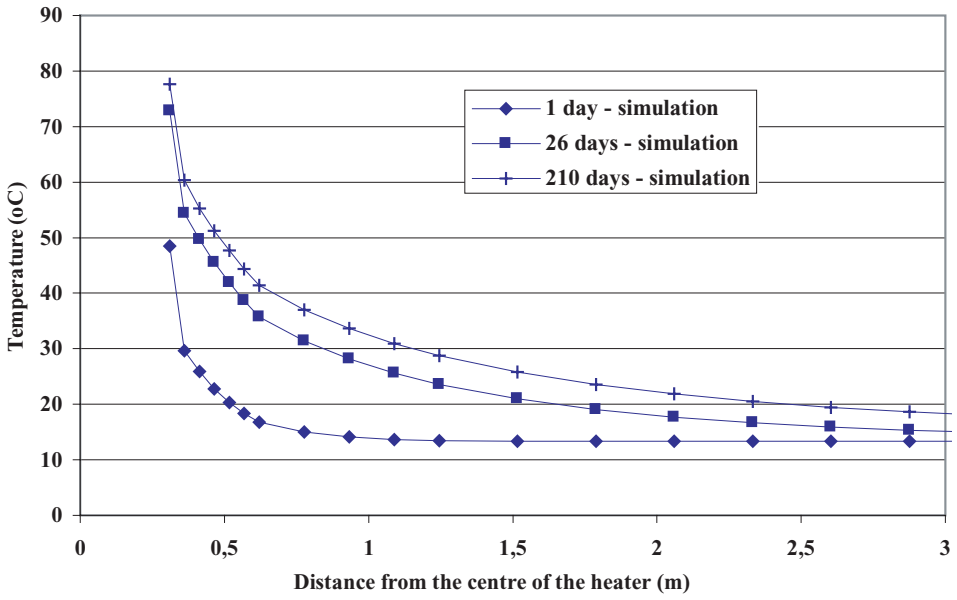

Figure 11-3. *Temperature distributions along the mid-height of the canister.*

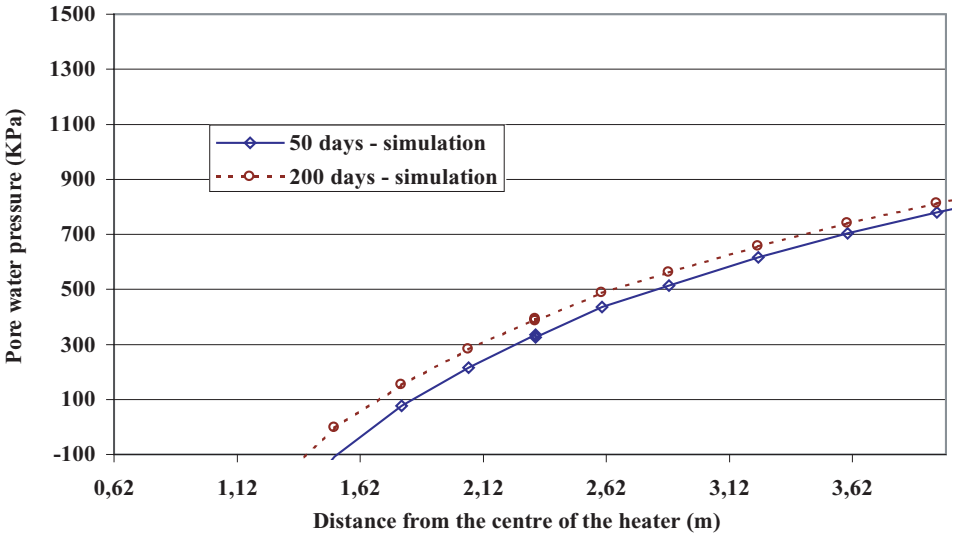

Figure 11-4. *Porewater pressure profiled with time during the heating period.*

11.3.3 Code "ABAQUS", L Börgesson, Clay Technology AB, Lund, Sweden /3/

The finite element code ABAQUS is used for calculating processes in a number of cases in SKB's R&D as shown in preceding chapters. While ABAQUS was originally designed for non-linear stress analyses it has in its present form a capability of describing a large range of transient processes that are relevant to buffers and backfills.

The code includes special material models for rock and soil and ability to model geological formations with infinite boundaries and in situ stresses by e.g. the own weight of the medium. Detailed information of the available models, application of the code and the theoretical background is given in the ABAQUS Manuals.

The model used for water-unsaturated, swelling clay is described here, for the purpose of showing similarities and deviations from other codes used in the Prototype Repository Project.

Hydro-mechanical analysis

The hydro-mechanical model consists of a porous medium and wetting fluid and is based on equilibrium conditions, constitutive equations, energy balance and mass conservation using the effective stress theory.

Equilibrium is expressed by writing the principle of virtual work for the volume under consideration in its current configuration at time *t*:

$$\int_V \sigma : \delta\varepsilon \, dV = \int_S \mathbf{t} \cdot \delta\mathbf{v} \, dS + \int_V \hat{\mathbf{f}} \cdot \delta\mathbf{v} \, dV \qquad (11\text{-}24)$$

where $\delta\mathbf{v}$ is a virtual velocity field, $\delta\varepsilon \overset{def}{=} sym(\partial\delta\mathbf{v}/\partial\mathbf{x})$ is the virtual rate of deformation, $\boldsymbol{\sigma}$ is the true (Cauchy) stress, $\mathbf{t}$ are the surface tractions per unit area, and $\hat{\mathbf{f}}$ are body forces per unit volume. For our system, $\hat{\mathbf{f}}$ will often include the weight of the wetting liquid:

$$\mathbf{f}_w = S_r n \rho_w \mathbf{g} \qquad (11\text{-}25)$$

where S_r is the degree of saturation, n the porosity, ρ_w the density of the wetting liquid and $\boldsymbol{g}$ the gravitational acceleration, which we assume to be constant and in a constant direction (so that, for example, the formulation cannot be applied directly to a centrifuge experiment unless the model in the machine is small enough that g can be treated as constant). For the sake of simplicity we consider this loading explicitly so that any other gravitational term in $\hat{\mathbf{f}}$ is only associated with the weight of the dry porous medium. Thus, we write the virtual work equation as:

$$\int_V \sigma : \delta\varepsilon dV = \int_s \mathbf{t} \cdot \delta\mathbf{v} dS + \int_V \mathbf{f} \cdot \delta\mathbf{v} dV + \int_V S_r n \rho_w \mathbf{g} \cdot \delta\mathbf{v} dV \qquad (11\text{-}26)$$

where **f** are all body forces except the weight of the wetting liquid.

The simplified equation used in ABAQUS for the effective stress is:

$$\overline{\sigma}^* = \sigma + \chi\, u_w \mathbf{I} \qquad (11\text{-}27)$$

where $\boldsymbol{\sigma}$ is the total stress, u_w is the porewater pressure, χ is a function of the degree of saturation (usual assumption $\chi = S_r$), and **I** the unitary matrix.

The conservation of energy implied by the first law of thermodynamics states that the time rate of change of kinetic energy and internal energy for a fixed body of material is equal to the sum of the rate of work done by the surface and body forces. This can be expressed as:

$$\frac{d}{dt}\int_V \left(\tfrac{1}{2}\rho \mathbf{v} \cdot \mathbf{v} + \rho U\right) dV = \int_s \mathbf{v} \cdot \mathbf{t} dS = \int_V \mathbf{f} \cdot \mathbf{v} dV \qquad (11\text{-}28)$$

where:

ρ = current density
v = velocity field vector
U = internal energy per unit mass
t = surface traction vector
f = body force vector

Constitutive equations

The constitutive equation for the solid is expressed as:

$$d\boldsymbol{\tau}^c = \mathbf{H} : d\boldsymbol{\varepsilon} + \mathbf{g} \qquad (11\text{-}29)$$

where $d\boldsymbol{\tau}^c$ is the stress increment, **H** the material stiffness, $d\boldsymbol{\varepsilon}$ the strain increment and **g** is any strain independent contribution (e.g. thermal expansion). **H** and **g** are defined in terms of the current state, direction for straining, etc, and of the kinematic assumptions used to form the generalised strains.

The constitutive equation for the liquid (static) in the porous medium is expressed as:

$$\frac{\rho_w}{\rho_w^0} \approx 1 + \frac{u_w}{K_w} - \varepsilon_w^{th} \qquad (11\text{-}30)$$

where ρ_w is the density of the liquid, ρ_w^0 is its density in the reference configuration, $K_w(T)$ is the liquid's bulk modulus, and

$$\varepsilon_w^{th} = 3\alpha_w(T - T_w^0) - 3\alpha_{w|T^I}(T^I - T_w^0) \tag{11-31}$$

is the volumetric expansion of the liquid caused by temperature change. Here α_w (T) is the liquid's thermal expansion coefficient, T is the current temperature, T^I is the initial temperature at this point in the medium, and T_w^0 is the reference temperature for the thermal expansion. Both u_w/K_w and ε_w^{th} are assumed to be small.

The mass continuity equation for the fluid combined with the divergence theorem implies the pointwise equation:

$$\frac{1}{J}\frac{d}{dt}(J\rho_w S_r n) + \frac{\partial}{\partial \mathbf{x}} \cdot (\rho_w S_r n \mathbf{v}_w) = 0 \tag{11-32}$$

where J is the determinant of the Jacobian matrix and **x** is position.

The constitutive behaviour for pore fluid is governed by Darcy's law, which is generally applicable to low fluid velocities. Darcy's law states that, under uniform conditions, the volumetric flow rate of the wetting liquid through a unit area of the medium, $S_r n \mathbf{v}_w$, is proportional to the negative of the gradient of the piezometric head:

$$S_r n \mathbf{v}_w = -\hat{\mathbf{k}} \frac{\partial \phi}{\partial \mathbf{x}} \tag{11-33}$$

where $\hat{\mathbf{k}}$ is the permeability of the medium and ϕ is the piezometric head, defined as:

$$\phi \overset{\text{def}}{=} z + \frac{u_w}{g\rho_w} \tag{11-34}$$

where z is the elevation above some datum and g is the magnitude of the gravitational acceleration, which acts in the direction opposite to z. $\hat{\mathbf{k}}$ can be anisotropic and is a function of the saturation and void ratio of the material. $\hat{\mathbf{k}}$ has units of velocity (length/time). (Some authors refer to $\hat{\mathbf{k}}$ as the hydraulic conductivity and define the permeability as:

$$\hat{\mathbf{K}} = \frac{\nu}{g}\hat{\mathbf{k}} \tag{11-35}$$

where ν is the kinematic viscosity of the fluid.)

We assume that g is constant in magnitude and direction, so:

$$\frac{\partial \phi}{\partial \mathbf{x}} = \frac{1}{g\rho_w}\left(\frac{\partial u_w}{\partial \mathbf{x}} - \rho_w \mathbf{g}\right) \tag{11-36}$$

Vapour flow

Vapour flow is modelled as a diffusion process driven by a temperature gradient (coded as UEL user supplied routine with stiffness and flow).

$$\mathbf{q}_v = -D_{Tv}\frac{\partial T}{\partial \mathbf{x}} \tag{11-37}$$

where $\mathbf{q}_v$ is the vapour flux and D_{Tv} the thermal vapour diffusivity.

Uncoupled heat transfer analysis

The basic energy balance is:

$$\int_v \rho \dot{U} dV = \int_s q dS + \int_v r dV \tag{11-38}$$

where V is a volume of solid material, with surface area S; ρ is the density of the material; $\dot{U}$ is the material time rate of the internal energy; q is the heat flux per unit area of the body, flowing into the body; and r is the heat supplied externally into the body per unit volume.

It is assumed that the thermal and mechanical problems are uncoupled in the sense that $U = U(T)$ only, where T is the temperature of the material, and q and r do not depend on the strains or displacements of the body. For simplicity a Lagrangian description is assumed, so "volume" and "surface" mean the volume and surface in the reference configuration.

Constitutive equations

The relationship is usually written in terms of a specific heat, neglecting coupling between mechanical and thermal problems:

$$c(T) = \frac{dU}{dT} \tag{11-39}$$

Heat conduction is assumed to be governed by the Fourier law:

$$\mathbf{f} = -\mathbf{k}\frac{\partial T}{\partial \mathbf{x}} \tag{11-40}$$

where $\mathbf{f}$ is the heat flux and $\mathbf{k}$ is the heat conductivity matrix, $\mathbf{k} = \mathbf{k}(T)$. The conductivity can be fully anisotropic, orthotropic, or isotropic.

Coupling of thermal and hydro-mechanical solutions

In ABAQUS the coupled problem is solved through a "staggered solution technique" as shown in Figure 11-5 and below:

1. First a thermal analysis is performed where heat conductivity and specific heat are defined as functions of saturation and water content. In the first analysis these parameters are assumed to be constant and in the subsequent analyses they are read from an external file.
2. The hydromechanical model calculates stresses, pore pressures, void ratios, degree of saturation etc as function of time. Saturation and void ratio histories are written onto an external file.
3. The material parameters update module reads the file with saturation and void ratio data and creates a new file containing histories for saturation and water content. The saturation and water content histories are used by the thermal model in the subsequent analysis.

Steps 1–3 are repeated if parameter values are found to be different compared to those of the previous solution.

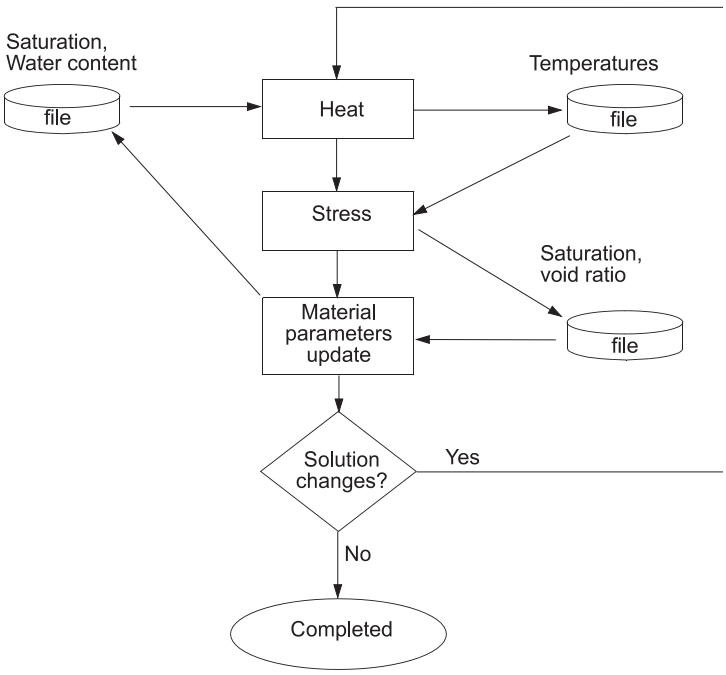

Figure 11-5. *Heat transfer and hydro-mechanical calculations are decoupled. By using the iteration procedure schematically shown above, the effects of a fully coupled THM model are achieved.*

Description of the parameters of the material model of the buffer

Thermal flux that is modelled using the following parameters:

λ = thermal conductivity
c = specific heat

Flux of water in liquid form is modelled by applying Darcy's law with the water pressure difference as driving force in the same way as for water saturated clay. The magnitude of the hydraulic conductivity K_p of partly saturated clay is a function of the void ratio, the degree of saturation and the temperature. K_p is assumed to be a function of the hydraulic conductivity K of saturated clay and the degree of saturation S_r according to Equation (11-41):

$$K_p = (S_r)^{\delta} K \qquad (11\text{-}41)$$

where:

K_p = hydraulic conductivity of partly saturated soil (m/s)
K = hydraulic conductivity of completely saturated soil (m/s)
δ = parameter (usually between 3 and 10)

Flux of water in vapour form is modelled as a diffusion processes driven by the temperature gradient and the water vapour pressure gradient (at isothermal conditions) according to Equation (11-42):

$$q_v = -D_{Tv}\nabla T - D_{pv}\nabla p_v \qquad (11\text{-}42)$$

where:

q_v = vapour flow
D_{Tv} = thermal vapour flow diffusivity
T = temperature
D_{pv} = isothermal vapour flow diffusivity
p_v = vapour pressure

The thermal water vapour diffusivity D_{Tv} can be evaluated from moisture redistribution tests by calibration calculations. The following relations were found to yield acceptable results:

$$D_{Tv} = D_{Tvb} \qquad 0.3 \le S_r \le 0.7 \qquad (11\text{-}43)$$

$$D_{Tv} = D_{Tvb} \cdot cos^{a}\left(\frac{S_r - 0.7}{0.3} \cdot \frac{\pi}{2}\right) \qquad S_r \ge 0.7 \qquad (11\text{-}44)$$

$$D_{Tv} = D_{Tvb} \cdot sin^{b}\left(\frac{S_r}{0.3} \cdot \frac{\pi}{2}\right) \qquad S_r \le 0.3 \qquad (11\text{-}45)$$

where:

a and b are factors that regulates the decreased vapour flux at high and low degree of saturation.

The diffusivity is thus constant with a basic value D_{Tvb} between 30% and 70% degree of saturation. It decreases strongly to D_{Tv}=0 at 0% and 100% saturation. The influence of temperature and void ratio on the diffusivity is not known and not considered in the model.

Hydraulic coupling between the pore water and the pore gas

The pore pressure u_w of the unsaturated buffer material, which is always negative in incompletely saturated material, is modelled as a function of the degree of saturation S_r independently of the void ratio.

$$u_w = f(S_r) \tag{11-46}$$

ABAQUS also allows for hysteresis effects, which means that two relationships can be derived (drying and wetting curves).

Mechanical behaviour of the particle skeleton

The mechanical behaviour is modelled using a non-linear Porous Elastic Model and a Drucker-Prager Plasticity model. The effective stress theory as defined by Bishop is applied and adaptated to unsaturated conditions.

The *Porous Elastic Model* implies a logarithmic relation between the void ratio e and the average effective stress p according to Equation (11-47).

$$\Delta e = \kappa \Delta \ln p \tag{11-47}$$

where κ = porous bulk modulus and ν Poisson's ratio.

The *Drucker Prager Plasticity* model contains the following parameters:

β = Friction angle in the p–q plane
d = Cohesion in the p–q plane
ψ = Dilation angle
$q = f(\varepsilon^d_{pl})$ = yield function

The yield function is the relation between Mises' stress q and the plastic deviatoric strain ε^d_p for a specified stress path. The dilation angle determines the volume change during shear.

Thermal expansion

The volume change caused by the thermal expansion of water and particles can be modelled with the parameters:

α_s = coefficient of thermal expansion of solids (assumed to be 0)
α_w = coefficient of thermal expansion of water

Only the expansion of the separate phases is taken into account. The possible change in volume of the structure by thermal expansion (not caused by expansion of the separate phases) is not modelled. However, a thermal expansion in water volume will change the degree of saturation which in turn will change the volume of the structure.

Mechanical behaviour of the separate phases

The water and the particles are mechanically modelled as separate phases with linear elastic behaviour. The pore air is not mechanically modelled.

Mechanical coupling between the microstructure and the pore water

The effective stress concept according to Bishop is used for modelling the mechanical behaviour of the water-unsaturated buffer material:

$$s_e = (s - u_a) + \chi(u_a - u_w) \qquad (11\text{-}48)$$

Equation (11-48) is simplified in the following way:

$u_a = 0$ (no account is taken to the pressure of enclosed air)
$\chi = S_r$

Required parameters

The required input parameters for the described THM model (ABAQUS) are the following:

- Thermal conductivity λ and specific heat c as function of void ratio e and degree of saturation S_r.
- Hydraulic conductivity of water saturated material K as function of void ratio e and temperature T.
- Influence of degree of saturation S_r on the hydraulic conductivity K_p.
- The basic water vapour flow diffusivity D_{vTb} and the parameters a and b.
- The matric suction u_w as a function of the degree of saturation S_r.
- Porous bulk modulus κ and Poisson's ratio ν.
- Drucker Prager plasticity parameters β, d, Ψ, and the yield function.
- Bulk modulus and coefficient of thermal expansion of water (B_w, α_w)and bulk modulus solids (B_s).
- Bishops parameter χ (usual assumption $\chi = S_r$).
- The volume change correction ε_v as a function of the degree of saturation S_r (the "moisture swelling" procedure).

For the initial conditions one has the following parameters:

- Void ratio e
- Degree of saturation S_r
- Pore pressure u
- Average effective stress p

The software package, ABAQUS, has been developed to implement the numerical approach like the COMPASS code. The engine, written in FORTRAN 90, is a modularly structured finite element analysis programme. An extensive library of finite elements is included which allows 1D, 2D plane, 2D axisymmetric and 3D geometry problems to be analysed. The finite element code ABAQUS is originally designed for non-linear stress analyses. It has been extended very much in the last 10 years and today contains a capability of modelling a large range of processes in many different materials as well as complicated three-dimensional geometry.

The code includes special material models for rock and soil and ability to model geological formations with infinite boundaries and in situ stresses by e.g. the own weight of the medium. Detailed information of the available models, application of the code and the theoretical background is given in the ABAQUS Manuals.

Generic repository

A descriptive example similar to the one based on the COMPASS code is given here. It concerns HM modelling of the buffer and calculation of the displacement of a KBS-3 canister.

HM-modelling of the buffer hydraulically interacting with rock

The boring-induced EDZ extends only to a depth of a few tens of millimeters but yet appears to have an impact on the distribution of water taken up by the buffer as concluded from the Stripa Project (IPR-01-72). Still, the major water-supplying components in the rock are discrete water-bearing fractures that intersect the deposition holes or the EDZ including stress-induced fractures and fissures.

Rock with no fractures but with a EDZ with a hydraulic conductivity of E-10 m/s within 10 mm from the walls of a deposition hole, and rock with two subhorizontal fractures intersecting the hole, have been considered in early calculations using the ABAQUS code. The outcome of the calculation of porewater pressure is illustrated in Figure 11-6. It shows that the negative water pressure in the rock after 4 years with and without fractures is still very substantial, particularly in the fracture-free case.

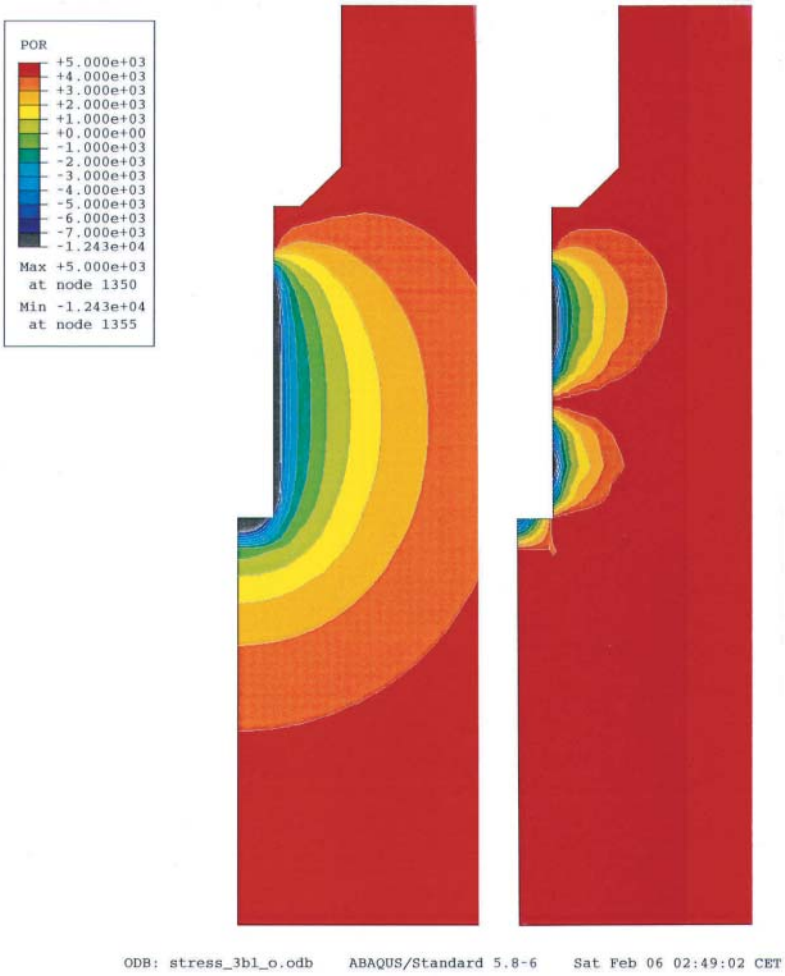

Figure 11-6. *Pore water pressure (kPa) in the rock after 4 years without fracture (left) and with fracture. The suction in the rock is tremendous. (After Börgesson and Hernelind).*

THM-modelling of the buffer saturation

Application of the ABAQUS code shows that it may take between a couple of years and more than 20 years to reach 95% degree of saturation depending on the ability of the rock to give off water to the buffer, the external water pressure, and the hydraulic performance of the EDZ.

Figure 11-7 (upper part) shows the predicted degree of water saturation as a function of the radial distance from the centre of the canister top after 0.5 years (/2), 1.0 year (/3), 2.0 years (/4), 4.0 years (/5), 8.0 years (/6), 16.0 years (/7), and 32.0 years (/8) years assuming rock with no fractures.

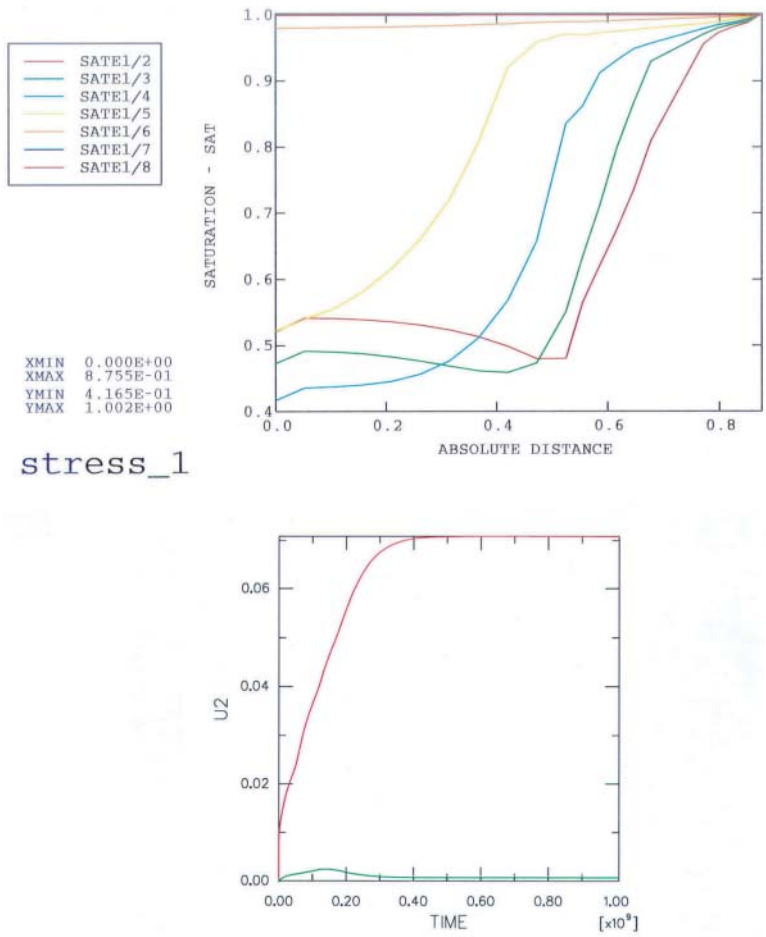

Figure 11-7. *Upper diagram: Degree of saturation as a function of the radial distance from the centre of the canister top after 0.5 years (/2), 1.0 year (/3), 2.0 years (/4), 4.0 years (/5), 8.0 years (/6), 16.0 years (/7), and 32.0 years (/8) years. Lower diagram: Displacement (m) of the canister (green) and the centre of the boundary between the buffer and backfill (red) as a function of time (s). (After Börgesson and Hernelind).*

HM-modelling of rock, buffer and canister – displacement of canister

The expanding buffer displaces the canister and backfill. Figure 11-7 (lower part) shows the predicted displacement (in meters) of the canister (green) and of the boundary between the buffer and backfill (red) as a function of time (s). The upheaval of the interface between buffer and backfill is predicted to be on the order of 7 cm after about one year and stay so for any period of time, and that the canister will move up by a couple of centimeters in half a year and then sink back.

The predicted upward expansion causing displacement of the backfill seems to be in agreement with measurements in the Stripa BMT field experiments where the movement was found to be 7 cm in about 4 years.

11.4 Comments

Several of the other codes used in the Prototype Repository Project show great similarities to the two described here and do not need to be presented. A major deficiency of all the codes is that they do not offer a possibility of including mechanisms involved in chemical degradation of the clay component for showing the associated long-term changes in permeability and expandability. Development of the codes to make it possible to foresee the rate of such mechanisms and their practical influence of the isolating capacity of buffers and backfills remains to be made.

11.5 References

/1/ **Pusch R, Börgesson L, Ramqvist G, 1985.** Final Report of the Buffer Mass Test – Volume II: test results. Stripa Project. SKB TR 85-12. Svensk Kärnbränslehantering AB.

/2/ **Cleall P J, Thomas H R, Melhuish T A, Owen D H, 2002.** Simulation of the behaviour of deep geological repositories – some computational challenges. Numerical Models in Geomechanics – Proceedings of the 8th International Symposium NUMOG VIII, ISBN: 90 5809 359 X.

/3/ **Hibbitt, Karlsson, and Sorensen, Inc, 2002.** ABAQUS manuals.

ISSN 1404-0344

CM Digitaltryck AB, Bromma, 2003